Design at Nano-Scale: Biomimetic Block Copolymers for Polymer-Protein Hybrid Materials

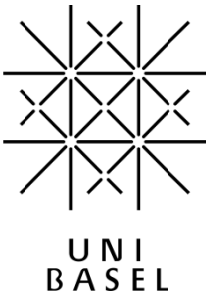

Inauguraldissertation zur Erlangung der Würde eines Doktors der Philosophie, vorgelegt der Philosophisch-Naturwissenschaftlichen Fakultät der Universität Basel

Von

Mariusz Piotr Grzelakowski

Aus Kolobrzeg, Poland

Basel, 2009.

Genehmigt von der Philosophisch-Naturwissenschaftlichen Fakultät auf Antrag von Prof. Dr. Wolfgang Meier (Universität Basel)

und

Prof. Dr. Prof. Dr. Jan van Hest (Radbound University Nijmegen, Netherlands)

Basel, den 28 April 2009

Prof. Dr. Eberhard Parlow

Dekan

ABSTRACT

In this thesis, the synthesis and applications of biomimetic amphiphilic ABA triblock copolymers are discussed. Polydimethylsiloxane hydrophobic middle block was synthesized and end-functionalized. Hydrophilic poly-2-methyl-2-oxazoline blocks were polymerized onto the PDMS macroinitiator, in symmetric cationic ring opening polymerization reaction. The end-groups of the synthesized block copolymers were further functionalized with biotin and methacrylate groups. Block copolymers were designed to self-assemble into vesicular structures in dilute aqueous solutions and the properties of the resulting membranes were tuned by the molecular weight of the hydrophobic blocks and the hydrophilic to hydrophobic ratio. Membranes built from the synthesized triblock copolymers were used to mimic the properties of natural lipid bilayers providing higher stability.

Block copolymer membranes were reconstituted with a number of natural membrane proteins, thus introducing biological activity and functionality to synthetic materials. Insertion of a bacterial Aquaporin-Z channel protein into water (and solutes) impermeable polymeric membrane resulted in novel hybrid materials promising great improvement in the area of water purification. High impermeability and stability of the triblock copolymer membranes provided an excellent tool to investigate the influence of environmental conditions on transport properties of Aquaporin-Z. Combining the outer membrane protein F - reconstituted polymer vesicles, encapsulating water-soluble enzymes, with receptor-ligand mediated immobilization resulted in an development of immobilized polymeric nanoreactors system. Its potential relevance is in the field of microfluidics, sensors and single molecule spectroscopy, as well as basic research on sensitive molecules and chemically/biologically active surfaces. Block copolymer membranes, in combination with a complex membrane protein, NADH: Ubiquinone Oxidoreductase, were used in the design of the electron -transfer nanodevice that allows site-specific reactions driven by redox-potential differences. Vesicular morphology of aggregates formed by triblock copolymers in dilute aqueous solutions was also utilized in the studies towards potential applications as a drug delivery platform. Interactions of block copolymers with lipids of different properties are also discussed.

The structure of the thesis guides the reader through a general introduction to amphiphilic materials, their self-assembly properties and applications (Chapter 1). Polymer-protein hybrid materials are introduced together with membrane proteins used in this work (Chapter 1). The experimental part is divided into two sections: the first describing synthetic routes and characterization of the block copolymers, and the second in the form of original publications, presenting applications of the block copolymers (Chapter 2). Conclusions drawn from our experiments are presented in Chapter 3 and the outlook of our work is outlined in Chapter 4. Information about the materials and methods used and not presented in original publications is shown in Chapter 5 and literature references listed in Chapter 6.

Abreviations list:

AFM	atomic force microscopy
AQP-Z	aquaporin-Z
CLSM	confocal laser scanning microscopy
Complex-I	NADH:Ubiquinone Oxidoreductase
Cryo-TEM	cryogenic transmission electron microscopy
Da	Dalton (g/mol)
DCC	dicyclohexyl carbodiimide
DLS	dynamic light scattering
DMAP	4-dimethylaminopyridine
FCS	fluorescence correlation spectroscopyh hour(s)
FTIR	fourier transform spectroscopy
GPC	gel permeation chromatography
H	hour(s)
IEM	2-isocyanatoethylmethacrylate
IR	infrared spectroscopy
LamB	Maltoporin
MALDI-TOF-MS	matrix assisted laser desorption absorption-time of flight-mass spectrometry
M	mol/L
Mn	number average molecular weight
sec	second
NMR	nuclear magnetic resonance spectroscopy
OmpF	*E. coli* outer membrane porin F
PDI	polydispersity index
PDMS	poly(dimethyl siloxane)
PEG	poly(ethylene glycol)
PMOXA	poly(methyl oxazoline)
ppm	parts per million
Rg	radius of gyration
Rh	hydrodynamic radius
SLS	static light scattering
TEA	triethylamine
TfSA	triflic anhydride
Tg	glass transition temperature
TEM	transmission electron microscopy
THF	tetrahydrofurane
UF	ultra filtration
UV	ultra violet

Objectives and scope

The main objective of this work was to explore the possibility of application of synthetic ABA block copolymers, in new polymer - membrane protein hybrid materials. Combining the advantages of using stable polymer membranes of tunable properties with functions of the specific membrane proteins, incorporated in the membranes of vesicular aggregates, allows the design of bioinspired nanoscale devices with potential application in:

- **Water treatment**: by incorporation of highly selective membrane protein channel, Aquaporin-Z, into otherwise highly impermeable polymer membranes (Chapter 2.4.1).
- **Sensors**: by development of the immobilized protein-polymer nanoreactor system (Chapter 2.4.2).
- **Biomimetics**: by providing a stable and impermeable platform for studying the functions of membranes reconstituted with membrane proteins: water transport and its gating in Aquaporin-Z in different external environmental conditions (Chapter 2.4.3), and proton transfer in NADH: ubiquinone reductase (Chapter2.4.4)
- **Drug delivery:** Receptor-targeted polymer vesicle-based Drug Delivery Formulation of Pravastatin (chapter 2.4.5) and Functionalized Nanocompartments (Synthosomes) with a Reduction-Triggered Release System (Chapter 2.4.6).

In the scope of this thesis, synthesis, modifications, characterization and applications of bio-inspired, symmetric, amphiphilic ABA tri-block copolymers, mimicking and/or substituting natural membranes functions, will be discussed. The self-assembly of the synthesized ABA block copolymers into vesicular structures, mimicking and/or substituting the function of natural membranes, in dilute aqueous solutions was targeted and characterized. Due to the unavoidable presence of lipid molecules in purified membrane protein extracts, interactions of ABA block copolymers with lipids of different chemical and physical properties are also discussed in Chapter 2.4.7.

1. Introduction:

1.1 The science of macromolecules

The science of macromolecules can be divided into two important sections: biomacromolecules (proteins, polysaccharides, etc.) and synthetic polymers. While the former has been mostly studying biomacromolecules in living organisms, the latter focused on the industrial production and improvements of everyday use plastics since the emergence of the interest in high molecular weight materials in 1930`s.[1] The issues addressed in molecular biology, that are so central to protein structure - secondary and tertiary structural motifs, ligand-receptor interactions, had no real analogue in synthetic polymer science. Meanwhile, subjects of polymer science, such as: crystallization, melt dynamics, and rheology had little relevance to biology. With the development of modern techniques and methods, both research routes met each other resulting in multidisciplinary research combining mutual approaches.[2] Thus, in polymer science, we have seen that the focus shifts away from the properties of bulk materials to the search for new functionality by design at the molecular level and control over molecular architecture. In cell biology, new methods of single molecule biophysics allow us to study the behavior of biological macromolecules in their natural environment, rather than in e.g. a protein crystal.[3] This is not yet a full control and understanding of molecular "machines" and their mechanisms, but a step forward towards the understanding of natural processes. The mutual goal of this multidisciplinary research is to create synthetic analogues of the natural systems of molecular sensing and communication of the cell. [4]

One of the examples of successful cooperation between synthetic polymer science and biology, is the development of new macromolecular systems mimicking the structure and behavior of biological objects.[5] Employing of such biomimetics allows not only elucidation and study of the mechanisms of complex biological reactions, energy-efficient separation, and sorting of molecules, but also creation of new candidates for medical applications. The macromolecular self-assemblies are the most promising cell membrane mimetic system so far.[6] Creating complex nanostructures by programmed and controlled interactions of macromolecules, offers the variety of morphologies that can be obtained from block copolymer systems in aqueous solutions[5]. Potential devices inspired by reverse engineering of biology would be of huge practical benefit. Equally significant benefit would be related to deeper understanding of the mechanisms of biology, which would arise from trying to copy it.[2] The following chapter provides an overview on architectures and self assembly of amphiphilic block copolymers, which prove to be excellent candidates for biological – synthetic hybrid materials.

1.2 Amphiphilic block polymers and their self assembly

1.2.1 Amphiphilic block copolymers

Amphiphilic block copolymer, as a term derives from amphiphile (Greek αμφις, amphis: both and φιλία, philia: love, friendship) and describes a chemical compound of polymeric nature, composed of repeating units of hydrophilic and hydrophobic segments linked together by a covalent bond.[7] The architectures of amphiphilic block copolymers, follows the same variety as seen for homopolymers: linear, cycle, multi-arm star, comb, hyperbranched or dendrimeric[8,9]. Figure 1 shows the possible amphiphilic block copolymers architectures. The number of different blocks involved, is limited only by the synthetic route and desired further applications[10].

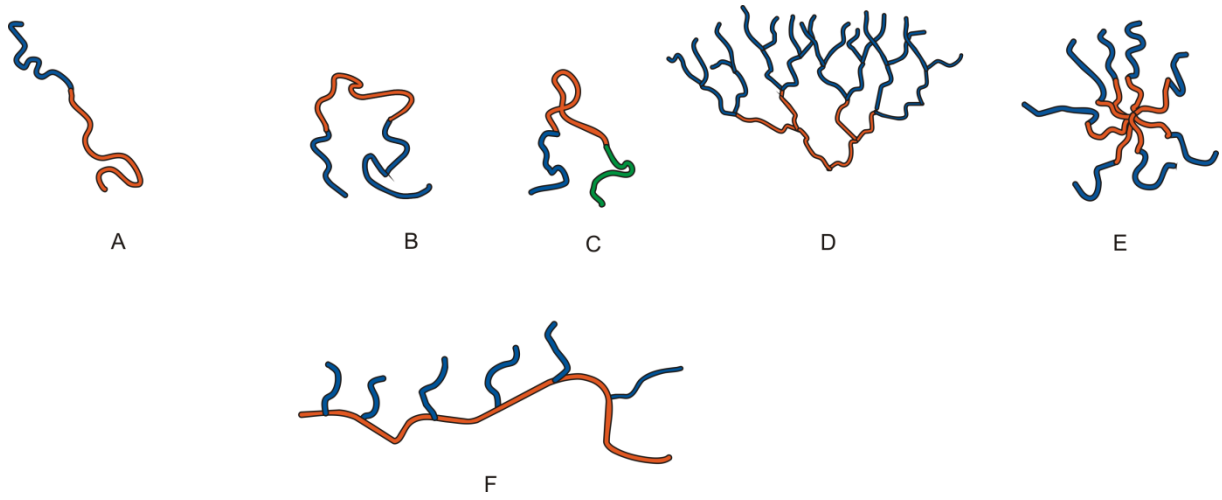

Figure 1. Possible amphiphilic block copolymers architectures: A – AB – diblock, B – ABA triblock, C – ABC – triblock, D – dendrimeric, E – star-shape, F – grafted.[11]

1.2.2 Self assembly of amphiphilic polymers

Similarly to their low molecular mass analogues (surfactants[12] and lipids[13]), amphiphilic block copolymers aggregate in solution. The driving force for self assembly is of a non-covalent nature. The unfavorable contact between one of the blocks, with solvent molecules of different polarity, triggers organization of macromolecules[11], while the covalent bond between the "incompatible" blocks prevents the macrophase separation. Thus, the process is driven by an unfavorable mixing enthalpy and low mixing entropy.[10] The kinetic behavior of chain rearrangements, due to high molecular weights of the block copolymers, can influence the phase behavior of amphiphilic systems. Figure 2 shows a schematic representation of possible aggregate morphologies from amphiphilic block copolymers.

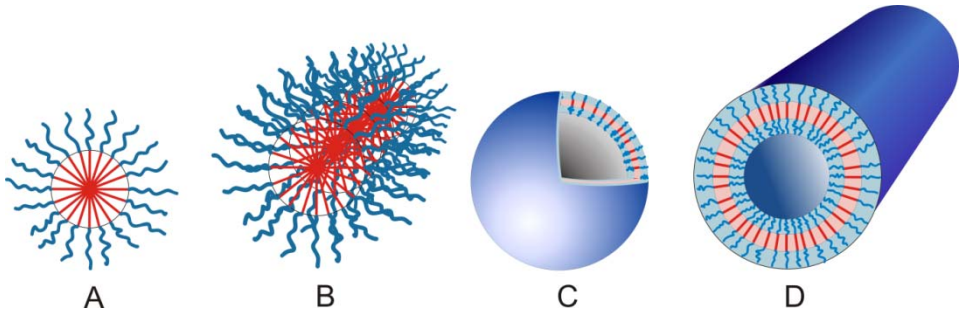

Figure2. A schematic representation of possible aggregate morphologies from amphiphilic block copolymers: A – spherical micelle, B - worm-like micelle, C - vesicle, D - tube.[11]

The morphology of resulting aggregates is governed by the nature of the building blocks, architecture of the block copolymer, weight fraction of the hydrophilic block and solvent type[10]. Additional factors influencing morphologies of the aggregates are: concentration of the block copolymer[14], temperature[15, 16], pH[15], presence of salts[15,16] and polymer purity (molecular weight distribution and presence of the homopolymer)[17].

In Figure 3, the phase diagram of amphiphilic poly(ethylenoxide)-co-poly(butylene oxide) (PEO-PBO) is presented, showing the evolution of the aggregates from bulk lamellae, interconnected sponge, hexagonally packed vesicles and dilute single vesicles upon increase of water content[14].

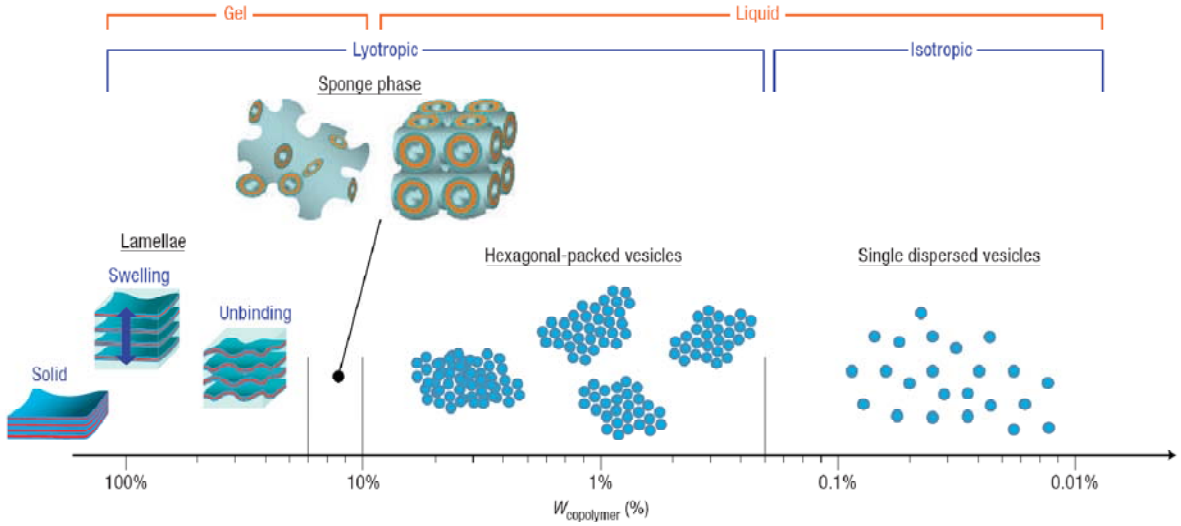

Figure 3. The phase diagram of $PEO_{115}PBO_{103}$ in water. Four different phases have been identified. On dilution the phase sequence is shown to be lamellae, sponge phase, hexagonal-packed vesicles and singularly dispersed vesicles; $W_{copolymer}$ is the w/w percentage of copolymer in solution.[14]

1.3 Membrane formation

1.3.1 Natural membranes and liposomes

In nature lipids, proteins and polysaccharides self assemble into bilayers, setting up the cell boundary - cell membrane - crucial to cell`s life. Cell membranes maintain the essential differences between the cytosol and the extracellular environment, and content of organelles and cytosol. Cell membranes are fluid dynamic structures where all of their building molecules are able to diffuse in plane of ca. 5 nm thick lipid bilayer. Figure 4 shows a schematic representation of a lipid-based membrane, with different classes of membrane associated proteins.[18]

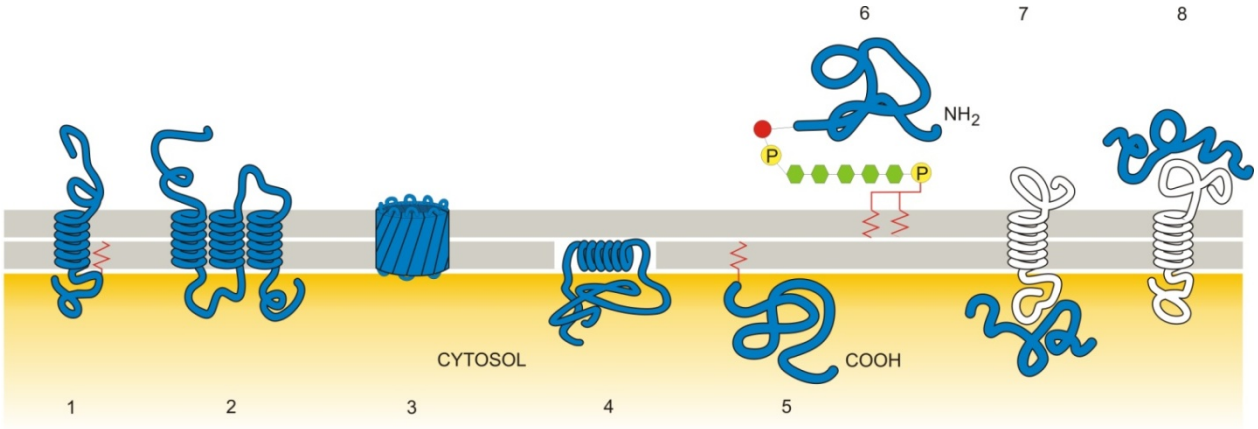

Figure 4. Association of different types of membrane proteins with a lipid bilayer. (1) Single α helix, (2) multiple α helices, (3) a rolled-up β sheet (ß barrel), (4) α helix partitioned into cytosolic lipid monolayer by hydrophobic face of the helix, (5) covalent attachment to lipid molecule, (6) attachment via oligosaccharide linker, (7) and (8) noncovalent attachment by protein-protein interations.[18]

Membrane models, such as liposomes (vesicles built from lipid molecules), resulted from gradual understanding of natural membrane properties like composition, dimensions, selectivity, permeation pathways, response to solutes, influence of temperature and pressure.[13] Another important aspect of studying liposomes - encapsulation of hydrophilic molecules - made great impact on the pharmaceutical industry. Liposomes were first proposed as a drug delivery system around 1974 by Gregoriadis[19]. As the most important requirements for effective liposomal drug delivery system, one should mention: quantitative retention of drugs, control over the rate of clearance from circulatory system (or from compartments of the body where the drug was locally administered), and access or preferential uptake by the target. Despite the number of liposome-based injectable formulations that have arrived to the market, the stability of lipid vesicles remains a key issue. In order to prolong the

circulation time of small liposomes, they are modified by covalent attachment of polyethylene glycol chains. This makes the liposome surface more hydrophilic, providing "invisibility" to the immune system and protects them from high-density lipoprotein-promoted destabilization.[20] This approach is the most exploited in pharmaceutical macromolecular drug delivery systems.

To achieve higher specificity of liposomal drug carriers towards the targeted cells, liposomes were modified with covalently attached cell-specific ligands, in order to recognize the target, bind to it, and, if possible, penetrate the cell membrane towards the cell interior. The use of polyclonal antibodies against a variety of tumor cell lines was shown to be successful in vitro[20]. In vivo experiments used polyclonal antibodies targeting solid tumor and galactose-terminating glycoprotein (known for its specific binding to liver`s galactose recepton) [20]. Those results and subsequent studies, using vesicles of varying structural characteristics, incorporating anti-target monoclonal antibodies (immunoliposomes) or other cell-specific ligands[20], lead to established conditions for optimal targeting, and showed the limitations of this approach. For example, the presence of immunoglobulin on the liposome surface promotes accelerated interception of the aggregates by liver and spleen. A promising solution to overcome the clearance of such liposomes, is to combine the immunoliposomal approach with described above PEGylation, thus extending the liposome life time in the circulation system.[20]

1.3.2 Properties of the ABA platform

Despite all advantages of using natural or synthetic lipids for model membranes or carrier systems, there are serious drawbacks resulting from the nature of the lipid molecules themselves. The molecular weight of a typical lipid does not exceed 1000 g/mol resulting in formation of thin (ca. 5 nm) and, in most cases, fluid membrane structures. Due to lipid sensitivity to lipid oxidation, these membranes are characterized by relatively high permeability and fragility[21], thus limiting the scope of aplications.[4, 5] As described in chapter 1.1, the so far best solution to the insufficient stability of liposomal systems is to transfer the methodology of lipidic membranes to macromolecular amphiphilic systems. We have the possibility to design and synthesize amphiphilic block copolymers of different types (AB, ABA, ABC), which self-assemble to superstructures resembling lipid bilayers.

The platform chosen for our studies is based on ABA block copolymers, where hydrophilic – (A) blocks are composed of 2-methyl-2-oxazoline repeating units and the hydrophobic – (B) blocks of dimethylsiloxane repeating units. Polydimethylsiloxanes possess the unique combination of properties, not shown by any other polymeric material, including: extremely low glass transition temperatures (-120°C), very high chain flexibility, good oxidative, thermal and UV stability, water repellency, physiological inertness, high gas permeability and excellent atomic oxygen and oxygen plasma

resistance. From the synthetic point of view, an additional attractive feature of these highly hydrophobic and surface active polymers is their solubility in many commonly used nonpolar solvents, in contrary to comparable, but insoluble highly fluorinated polymers.[22] The interest in hydrophilic polyoxazolines originates from the research in the field of biocompatible materials for medical applications.[23] It was reported that both homo- and co-polymers of poly(2-oxazoline)s are non-toxic.[24] Polyoxazolines possess the same protein-repellent properties as PEG. Thus, particles from polyoxazoline-containing amphiphilic block copolymers are interesting candidates for drug-delivery systems. In addition, in contrary to PEG, it is relatively easy to bring desired end-functionality[25], as well as partial or full chain functionality in the polyoxazoline blocks.[23]

1.4 Polymer - membrane protein hybrid materials

As indicated in Chapter 1.3.1, membrane proteins are active components of cell membranes. They regulate cell communication and response to the environment through signaling pathways and molecular transport. Many membrane proteins were identified as drug targets and are the subject of intense studies because of their biotechnological potential. Hybrid materials consisting of naturally occurring proteins embedded in artificial membranes have the application potential in sensor technology, diagnostics, gene therapy, rapid drug screening, targeted drug delivery and as protein investigation platform (e.g. structural biology via protein crystallization). There were many attempts to realize these applications using lipid membranes[26, 27], however, load retention, and poor stability often pose problems. These problems could be overcome by substitution of lipids by synthetic polymers. In addition, block copolymer chemistry broadens the range of achievable material properties. There are two main experimental approaches to study proteins embedded in polymer membranes, either using planar membranes or vesicles. The former system is useful for conductance measurements or the fabrication of functionalized surfaces, but does not resemble the natural membranes[28 29]. Many details of the mechanism of membrane protein incorporation in polymeric bilayers are still poorly understood. Natural receptors and channels are designed to span a hydrophobic lipid membrane core of 3–4 nm. Since in block copolymer membranes this thickness is exceeded by several fold, they would appear unsuitable to host transmembrane proteins in their functional state. Despite this thickness mismatch, however, experimental and theoretical evidence confirms the successful incorporation of natural proteins in such an artificial matrix. Figure 5 shows a schematic representation of AB diblock copolymer chains conformation near a protein inserted in a polymeric bilayer.[30]

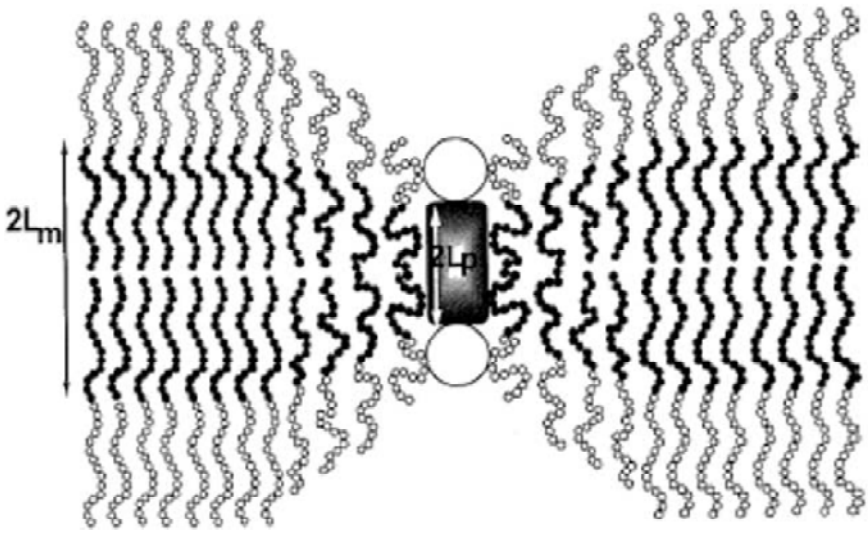

Figure 5. A schematic representation of AB diblock copolymer chains near a protein inserted in a polymeric bilayer. [30]

For instance, the channel proteins Outer membrane protein F (OmpF) and maltoporin (LamB) were successfully incorporated into free-standing PMOXA-PDMS-PMOXA block copolymer membranes with a hydrophobic thickness of 10 nm.[31] Conductance measurements revealed that the protein functionality is not influenced by the surrounding membrane and is preserved even after cross-linking of the polymer chains[32]. The experimental data were confirmed by a theoretical model by mean-field analysis, which calculated the energetics and thickness profiles of diblock copolymer membranes in the presence of a transmembrane protein.[30] It was found that membrane perturbations by the protein may extend laterally to distances of 25–30 nm (or 3–4 times the bilayer thickness). This length scale also determines the range over which embedded proteins interact. The perturbation energy increases as a function of thickness mismatch, although only moderately. This means proteins are able to insert into polymer membranes even if they are considerably shorter than the unperturbed membrane width.

This line of research produces materials that are not just passive structural components but promise design of stable structures that are biologically active and able to respond to outside stimuli.[33]

1.4.1 Aquaporins

Water transport across biological membranes is not fully explained by simple diffusion through the lipid bilayer. Observations of highly water-permeable tissues led to the development of theoretical tools for the study of osmotic and diffusion processes across membranes and pores, and prompted the long pursuit of the molecular entity responsible for water transport. The first characterized water

channel, aquaporin-1 (AQP-1), was serendipitously identified and purified from human red blood cells. Expression of AQP1 mRNA in *Xenopus oocytes* led to its recognition as the erythrocyte water channel, a conclusion confirmed by liposome reconstitution with highly purified AQP1[25]. Screening of mRNA libraries prepared from different tissues permitted identification of at least ten mammalian homologues. Multiple homologues have also been identified in other vertebrates, plants, yeast and bacteria. Some of the identified proteins are highly specific for water transport ("orthodox aquaporins"), whereas others transport water, glycerol and other small molecules ("aquaglyceroporins"). The amino acid sequences of aquaporins are approximately 30% identical; however, the conserved residues are distributed in defined clusters, which themselves are fully conserved throughout the family[32]. All homologues are predicted to contain six transmembrane segments formed by the tandem duplication of three transmembrane domains joined in obverse symmetry. The N and C termini reside in the intracellular space, leaving three extracellular and two intracellular connecting loops. Figure 6 shows a schematic representation of predicted primary sequence and membrane topology of 10-His-Aqaporin-Z.[26, 34]

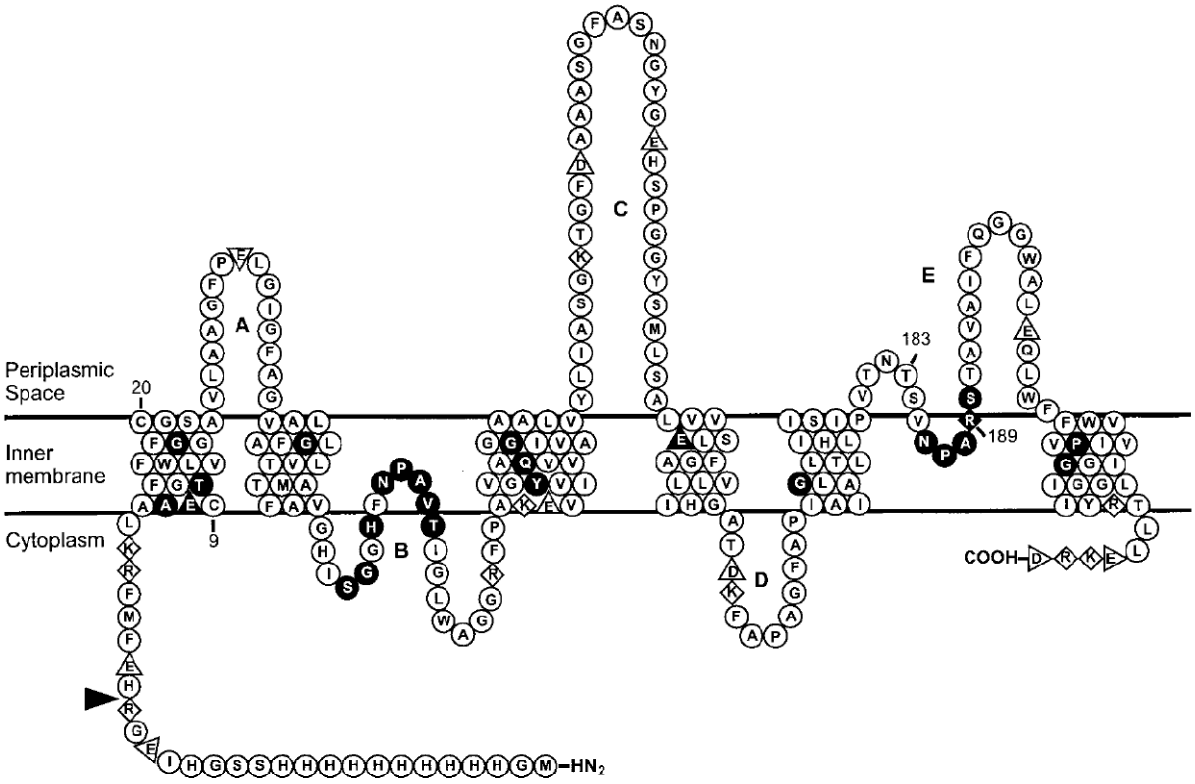

Figure 6. Predicted primary sequence and membrane topology of 10-His-AqpZ.[26]

Loops B and E share the most highly conserved residues, suggesting that they may be directly responsible for the channel selectivity. Because several residues in these loops are hydrophobic, it was proposed[26] that loops B and E fold into the membrane-spanning region of each subunit and are surrounded by the six transmembrane segments forming a structure referred to as the ”hourglass”. Although each subunit apparently contains a single water pore, AQP1 and other aquaporins are believed to exist as tetramers in mild detergents and in the native membranes[26]. Even though certain well-defined residues distinguish aquaporins from aquaglyceroporins, the molecular determinants of the functional differences between the two groups are far from clear. Their elucidation awaits the structural and biophysical characterization of multiple homologues, chimeras and mutants. Single channel water permeability is hard to determine in this system due to the lack of an accurate method for quantification of plasma membrane protein expression, the possible contribution of endogenous proteins, and differences in membrane trafficking. Because AQP1 is commonly purified from human red blood cells, structure-function analysis is currently limited to the wild-type molecule. Thus, development of expression systems and purification methods for large quantities of wild-type and modified aquaporins is essential for understanding the molecular basis of aquaporin`s biophysical properties. AQP-Z, the aquaporin from E. coli, was identified as a good candidate for purification following overexpression in bacteria, and recognized as a good substrate for structure-function studies.[26, 34]

Figure 7 shows the shape of the aqueous pore (blue), derived from calculations based on the structure of bovine AQP1[35]. The four water molecules shown in bold colors represent transient interactions with the pore-lining residues at discrete sites. Bulk water in the extracellular and intracellular vestibules is depicted in pastels. Three features of the channel specify selectivity for water: (a) Size restriction: 8 Å above the midpoint of the channel, the pore narrows to a diameter of 2.8 Å (approximately the diameter of a water molecule). (b) Electrostatic repulsion: the conserved residue (Arg-195), at the narrowest constriction of the pore, imposes a barrier to cations, including protonated water (H_3O^+). (c) Water dipole reorientation: two partial helices meet at the midpoint of the channel, providing positively charged dipoles that reorient a water molecule as it crosses this point. Disrupting hydrogen bonds in the single-file chain of water molecules prevents proton conductance.[35]

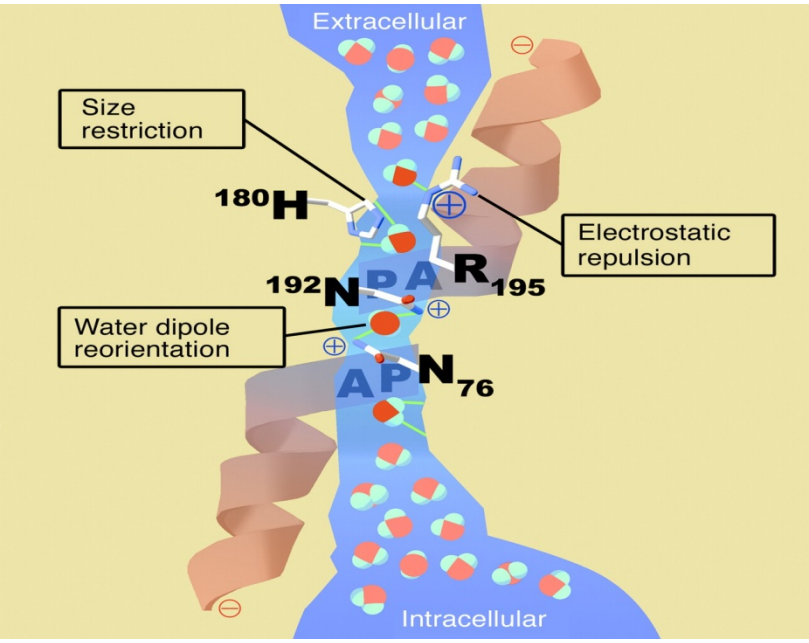

Figure 7. A schematic architecture of the channel within an AQP1 subunit.[35]

1.4.2 Outer membrane protein F (OmpF)

The outer membrane protects Gram-negative bacteria against harsh environment. At the same time, the embedded proteins fulfill a number of tasks that are crucial to the bacterial cell, such as solute and protein translocation, as well as signal transduction. Unlike membrane proteins from other organisms, integral outer membrane proteins do not consist of transmembrane α-helices, but instead fold into antiparallel ß-barrels. [36] Over recent years, the atomic structures of several outer membrane proteins from six families have been determined. They include general porins (e.g. OmpF) and substrate-specific porins (e.g. LamB). Crystallographic studies yielded invaluable insight into and significantly advanced the understanding of the functions of these intriguing proteins.[36]

Membrane proteins expose their hydrophobic surface to the lipid bilayer core, a property that distinguishes them from water-soluble proteins. As mentioned before, all integral membrane proteins, known till now, consist of either α-helical bundles, or β-pleated sheets in the form of a closed barrel. These architectures not only define two classes of membrane proteins, but also correlate with the location: while α-helical bundles are only found in the cytoplasmic membrane, β-barrels are restricted to the outer membrane. It is generally assumed that this differentiation originates from the biogenesis of outer membrane proteins: their polypeptide chains have to cross the cytoplasmic membrane, which

would not be possible if they were too hydrophobic.[36] Figure 8 shows a bacterial β-barrel membrane protein, OmpF, as seen from the plane of the membrane and from the top of the membrane.

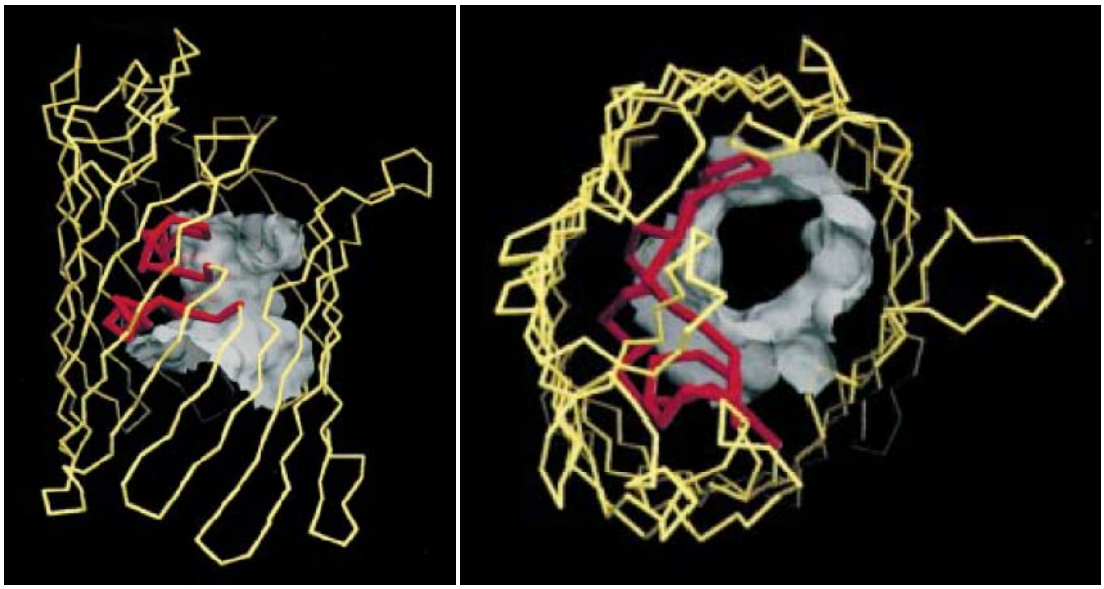

Figure 8. Bacterial β-barrel membrane protein OmpF , as seen from the plane of the membrane (left) and from the top of the membrane (right). The polypeptide backbone is shown in yellow, and protein segments that constrict the barrel interior (loop L3) are shown in red.[36]

The general diffusion pores formed by porins allow the diffusion of hydrophilic molecules (up to 600 Da) and show no particular substrate specificity, despite some selectivity for either cations or anions. A general porin, OmpF, was the first membrane protein to yield crystals of a size and order suitable for high resolution structural analysis by X-ray crystallography. However, it took more than 10 years before the atomic structure of the osmotically regulated bacterial porin OmpF was elucidated. [36]

Unlike other loops, the OmpF`s third loop, L3, is not exposed to the cell surface but folds back into the barrel, forming a constriction zone at half the height of the channel, giving it an hourglass-like shape. Therefore, this loop contributes significantly to the permeability properties of the pore, such as exclusion limit and ion selectivity. At the constriction site, strong transverse electrostatic field is caused by acidic residues in loop L3 and a cluster of basic residues at the opposite barrel wall (Fig. 9).

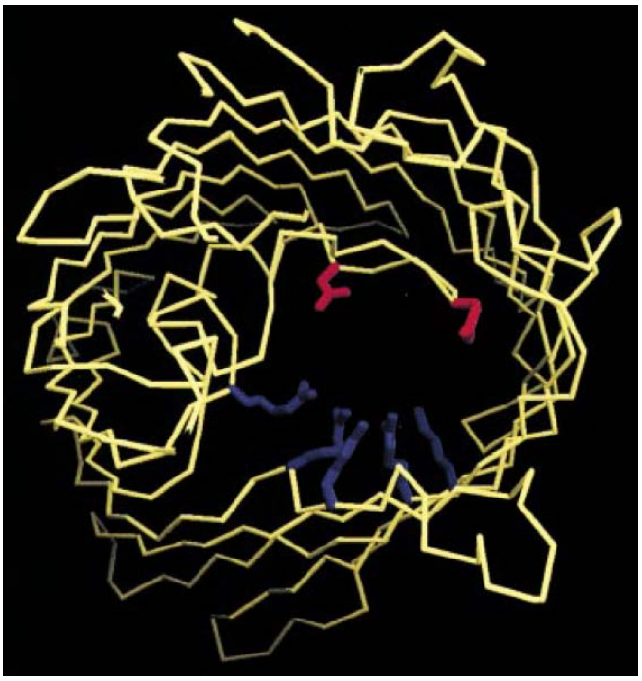

Figure 9. Constriction site of OmpF, as seen from the top of the outer membrane. The polypeptide backbone is shown in yellow. Side chains of positively and negatively charged residues that are involved in the formation of transverse electrostatic field are shown in blue (Lys-16, Arg-42, Arg-82, Arg-132) and red (Asp-113, Glu-117), respectively[36].

The total charge arrangement contributes to the formation of specific electric field, giving each porin its unique properties.[36] Porins are extremely stable proteins that can resist denaturation in the presence of 5 M guanidium hydrochloride or 2% sodium dodecyl sulfate at 70°C. Recent studies showed that the latching loop L2 of OmpF, which bends over the wall of the adjacent monomer, contributes strongly to this exceptionally high stability. The hydrophobic trimer interface is also thought to add to the robustness of trimeric porins, as removing specific monomer-monomer interactions by site-directed mutagenesis results in a dramatic stability decrease in the case of OmpF and PhoE[36]. It seems unlikely that stability results from the hydrophobic interface only. Probably, this interface drives the molecules to oligomerize in the periplasm before insertion into the outer membrane. In this lipophilic environment, hydrophobic interactions play a less significant role, and stability is ensured by other types of interactions. Lipid bilayers can be reconstituted with purified porins, where ion-permeable pores form. Conductance measurements showed that most porins exist in either open or closed states, depending on the transmembrane potential.

1.4.3 NADH: ubiquinone reductase (Complex I)

Respiratory complex I plays a central role in cellular energy production in bacteria and mitochondria. Its dysfunction is implicated in many human neurodegenerative diseases, as well as in aging.[37] This enzyme catalyzes electron transfer from NADH to ubiquinone and couples this transfer to the translocation of protons across the inner mitochondrial membrane. Proton-pumping NADH: ubiquinone oxidoreductase is the most complicated and least understood enzyme of the respiratory chain. Clearly, this is due to the fact that complex I is very large and has numerous subunits and redox centers (the subunits of complex I are named according to their apparent molecular weights). It contains a core of 14 subunits that are conserved in prokaryotes and eukaryotes and comprises eight to nine iron–sulfur clusters and one flavine mononucleotide cluster (FMN). Seven of these subunits are encoded by the mitochondrial genome in most eucaryotes and form the common membrane-integral part of complex I. Up to 31 additional "accessory" subunits are found in mitochondrial versions of complex I. All redox prosthetic groups reside in the peripheral arm of the L-shaped structure. The NADH oxidation domain harbouring the FMN cofactor is connected via a chain of iron–sulfur clusters to the ubiquinone reduction site that is located in a large pocket formed by the PSST- and 49-kDa subunits of complex I (Figure 10).[38]

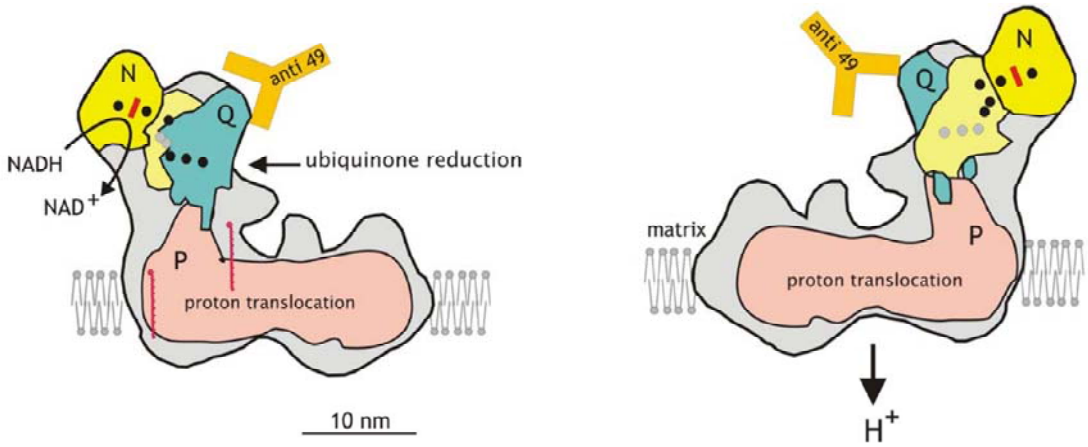

Figure 10. Two views of the proposed overall architecture of complex I. Complex I consist of three functional modules: N (NADH oxidation, yellow), Q (ubiquinone reduction, blue-green) and P (proton pumping, light red). The binding region of an antibody against the 49-kDa subunit of the Q module is indicated by an orange Y. The mass corresponding to the 51-kDa and 24-kDa subunits is depicted in the darker shade of yellow. Iron–sulfur centers are shown as black and grey (if hidden) circles. Ubiquinone molecules in an extended conformation are drawn to scale in red. The red bar indicates the approximate position of FMN.[38]

The reaction catalyzed by the protein is well established for the mitochondrial enzyme and plays a central role in oxidative phosphorylation by catalyzing the transfer of two electrons from NADH to ubiquinone - 10, with concomitant translocation of 3-5 protons from the matrix to the cytosolic side of the inner mitochondrial membrane:

$$NADH + ubiquinone + 5H^{+}Matrix \rightarrow NAD^{+} + ubiquinol + 4H^{+}Intermembrane\ space$$

Complex I contributes significantly to cellular oxidative stress and possibly redox-signaling by the generation of superoxide.[38]

1.5 Block copolymer lipid interactions

Literature data show, that drug-loaded self-assemblies (vesicles) are able to enter cells and release their cargo, which subsequently leads to effects such as tumor size decrease[39]. All those phenomena involve the vesicle integration with cells: at some stage of that process the vesicular membrane will come into close contact with a cellular membrane (either outside or inside the cell) and interactions between the two membranes can be expected. This process may be critical for the drug delivery process and depending on the synergy / antagonism between the cell membrane components and the polymeric amphiphile may lead to stabilization or disruption of the cell membrane. Therefore, it is important to study the membrane interactions in such mixed lipid-polymer systems, in order to optimize the delivery vehicles and avoid their unwanted effects on the cell membranes.

Our goal was to investigate interactions between lipids and amphiphilic block copolymers by a monolayer technique. This method allows for simultaneous monitoring of the morphology of spread films (by Brewster angle microscopy) and energetic effects associated to the mixing / demixing phenomena in two-dimensional binary systems. Additionally due to presence of natural lipids in the membrane protein extracts their interactions with synthetic block polymer components may contribute to understanding of the reconstitution in synthetic bilayer-like membranes.

2. Experimental part

In sections 2.1 – 2.3 the synthesis, characterization and end-group functionalization of the PMOXA-PDMS-PMOXA block copolymers are discussed. Further on, applications of the synthesized block copolymers in novel functional polymer-protein hybrid materials and natural membrane mimics are shown in the form of separate original publications or submitted manuscripts. Experiments involving characterization of the self-assembly properties of synthesized block copolymers and their applications that were not published are presented in the Appendix.

2.1 ABA block copolymers synthesis

The synthesis of symmetric poly(2-methy-2-oxazoline)-b-polydimethylsiloxane-b-poly(2-methyl-2-oxazoline) (PMOXA-PDMS-PMOXA) block copolymers library used for our studies, followed the procedure published by Nardin et al[25] with certain modifications. The first step of the synthetic route involved acid-catalyzed polycondensation of dimethoxydimethylsilane in the presence of water and end-capper, resulting in butylhydroxy-terminated bifunctional PDMS. Liquid PDMS was than purified by vacuum stripping at 80°C and a sequence of precipitations in 1:1 w/w water/methanol mixture.[40] Purified PDMS was reacted with triflic acid anhydride in hexane at -10°C for 3 h, resulting in triflate-PDMS bifunctional macroinitiator. Solvent was then removed under high vacuum. The reaction mixture was solubilized in freshly dried hexane and filtered under argon through a G4 filter. Hexane was evaporated under vacuum and dry ethyl acetate was added as reaction solvent. Addition of dry 2-methyl-2-oxazoline resulted in symmetric ring-opening cationic polymerization of PMOXA blocks on the macroinitiator. The reaction was terminated by addition of 0.5 M potassium hydroxide in methanol solution. Figure 11 shows the schematic representation of synthetic procedure.

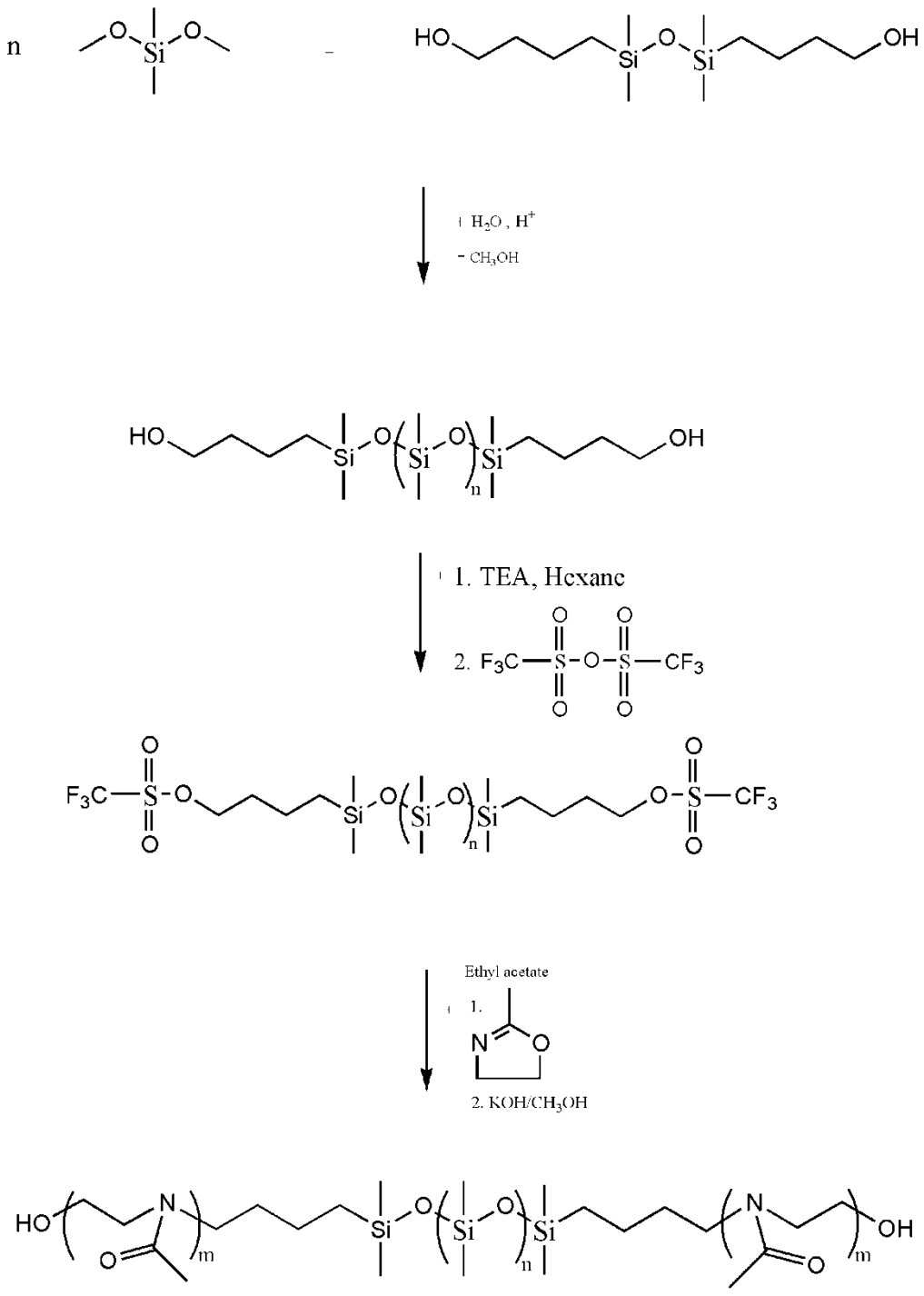

Figure11. Synthetic route of ABA block copolymers.

The synthetic route involved multiple purification steps, and required additional care in handling. Activation of the PDMS, filtration of macroinitiator and 2-methyl-2-oxazoline polymerization required water-free conditions and all these steps were performed under inert argon atmosphere. Modifications of existing protocols started with the middle block (PDMS) synthesis, followed by careful, multistep purification. Synthesis of the starting hydrophobic block, with full control over its

molecular weight, provided the possibility to tune the membrane thickness in resulting block copolymer aggregates.

Purification of the bi-triflate functionalized polydimethylsiloxane utilized filtration via ceramic G4 filter under argon atmosphere. Filtration was carried out in the self-made glass filtration unit allowing cooling of the filtration mixture (-11°C), thus enhancing the precipitation of organic salts. The resulting colorless, activated PDMS did not require additional purification, steps such as addition of activated char-coal for organic salt removal. The goal of the modifications introduced to the synthetic procedure was to reduce the molecular weight distribution of the resulting polymers (polydispersity index, PDI). The PDI increase for amphiphilic block copolymers may result in broadening the range of possibly coexisting morphologies of self-assemblies in solution[41]. In addition, increase of the molecular weight distribution triggers reduction of aggregate sizes. Figure 12 shows the series of TEM micrographs of vesicles, prepared from polystyrene-b-poly(acrylic acid) copolymers, with increasing polydispersity, where the influence on size and size distribution is clearly visible.[17,41, 42]

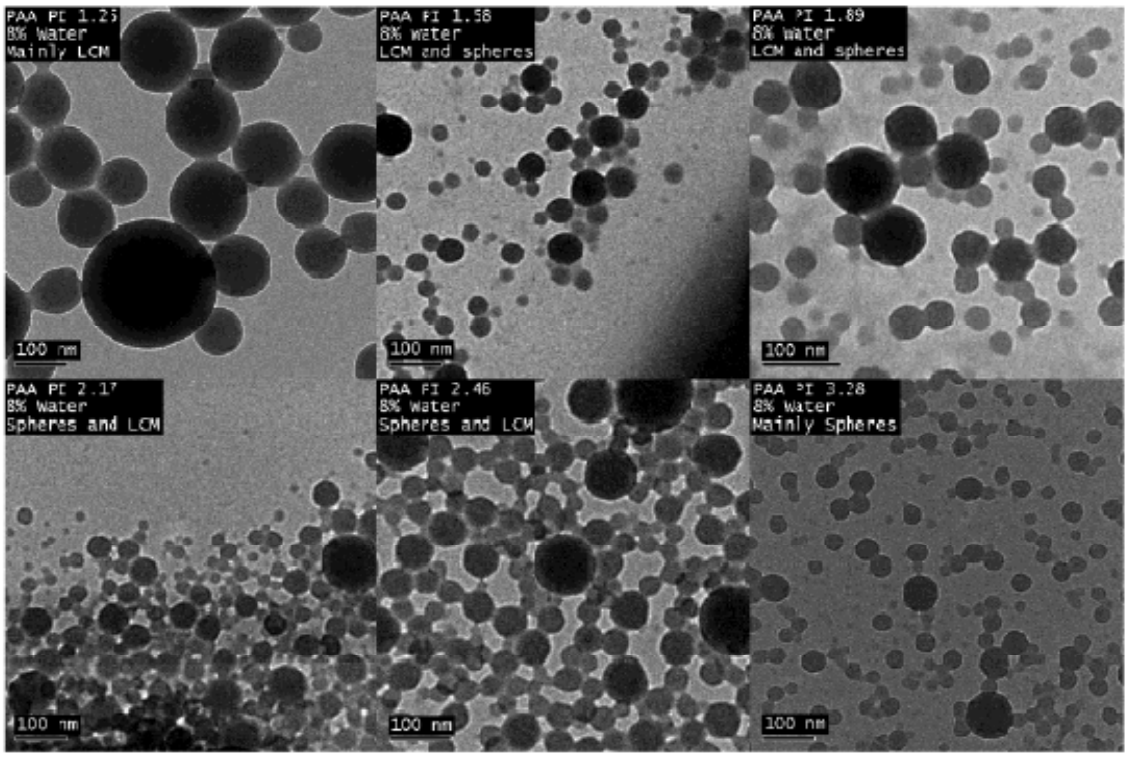

Figure 12. TEM micrographs of vesicles prepared from polystyrene-b-poly(acrylic acid) copolymers, with increasing polydispersity, influencing their size and size distribution[41].

2.2 Analysis of ABA block copolymers library

Characterization of the synthesized block copolymer utilized ^{1}H Nuclear Magnetic Resonance (NMR) analysis providing the values of number average molecular weights of polymers and block copolymers, and thus their blocks length ratios[43]. The size distribution of the polymers and block copolymers was estimated by Gel Permeation Chromatography (GPC)[1, 43] in chloroform and/or tetrahydrofurane, with polystyrene standards.

2.2.1 NMR

NMR analysis was used to estimate the number average molecular weight (Mn) of synthesized polymers and block copolymers.[43] Mn of the synthesized bi-hydroxybutyl-PDMS was calculated on the base of ratio between the integrals of peaks corresponding to the protons in the end-hydroxybutyl groups and the integral of the signal of protons assigned to the methyl groups bound to silicon atom in polymer repeating units. Figure 13 shows an example ^{1}H NMR spectrum of PDMS in $CDCl_3$ (55 repeating units).

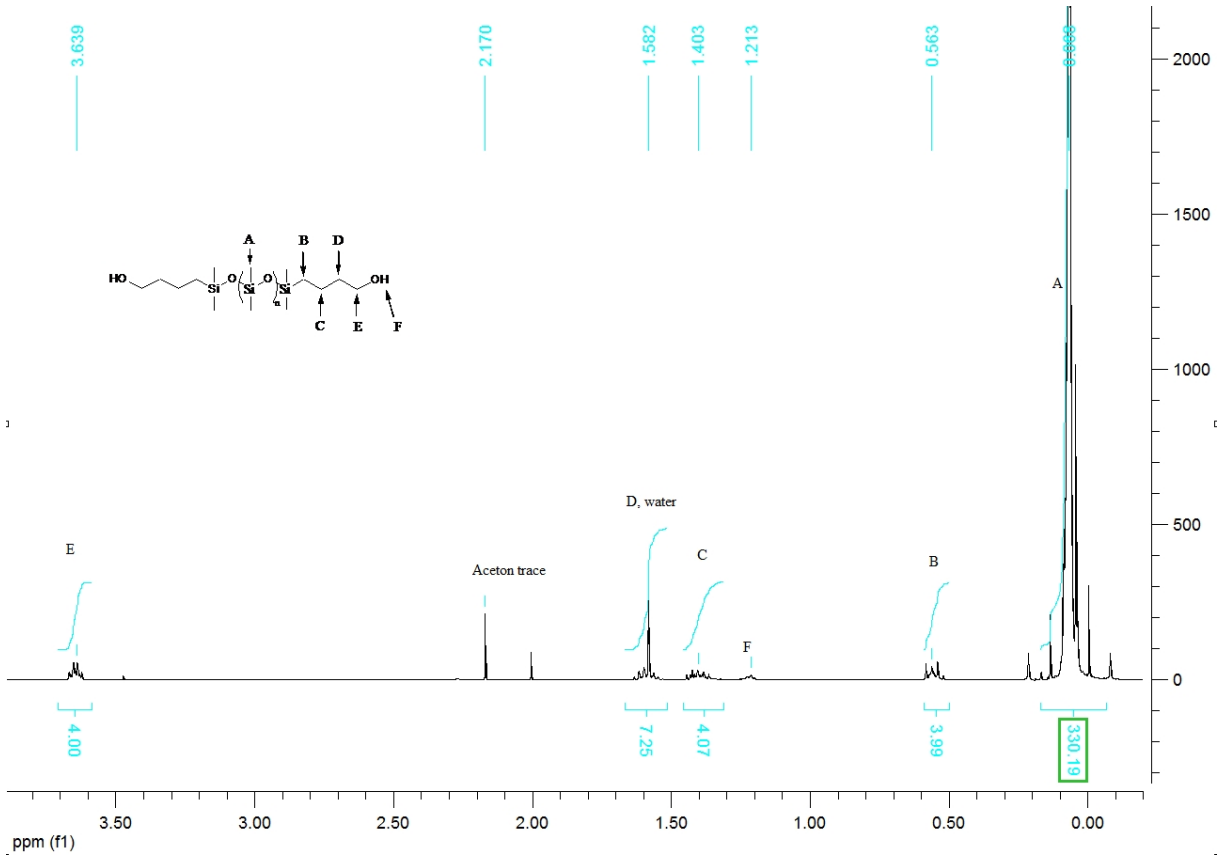

Figure 13. ^{1}H NMR of the bi-hydroxybutyl-PDMS, with corresponding peaks assignment in $CDCl_3$.

The peak at 3.64 ppm corresponds to the protons of CH_2 – groups (E) and can be attributed to 4 protons (bi-functionality of the polymer). The integral of the broad peak around 0 ppm, assigned to methyl groups of the polymer repeating unit (A) - 330.19, divided by number of protons in repeat unit (6) gives the degree of polymerization of 55.

In order to estimate the degree of polymerization of the symmetric PMOXA chains grown onto the PDMS macroinitiator, two approaches can be used. Either the integral signal of the PDMS with known degree of polymerization or the integral of the signals of the PDMS end-linkers are used as a reference. Figure 14 shows an example ^{1}H NMR spectrum of the $A_{12}B_{55}A_{12}$ block copolymer, indicating peak assignments relevant to PMOXA hydrophilic blocks in $CDCl_3$.

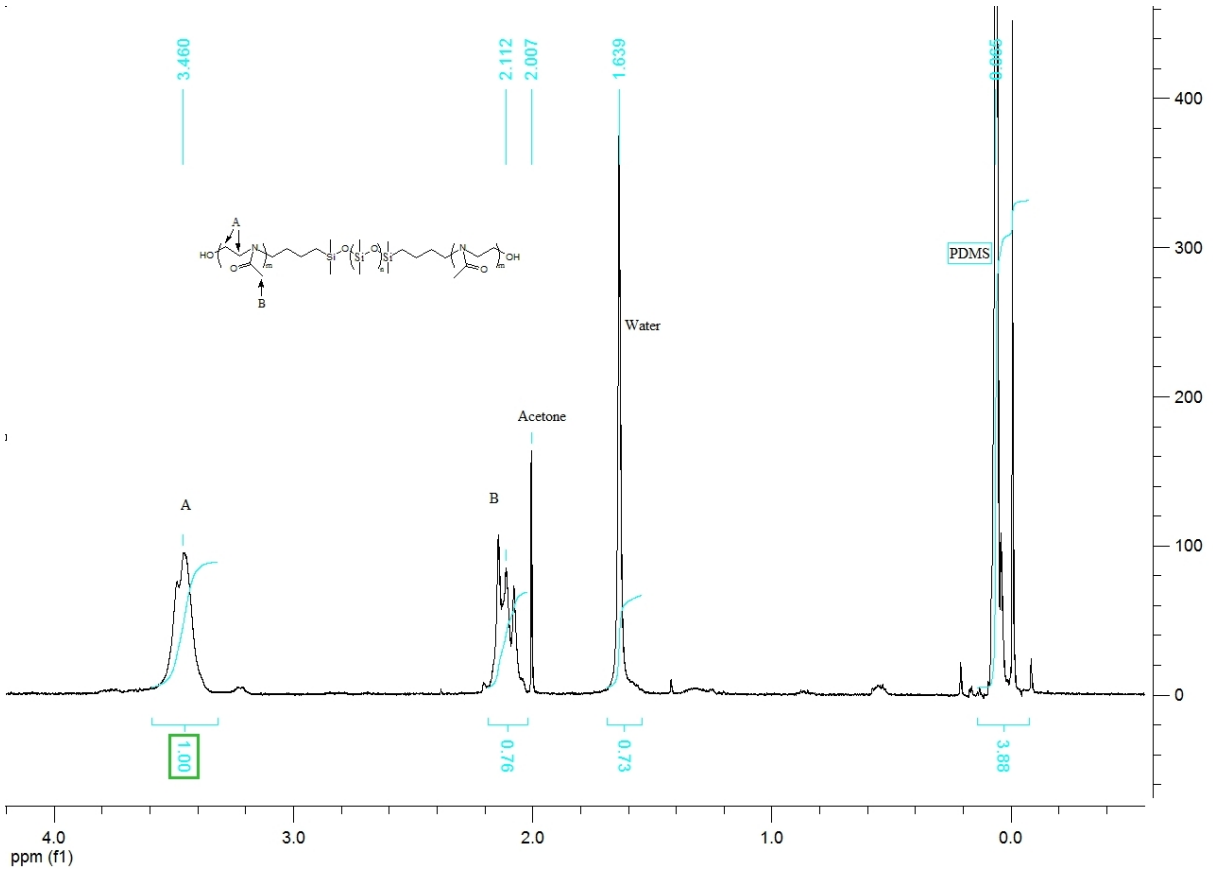

Figure 14. ^{1}H NMR spectra of $A_{12}B_{55}A_{12}$ PMOXA-PDMS-PMOXA block copolymer in $CDCl_3$.

The described methodology of ABA block copolymers ^{1}H NMR characterization, where the end-linkers of the hydrophobic block are used as a reference is applicable only in the case of low molecular weight copolymers. The higher the total Mn of the block copolymer the higher the error resulting from

the end-linker analysis, due to the increasing intensity of the peaks related to the repeating units. Therefore the PDMS peak around 0 ppm was used for the characterization of block copolymer library.

Results of ^{1}H NMR and GPC analysis of the polymer library are shown in table 1 of the following section.

2.2.2 Gel Permeation Chromatography

The lack of suitable solvents for ABA triblock copolymers made the GPC analysis difficult. The partial aggregation of the material in the solvent used as eluent was impossible to avoid. Therefore sample solutions (20-40 mg in 10 mL HPLC grade THF) were filtered through a 0.2 μm filter before loading into the autosampler. Lack of availability of the standards for amphiphilic copolymers limited the analysis to examination of the size distribution of the synthesized block copolymers (polydispersity index, PDI). The PDI indexes of polymers are the library and blocks lengths are listed in Table 1. Figure 15 shows example of the GPC trace for $A_{12}B_{55}A_{12}$ block copolymer in THF.

Polymer composition^{NMR}	M_n (g/mol)^{NMR}	Polydispersity^{GPC}
$A_{12}B_{55}A_{12}$	6222	1.64
$A_9B_{106}A_9$	9486	1.38
$A_{15}B_{110}A_{15}$	10700	1.62
$A_{65}B_{165}A_{65}$	23372	1.63
$A_{13}B_{110}A_{13}$	10462	1.44
$A_{14}B_{110}A_{14}$	10632	1.36

Table 1. Block copolymer library, A - PMOXA, B - PDMS.

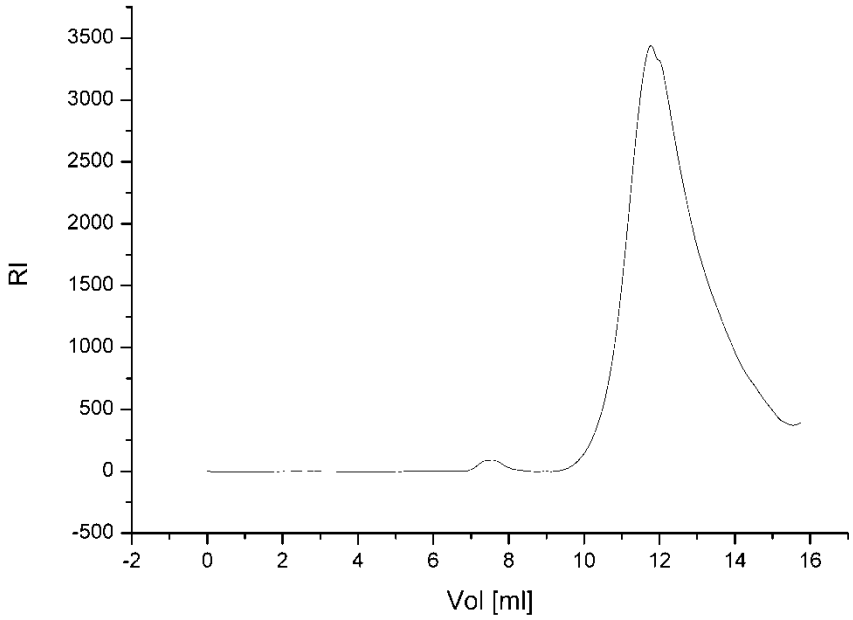

Figure 15. GPC chromatogram of $A_{12}B_{55}A_{12}$ in THF.

Partial aggregation of the material in THF is represented by small peak (7.5 – 8 ml) Figure 15.

2.3 End-functionalization of ABA block copolymers

End groups of synthesized block copolymers were further modified, in order to introduce additional functionality. Covalent attachment of functional groups to the end of the hydrophilic blocks of the ABA block copolymers allowed introduction of the desired functionality to the surface of resulting aggregates.

2.3.1 Introduction of "bio-linker"

$A_{14}B_{110}A_{14}$ and $A_{65}B_{165}A_{65}$ block copolymers were functionalized with biotin end-groups. The reaction utilized attachment of D-biotin to the polymer`s hydroxyl groups in N,N'-dicyclohexylcarbodiimideate (DCC)/ 4-dimethylaminopyridine (DMAP) catalyzed esterification[44] in chloroform[45]. The product was purified from unreacted biotin by subsequent ultra-filtration, in 1:5 ethanol – water mixture. Figure 16 shows the biotinylation reaction scheme.

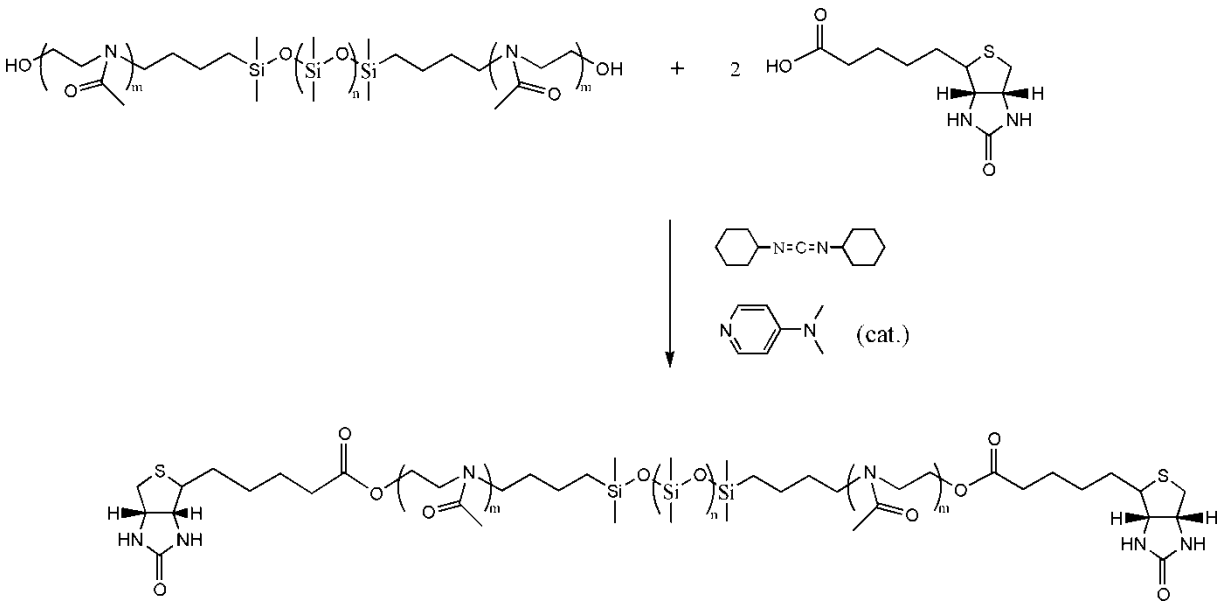

Figure 16. DCC/DMAP catalyzed esterification of ABA block copolymer.

Introduction of biotin end groups to the hydrophilic clocks of the polymers allowed utilization of biotin-streptavidin interaction as "bio-linker". Streptavidin is a 53 kDa tetrameric protein known for its strong binding affinity to biotin group. The dissociation constant (K_d) of the biotin-streptavidin complex is on the order of ~10^{-15} mol/L, thus the strongest known non-covalent interaction. Four binding sites on the tetrameric streptavidin make it an excellent platform for coupling, labeling and immobilization experiments involving nano-particles[46]. Figure 17 shows a schematic representation of coupling, labeling and immobilization strategies utilizing biotin-streptavidin interaction.

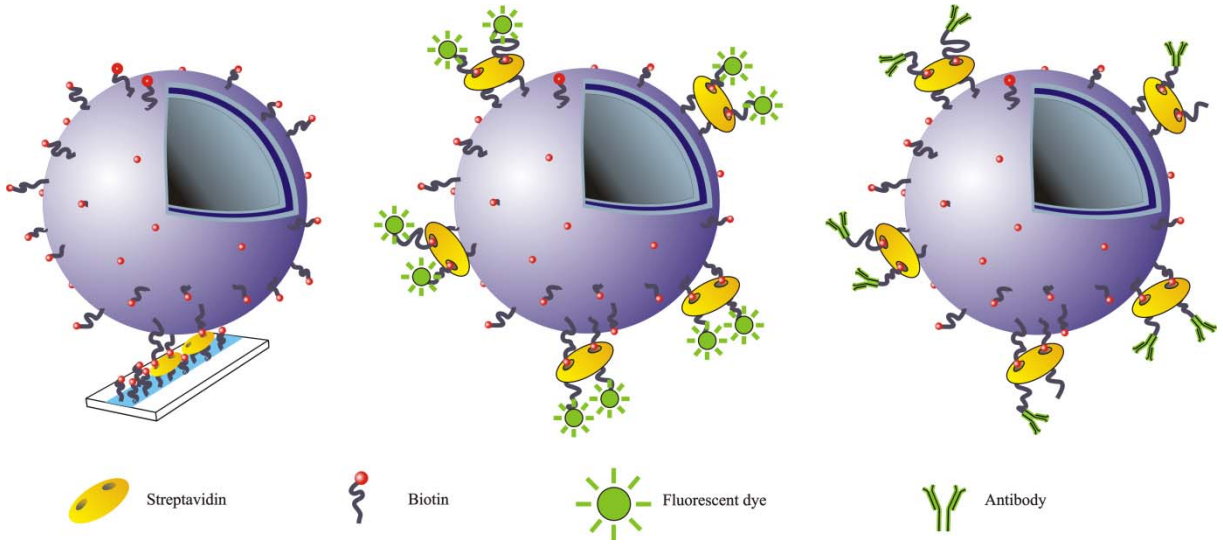

Figure 17. A schematic representation of immobilization, labeling and coupling strategies, utilizing biotin-streptavidin interactions.

Due to the high molecular weights of the block copolymers functionalized with biotin, the quantification of the degree of biotinylation of the copolymers end-groups utilizing ^{1}H NMR was inaccurate (weak signals of the biotin groups). Therefore, the presence and availability of biotin groups was determined by fluorescence correlation spectroscopy in solutions of vesicles prepared from the biotinylated block copolymers. Biotinylated vesicles from $A_{14}B_{110}A_{14}$ (10 mg/ml, 10% biotinylated) were prepared with solvent displacement method and incubated with fluorescently labeled streptavidin (3×10^{-8} M). Upon binding of the fluorescent streptavidin to the biotin groups at the surface of the vesicles, significant diffusion time increase of the labeled protein was observed proving presence and availability of the biotin end-groups of the block copolymers. Figure 18 shows the comparison of the diffusion of the free dye, labeled streptavidin and the labeled streptavidin bound to biotinylated vesicles.

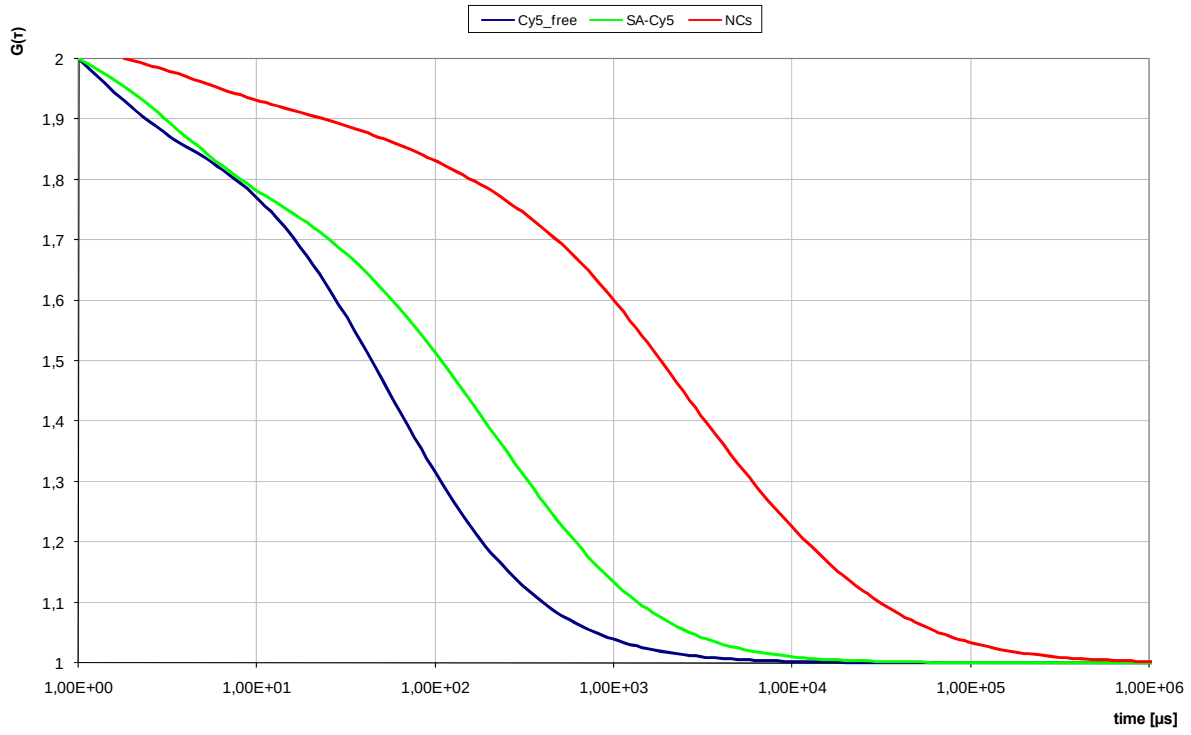

Figure 18. FCS normalized autocorrelation curves comparison of the diffusion of the free dye Cy5 (blue), free Cy5 labeled streptavidin (green) and the Cy5 labeled streptavidin bound to $A_{14}B_{110}A_{14}$ vesicles (red).

Figure 19 shows confocal-LSM images of $A_{14}B_{110}A_{14}$ biotinylated vesicles after addition of Avidin488 (about 5 min incubation time) (A) and $A_{14}B_{110}A_{14}$vesicles (no biotin) after addition of Avidin488 (about 7 min incubation time) (B), showing specific binding of streptavidin to biotinylated vesicles.

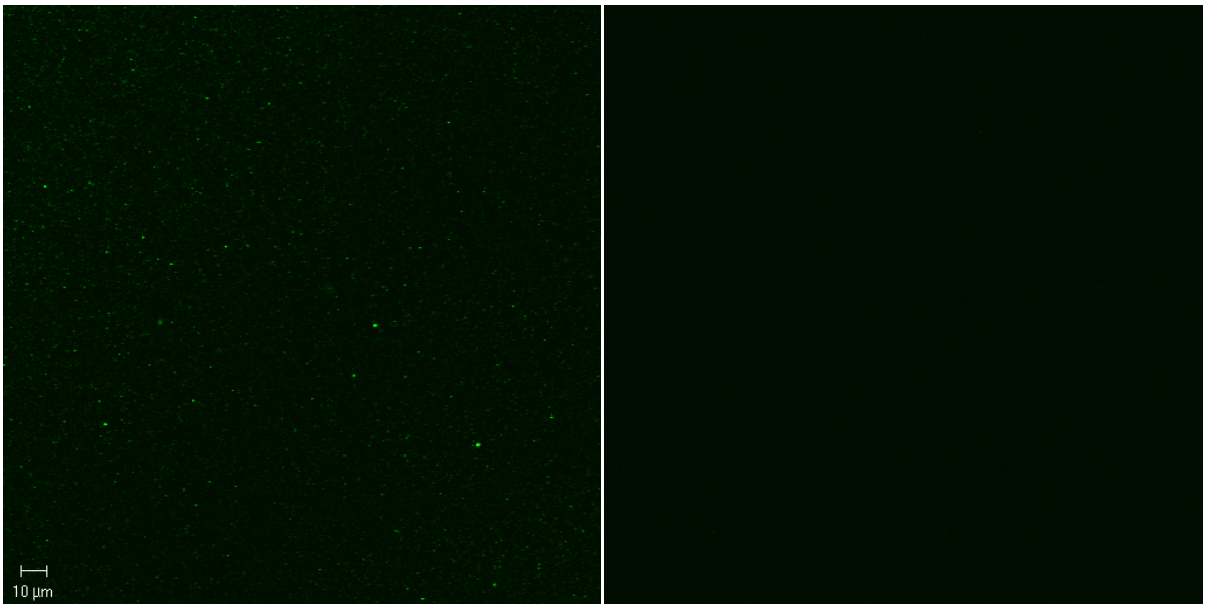

A B

Figure 19. (A) - CLSM image of biotinylated $A_{14}B_{110}A_{14}$ vesicles, after addition of Avidin488 (about 5 min incubation time). (B) - CLSM image of $A_{14}B_{110}A_{14}$ vesicles (no biotin) after addition of Avidin488 (about 7 min incubation time) (B).

Figure 20 shows CLSM images of $A_{14}B_{110}A_{14}$ biotinylated vesicles, after addition of Avidin488 (about 35 min incubation time) (A) and CLSM image from $A_{14}B_{110}A_{14}$ vesicles (no biotin) after addition of Avidin488 (about 20 min incubation time) (B). Increasing amounts of visible fluorescent particles indicate non-specific adsorption of Avidin488 to $A_{14}B_{110}A_{14}$ vesicles at extended incubation times (B).

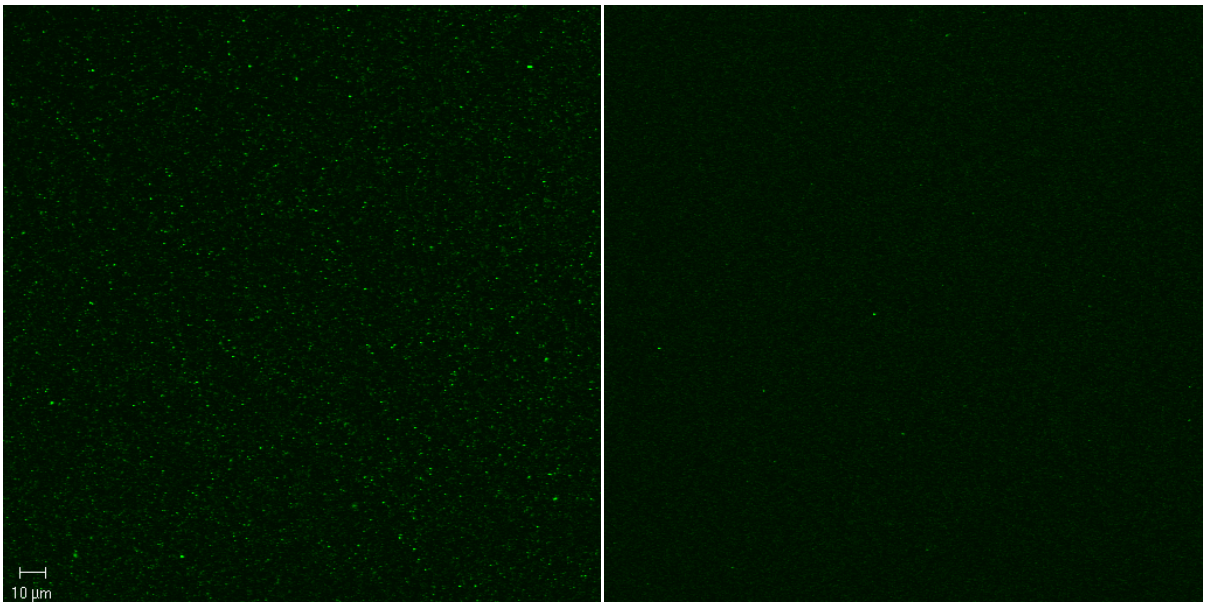

A B

Figure 20. (A) - CLSM image of biotinylated $A_{14}B_{110}A_{14}$ vesicles after addition of Avidin488 (about 35 min incubation time). (B) - CLSM image of $A_{14}B_{110}A_{14}$vesicles (no biotin), after addition of Avidin488 (about 20 min incubation time).

The same approach was used to confirm the presence and availability of the biotin end-groups in $A_{65}B_{165}A_{65}$ block copolymer aggregates. Figure 21 shows binding of Alexa Fluor 488 labeled streptavidin to biotinylated particles, by increase in diffusion time of the protein bound to the polymer particles.

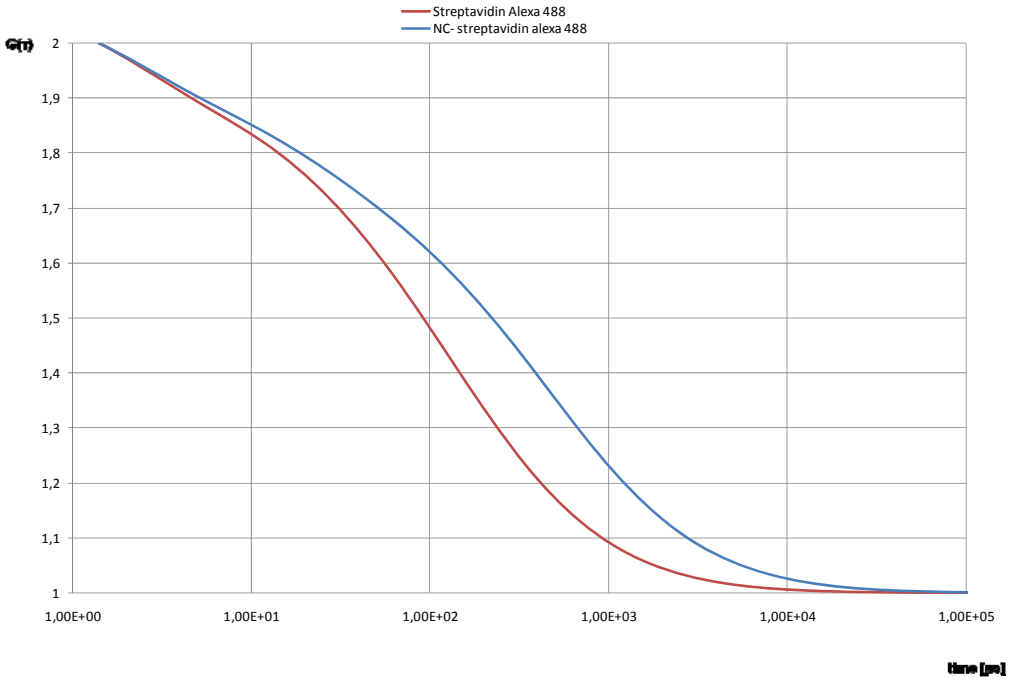

Figure 21. Normalized autocorrelation curves showing binging of Alexa Fluor 488 labeled streptavidin to $A_{65}B_{165}A_{65}$ biotinylated particles.

2.3.2 Introduction of "cross-linker" groups

$A_{15}B_{110}A_{15}$ and $A_{12}B_{55}A_{12}$ block copolymers were functionalized with methacrylate groups, allowing cross-linking upon exposure to UV light for the stabilization of the vesicular structures. Hydroxyl groups of ABA block copolymers were reacted with 2-isocyanatoethylmethacrylate, using dibutyltin dilaurate as catalyst in dry ethyl acetate.[47] Figure 22 shows the methacrylation reaction scheme.

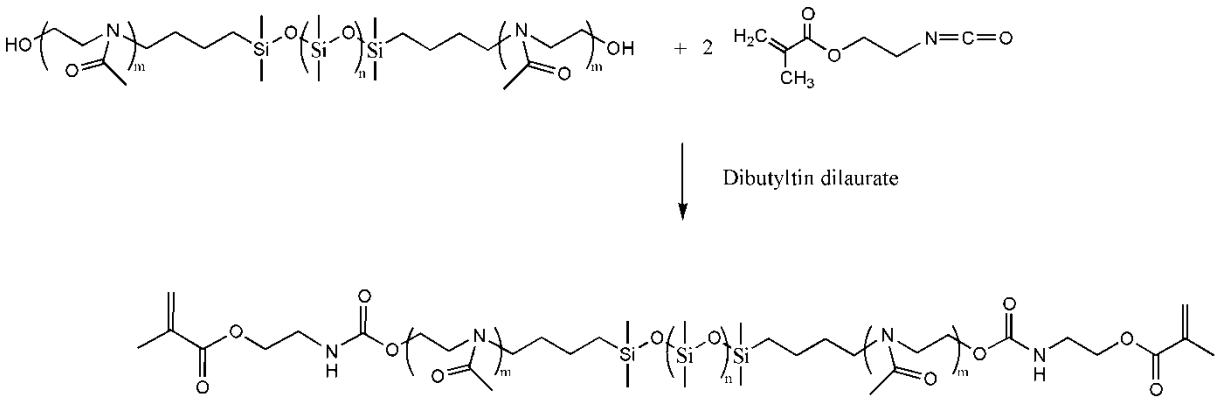

Figure 22. Methacrylation of ABA block copolymer.

The product was purified by subsequent ultra-filtration in 1:5 ethanol - water mixture. Methacrylation of both copolymers ($A_{14}B_{110}A_{14}$ and $A_{65}B_{165}A_{65}$) was confirmed by FTIR experiments and cross-linking kinetics upon UV-light exposure was studied.

A series of experiments were conducted to systematically investigate UV induced crosslinking behavior of methacrylated ABA triblock copolymers. Knowledge of the kinetics and dose requirements of this process is important for application of such triblock copolymers in situations where the mechanical and chemical stability of the polymer resulting from crosslinking would be important. Two methacrylated copolymers were used: $PMOXA_{15}$-$PDMS_{110}$-$PMOXA_{15}$ and $PMOXA_{12}$-$PDMS_{55}$-$PMOXA_{12}$. A glass slides were coated with a polymer solutions in chloroform to make a thick film, from which chloroform was evaporated by leaving over night in case of $PMOXA_{15}$-$PDMS_{110}$-$PMOXA_{15}$ and glass slide was put in a vacuum evaporator to dry off the $CHCl_3$ from the $PMOXA_{12}$-$PDMS_{55}$-$PMOXA_{12}$ film. Attenuated Total Reflection – Fourier Transform Infra Red (ATR-FTIR) spectroscopy was performed on those functionalized copolymer films. The polymer was then subjected to UV irradiation from a solar simulator with UV intensity of 17mW/cm^2 in the 340 - 390 nm range and an overall intensity of 407 W/cm^2 over different periods of time. The polymer sample was analyzed after each exposure with FTIR to determine the kinetics of crosslinking between the methacrylated groups. Solubility of the crosslinked polymers was evaluated by conducting dissolution tests of the crosslinked polymer in ethanol.

For both copolymers the FTIR spectrum shows distinct peaks for the PDMS and the PMOXA parts of the polymer, indicating that this method is excellent to characterize this class of polymers (Figure 20).

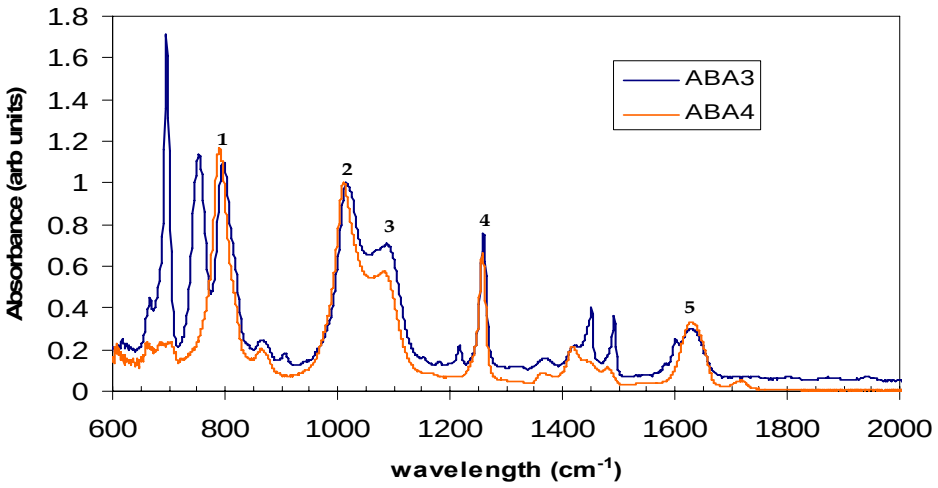

Figure 20: FTIR spectra of methacrylated $PMOXA_{15}$-$PDMS_{110}$-$PMOXA_{15}$ (blue) and $PMOXA_{12}$-$PDMS_{55}$-$PMOXA_{12}$ (red) copolymers. Peaks represent the PDMS and PMOXA components of the block copolymer. These are identified as 1. (~798 cm^{-1}) Si-C stretching and CH_3 rocking (from PDMS). **2. & 3.** (~1018 and 1092 cm^{-1}) Si-O-Si stretching vibrations (from PDMS). **4.** (~1260cm^{-1}) CH_3 symmetric deformation of Si-CH_3 (from PDMS). **5.** (~1632 cm^{-1}) amide C=O bond (from PMOXA). Two additional peaks found in the spectra of $PMOXA_{15}$-$PDMS_{110}$-$PMOXA_{15}$ correspond to residual amount of chloroform (680, 774 cm^{-1}, no vacuum treatment).

The peaks corresponding to pure PDMS are very evident in the spectrum (Figure 20). These peaks include the 798 cm^{-1} representing the Si-C stretching and CH_3 rocking vibrations. The twin peaks at 1018 and 1092 cm^{-1} represent the Si-O-Si stretching vibrations. The peak at 1260 cm^{-1} represents the CH_3 symmetric deformation of Si-CH_3 bonds. The peak at 1632 cm^{-1} represents the amide C=O bond from the PMOXA. These peaks are common to $PMOXA_{15}$-$PDMS_{110}$-$PMOXA_{15}$ and $PMOXA_{12}$-$PDMS_{55}$-$PMOXA_{12}$ copolymers.

The samples were exposed to UV light in a collimated beam apparatus to induce crosslinking of the methacrylate end-groups. UV treatment was carried out over different periods of time (0.5 min to 3.5 hours) to vary the irradiation dose. After each exposure, samples were analyzed using FTIR to monitor changes in functional end-groups. Exposure of methacrylate end-functionalized block copolymers to UV irradiation results in an increase of the intensity of the peak at ~790 cm^{-1}. It represents the formation of methylene bonds δ (-CH_2-) bonds which are usually observed at 814 cm^{-1}.[1, 46] The methacrylate end-group was bound to the large PMOXA block which may result in a shifting of this peak. The change in area under the 790 cm^{-1} peak provided values for the crosslinking rate with time.

The spectra of $PMOXA_{15}$-$PDMS_{110}$-$PMOXA_{15}$ copolymer, after exposure to different UV doses are shown in Figure 21-A. The degree of crosslinking was calculated by determining the area under peak at 790 cm^{-1} (Figure 21-B) and its evolution over time represents the kinetic of crosslinking for this polymer (Figure 21-C).

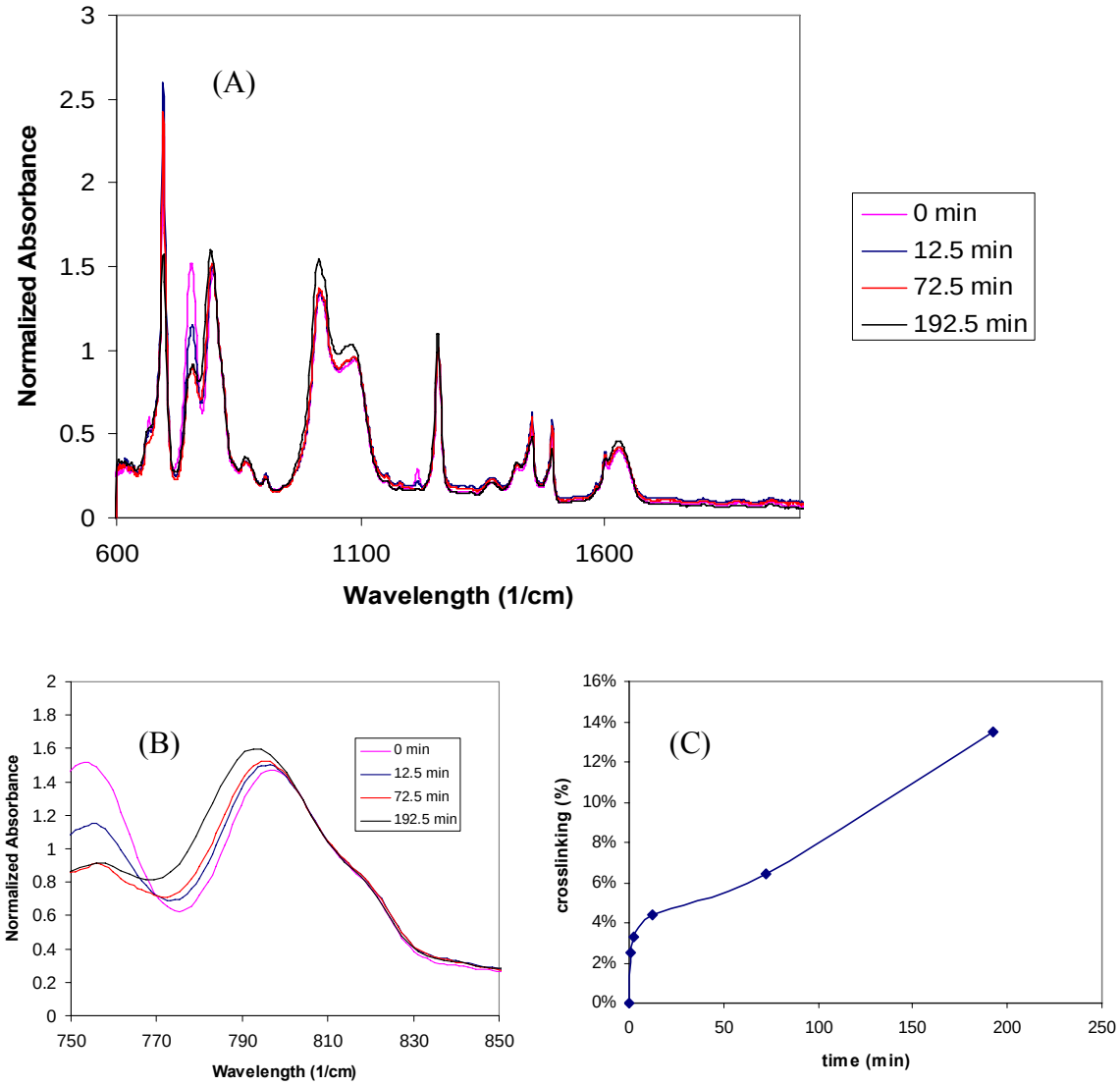

Figure 21: (A) FTIR Spectra of $PMOXA_{15}$-$PDMS_{110}$-$PMOXA_{15}$ copolymer exposed to increasing UV dose (time), (B) magnification of the peak at 790cm^{-1} used for monitoring of crosslinging (C) Kinetics of crosslinking of $PMOXA_{15}$-$PDMS_{110}$-$PMOXA_{15}$ polymer.

Figure 22 presents the results obtained for $PMOXA_{12}$-$PDMS_{55}$-$PMOXA_{12}$ methacrylated copolymer, with analytical approach as described before. A lower level of crosslinking was found for this polymer as seen in Figure 22 B.

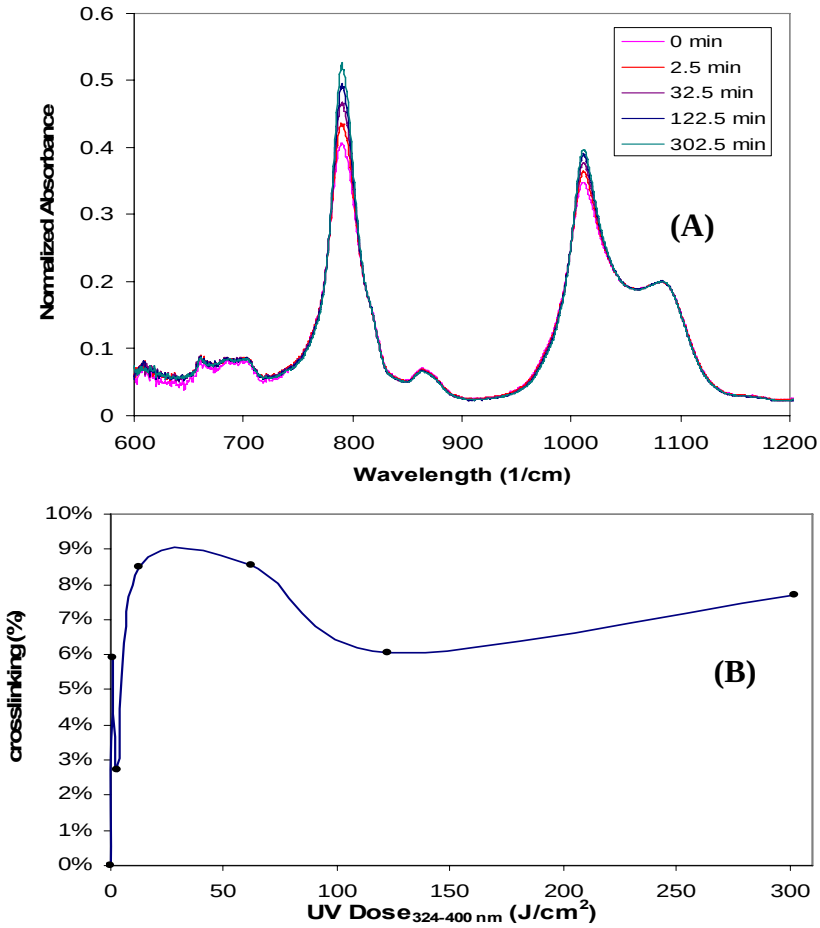

Figure 22: (A) FTIR Spectra of methacrylated $PMOXA_{12}$-$PDMS_{55}$-$PMOXA_{12}$ copolymer exposed to increasing UV dose (time) (B) Kinetics of crosslinking of methacrylated $PMOXA_{12}$-$PDMS_{55}$-$PMOXA_{12}$ copolymer

The crosslinking kinetic curve shown in Figure 22B exhibits unexpected trace and the effective methacrylation may lead to better UV curving.

The methacrylated $PMOXA_{15}$-$PDMS_{110}$-$PMOXA_{15}$ copolymer was soluble in ethanol prior to UV exposure and became insoluble after 192.5 minutes of UV treatment. Two days of exposure to ethanol led to less than 10% of initial mass loss.

Both the non-treated mathacrylated and UV-treated $PMOXA_{12}$-$PDMS_{55}$-$PMOXA_{12}$ copolymers dissolved easily in 100% ethanol. This is consistent with the low level of crosslinking observed for $PMOXA_{12}$-$PDMS_{55}$-$PMOXA_{12}$ copolymer. Methacrylation of this polymer appears to be low, most

probably due to contamination with water during the synthetic procedure. Increasing methacrylation might lead to better UV curing and solvent resistance properties of this block copolymer.

2.4 Applications of synthesized ABA block copolymers

2.4.1 Highly permeable polymeric membranes based on the incorporation of the functional water channel protein Aquaporin Z

Highly permeable polymeric membranes based on the incorporation of the functional water channel protein Aquaporin Z

Manish Kumar*, Mariusz Grzelakowski†, Julie Zilles*, Mark Clark*, and Wolfgang Meier†‡

*Department of Civil and Environmental Engineering, University of Illinois at Urbana–Champaign, 205 North Mathews Avenue, Urbana, IL 61801; and †Department of Chemistry, University of Basel, Klingelbergstrasse 80, CH-4056 Basel, Switzerland

Edited by Nicholas J. Turro, Columbia University, New York, NY, and approved October 30, 2007 (received for review September 15, 2007)

The permeability and solute transport characteristics of amphiphilic triblock-polymer vesicles containing the bacterial water-channel protein Aquaporin Z (AqpZ) were investigated. The vesicles were made of a block copolymer with symmetric poly-(2-methyloxazoline)-poly-(dimethylsiloxane)-poly-(2-methyloxazoline) ($PMOXA_{15}$-$PDMS_{110}$-$PMOXA_{15}$) repeat units. Light-scattering measurements on pure polymer vesicles subject to an outwardly directed salt gradient in a stopped-flow apparatus indicated that the polymer vesicles were highly impermeable. However, a large enhancement in water productivity (permeability per unit driving force) of up to ≈800 times that of pure polymer was observed when AqpZ was incorporated. The activation energy (E_a) of water transport for the protein-polymer vesicles (3.4 kcal/mol) corresponded to that reported for water-channel-mediated water transport in lipid membranes. The solute reflection coefficients of glucose, glycerol, salt, and urea were also calculated, and indicated that these solutes are completely rejected. The productivity of AqpZ-incorporated polymer membranes was at least an order of magnitude larger than values for existing salt-rejecting polymeric membranes. The approach followed here may lead to more productive and sustainable water treatment membranes, whereas the variable levels of permeability obtained with different concentrations of AqpZ may provide a key property for drug delivery applications.

permeability | triblock copolymer | water treatment

Biological membranes have excellent water transport characteristics, with certain membranes able to regulate permeability over a wide range. The permeability of membranes such as those present in the proximal tubules of the human kidney (1) can be increased by insertion of specific water-channel membrane proteins known as Aquaporins (AQPs). Other biological membranes, such as those in mammalian optic lenses (2), erythrocytes (3), and many other cell membranes (4) are constitutively AQP-rich. The permeabilities of AQP-rich membranes are orders of magnitude higher than those observed for unmodified phospholipid membranes (5). Additionally, some members of the AQP family have excellent solute retention capabilities for small solutes such as urea, glycerol, and glucose, even at high water transport rates (5, 6). These properties result from the unique structure of the water-selective AQPs. These AQPs have six membrane-spanning domains and a unique hourglass structure (7) with conserved charged residues that form a pore that allows both selective water transport and solute rejection. The AQP used in this study was a bacterial aquaporin from *Escherichia coli*, Aquaporin Z (AqpZ). AqpZ was selected because it can enhance the permeability of lipid vesicles by an order of magnitude while retaining small uncharged solutes (5). Additionally, AqpZ can be expressed in relatively large quantities in *E. coli* and has been reported to be quite stable under different reducing conditions and at temperatures of 4°C (5)—properties that make it attractive for drug delivery and water treatment applications.

The AQP's high permeability and high specificity could be valuable for a variety of applications. High permeabilities and excellent solute retention of small solutes are important for water treatment in critical medical applications such as dialysis (8, 9) because they could lead to reduced equipment size and more efficient energy use. A significant improvement in the permeability of solute-rejecting membranes would also be a large step in improving the economics of desalination for drinking water applications. Desalination is becoming increasingly important for water production in semiarid coastal regions (10, 11). Reverse-osmosis membranes are most commonly used for this application, whereas the use of membranes in a forward-osmosis scheme is becoming more interesting to water planners (10, 12). Both of these processes need extensive pretreatment of the source water to remove particulates and microbial contaminants, but they provide excellent treatment for properly pretreated water. However, reverse osmosis requires large energy consumption, and forward osmosis will require large membrane areas. This is because of the low productivity of currently used commercial reverse-osmosis and forward-osmosis membranes. The AQP-rich membrane proposed here, when suitably supported, could be used in similar processes with lower energy or membrane area requirements. Finally, the ability to produce membranes with low initial permeabilities is desirable for drug delivery applications (13), whereas a high level of control over permeability could be an additional advantage in designing alternative delivery methods (14).

The effects of AQPs on the permeability of liposomes (5), frog oocytes (3), and cellular secretory vesicles have been studied (15). However, the low stability of biological membranes or synthesized lipid membranes for water treatment and drug delivery applications is an important disadvantage (16). Obtaining and processing large volumes of such membranes would also present technical challenges.

The use of synthetic polymers, in particular, lipid-bilayer-like amphiphilic block copolymers, is intriguing because they are chemically and mechanically stable while still providing an amphiphilic structure that allows incorporation of membrane proteins such as AQPs (17). Some membrane proteins have been functionally inserted into block copolymer membranes (18–21). These include the β-barrel *ompF* protein, the bacterial receptor *lamB* protein, and bacteriorhodopsin. Directed insertion of the eye lens AQP (Aquaporin 0) into similar block copolymer membranes has also been demonstrated (22), although this

Author contributions: M.K., J.Z., M.C., and W.M. designed research; M.K., M.G., and J.Z. performed research; M.K. and M.G. analyzed data; and M.K., J.Z., M.C., and W.M. wrote the paper.

The authors declare no conflict of interest.

This article is a PNAS Direct Submission.

See Commentary on page 20643.

‡To whom correspondence should be addressed. E-mail: wolfgang.meier@unibas.ch.

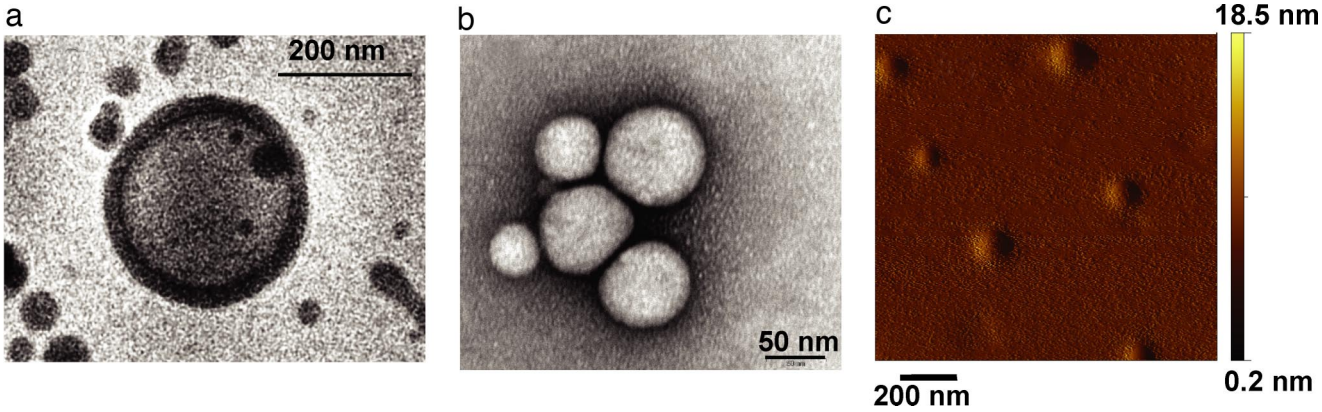

Fig. 1. Examination of polymer vesicles by using microscopy. The cryogenic transmission electron microscope images were used for size determination because regular transmission electron microscopy and atomic force microscopy influence the structure of the observed vesicles. (*a*) Cryogenic transmission electron micrograph of an ABA polymer vesicle. (Scale bar: 200 nm.) (*b*) Electron micrograph of a cluster of vesicles. (Scale bar: 50 nm.) (*c*) Atomic force micrograph of vesicles on mica in nontapping mode shows that a film of polymer is formed on the hydrophilic mica surface with vesicles located in the film. (Scale bar: 200 nm.)

initial study did not examine function. Additionally, there are few studies on the permeability of block copolymer membranes (13, 23), and no previous studies have reported on the magnitude of permeability improvement obtained by insertion of AQPs in block copolymer membranes. Data on rejection of dissolved ionic solutes such as salt (NaCl) have also not been reported for AQP-rich membranes.

To investigate the potential of protein-polymer membranes for the applications described above, solute and water transport properties and physical characteristics were analyzed for a specific protein-polymer membrane. This membrane was composed of a triblock copolymer with inserted AqpZ and is referred to throughout the text as an AqpZ-ABA membrane. The composition of the symmetric triblock copolymer was poly(2-methyloxazoline)-block-poly(dimethylsiloxane)-block-poly(2-methyloxazoline) ($PMOXA_{15}$-$PDMS_{110}$-$PMOXA_{15}$). This ABA polymer has a larger hydrophobic block (110 dimethylsiloxane units)-to-hydrophilic block (15 methyloxazoline units) ratio than those tested in previous studies (18, 19, 24–27). The physical characteristics of the ABA triblock copolymer were studied by using microscopy techniques, whereas light scattering was used to characterize the permeability.

Results

Synthesis of AqpZ-ABA Polymer Membranes. AqpZ was produced by a recombinant strain of *E. coli* by using a plasmid that allowed high levels of expression and incorporated 10 histidine residues at one end of the expressed protein to facilitate purification. This recombinant AqpZ was purified by using nickel affinity chromatography (5, 28). A large yield of pure protein (between 2.5 and 15 mg/liter of culture) was obtained for three different purification runs, indicating the potential for large yields by using the procedures described. $PMOXA_m$-$PDMS_n$-$PMOXA_m$ (ABA) triblock copolymers were synthesized by using a ring-opening cationic polymerization procedure. Polymer vesicles were produced by using the film rehydration method described in detail in *Materials and Methods*.

Characterization of Polymer Vesicles. To determine the permeability and solute rejection properties of polymer vesicles by using stopped-flow spectroscopy, a knowledge of the physical dimensions (radius in hydrated state) and morphology (hollow vs. solid sphere structure) is necessary. ABA polymer vesicles were therefore characterized by using static and dynamic light scattering, transmission electron microscopy, cryogenic transmission electron microscopy, and atomic force microscopy.

A hydrodynamic radius (R_h) of ≈160 nm was estimated from dynamic light scattering. This size is consistent with similar PMOXA-PDMS-based block copolymers with different hydrophilic-to-hydrophobic block length ratios (26). Dividing the radius of gyration (R_g) from static light-scattering experiments by the hydrodynamic radius from dynamic light scattering yields a value close to one ($R_g/R_h = 1.03$); this result is consistent with a hollow-sphere morphology (26). Static light scattering indicated a vesicle molecular weight of 52×10^6 g/mol.

The transmission electron microscope images indicate that the different vesicles have relatively uniform sizes. Cryogenic transmission electron microscopy indicated a hydrated vesicle radius of 117 nm. Fig. 1 shows representative images obtained from electron microscopy. Radii estimated from cryogenic transmission electron microscopy were used in further calculations of permeability as the rapid freeze used in this technique best preserves the hydrated vesicle's structural features (29).

The presence of spherical vesicle-like aggregates with a hydrophilic corona was further supported by atomic force microscopy measurements. When a dilute suspension of vesicles was spread on a hydrophilic mica surface, a film, punctuated with emerging vesicles, was observed (Fig. 1).

Permeability Measurements. The permeabilities of ABA and AqpZ-ABA vesicles were investigated by using stopped-flow light-scattering experiments as described in Borgnia *et al.* (5). Vesicle suspensions were rapidly mixed with osmotic solutions (1.7 osmol/liter) of salt (NaCl). The shrinkage of these vesicles was followed by monitoring the increase in light scattering over time. The initial rise in the experimental data was fitted to an exponential rise equation, and the exponential coefficient (k) was used to calculate permeability. These results are shown in Fig. 2 for the ABA and AqpZ-ABA vesicles with a protein-to-polymer molar ratio of 1:200. The time scale of initial rise for AqpZ-ABA vesicles was between 5 and 20 ms, whereas the lower permeability of the ABA vesicles led to a much longer rise time on the order of 10 s. The calculated permeabilities of the ABA and the AqpZ-ABA vesicles were 0.8 μm/s and 74 μm/s, respectively. This indicates that protein incorporation leads to a large permeability increase—almost 90 times greater than the polymer vesicles. Assuming the polymer vesicles have the molecular weight estimated from the light-scattering experiments, a maximum of 25 monomers per vesicle is possible. Then, using the calculated permeability of 74 μm/s and the estimated vesicle surface area based on radius measurements, the water permeability for each AqpZ tetramer is calculated as 13×10^{-14} cm^3/s,

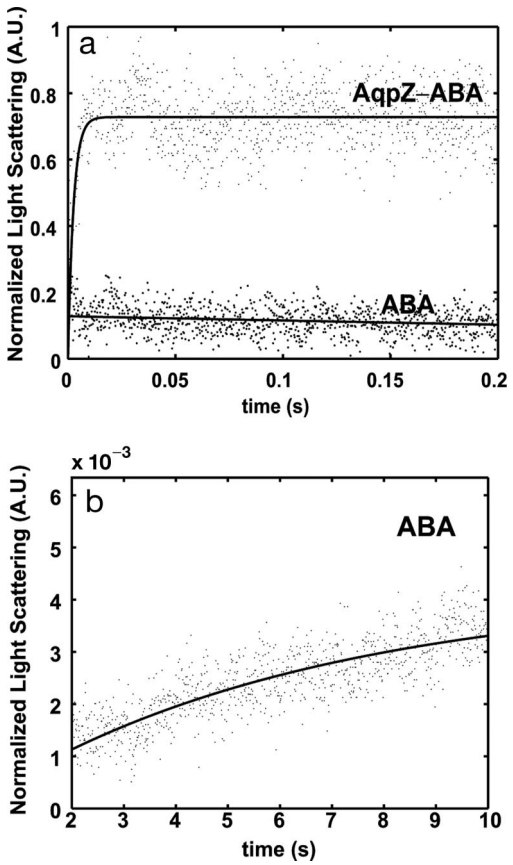

Fig. 2. Stopped-flow light-scattering experiments. (*a*) Increase in relative light scattering with and without reconstituted AqpZ into the ABA polymer at 5.5°C at a molar ratio of 200:1 (polymer:protein). Fits are shown as guides. The initial rise rates were used to calculate the permeability. As seen from *a*, a rise cannot be calculated for the pure ABA polymer vesicles. (*b*) Shown is the rise in scattering between 2 and 10 s for the ABA vesicles that was used in calculating permeability at 5.5°C.

which is similar to values reported for AqpZ reconstituted into liposomes [$\geq 10 \times 10^{-14}$ (5)].

Calculation of Activation Energies. Activation energies for water transport are calculated by conducting experiments over a wide range of temperatures, and these energies can be used to determine whether transport across vesicle membranes is diffusion-driven or channel-mediated. Calculated permeabilities for the AqpZ-ABA vesicles indicate an increase of 38 to 94 times over ABA vesicles in these experiments. In Fig. 3, the exponential constants obtained from these experiments are plotted against the inverse of temperature to determine the Arrhenius activation energies. The Arrhenius activation energy calculated for the ABA vesicles was 8.7 kcal/mol, whereas the AqpZ-ABA vesicles had a value of 3.4 kcal/mol. The higher value obtained for the ABA membrane is consistent with the values of activation energies reported for polymer membranes in the measured temperature range (30, 31), indicating transport by diffusion through the polymer. The low-activation energy for the AqpZ-ABA vesicles is strong evidence for channel-mediated water transport through AqpZ molecules. This value is also consistent with the low-activation energy values found in AqpZ-incorporated proteoliposomes (5) and AQP1-incorporated oocytes (3).

Reflection Coefficients. Solute reflection coefficient determines the extent to which a membrane excludes a particular solute. The

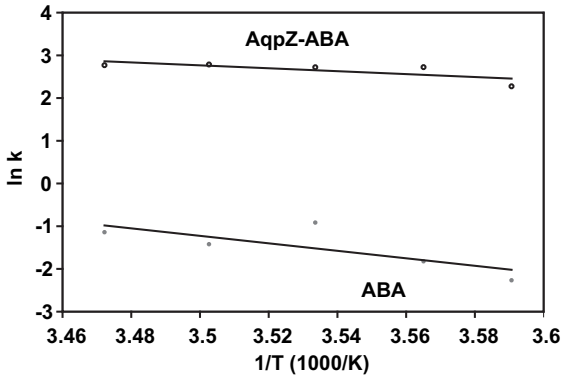

Fig. 3. Arrhenius plots for calculation of activation energy for osmotic transport of water across polymer membranes with incorporated AqpZ (AqpZ-ABA) and pure polymer membranes (ABA).

relative reflection coefficients of salt, urea, glucose, and glycerol were determined by using a procedure described by Meinild *et al.* (6). Glucose, with an assumed reflection coefficient of unity, was taken as the reference solute because of its relatively large molecular size. The calculated reflection coefficients of salt, glycerol, and urea were greater than one, indicating higher relative rejection of these solutes (data not shown). These reflection coefficients are higher than the values reported by Meinild *et al.* (6) for the same solutes, but agree within the experimental error for our calculations.

Effect of Protein-to-Polymer Ratio on Permeability. Stopped-flow experiments were conducted at 5.5°C with protein-to-polymer molar ratios of 1:25, 1:50 1:100, 1:200, 1:500, and 1:1000. Fig. 4 indicates a sharp permeability increase followed by a sharp decrease as the concentration of protein is increased. Permeability peaks at a protein-to-polymer ratio of 1:50 where the vesicle permeability is ≈3,000 times greater than the pure polymer.

Discussion

Large improvements in the efficiency of water treatment membranes may result from the development of biomimetic membranes with high permeability and selectivity. In this work, we describe the incorporation of the bacterial water-channel protein AqpZ into an ABA triblock copolymer and provide data on the permeability and selectivity of this new membrane. Permeability varied with the AqpZ:ABA ratio and showed an activation energy indicative of channel-mediated transport. Furthermore, the selectivity of the AqpZ-ABA membrane for water over small solutes such as salt, glucose, urea, and glycerol was demonstrated.

The orders-of-magnitude increase in permeability observed on incorporation of AqpZ indicates that the water-channel protein is functional in the synthetic context, as seen for other membrane proteins in a similar polymer (19). The magnitude of increase in permeability and the excellent solute rejection capabilities demonstrate the potential benefit of such membranes for water treatment and drug delivery. The ABA triblock copolymer was found to be relatively impermeable when compared with other membranes; its productivity was 0.22 $\mu m \cdot s^{-1} \cdot bar^{-1}$ at 20°C, which can be compared with the value of 5.7 $\mu m \cdot s^{-1} \cdot bar^{-1}$ at 20°C for a similar diblock copolymer [polyethylethylene–polyethylene oxide; calculated from Discher *et al.* (13)]. The large difference in the size and type of the hydrophobic blocks used here (110 units of dimethylsiloxane) and the diblock copolymer studied by Discher *et al.* (37 units of ethyleneethylene) could account for this difference. The permeabilities of lipid membranes are reported to be an order of magnitude

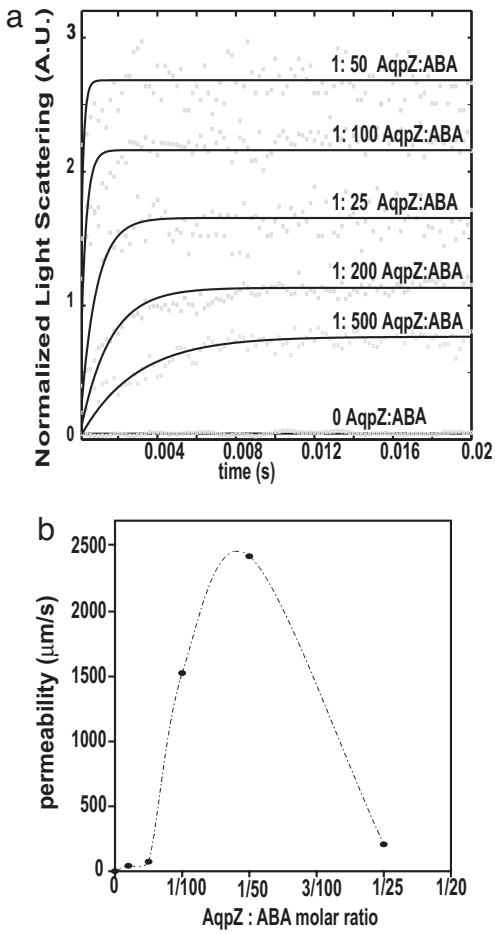

Fig. 4. Effect of increasing AqpZ concentrations on the permeability of ABA polymers. (*a*) Light-scattering results normalized to fit between 0 and 1. Curves for different ratios have been offset for clarity and fits are shown as guides. Data at 0 AqpZ:ABA ratio shown at a fixed offset. (*b*) Increase in calculated permeability with increase in protein-to-polymer molar ratio.

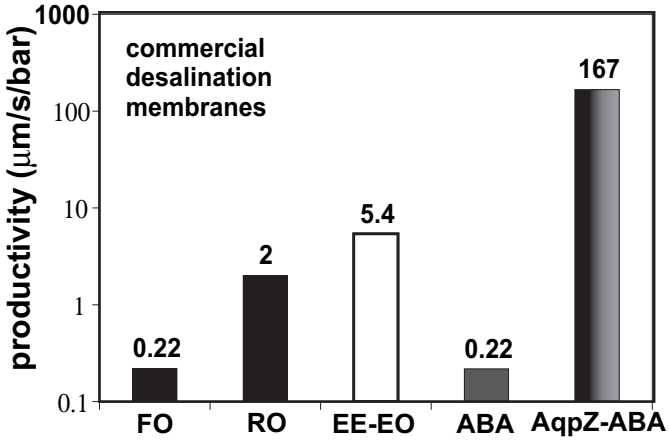

Fig. 5. Comparison of reported permeability values for polymeric membranes to those obtained in this study. FO is a commercial forward-osmosis membrane with data from McCutcheon and Elimelech (37) at 20°C. RO is a commercial reverse-osmosis desalination membrane with data from Matsura (38) at room temperature (assumed 25°C). EE-EO is a polyethylethylene-polyethylene oxide diblock polymer with data from Discher *et al.* (13) at 20°C. ABA represents the polymer vesicles used in this study with permeability calculated at 20°C. AqpZ-ABA represents the polymer vesicles with incorporated AqpZ at 1:50 molar ratio used in this study at 20°C. Data for ABA and AqpZ were obtained at 5.5°C and calculated at 20°C by using E_a values.

higher than the polyethylethylene–polyethylene oxide copolymer (13). The incorporation of AqpZ increases the productivity of ABA membranes by ≈800 times (Fig. 5). Additionally, the productivities of AqpZ-ABA membranes reported here exceed those for any salt-rejecting membrane (Fig. 5). Although these values were measured by using different procedures, it can be seen from this comparison that the AqpZ-ABA protein-polymer system investigated here represents more than an order-of-magnitude improvement over existing reverse-osmosis and forward-osmosis membranes. Additional research will be needed to identify appropriate support materials and pretreatment that could lead to successful new water treatment schemes.

The AqpZ-ABA system studied here may benefit from further optimization of the protein incorporation conditions, leading hopefully to membranes with greater permeability. Increasing the amount of AqpZ leads first to a permeability increase, then to a permeability decrease—similar to the performance of lipid membranes. In experiments with lipid membranes, a limiting concentration of AqpZ was observed around a protein-to-polymer weight ratio of 1:200 (5). We see such a limiting concentration at a protein-to-polymer ratio of 1:19 (1:50 molar ratio). The difference may result from the fact that the molecular weight of the polymers used here is greater than lipid molecular weight. The limiting concentration observed is probably due to the method of incorporation used. Detergent concentration increases at the higher AqpZ concentrations because detergent is present in the AqpZ stock solution. This may have resulted in a low AqpZ reconstitution efficiency and lower permeabilities when higher volumes of AqpZ stock solution are used. Unfortunately, the number of AqpZs inserted per vesicle has not been determined in this or other AqpZ studies (5); hence, we cannot offer a definitive conclusion. However, other studies have shown that vesicles with a AqpZ-to-lipid weight ratio of 1:1 can be synthesized by using slow detergent removal methods (32, 33). This indicates that higher permeabilities might be possible with other reconstitution methods. These results also indicate that membranes with specified levels of water permeability can be synthesized by controlling the concentration of AqpZ—a property that may be useful for drug delivery applications.

The protein-polymer membranes developed here have salt rejection and permeability ideal for desalination. Excellent control over the permeability of polymers was also demonstrated. Incorporation of AQPs (or suitable molecular mimics) into compatible synthetic polymers (such as the block copolymer system investigated in this study) is an innovative approach for making membranes for medical, industrial, and municipal desalting applications.

Materials and Methods

The detergent dodecyl maltoside used in protein purification was obtained from Anatrace Chemicals. Ni-NTA agarose beads were obtained from Qiagen. Sepharose 4B was used for chromatographic separation and was obtained from Sigma Aldrich. Other chemicals were obtained as described in the following sections.

Expression and Purification of AQP-Z. The plasmid allowing overexpression of histidine-tagged AqpZ (pTrc10HisAqpZ) was obtained from Dr. Peter Agre (Duke University Medical Center, Durham, NC) (5). It was transformed into the *E. coli* strain JM109 by electroporation. The resulting strain was grown and protein production induced by addition of isopropyl-β-D-thiogalactoside according to Borgnia *et al.* (5) with two modifications. The induction time was optimized at 7–8 h. The ultracentrifugation setup for recovery of membrane fractions was replaced by the use of a Biomax filter (MWCO of 30 kDa) in a centrifuge for 45–60 min for removal of smaller-molecular-weight material. Protein purification was performed by using nickel affinity chromatography (5).

Protein purification was followed by solubilization with a standard SDS

cracking buffer (34) with an additional component, 1% dodecyl maltoside, and polyacrylamide gel electrophoresis (34) to determine presence of protein. The purified protein was quantified by using the Lowry method (35).

Synthesis of ABA Polymer. The ABA was a symmetric poly-(2-methyloxazoline)-block-poly-(dimethylsiloxane)-block-poly-(2-methyloxazoline) ($PMOXA_{15}$-$PDMS_{110}$-$PMOXA_{15}$) polymer. The first step of the synthesis procedure involved acid-catalyzed polycondensation of dimethoxydimethyl silane in the presence of water and end-capper, resulting in butylhydroxy-terminated bifunctional PDMS. Liquid PDMS was purified by vacuum stripping at 80°C and precipitation in an equal (by weight) water/methanol mixture. Purified PDMS was reacted with triflic acid anhydride in hexane at −10°C for 3 h, resulting in triflate-PDMS bifunctional macroinitiator. The reaction mixture was then filtered under argon through a G4 filter. Hexane was evaporated under vacuum and dry ethyl acetate was added as reaction solvent. Addition of dry 2-methyl-2-oxazoline resulted in symmetric ring-opening cationic polymerization of PMOXA blocks on the macroinitiator. The reaction was terminated by addition of a methanol solution of 0.5 M potassium hydroxide. The synthesis of a similar, lower-molecular-weight polymer system with a lower hydrophobic-to-hydrophilic block-length ratio is described in further detail in Nardin *et al.* (26).

Preparation of ABA Vesicles and AQP Incorporation. Block copolymer vesicles (1–2 wt % of polymer in PBS at pH 7.4) were prepared by using the film rehydration method. Sixty milligrams of polymer was first dissolved in chloroform (5–10 ml), and the chloroform was evaporated slowly in a rotary vacuum evaporator at 40°C and a vacuum of <400 mbar to form an even film on the inside of round-bottomed flasks. This film was then further dried under a 0.3-mbar high vacuum for at least 4 h. Ten milliliters of PBS was then added dropwise to the film with alternating vigorous vortexing and periodic sonication (of durations <30 s) for several minutes. This mixture was then left stirring for at least 8 h. The resulting suspension was extruded several times through a 0.4-μm track-etched filter (Isopore, Millipore), followed by a 0.2-μm track-etched filter (Nucleopore, Whatman) to obtain monodispersed unilamellar vesicles. For reconstitution experiments, 500 μl of an AqpZ stock solution (1.6 mg/ml in 1.5% dodecyl maltoside, 66 mM KH_2PO_4, 133 mM NaCl, 13% glycerol, 3.33 mM β-mercaptoethanol, and 33.33 mM Tris) was added during the formation of the polymer vesicles, and subsequent steps were completed on ice. The resulting protein-containing vesicles were purified chromatographically by using a column packed with Sepharose 4B to remove nonincorporated protein and trace detergent.

Characterization of Vesicles. *Light scattering*. The static and dynamic light-scattering experiments were performed according to Nardin *et al.* (26) by using a commercial goniometer (ALV) equipped with a He-Ne laser (wavelength, 633 nm) at scattering angles between 30° and 150°. An ALV-5000/E correlator was used to calculate the photon intensity, and an autocorrelation function was used to calculate vesicle size.

Atomic force microscopy. These measurements were conducted by using a Picoscan SPM LE scanning-probe microscope equipped with a Picoscan 2100 SPM controller (Agilent Technologies). Measurements were conducted in tapping mode by using a Si cantilever (NCH) (Nanosensors). The length of this cantilever was 125 μm and the nominal force constant was 42 N/m. Samples were prepared by placing a dilute vesicle suspension on freshly cleaved mica for 1 min and then carefully washing with double-distilled water. This sample was dried and the measurements were performed on dry samples.

Transmission electron microscopy. These measurements were conducted on vesicle samples by using a Philips 400 microscope (Philips). The samples were prepared by dilution up to 1,000 times and then stained with 2% uranyl acetate on plasma-treated copper grids.

Cryogenic transmission electron microscopy. The vesicle suspension was deposited on a holey carbon grid and frozen rapidly by plunging into liquid ethane above its freezing point by using a cryo holder. This holder was then transferred to the microscope and imaged in transmission mode at 200 kV at liquid nitrogen temperature. The equipment used for this measurement was a Zeiss 922 Omega microscope with a Gatan CT3500 cryo holder and a Gatan Ultrascan 1000 camera system.

Permeability measurements. The permeability of the two types of vesicles were determined by using a stopped-flow procedure (5). The stopped-flow apparatus was a SX.17 MV spectrometer (Applied Photophysics). Vesicles were rapidly mixed with a solution containing the osmotic agent (salt, glucose, glycerol, or urea) causing water efflux from the vesicles. The changes in light scattering caused by vesicle shrinkage were recorded at an emission wavelength of 600 nm in the stopped-flow apparatus [Borgnia *et al.* (5) and Milon *et al.* (36)]. These experiments were conducted with a constant 7-bar pressure to minimize pressure variations that could complicate kinetics analysis. Results were corrected for pressure-related mechanical compression by subtracting the baseline observed in control experiments without osmotic agents. These data were then fitted to an exponential rise equation to calculate the exponential coefficient, and the osmotic water permeability (P_f) was calculated by using the following expression (5):

$$P_f = k/(S/V_o) \times V_W \times \Delta_{osm},$$

where k is the exponential rise rate constant for the initial rise in the light-scattering curve, S is the initial surface area of the vesicles, V_o is the initial volume of the vesicles, V_w is the molar volume of water(18 cm^3), and Δ_{osm} is the difference in osmolarity driving the shrinkage of the vesicles.

Several sets of experiments were conducted with similar conditions but different preparations (prepared in different batches) to ensure repeatability. Additionally, initial experiments with up to 12 traces per experimental condition showed that five traces were adequate for providing sufficient data for analysis. Therefore, in subsequent analyses, a minimum of five traces were fit to the initial exponential rise by using the curve-fitting toolbox available through the MATLAB software (Mathworks).

Stopped-flow experiments were repeated at different temperatures (5.5, 7.5, 10, 12.5, and 15°C) for the ABA and AqpZ-ABA vesicles. The exponential rise rates calculated from these experiments were plotted against the inverse of temperature to determine the Arrhenius activation energies.

The reflection coefficients for salt, urea and glycerol were calculated based on the method presented by Meinild *et al.* (6). Glucose was used as the reference solute and the comparative experiments were all conducted at 15°C.

ACKNOWLEDGMENTS. We thank Dr. Reinhard Kissner, Swiss Federal Institute of Science and Technology (ETH), Zurich, Switzerland, for his valuable comments and assistance with conducting the stopped-flow experiments and for providing access to the instrument; Dr. Robert Gennis and Krithika Ganesan, University of Illinois at Urbana Champaign, for providing access to the stopped-flow apparatus in Urbana, IL, for initial experiments; Dr. Peter Agre for providing the pTrc10HisAqpZ plasmid; and Dr. Markus Drechsler at the University of Bayreuth for providing assistance with cryogenic transmission electron microscopy of polymer vesicles and interpretation. This work was supported, in part, by a University of Illinois Fellowship, a National Water Research Institute Fellowship, and a University of Illinois Dissertation Travel Grant. This work was also a part of the European Science Foundation EUROCORES Program SONS, and financial support was provided by the National Center of Competence in Nanoscale Science, the Swiss National Science Foundation, and MRTN-CT-2004-005516.

1. Knepper MA, Wade JB, Terris J, Ecelbarger CA, Marples D, Mandon B, Chou CL, Kishore BK, Nielsen S (1996) *Kidney Int* 49:1712–1717.
2. Gorin MB, Yancey SB, Cline J, Revel J-P, Horwitz J (1984) *Cell* 39:49–59.
3. Preston GM, Carroll TP, Guggino WB, Agre P (1992) *Science* 256:385–387.
4. Nielsen S, Smith BL, Christensen EI, Agre P (1993) *Proc Natl Acad Sci USA* 90:7275–7279.
5. Borgnia MJ, Kozono D, Calamita G, Maloney PC, Agre P (1999) *J Mol Biol* 291:1169–1179.
6. Meinild AK, Klaerke DA, Zeuthen T (1998) *J Biol Chem* 273:32446–32451.
7. Jung JS, Preston GM, Smith BL, Guggino WB, Agre P (1994) *J Biol Chem* 269:14648–14654.
8. Pontoriero G, Pozzoni P, Andrulli S, Locatelli F (2003) *Nephrol Dial Transplant* 18(Suppl 7):vii21–vii25.
9. Pastan S, Bailey J (1998) *N Engl J Med* 338:1428–1437.
10. Service RF (2006) *Science* 313:1088–1090.
11. Tal A (2006) *Science* 313:1081–1084.
12. Patel-Predd P (2006) *Environ Sci Technol* 40:3454–3455.
13. Discher BM, Won YY, Ege DS, Lee JCM, Bates FS, Discher DE, Hammer DA (1999) *Science* 284:1143–1146.
14. Dinsmore AD, Hsu MF, Nikolaides MG, Marquez M, Bausch AR, Weitz DA (2002) *Science* 298:1006–1009.
15. Coury LA, Mathai JC, Brodsky JL, Agre P, Zeidel ML (1996) *J Am Soc Nephrol* 7:A0088–A0088.
16. Duncan R (2003) *Nat Rev Drug Discov* 2:347–360.
17. Taubert A, Napoli A, Meier W (2004) *Curr Opin Chem Biol* 8:598–603.
18. Meier W, Nardin C, Winterhalter M (2000) *Angew Chem Int Ed* 39:4599–4602.
19. Graff A, Sauer M, Van Gelder P, Meier W (2002) *Proc Natl Acad Sci USA* 99:5064–5068.
20. Choi HJ, Montemagno CD (2005) *Nano Lett* 5:2538–2542.
21. Choi HJ, Germain J, Montemagno CD (2006) *Nanotechnology* 17:1825–1830.
22. Stoenescu R, Graff A, Meier W (2004) *Macromol Biosci* 4:930–935.

23. Leson A, Filiz V, Forster S, Mayer C (2007) *Chem Phys Lett* 444:268–272.
24. Nardin C, Winterhalter M, Meier W (2000) *Langmuir* 16:7708–7712.
25. Nardin C, Thoeni S, Widmer J, Winterhalter M, Meier W (2000) *Chem Commun* 1433–1434.
26. Nardin C, Hirt T, Leukel J, Meier W (2000) *Langmuir* 16:1035–1041.
27. Grumelard J, Taubert A, Meier W (2004) *Chem Commun* 1462–1463.
28. Sulkowski E (1985) *Trends Biotechnol* 3:1–7.
29. Almgren M, Edwards K, Karlsson G (2000) *Colloids Surfaces A* 174:3–21.
30. Garybobo CM (1971) *J Gen Physiol* 57:610–622.
31. Mehdizadeh H, Dickson JM, Eriksson PK (1989) *Ind Eng Chem Res* 28:814–824.
32. Scheuring S, Ringler P, Borgnia M, Stahlberg H, Muller DJ, Agre P, Engel A (1999) *EMBO J* 18:4981–4987.
33. Dolder M, Engel A, Zulauf M (1996) *FEBS Lett* 382:203–208.
34. Sambrook J, Fritsch EF, Maniatis T (1989) *Molecular Cloning: A Laboratory Manual* (Cold Spring Harbor Lab Press, Cold Spring Harbor, NY).
35. Lowry OH, Rosebrough NJ, Farr AL, Randall RJ (1951) *J Biol Chem* 193:265–275.
36. Milon A, Lazrak T, Albrecht AM, Wolff G, Weill G, Ourisson G, Nakatani Y (1986) *Biochim Biophys Acta* 859:1–9.
37. McCutcheon J, Elimelech M (2006) *J Membr Sci* 284:237–247.
38. Matsura T (2001) *Desalination* 134:47–54.

2.4.2 Immobilized Protein-Polymer nanoreactors

Immobilized Protein-Polymer nanoreactors

Mariusz Grzelakowski[†], Ozana Onaca[†], Per Rigler[†], Manish Kumar[‡], Wolfgang Meier[†,]*

† University of Basel, Department of Chemistry Klingelbergstrasse 80, CH-4056 Basel, Switzerland,

‡Department of Civil and Environmental Engineering, University of Illinois at Urbana–Champaign, 205 North Mathews Avenue, Urbana, IL 61801.

m.grzelakowski@unibas.ch, ozana.onaca@unibas.ch, per.rigler@unibas.ch, kumar11@illinois.edu, wolfgang.meier@unibas.ch

Block copolymers can be used to construct robust nanoscale reactors permeabilized by protein channels. We demonstrate the use of these nanoreactors as a novel immobilization platform for generating precisely patterned chemically and/or biologically active surfaces. These were used to study enzymatic conversion of the phosphatase substrate, ELF97® by encapsulated acid phosphatase. The model methodology utilized can be easily adapted to study complex multi-component reactions with potential applications in sensors, analytics and microfluidics.

Nanoreactors, active surfaces, immobilization, block copolymer vesicles, enzymatic conversion, kinetics.

In living organisms enzymatic reactions occur in precisely defined time and space. An important goal of interdisciplinary research is to not only study the behavior of biological macromolecules in their natural cellular environment[1], but also create synthetic analogues of complex natural functions such as

molecular sensing and communication.[2] It also strives to apply the resulting knowledge to develop devices inspired by reverse engineering of biology.[3] Bioinspired polymeric vesicles[4], with integrated transport proteins[5] and encapsulated enzymes[6] are such a system.

An immobilization system for liposomes has been previously reported by Vermette at el.[7] In this study intact liposomes were immobilized on different solid substrates by the NeutrAvidin™ approach. There are several drawbacks of lipidic systems related to the nature of the lipid molecules themselves. The molecular weight of a typical lipid is less than 1000 g/mol resulting in formation of thin (ca. 5 nm) membrane structures. Due to potential for lipid oxidation, these membranes are characterized by relatively high permeability and fragility[6] thus limiting the scope of aplications.[2, 8] A solution to these limitations is to transfer this methodology to the macromolecular scale utilizing block copolymers. We have designed amphiphilic ABA block copolymers to form highly impermeable bilayer like membranes in aqueous solutions.[6, 9] Additionally, we have developed a method to functionalize resulting vesicles with several functional groups including biotin. Immobilization of block copolymer vesicles enabled the design of new stable reactive surfaces. This provides us with an ability to carry out conversions (chemical and biological) at a precise location and enables control over the reaction micro-environment in situ. This is potentially relevant for application in the field of analytics, specifically sensors. It also extends our ability to conduct basic research on enzymatic reactions in confined environments which use unstable or sensitive materials, by shielding of the reactive species in the cavity of the nanoreactor[6]. Furthermore this approach provides a tool for single molecule spectroscopy in tethered nanoreactors[10].

We present here the first successful application of polymer vesicles as an immobilization platform, for studying a model enzymatic conversion inside nanoreactors. The successful immobilization of nanoreactors on a glass substrate was realized by employing the receptor-ligand pair, biotin-streptavidin[11]. The surface of the glass substrate was structured by micro-contact printing[12] of bovine serum albumin, labeled with biotin. Exposure of biotinylated protein patterns to streptavidin followed by incubation with biotinylated particles lead to their immobilization.

In order to prove structurally controlled immobilization of the intact biotinylated vesicles, they were loaded with hydrophilic fluorescent dye (Sulphorhodamine-B) and incubated with glass surfaces structured with Alexa Fluor 488 labeled streptavidin. Figure 1A shows successful structuring of the glass slide surface with BSA-biotin-streptavidin-Alexa 488 (488nm green channel). Incubation of the streptavidin structured surface, with biotinylated dye loaded vesicles led to their structured immobilization (546nm red channel, Figure 1B). The vesicles remained intact upon immobilization and the fluorescent signal of the encapsulated hydrophilic dye can be observed in the areas resembling the exact structure of the immobilized streptavidin. In control experiments, glass slides were structured with biotin labeled bovine serum albumin and incubated with dye loaded biotinylated vesicles in absence of streptavidin. No immobilization was observed (Figure 1 C-D).

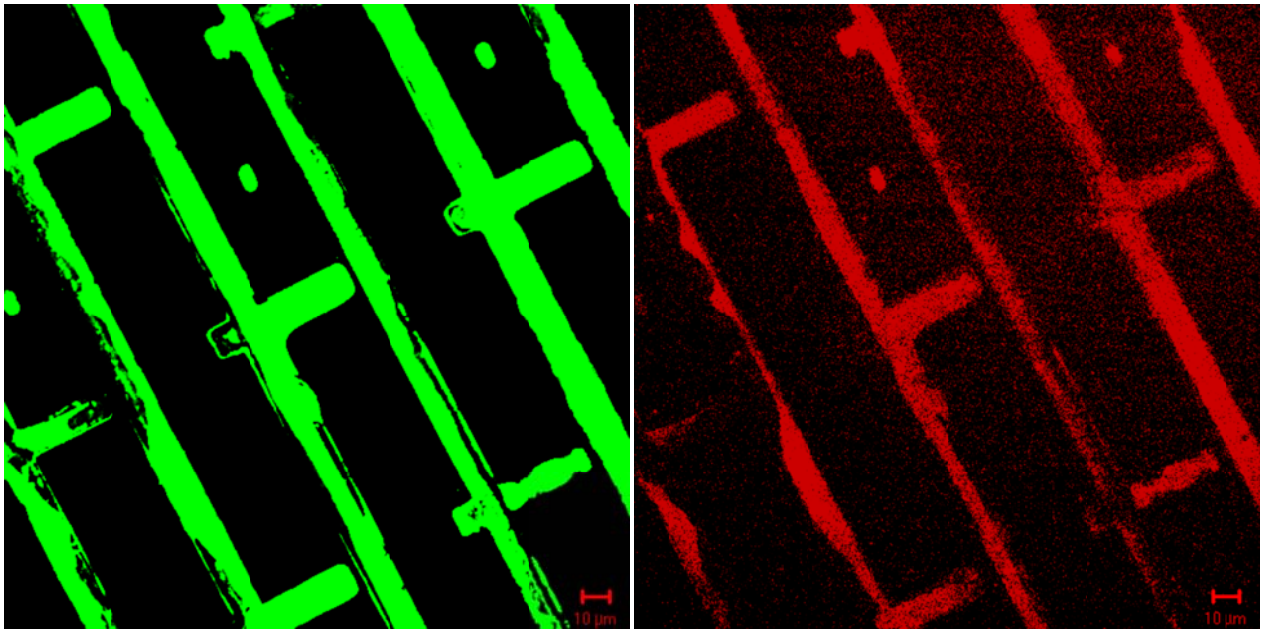

A B

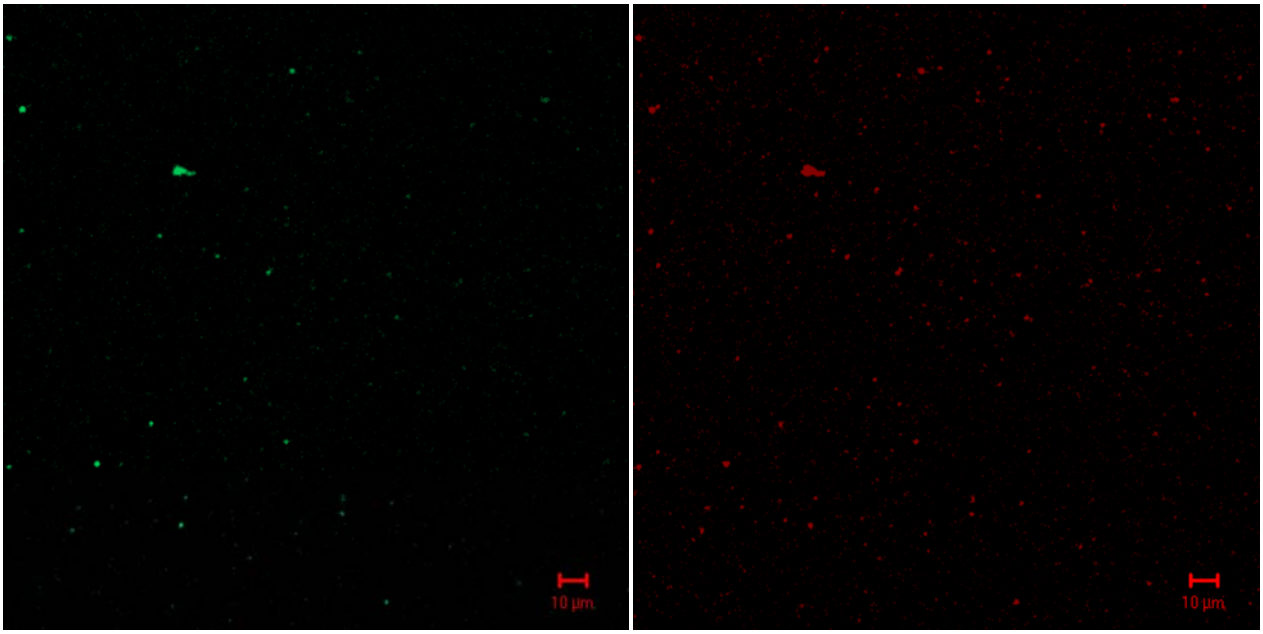

C **D**

Figure 1. Laser scanning microscopy images of structured immobilization of streptavidin-alexa 488 (3A) and vesicles loaded with sulforhodamine B (3B). Alexa 488 labeled streptavidin was incubated with the glass surface structured with biotinylated BSA resulting in its immobilization resembling the exact structure of the micro-contact printing mask. Incubation of the streptavidin functionalized surface with biotinylated dye loaded vesicles led to their successful immobilization on the surface. Vesicles remained intact upon immobilization. Control samples structured with BSA-biotin and incubated with sulforhodamin loaded biotinylated vesicles in green (1C) and red (1D) channel. No immobilization can be observed.

The model reaction chosen for studying enzymatic conversion inside nanoreactors was the dephosphorylation of the fluorogenic substrate - ELF 97® by acid phosphatase. The enzyme is known to dephosphorylate phosphate groups[13, 14] from ELF 97® substrate, optimally at pH=5.5. The product ELF 97 alcohol, becomes insoluble and fluorescent, enabling direct time resolved laser scanning microscopy (LSM) observation of product formation. Acid phosphatase was encapsulated[15] in biotinylated $A_{12}B_{55}A_{12}$ (poly-2-methyl-2-oxazoline-b-polydimethylsiloxane-b- poly-2-methyl-2-oxazoline) block copolymer vesicles[16]. The accessibility of the substrate to the enzyme was provided by reconstitution of the bacterial derived outer membrane protein F channels (OmpF) in otherwise highly impermeable[9] vesicular walls. The OmpF channels are known to be fully functional upon reconstitution in synthetic bilayer-like membranes, providing a molecular cut-off of 600 g/mol[17, 18], thus providing an

avenue for selective permeability of ELF 97® substrate (M.W.= 431 g/mol) to the interior of the nanoreactor.

In order to verify whether the encapsulation process affects enzyme activity, initial kinetic experiments were performed in solution. Time resolved fluorimetric studies, presented in Figure 2 (excitation wavelength of 350 nm and emission of 550 nm) performed for substrate, control native polymer vesicles (encapsulating acid phosphatase but without OmpF channels) and nanoreactors (encapsulating acid phosphatase and bearing OmpF channels) in solution, show that enzymatic turnover of the substrate takes place only in case of samples with reconstituted channel proteins, where the permeation of the ELF97® phosphate into the cavity of the vesicle is enabled.

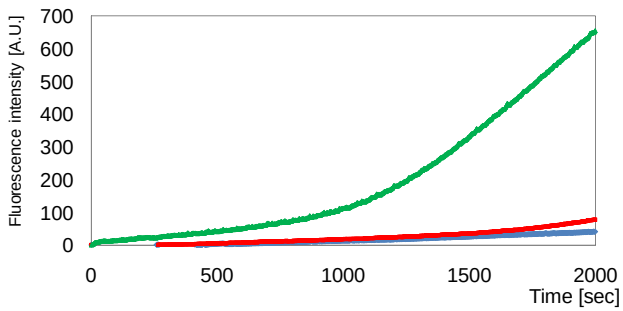

Figure 2. Enzymatic conversion of ELF®97 phosphate (5µM) inside nanoreactors with incorporated OmpF channel proteins (green) compared with vesicles encapsulating acid phosphatase without channel protein (red) and the free substrate (blue) in solution.

The nanoreactors with OmpF channels and with biotin functionalized polymer were then immobilized on the patterned functionalized glass surface. Figure 3 shows a schematic of the immobilization procedure and the nanoreactor system.

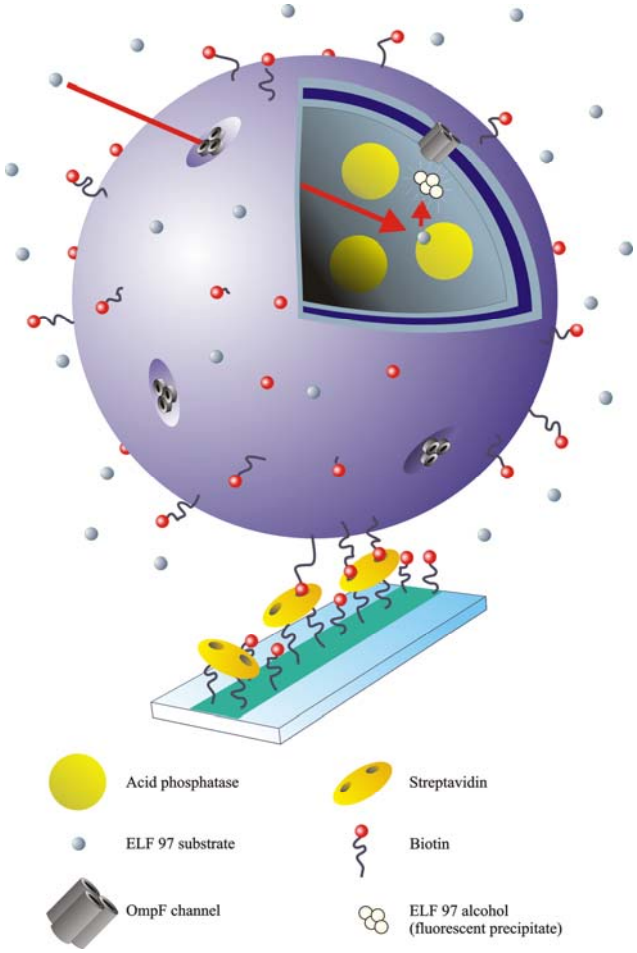

Figure 3. Schematic representation of the immobilization of nanoreactor system on glass surface. Acid phosphatase was encapsulated in the OmpF bearing biotinylated vesicles and immobilized on the surface of the glass structured with streptavidin.

Incubation of structurally immobilized nanoreactors with the substrate (ELF97®) resulted in enzymatic turnover of the substrate, leading to product formation (ELF 97 alcohol). The product formation results in increase of fluorescence intensity in the area structured with nanoreactors. Figure 4 shows LSM images of structured nanoreactors on the surface of the glass slide before (4A) and after incubation (20 minutes) with 75 µM substrate (4B). The structure of the intense fluorescence signal from the surface resembles the morphology of the micro-contact printing mask, thus proves successful selective immobilization of the nanoreactors on the surface (Figure 4B).

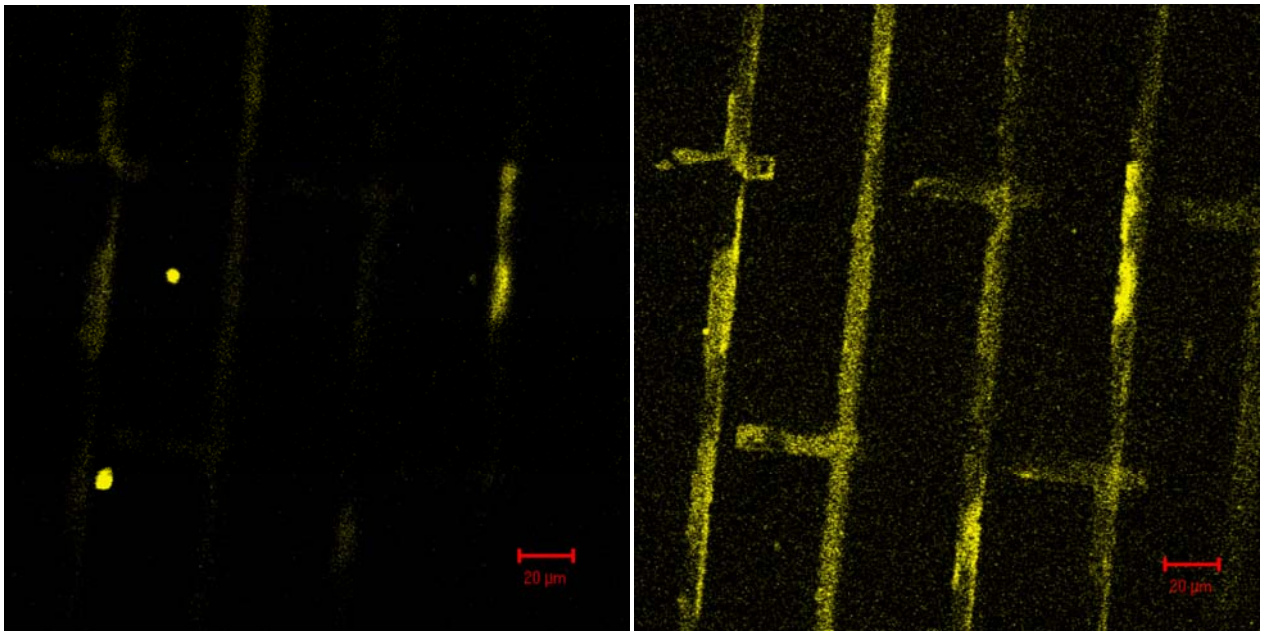

A B

Figure 4. LSM images of structurally immobilized nanoreactors before (4A) and after incubation (20 minutes) with ELF® 97 substrate (4B). Nanoreactors were immobilized on the glass slide imaged and the fluorescent product formation was followed by time resolved LSM.

Comparison of time resolved intensity profiles of nanoreactors bearing OmpF channels reconstituted in the vesicular wall, with the control vesicles immobilized on the glass slide surface confirmed results obtained from measurements in bulk solutions. Figure 5 represents the time resolved fluorescence intensity profile (excitation 405 nm) of the immobilized nanoreactors and control vesicles incubated with 75 µM ELF 97®and indicates that the reaction occurred only in the case of nanoreactors with reconstituted OmpF.

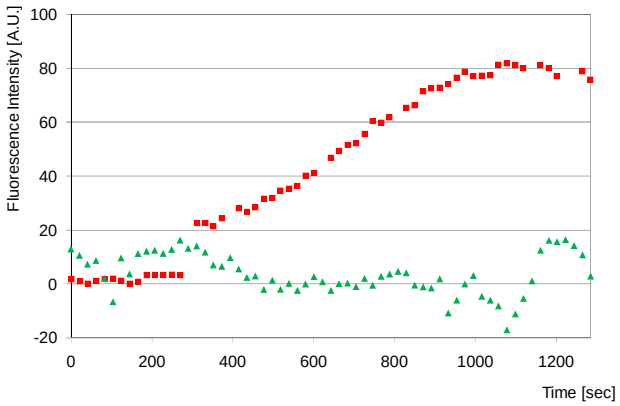

Figure 5. Time resolved fluorescence intensity profile of reaction in nanoreactors encapsulating acid phosphatase and bearing OmpF channel (green) and control vesicles encapsulating acid phosphatase (red) immobilized on the surface incubated with 75 µM Elf 97® substrate. Enzymatic turnover of the substrate inside of the immobilized nanoreactors results in increase of the fluorescence intensity.

The fluorescence intensity profile of the reaction at the surface resembles the kinetic behaviour of the free enzyme and nanoreactors in solution. The lag time of the enzymatic turnover was different for the set of the measurments of free enzyme (~14 sec, 10 µM ELF®), nanoreactors in bulk (~600 sec, 10 µM ELF®) and immobilized nanoreactors (~1600 sec, 10 µM ELF®). This increasing lag time can be explained by limited access of the substrate to the enzyme due to reduced mixing. The saturation of the profile in case of immobilized nanoreactors can be atributed to the inhibition of the enzyme, by steric hindrance due to precipitation of the fluorescent product in the cavity of the nanoreactor.

In order to verify the possibility of studying reaction kinetics inside the nanoreactors, substrate concentration was varied and time resolved measurements conducted. Figure 6 shows the influence of substrate concentration on the kinetics of fluorescent product formation. Differences in the slopes of the normalized curves can be observed and attributed to increasing substrate concentrations. Data in Figure 6 has been fitted with a guided exponential rise equation using MATLAB®.

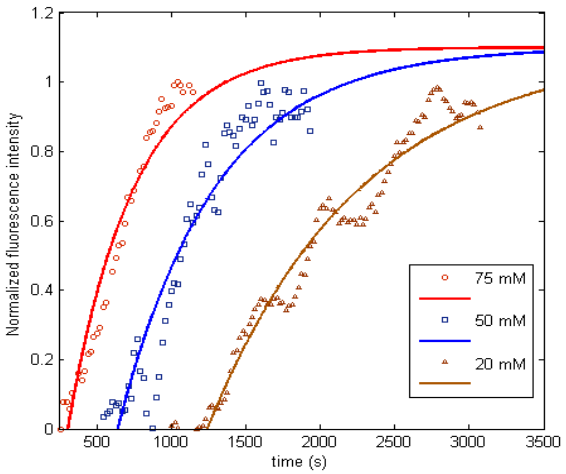

Figure 6. Relative fluorescence intensity increase for immobilized nanoreactors incubated with 20, 50 and 75 µM ELF 97®. Fits are shown as guides and not used for kinetic analyses.

The Michealis-Menten[19] approach was used to determine the kinetic parameters of the acid phosphatase encapsulated in nanoreactors in solution and immobilized at the surfaces.[20] The Michaelis constant Km resulting from Lineweaver–Burke[20] plot was found to be 4 µM for the free enzyme, 7 µM for the nanoreactors in bulk and 46 µM for the immobilized nanoreactors. Obtained values lies in the range observed for most enzymes (10^{-1} – 10^{-7}M)[20]. The observed 6.5 times lower activity of the immobilized nanoreactors, in comparison to the nanoreactors in solution, could be due to the presence of unstirred aqueous layers at the polymer membrane/solution interface posing a diffusional barrier for otherwise rapidly permeating substrate.[21] The thickness of such unstirred layers in biological membranes can range from 5 µm to 0,5 mm depending on the mixing conditions. Influence of such diffusional barrier is more expressed in case of membranes characterized by fast solute transport[21, 22]. Additionally, reduced accessibility of the membrane proteins due to their positioning towards the surface, resulting from immobilization on solid support, may contribute to the observed decrease of the enzyme activity.

The described system may serve as an investigation tool for studies over a wide range of different reactions or bioconversions and can be applied as a novel method for construction of chemically/biologically active surfaces for analytics, sensors and even controlled reactions. This enables several possibilities, including for instance control of a precisely localized reaction and delivering the product at desired time and space. The studied immobilization methodology can be easily extended by the use of covalent attachment onto different types of substrates, by modifications of the functional end-groups of the block copolymer with control over the density of reactive species. In addition, post modification of the block-copolymer may lead to introduction of further functionality at the surface of the nanoreactors and accompanied by inclusion of active compounds in the hydrophobic part of the membrane - enabling studies of cascade reactions[23]. The morphology of the reactive surface is dependent on the structure of the PDMS mask used and may be chosen for specific application (total coverage vs. various shapes).

Model reaction kinetics were studied in nanoreactors and immobilized nanoreactors. The influence of the substrate concentration on the kinetics of enzymatic turnover (presented in Figure 6) shows an increase in reaction rate with increasing substrate concentration. The kinetic parameters obtained for nanoreactors in bulk and at the surfaces were compared to free enzyme and the analysis indicated reduced activity of the enzyme inside the nanoreactor system, with preservation of its key characteristics in the studied concentration range. The Km values estimated for the nanoreactors at the surfaces were obtained from the LSM measurements with the use of 405 nm laser-line, therefore the detection of the product formation was not optimal resulting in decrease of the signal-to-noise ratio. Thus the reported Km values for immobilized nanoreactors shall be treated as an estimate.

In this work we have shown successful application of immobilized polymer vesicles incorporating membrane protein channels as nanoreactors for studying model enzymatic reaction of water soluble enzymes. This work is an initial step of more detailed and systematic studies on immobilization of nanoreactor systems employing different enzyme-substrate pairs and complex reaction cascades.

Acknowledgment. We thank Dimitri Stamou IBM Zurich Research Laboratory for providing the PDMS mask; Julia Razumovitch University of Basel for interesting and useful discussions concerning laser scanning microscopy and David W. Hughes University of Basel for manuscript editing. This work was supported by the NCCR Nanoscale Science, the Swiss National Science Foundation and NEST Projects 029084 and 043431.

Supporting Information Available: OmpF expression and purification, block copolymer synthesis, nanoreactors formation, ABA block copolymer self-assembly characterization (DLS/SLS, TEM, AFM), micro-contact printing procedure, immobilization procedure, time resolved laser scanning microscopy measurements, data collection and evaluation, system lag-time comparison.

SUPPORTING INFORMATION

OmpF expression and purification:

OmpF gene was transformed into the expression host *E coli* B^E strain BL21 (DE) opm8 (Prilipov et al. 1998). 10 ml of overnight culture were used to inoculate 1 l LB medium (2 l shaking flasks; Infors HT Multitron; 250 rpm, 37˚C). The OmpF expression was induced at an OD_{600} of 0.6 by addition of isopropyl-β-D-thiogalactopyranoside (IPTG) to a final concentration of 1 mM. Cells were further grown until an OD_{600} 2.0 when they were harvested by centrifugation (Sigma 3-18k Fischer Biostock Scientific; 20 min, 6000rpm, 4˚C).

Cells were resuspended in 10 ml 20 mM Tris-Cl pH 8.0, 2% SDS buffer/ 1g cell pellet and the mixture was sonicated 30 sec x 6 times, amplitude 40 (Ultrasonic Processor GE130). The membrane fractions were removed by centrifugation (60 min @ 4°C, 22000 rpm).

A pre-extraction step has followed in 0.125% octyl-POE in 20mM phosphate buffer pH 7.4 with an incubation time of 1 h. (Memmert GMBH. Germany, 37°C, 250 rpm). The membrane fractions were removed by centrifugation (60 min @ 4°C, 22000 rpm) and further treated with 3% octyl-POE in 20mM phosphate buffer pH 7.4 for OmpF extraction. The solubilised OmpF was separated from the memebranes by centrifugation (10 min, 4000rpm, 4˚C).

The purity of the extracted protein was verified by SDS-acrylamide gel electrophoresis (12%).

Polymer synthesis:

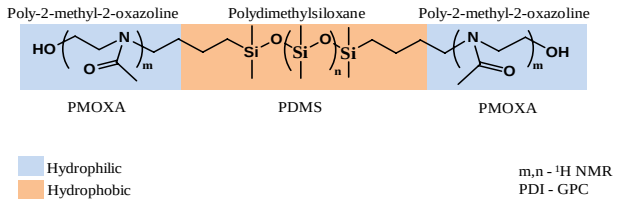

Figure S1. ABA block copolymer structure.

The $A_{12}B_{55}A_{12}$ block-copolymer was synthesized by cationic ring-opening polymerization of 2-methyloxazoline using a bi-triflate activated polydimethylsiloxane macroinitiator. The synthetic route followed the one described in Nardin et al.[24]. The molecular weight of the polymer obtained from ^{1}H NMR was 6325g/mol. Figure S1 shows the polymer structure.

Formation of Nanoreactors:

Biotinylated block copolymer vesicles were prepared by using the film rehydration method. Twelve milligrams of polymer (10% biotinylated) were first dissolved in ethanol (2–5 ml) together with 200 µL of OmpF solution (8 µM), and the ethanol was evaporated slowly in a rotary vacuum evaporator at 40°C to form an even film on the inside of round-bottomed flasks. This film was then further dried under a 0.3-mbar high vacuum for at least 4 h. Two milliliters of sodium acetate (100 mM) solution of acid phosphatase (Sigma-Aldrich Mw= 110 kDa, 10 µM) were then added to the film and rotated on the rotary evaporator at room temperature for 24 h in order to hydrate the polymer film. A small stir bar was then added and the solution was stirred for another 24h at room temperature. The resulting suspension was extruded several times through a 0.4 µm track-etched filter (Isopore, Millipore), followed by a 0.2 µm track-etched filter (Isopore, Millipore) to obtain monodispersed unilamellar vesicles. The resulting protein-containing and enzyme encapsulating vesicles were purified chromatographically with Sepharose 2B packed column to remove non encapsulated enzyme and non incorporated protein. Figure S2 shows a typical separation chromatogram.

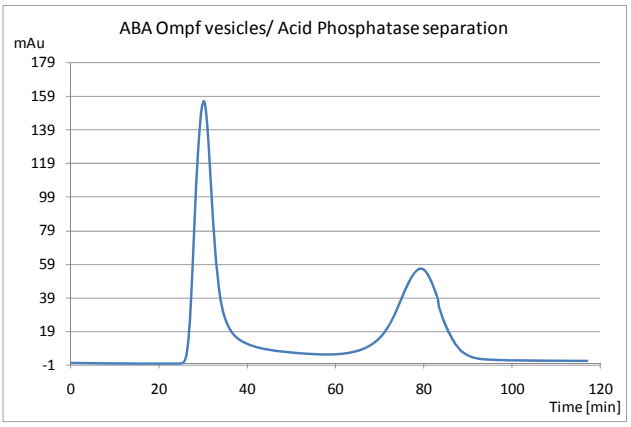

Figure S2. Size exclusion chromatogram of nanoreactors.

Samples for control experiments followed the same protocol, without the addition of OmpF channel protein.

Self assembly characterization:

ABA polymer vesicles were characterized using static and dynamic light scattering (DLS/SLS), transmission electron microscopy (TEM) and atomic force microscopy (AFM).

DLS/SLS

The static and dynamic lightscattering experiments were performed according to Nardin et al.[24] by using a commercial goniometer (ALV) equipped with a He-Ne laser (wavelength, 633 nm) at scattering angles between 30° and 150°. An ALV-5000/E correlator was used to calculate the photon intensity, and an autocorrelation function was used to calculate vesicle size.

A hydrodynamic radius (Rh) of 121 nm was estimated from dynamic light scattering, with size polydispercity index PDI < 0.18. This size is consistent with similar PMOXA-PDMS-based block copolymers [24]. The radius of gyration (Rg) of 121 obtained from static light scattering measurements of the same sample indicates hollow sphere morphology of the aggregates (Rg/Rh=1)[24].

AFM

Measurements were conducted using a Picoscan SPM LE scanning-probe microscope equipped with a Picoscan 2100 SPM controller (Agilent Technologies). Measurements were conducted in tapping mode using a Si cantilever (NCH) (Nanosensors). The length of this cantilever was 125 μm and the nominal force constant was 42 N/m. Samples were prepared by placing a dilute vesicle suspension on freshly cleaved mica for 1 min and then carefully washing with double-distilled water. This sample was than dried and the measurements were performed on the dry sample.

Analysis of topography and phase images obtained from dry state atomic force microscopy supported the conclusions drawn from light scattering measurements. Dilute vesicle solution was deposited on the hydrophilic substrate (mica) and the analyzed single particles exhibited typical profile of collapsed spheres of average size of 108 +/- 12 nm; see Figure S3.

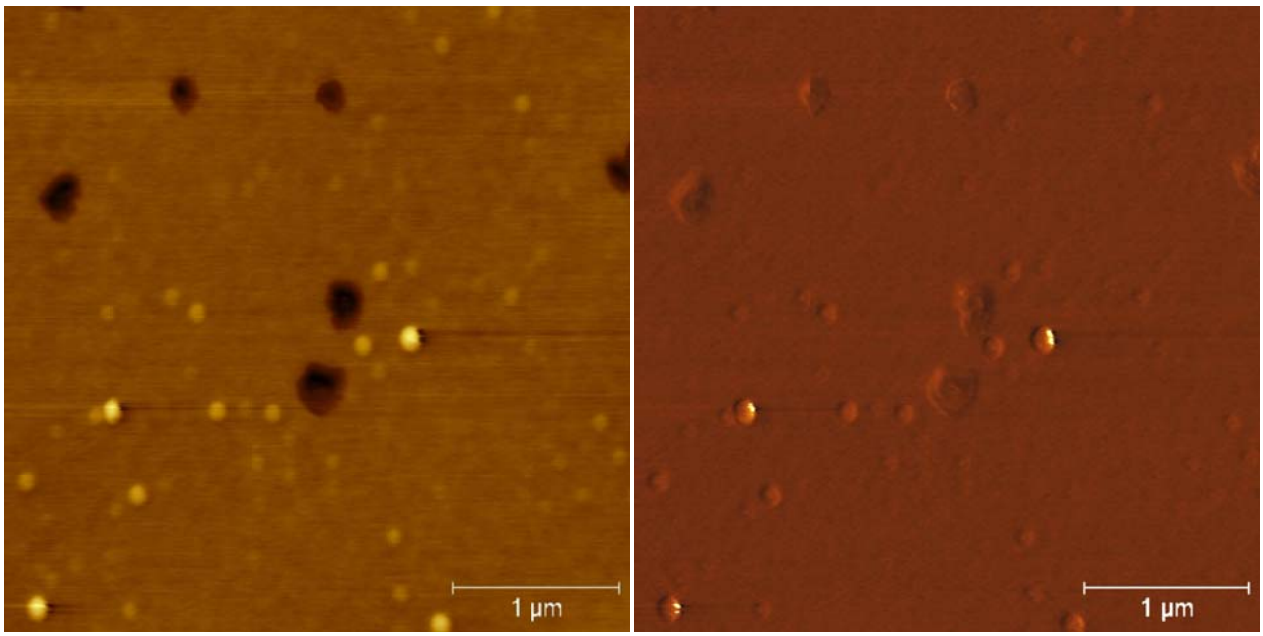

A B

Figure S3. Topography (A) and phase (B) images of vesicles adsorbed on mica substrate.

TEM

Measurements were conducted on vesicle samples using a Philips 100 microscope (Philips). The samples were prepared by dilution of 100 times and stained with 2% uranyl acetate on plasma-treated copper grids.

Transmission electron micrographs of vesicles stained showed spherical particles of uniform sizes, see figure S4.

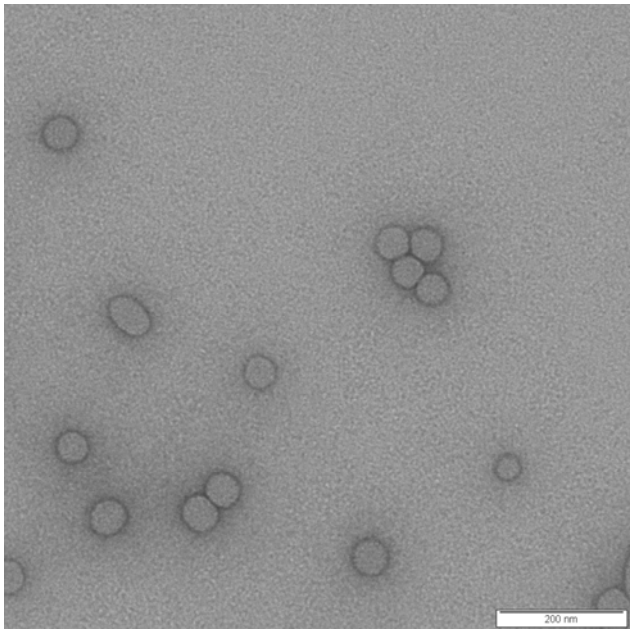

Figure S4. Transmission electron micrograph of polymer vesicles stained with 2%uranyl acetate.

Micro contact printing and immobilization procedure:

The structured polydimethylsiloxane PDMS mask (source) was cleaned with ethanol and dried with nitrogen flow. BSA-biotin solution was cast onto the mask (0.1 mg/ml BSA-biotin, sodium acetate

buffer, pH 5.5), incubated for 10 minutes and dried with nitrogen flow forming protein film. The BSA-biotin covered mask was than pressed to the surface of dried clean microscopy glass slides, cleaned by multiple sonication in 2% Hellmanex detergent, water and methanol) and incubated for 10 minutes resulting in patterning of the surface with BSA-biotin. The glass slide was than mounted into the chamber of the flow cell and sealed. The surface was passivated by incubation with BSA solution (1mg/ml, sodium acetate pH 5.5), washed with buffer and incubated with streptavidin solution (0.1 mg/ml, sodium acetate pH 5,5) resulting in its immobilization in structured manner followed by washing steps. Biotinylated nanoreactors were than immobilized on the streptavidin stripes resulting in formation of BSA-biotin-streptavidin-biotin-nanoreactor link.

Time resolved Fluorescent measurements:

The free enzyme and nanoreactors in solution kinetic experiments were performed using Perkin Elmer LS55 fluorimeter, with the excitation wavelength of 350 nm and emission wavelength of 550 nm, at the slit width of 5nm. The free enzyme and nanoreactors kinetic measurements were performed in 500 µL total volume. To the 1 µM acid phosphatase solution in sodium acetate (pH=5.5), varied amounts of substrate were added (0.5, 5, and 10 µM final ELR 97® concentration). The kinetic trace was recorded and the kinetic parameters were evaluated using Lineweaver-Burk plot.[20] Same methodology was applied to the nanoreactors in solution kinetic studies, where the nanoreactors (2 mg/ml polymer) were incubated with the substrate of increasing concentration (1, 5, 10, 50, 100 and 150 µM final ELR 97® concentration).

Time resolved Laser Scanning Microscopy measurements:

The flow cell containing immobilized nanoreactors was mounted onto the Zeiss Confocor 2 LSM/FCS stage. The increase of fluorescence intensity upon exchanging the content of the flow cell with the ELF 97® substrate solution (Invitrogen, Mw=431.08 Da) was followed in the time series (excitation: 405 nm 19%, long pass 475 filter, 40x/1.2 objective).

LSM data collection and evaluation:

Data collection involved choosing and averaging of the results obtained for patterned areas of the same starting intensity. Background was collected in the same manner for areas neighboring the patterns, averaged and subtracted from initial averaged signals. Intensities were normalized and the curves obtained for different concentrations were offset in time for clarity. Resulting curves were fitted with guided exponential rise with MATLAB software. The choice of the concentration was mostly driven by the sensitivity of the LSM setup. Concentrations below 20 µM Elf 97® are characterized by a very low signal-to-noise ratio. In the high concentration regime (above 50 µM Elf 97®) there is no significant influence of the increasing concentration of the substrate on the reaction kinetics. Most of the commercially available LSM instruments are equipped with laser lines going down to a wavelength of 405 nm. The excitation spectra of Elf 97 alcohol is characterized by a broad peak, with the maximum at 350 nm. Performing our measurements at 405 nm decreases the sensitivity and limits us to the concentration range of the substrate used for the study of reaction kinetics of this particular enzyme-substrate pair

Enzymatic turnover lag time comparison for the systems:

Figure S5 shows the normalized intensity profile of the reaction for free enzyme, nanoreactors in bulk and at the surface.

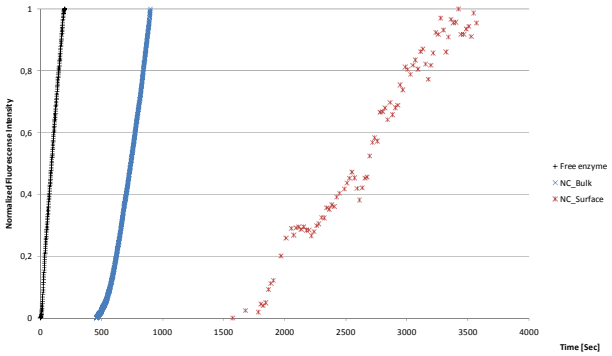

Figure S5. Comparison of the reaction lag-time for free enzyme (black), nanoreactors in bulk (blue) and immobilized nanoreactors (red) incubated with 10 µM ELF® 97 substrate. The data were normilized to the saturation of the fluorimeter detector in case of measurements in solution and to the reaction saturation in case of immobilized nanoreactors.

References:

1. Conroy, R. S.; Danilowicz, C. *Contemp. Phys.* **2004,** 45, (4), 277-302.
2. Barron, A. E.; Zuckermann, R. N. *Curr Opin Chem Biol* **1999,** 3, (6), 681-7.
3. Jones, R. A. L. *J. Polym. Sci., Part B: Polym. Phys.* **2005,** 43, (23), 3367-3368.
4. Discher, D. E.; Eisenberg, A. *Science (Washington, DC, U. S.)* **2002,** 297, (5583), 967-973.
5. Nardin, C.; Meier, W. *Rev. Mol. Biotechnol.* **2002,** 90, (1), 17-26.
6. Christian, D. A.; Cai, S.; Bowen, D. M.; Kim, Y.; Pajerowski, J. D.; Discher, D. E. *Eur. J. Pharm. Biopharm.* **2009,** 71, (3), 463-474.
7. Vermette, P.; Meagher, L.; Gagnon, E.; Griesser, H. J.; Doillon, C. J. *J Control Release* **2002,** 80, (1-3), 179-95.
8. Bates, F. S.; Fredrickson, G. H. *Phys. Today* **1999,** 52, (2), 32-38.
9. Kumar, M.; Grzelakowski, M.; Zilles, J.; Clark, M.; Meier, W. *Proc. Natl. Acad. Sci. U. S. A.* **2007,** 104, (52), 20719-20724.
10. Boukobza, E.; Sonnenfeld, A.; Haran, G. *J. Phys. Chem. B* **2001,** 105, (48), 12165-12170.
11. Stamou, D.; Duschl, C.; Delamarche, E.; Vogel, H. *Angew Chem Int Ed Engl* **2003,** 42, (45), 5580-3.
12. Delamarche, E. *Chimia* **2007,** 61, (4), 126-132.
13. Gellatly, K. S.; Moorhead, G. B. G.; Duff, S. M. G.; Lefebvre, D. D.; Plaxton, W. C. *Plant Physiol.* **1994,** 106, (1), 223-32.
14. Kruzel, M.; Morawiecka, B. *Acta Biochim. Pol.* **1982,** 29, (3-4), 321-30.
15. Rigler, P.; Meier, W. *J. Am. Chem. Soc.* **2006,** 128, (1), 367-373.
16. Broz, P.; Driamov, S.; Ziegler, J.; Ben-Haim, N.; Marsch, S.; Meier, W.; Hunziker, P. *Nano Lett.* **2006,** 6, (10), 2349-2353.
17. Nardin, C.; Widmer, J.; Winterhalter, M.; Meier, W. *Eur. Phys. J. E* **2001,** 4, (4), 403-410.
18. Koebnik, R.; Locher, K. P.; Van Gelder, P. *Mol. Microbiol.* **2000,** 37, (2), 239-253.
19. Michaelis, L.; Menten, M. L. *Biochem. Z.* **1913,** 49, 333-69.
20. J.M. Berg; J.L. Tymoczko; L. Stryer. *W.H. Freeman and Company* **2002**.
21. Sundaram, P. V. *J. Solid-Phase Biochem.* **1978,** 3, (3), 241-6.
22. Pedley, T. J. *Q. Rev. Biophys.* **1983,** 16, (2), 115-50.
23. van, D. S. F. M.; Nallani, M.; Cornelissen, J. J. L. M.; Nolte, R. J. M.; van, H. J. C. M. *Chemistry* **2009,** 15, (5), 1107-14.
24. Nardin, C.; Hirt, T.; Leukel, J.; Meier, W. *Langmuir* **2000,** 16, (3), 1035-1041.

2.4.3 pH Gating of Aquaporin-Z

pH gating of Aquaporin-Z reconstituted triblock copolymer membranes and in whole cells

Manish Kumar[*,§], Mariusz Grzelakowski[†,§] , Wolfgang Meier[†,‡] and Julie Zilles[*,‡]

* Department of Civil and Environmental Engineering, University of Illinois at Urbana Champaign, 205 N. Mathews Ave, Urbana, IL 61801, USA.

[†] Department of Chemistry, University of Basel, Klingelbergstrasse 80, Basel, CH 4056, Switzerland.

[‡]Corresponding Authors, JZ - Department of Civil and Environmental Engineering, University of Illinois at Urbana Champaign, 205 N. Mathews Ave, Urbana, IL 61801, USA, +1 217 244 2925, fax : +1 217 333 6968, email: jzilles@illinois.edu.

WM - Department of Chemistry, University of Basel, Klingelbergstrasse 80, Basel, CH 4056, Switzerland, ph: +41 (0)61 267 38 02, fax: +41 (0)61 267 38 55, email: wolfgang.meier@unibas.ch.

[§] These authors contributed equally to this paper.

Abstract

Water channel proteins, Aquaporins, are ubiquitous in living organisms. They mediate rapid water transport across cell membranes for specific functions including osmoregulation and turgor maintenance. Gating of aquaporins in cells is a common phenomena based on environmental conditions, including pH, to rapidly regulate water permeability. The bacterial aquaporin – Aquaporin Z (AqpZ) was reported not to be gated in a narrow pH range in previous studies, and the physiological relevance of this protein is unknown. The use of a synthetic biomimetic membrane forming polymer of low permeability allowed insightful examination of AqpZ permeability over a wide pH range. AqpZ incorporated in this polymer membrane was gated between pH values of 4 and 6 and gating was reversible. Whole experiments with *E. Coli* AqpZ mutants confirmed this observation. Furthermore, AqpZ mutants exhibit reduced survival under acid stress. pH gating of AqpZ may be important for cell survival at low pH values in concert with the decrease in activity observed in mechanosensitive channels.

Text

Aquaporins are a family of transmembrane proteins responsible for rapid water transport across cell membranes[1]. Certain aquaporins also transport small solutes across membranes[2]. They are present in organisms from all domains of life and contribute to several important functions.[3] They are critical to rapid response to change in osmotic pressure for large cells such as red blood cells and plant cells.[4] The large surface area to volume ratios of small microorganisms have made investigators question the physiological relevance of Aquaporins in microorganisms[5, 6]. They have however been linked to osmoregulation and increase in cell volume during growth[7].

Lipid bilayers are usually reconstituted with membrane proteins such as aquaporins to study their biophysical properties[8]. However, several properties of these lipid membranes, including high permeability for water and gases, make the study of isolated membrane proteins difficult[6]. The use of synthetic membranes with tailorable properties could provide an alternative to lipid membranes for evaluation of several unique properties of these proteins. Block copolymers are a class of polymers that can mimic lipid bilayers in many significant ways and can be modified to provide unique properties and functions by choice of appropriate blocks as well as modifications[9]. We have shown successful insertion of several membrane proteins in these polymer membranes and found proteins to be functional[10, 11]. Additionally, these polymer membranes are highly stable and can serve as a platform for long lasting devices enabling studies on incorporated membrane proteins.

Aquaporin mediated water transport can be regulated in the cell in several ways. These include mechanisms for control of aquaporin production and degradation, its delivery and insertion into the membrane and modulation of the activity of the inserted aquaporin by gating. [12, 13] Gating of aquaporins occurs by phosphorylation, pH, divalent cations, effect of other proteins and osmolarity.[14] Oxidative stress and mechanical stress have also been shown to induce gating[13, 15]. It also provides a rapid way for modulating cell response and has been shown to be responsible for helping plants survive drought and flooding.[16] The role of gating in mammalian aquaporins such as AQP1 and AQP0 in still unclear. Aquaporin Z was reported not to be gated in a pH range of 5-7 in literature[17]. In this study, we show that AqpZ is gated between pH values of 4 and 6.

Mechanosensitive channels, like aquaporins, have also been shown to be important for osmoregulation and cell survival under changing osmotic environments. In particular, MsCL and MsCM have been shown to open and rapidly release small solutes to prevent cell plasmolysis when a sudden decrease is osmotic pressure occurs[18]. This is important for survival of bacteria such as *E. Coli*, which experience changes in osmotic pressure when passing through the digestive system. Additionally, it has been shown that MsCL opening rate might be modulated by a decrease in pH[19]. It is possible that mechanosensitive channels remain closed even under extreme turgor at low pH values to prevent acidosis of the cytoplasm in such environments. The effect of Aquaporins and Mechanosensitive channels of cell water homeostasis seems to be coordinated under neutral pH conditions[20]. Such coordination may also exist between the gating of these channels at low pH values.

In order to study gating of AqpZ channels, they were incorporated into PDMS-PMOXA based triblock copolymers at a constant protein to polymer molar ratio of 1:100. Experiments were conducted on these vesicles in the pH range of 2 to 12 using stopped flow light scattering experiments. The general experimental procedure is described in a previous work [11] and exact experimental approach in Supplementary Online Materials (SOM). **Figure 1** shows the variation in permeability of vesicles reconstituted with AqpZ channels over above indicated pH range. The activation energy of water transport at pH values of 4, 7.2 and 12 are in the range of 1.8 to 4 kcal/mole indicating that transport is channel mediated.

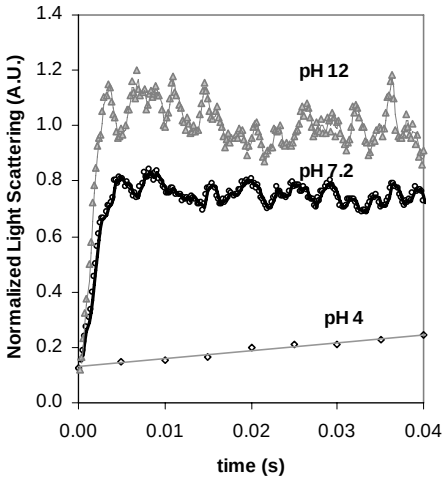

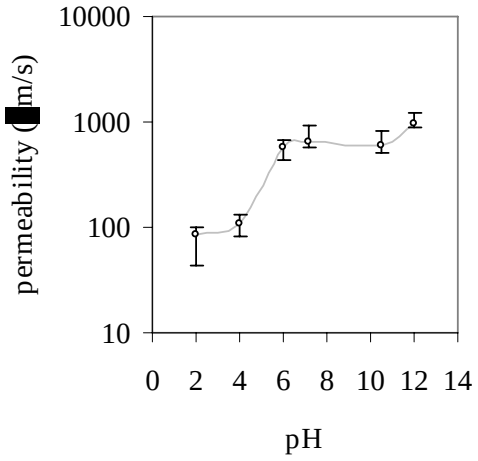

Figure 1: ***Polymeric vesicles reconstituted with AqpZ show different permeabilities at different pH values*****. a) The above figure shows normalized light scattering response on subjecting vesicles prepared in a buffer solution of pH 4, 7.2 and 12 respectively to an outwardly directed osmotic gradient in a stopped flow apparatus. The initial exponential rise in the light scattering signal can be correlated to membrane permeability as described in the materials and methods section. b) A sharp increase in permeability is seen between pH 4 and 6 indicating gating behavior of the AqpZ. Permeability was calculated using stopped flow light scattering experiments where AqpZ reconstituted in polymer vesicles were subjected to an outwardly directed osmotic gradient. Change in the size of vesicles was monitored with change in intensity of scattered light and this was related to permeability.**

Reversibility of AqpZ channel gating in polymer vesicles reconstituted with AqpZ was investigated by recovering vesicles subjected to stopped flow experiments at a pH of 7.2 or 4.0. Buffer was then replaced with the one of a different pH. The possibility of reusing of vesicles subjected to osmotic shock was enabled by the stable nature of ABA block copolymer membranes. The permeability of recovered vesicles was then remeasured to determine reversibility of the gating phenomenon, when going from a low pH to high pH and from a low pH to high pH. It was found that changing the pH from 7.2 to pH 4 reduces permeability of protein reconstituted vesicles to levels expected for pH 4 and when pH is changed from pH 4 to pH 7.2 there is a large increase in permeability indicating "re-opening" of the AqpZ channels.

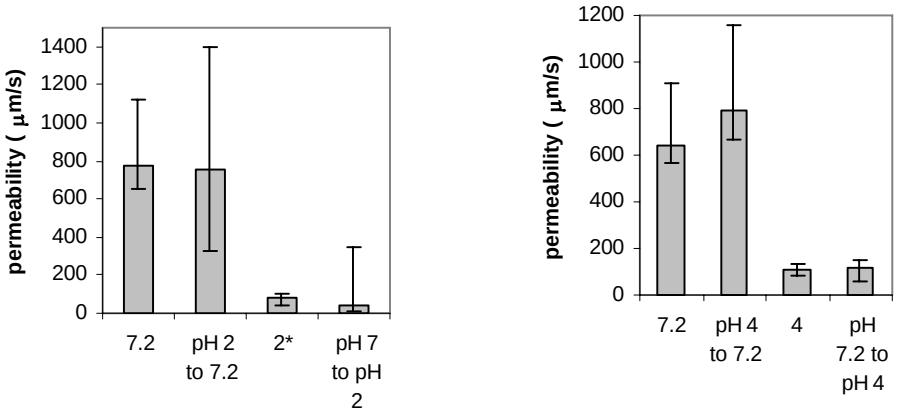

Figure 2: ***The pH gating effect in AqpZ-ABA vesicles is reversible*****. Vesicles were first subjected to an outwardly directed osmotic gradient at pH 7.2. These vesicles were then spun down in a centrifugal filter and washed repeatedly with pH 2 or pH 4 buffer to change the ambient pH to pH 2 or pH 4. It was seen that the permeability is reduced to that observed under pH 2 or pH 4 conditions by conducting stopped flow experiments. Similarly the proteovesicles solutions from experiments at pH 2 or 4 was recovered in pH 7.2 buffer. Stopped flow experiments revealed that the original permeability at pH 7.4 could be recovered from both pH 2 and pH 4 indicating reversibilityx**

A series of experiments were conducted with *E.Coli* cells to investigate the occurrence and physiological relevance of the AqpZ gating phenomena observed in polymer vesicles. Three strains of bacteria. including a parent strain (ME 9062), a AqpZ knockout strain ($AqpZ^-$) from ME9062, and an overexpression strain ($AqpZ^+$) based on the strain JM109[17], were tested. These strains were grown to the log phase and subjected to permeability measurements using stopped flow light scattering[21] under different pH conditions. The $AqpZ^+$ strain was tested under both induced and uninduced conditions. The low pH value chosen for these tests was 4 as the outer membrane proteins, particularly OmpF, have been shown to be closed at a pH below 3.85 (reference). We found that for the ME9062 and $AqpZ^+$ strains the permeability measured is lower at pH 4 when compared to pH 7. As expected, the permeability measured for the AqpZ+ strains are higher than for the ME9062 strain. For both, the uninduced $AqpZ^+$ strain as well as the ME9062 strain there is a decrease of 15-16% in permeability when pH is reduced from 7.4 to 4. For $AqpZ^+$ induced strain this difference is higher at 50%.

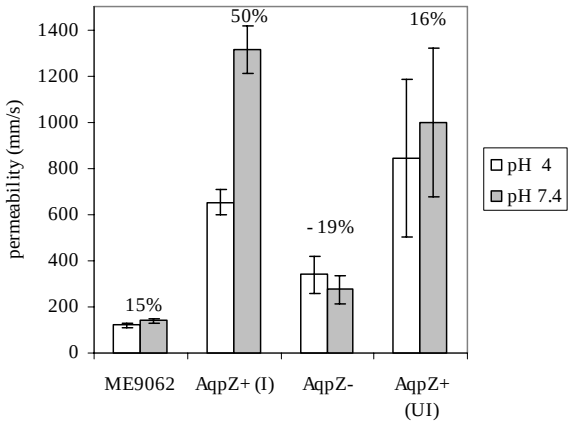

Figure 3: ***pH gating is observed in both wild type and mutant strains overexpressing AqpZ.*** **Strains were grown in LB and diluted 1:100 after 15 hours of growth. These cells were harvested after 8 hours of growth and resuspended in 100mM PBS solution (with kanamycin) at pH 4 or 7.4. ME9062 is the parent strain and shows a significant decline in permeability at pH 4. $AqpZ^+$(I) is an over expression strain which was induced for 4 hours before harvesting. AqpZ (UI) is the same overexpression strain with no induction. Both these strains show a higher permeability that the parent strain and the reduced permeability at pH 4 is significant. $AqpZ^-$ represents the AqpZ knockout strain from the parent strain (ME 9062). It shows negligible difference between**

pH 4 and pH7. OmpF$^-$ is the AqpZ knockout strain from the same parent strain (ME 9062) and shows negligible difference between pH 4 and pH 7.

The permeability difference between pH 7.4 and 4 for the AqpZ- strain is not significant. However, this difference increases when the level of expression of AqpZ increases (from ME9062 strain to uninduced AqpZ$^+$ strain to induced AqpZ+ strain) indicating that the difference in permeability for the other strains is due to the presence of AqpZ gating phenomena between these pH values. The actual permeability of the AqpZ knockout strain (AqpZ-) is significantly higher than the ME 9062 strain. This may indicate that the expression of another water channel with higher permeability than the AqpZ channel might be upregulated by this change.

The reversibility of permeability change between pH values of 7.4 and 4 (and between pH 4 and 7.4) was tested by re-suspending one portion of a culture of AqpZ$^+$ (induced) strain in pH 7.4 (or 4) buffer[21], removal of the buffer and resuspending it in pH 4 (or pH 7.4) buffer. Thus the same batch was tested at both the pH values to make sure the permeability change occurs in both directions. Figure 4 shows that when pH is decreased from pH 7.4 to pH 4 the resulting cells permeability is 101% of that at pH 4 while when pH is increased from pH 4 to pH 7.4 the resulting permeability is 73% of that at pH 7.4 indicating most of the decrease in permeability at low pH is reversible.

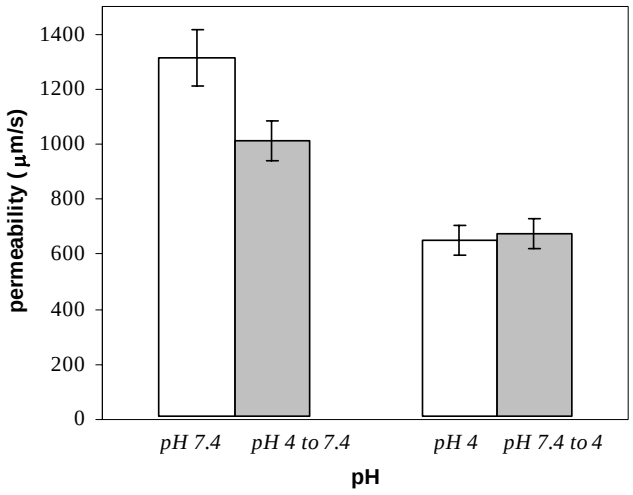

Figure 4: *The pH gating effect in E. Coli strains overexpressing AqpZ is reversible.* Harvested (pelleted) cells were resuspended in pH 4 buffer and the permeability measured on a part of the resuspended cells. The remainder of the cells were pelleted again, washed with and resuspended in pH 7.4 buffer. The permeability of

of pH 4 vesicles was seen to be the same as the pH 4 E. Coli cells. However when washed and resuspended in pH 7. 4 buffer the permeability increased back to levels similar to those observed in E.Coli cells originally resuspended in pH 7.4 cells indicating pH based reversibility of the water transport activity of AqpZ.

The activation energy of water transport measured by conducting the above measurements in the temperature range of 5 to 25 deg C was 1.2 kcal/mol for ph 7.4 and 2.1 kcal/mol for pH 4 indicating transport at both pH values are channel mediated similar to that found for AqpZ incorporated in polymer vesicles.

The occurrence of pH mediated AqpZ gating in both polymer vesicles and whole cells indicate that pH has a direct effect on the conformation of AqpZ monomer leading to a decrease in its permeability. Molecular dynamics simulations have indicated the presence of two conformational states in Aquaporin monomers – an open and a closed state.[22] This may indicate that pH induced conformation changes within the water selective part of the channel could lead to a higher probability of the closed states leading to the reduction in permeability observed in our experiments.

Osmoregulation has been indicated as a possible function of water channels in microorganisms. Other channels such as the mechanosensitive channels (particularly MsCL and MsCS) are important for survival of bacteria acting as a pressure valve releasing solutes when there is a sudden downshift in medium osmolarity. In the absence of MsCL and MsCS there is a large mortality in bacterial cells with a small negative change in osmolarity. Down-regulation of AqpZ has also been indicated as a survival mechanism in bacteria as it slows down the rate of water entering the cells. Osmotic response is coordinated between the AqpZ and MsCL with AqpZ helping to maintain turgor. At the same time MsCl helps in preventing a fatal rapid increase in cell volume. pH regulation of MsCL has also been reported and indicates that a lower pH might lead to a lower rate of activation of MsCL to prevent H^+ entry into the cells. Thus the protective action of the MsCL might be reduced at a lower pH indicating that the cell will be more vulnerable to a downshift in osmotic pressure. Thus, in addition to downregulation of AqpZ synthesis - a slow process, the rapid reduction in permeability by gating of AqpZ might be an important protective step.

In order to study the effect of high water permeability on the viability of E.Coli under lowered pH conditions the uninduced $AqpZ^{+}$(UI) , $AqpZ^{-}$ and ME9062 strains were subjected to acid shock (pH 2.5) as well a small osmotic downshift (200 mM). It was found that both the ME9062 and $AqpZ^{-}$ strains had similar survival rates while the $AqpZ^{+}$ (UI) strain had a significantly lower survivability rate (Figure 5) when subjected to simultaneous osmotic downshift and pH shock. The $AqpZ^{+}$ (UI) strain modulates permeability with pH but it still has higher residual permeability than the wild type and knockout strains at lower pH values. The low survivability of this strain under combined osmotic and acid shock conditions indicates that a decrease in permeability of the expressed AqpZ in wild type strains may be an advantageous biophysical response to the coupled pH and osmotic variations. *E. Coli* is exposed to such conditions while passing through the digestive tracts of animals.

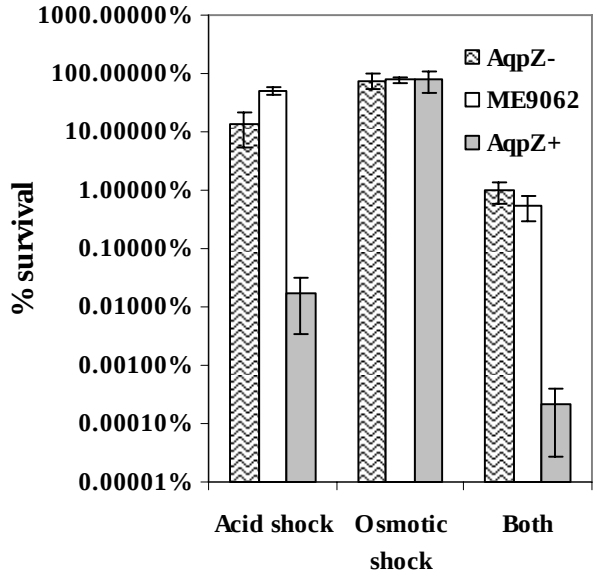

Figure 5: ***Lower permeability of knock out and parent strains have higher survival rate than overexpression strain under simultaneous hypoosmotic and acid shock conditions.***

The short term survival of bacterial cells under changing pH and osmotic conditions is made possible by cooperative activity between water channel proteins and mechanosensitive channels.

REFERENCES:

1. **Preston, G.M., et al.,** ***Appearance of Water Channels in Xenopus Oocytes Expressing Red-Cell Chip28 Protein.*** **Science, 1992. 256(5055): p. 385-387.**
2. **King, L., D. Kozono, and P. Agre,** ***From structure to disease: the evolving tale of aquaporin biology.*** **Nature Reviews Molecular Cell Biology, 2004. 5: p. 687-698.**
3. **Ringler, P., et al.,** ***Structure of the water channel AqpZ from Escherichia coli revealed by electron crystallography.*** **J. Mol. Biol., 1999. 291(5): p. 1181-1190.**
4. **King, L.S., D. Kozono, and P. Agre,** ***From structure to disease: the evolving tale of aquaporin biology.*** **Nat Rev Mol Cell Biol, 2004. 5(9): p. 687-98.**
5. **Tanghe, A., P. Van Dijck, and J. Thevelein,** ***Why do microorganisms have aquaporins?*** **Trends in Microbiology, 2006. 14(2): p. 78-85.**
6. **Hill, A., B. Shachar-Hill, and Y. Shachar-Hill,** ***What Are Aquaporins For?*** **Journal of Membrane Biology, 2004. 197(1): p. 1-32.**
7. **Calamita, G.,** ***The Escherichia coli aquaporin-Z water channel.*** **Molecular Microbiology, 2000. 37(2): p. 254-262.**
8. **Borgnia, M.J., et al.,** ***Functional reconstitution and characterization of AqpZ, the E. coli water channel protein.*** **J Mol Biol, 1999. 291(5): p. 1169-79.**
9. **Dongen, S.F.M., et al.,** ***A three-enzyme cascade reaction through positional assembly of enzymes in a polymersome nanoreactor.*** **Chemistry, 2009. 15(5): p. 1107-14.**
10. **Graff, A., et al.,** ***Virus-assisted loading of polymer nanocontainer.*** **Proceedings of the National Academy of Sciences of the United States of America, 2002. 99(8): p. 5064-5068; Broz, P., et al.,** ***Toward Intelligent Nanosize Bioreactors: A pH-Switchable, Channel-Equipped, Functional Polymer Nanocontainer.*** **Nano Lett, 2006. 6(10): p. 2349-2353; Onaca, O., et al.,** ***Functionalized Nanocompartments (Synthosomes) with a Reduction-Triggered Release System*.*** **Angew Chem Int Ed Engl, 2008.**
11. **Kumar, M., et al.,** ***Highly permeable polymeric membranes based on the incorporation of the functional water channel protein Aquaporin Z.*** **Proc Natl Acad Sci U S A, 2007. 104(52): p. 20719-24.**
12. **Alleva, K., et al.,** ***Plasma membrane of Beta vulgaris storage root shows high water channel activity regulated by cytoplasmic pH and a dual range of calcium concentrations.*** **Journal of Experimental Botany, 2006. 57(3): p. 609-621.**
13. **Kim, Y.X. and E. Steudle,** ***Gating of aqu`aporins by light and reactive oxygen species in leaf parenchyma cells of the midrib of Zea mays.*** **J. Exp. Bot., 2009. 60(2): p. 547-556.**
14. **Hedfalk, K., et al.,** ***Aquaporin gating.*** **Curr Opin Struct Biol, 2006. 16(4): p. 447-56.**
15. **Ye, Q. and E. Steudle,** ***Oxidative gating of water channels (aquaporins) in corn roots.*** **Plant, Cell Environ., 2006. 29(4): p. 459-470.**
16. **Tournaire-Roux, C., et al.,** ***Cytosolic pH regulates root water transport during anoxic stress through gating of aquaporins.*** **Nature (London, U. K.), 2003. 425(6956): p. 393-397.**
17. **Borgnia, M.J., et al.,** ***Functional reconstitution and characterization of AqpZ, the E. coli water channel protein.*** **J Mol Biol, 1999. 291(5): p. 1169-79.**
18. **Levina, N., et al.,** ***Protection of Escherichia coli cells against extreme turgor by activation of MscS and MscL mechanosensitive channels: identification of genes required for MscS activity.*** **The EMBO Journal, 1999. 18: p. 1730-1737.**
19. **Kloda, A., A. Ghazi, and B. Martinac,** ***C-Terminal Charged Cluster of MscL, RKKEE, Functions as a pH Sensor.*** **Biophysical Journal, 2006. 90(6): p. 1992-1998.**

20. Booth, I. and P. Louis, *Managing hypoosmotic stress: Aquaporins and medianosensitive channels in Escherichia coli.* Current Opinion in Microbiology, 1999. 2(2): p. 166-169.
21. Mallo, R. and M. Ashby, *AqpZ-Mediated Water Permeability in Escherichia coli Measured by Stopped-Flow Spectroscopy.* Journal of Bacteriology, 2006. 188(2): p. 820-822.
22. Khandelia, H., M.O. Jensen, and O.G. Mouritsen, *To Gate or Not To Gate: Using Molecular Dynamics Simulations To Morph Gated Plant Aquaporins into Constitutively Open Conformations.* J. Phys. Chem. B, 2009. 113(15): p. 5239-5244.

2.4.4 Amphiphilic Copolymer Membranes Promote NADH:Ubiquinone Oxidoreductase Activity: An Electron-Transfer Nanodevice

Classification: Physical sciences

Title:

Amphiphilic copolymer membranes promote NADH:Ubiquinone Oxidoreductase activity: An Electron-Transfer Nanodevice

Caroline Fraysse-Ailhas [a], Alexandra Graff [a], Cornelia G. Palivan [a*], Mariusz Grzelakowski [a], Thorsten Friedrich [b], Corinne Vebert [a], Georg Gescheidt [c], and Wolfgang Meier [a*]

Author affiliation:

[a] Department of Chemistry, University of Basel, Klingelbergstrasse 80, 4056 Basel, Switzerland; [b] Institut für Organische Chemie and Biochemie, Albert-Ludwigs-Universität Freiburg, Albertstrasse 21, D-79104 Freiburg, Germany; [c]Institute of Physical and Theoretical Chemistry, Graz University of Technology, Technikerstr. 4/I, A-8010 Graz, Austria

The authors declare no conflict of interest.

***Corresponding Authors:** Wolfgang Meier (Wolfgang.Meier@unibas.ch), Cornelia G. Palivan (Cornelia.Palivan@unibas.ch)

Keywords:

NADH:ubiquinone oxidoreductase

polymer vesicle

electron transfer

amphiphilic triblock copolymer

nanodevice

ABSTRACT:

Nanoscale devices involved in energy conversion require the transfer of electrons from one compartment to another in order to properly function. The enzyme NADH:ubiquinone oxidoreductase (complex I), which *in vivo* mediates the transfer of electrons from NADH to ubiquinone, is an intriguing candidate for such an electron-transfer role in nanodevices. However, complex I normally requires the presence of lipids to remain active, potentially limiting its application. Here we demonstrate for the first time that complex I can be actively reconstituted in the synthetic membrane of amphiphilic triblock copolymer vesicles, to form hybrid systems at the nanoscale that allow site-specific reactions driven by location and redox-potential differences. These electron-transfer nanodevices are suitable for a variety of applications such as signaling devices or nanoreactors for follow-up redox reactions inside the synthetic membrane.

INTRODUCTION:

Nanotechnology offers the possibility to design and manufacture specialized nanodevices with a range of applications in the fields of biomedicine, pharmacy, or energy conversion. A particularly difficult scientific challenge is to design devices able to store or transfer energy, and operating at the nanometer length scale.

There are in nature various molecular systems that promote energy conversion and serve as inspiration for nanotechology. One approach is to mimic natural electron transfer processes such as photosynthesis or nitrogen fixation (1). Another strategy consists of extracting biological molecules from living systems (bacteria or eucaryotic cells) and combining them to work in hybrid environments, as for example the reconstitution of membrane proteins in artificial liposomes (2, 3). For example, ATP-synthase was incorporated in liposomes together with bacteriorodopsin, a light-driven proton pump, to construct a device that allows sunlight to be converted into chemical energy and stored in ATP (4). However, the use of liposomes for technological applications has various drawbacks, such as significant leakage due to structural defects and mechanical instability (5),[Barenholtz2001] which have not been eliminated by using combinations of lipids and synthetic polymers (5, 6).

Advanced materials based on polymers have been introduced to design new hybrid systems in combination with proteins. In this respect, amphiphilic copolymers are of particular interest because they self-assemble in aqueous solution into structures, such as micelles, tubes and vesicles, similar to those observed in nature (7, 8). The structure and the membrane characteristics of amphiphilic copolymer vesicles are analogous to those of liposomes. Recently, it was reported that synthetic membranes serve as mimics for biological membranes, and were successfully used to incorporate membrane proteins (9-11). In particular, vesicles resulting from the auto-assembling of poly(2-methyloxazoline)-block-(polydimethylsiloxane)-block-(poly(2-methyloxazoline) copolymer (PMOXA-PDMS-PMOXA), have been shown to enable functional reconstitution of channel-forming proteins, such as OmpF, LamB, or Aquaporin Z (10, 12-14).

In addition, amphiphilic copolymer vesicles have been used to design and build nanoreactors, which protect enzymes encapsulated in their inner cavity and enable them to act *in situ* (15), or enable the tandem action of soluble and membrane-bound proteins (13, 16). Compared to natural lipids, polymers have the benefit of long-term stability arising from a combination of high mechanical stability and chemical inertness, making them more reliable for technological applications (17). Further, the use of synthetic copolymers opens the possibility to modulate and control the

chemical composition and properties of the synthetic membrane by changing the chemical nature of polymer blocks, varying their block lengths, or adjusting the ratio between hydrophobic and hydrophilic domains (7, 18, 19).

Here we have designed and tested a new hybrid system which allows electron transfer from the environment into the membrane of polymer vesicles. We chose the bacterial respiratory enzyme complex NADH:ubiquinone oxidoreductase (complex I) as electron transfer effector. Complex I couples the transfer of electrons from NADH to ubiquinone performed by a series of redox centers with a translocation of protons across the membrane. It thus contributes to the proton motive force, essential for energy consuming processes (3, 20-24). The activity of complex I is very sensitive to environmental changes and strongly dependent on the presence of phospholipids (25-27) This could compromise its reconstitution in a synthetic membrane.

Various studies have shown that the phospholipid environment plays a crucial role in maintaining membrane protein activity (28-31). For example, cardiolipin tightly bound to Ubiquinol:Cytochrome *c* Oxidoreductase (complex III) confers stability or is needed for proper assembly of the enzyme complex (32). Therefore, we attempted to determine the behavior of complex I in polymer media and devoid of most endogeneous lipids prior to its incorporation in the polymer membrane. We synthesized a library of various PMOXA-PDMS-PMOXA copolymers, modifying the length of the hydrophilic and hydrophobic blocks or the ratio between them in order to provide membranes with different thicknesses. With this library we established whether the synthetic media affect the protein functionality, and in which respect.

Electron microscopy revealed the L-shape structure of complex I with a peripheral arm containing the nucleotide binding site and a membrane arm containing the quinone-binding site (23). To enable electron transfer from outside the vesicle to the vesicle membrane or interior, complex I must be properly oriented in the membrane to expose the peripheral arm to the external solution. This is a more complex task than the incorporation of a rather symmetric channel protein in polymer membranes (12), and we needed to adjust the reconstitution processes used with membrane proteins in pre-formed liposomes to account for the different properties of polymers (33). Fortunately, the self-assembly process of vesicle formation offers a facile way to incorporate complex I together with various electron acceptors located in different regions of the vesicles, in order to test the function of complex I once incorporated into the polymer membrane.

RESULTS:

Complex I activity restored by copolymers. Complex I was isolated from *Escherichia coli* in the presence of the detergent dodecyl-maltoside, following an established protocol(34). During the preparation most of its endogeneous lipids were lost and 20 mol of phospholipids, predominantly phosphatidylethanolamine, per mol complex I were retained. Complex I, as isolated, showed a low NADH:decyl-ubiquinone oxidoreductase activity of 0.2 µmol NADH / min mg.

The preparation was titrated with increasing amounts of a mixture of phosphatidylethanolamine (75%), phosphatidylglycerol (20%), and Cardiolipin (5%), mimicking the composition of the *E. coli* plasma membrane (**Figure 1**). The addition of phospholipids did not significantly change the activity of complex I up to a lipid to enzyme ratio of 0.05 (w/w). Beyond this point the enzymatic activity of complex I increased dramatically. At a ratio of 0.25 (w/w), the activity was enhanced nearly six times. Further increase of the lipid content did not lead to a higher activation of the enzyme, as indicated by the plateau region in **Figure 1** (dark circles). The ratio between complex I activity at the plateau region and that at 0.005 (w/w) ratio, *activation ratio*, will be used as a parameter to compare various environments for complex I: either polymers to each other or polymers to lipids.

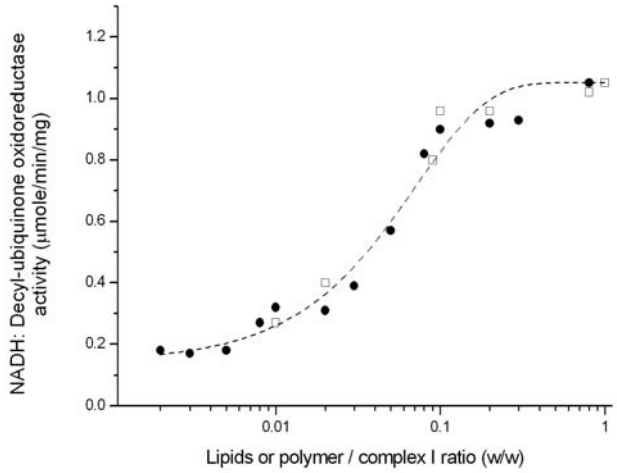

Figure 1. Dependence of the NADH:decyl-ubiquinone oxidoreductase activity of complex I (E. coli) on the ratio of phospholipids/complex I (dark circles) or polymer/complex I (open squares). The block copolymer is $PMOXA_{13}$-$PDMS_{110}$-$PMOXA_{13}$.

A similar titration curve was obtained with $PMOXA_{13}$-$PDMS_{110}$-$PMOXA_{13}$, indicating that the self-assembling block copolymer substitutes for the natural lipids and activates complex I to a similar extent as phospholipids (**Figure 1** – open

squares). It has been shown that polymer self-assembly is usually defined by slower dynamics of the constituent blocks compared to the lipids (35). We therefore optimized the incubation time and the temperature in order to take into account the different chemical composition and kinetics of polymers (Supplementary information, **Figure S1**). The optimum conditions for complex I NADH:decyl-ubiquinone oxidoreductase activity were obtained by an incubation time of 30 minutes at 0°C, compared to an incubation time of 20 minutes at 0°C used in the case of phospholipids.

Complex I activity depends on copolymer composition. In order to investigate the influence of the copolymer molecular properties on the physiological activity of complex I, we synthesized a small library of $PMOXA_x$-$PDMS_y$-$PMOXA_x$ copolymers with hydrophilic block PMOXA (**A**) ranging from 9 to 65 monomer units, and hydrophobic block PDMS (**B**) ranging from 23 to 165 monomer units (**Table 1**). The polydispersity of block copolymers imposed a slight variation of complex I activation ratio due to the simultaneous presence of polymer chains with slightly different block lengths. Thus, in every individual experiment the activation ratio of complex I we obtained must be considered as an average value.

Table 1. Library of $PMOXA_xPDMS_yPMOXA_x$ copolymers used for the assay of NADH: decyl-ubiquinone oxidoreductase activity of complex I. A represents the PMOXA block, and B the PDMS block; x and y are the average number of monomeric units of each block, N_A and N_B, respectively.

Polymer composition[a]	M_W [a]	Polydispersity
$A_9B_{106}A_9$ - **1**	9486	1.38
$A_{13}B_{62}A_{13}$ - **2**	6938	1.47
$A_{15}B_{62}A_{15}$ - **3**	7276	1.50
$A_{21}B_{69}A_{21}$ - **4**	8816	2.00
$A_{13}B_{23}A_{13}$ - **5**	4052	Insoluble in TFH
$A_{65}B_{165}A_{65}$ - **6**	23372	1.63
$A_{13}B_{110}A_{13}$ - **7**	10462	1.44
$A_{14}B_{110}A_{14}$ - **8**	10632	1.36

a. Polymer composition and M_w obtained with ^1H NMR spectroscopy. b. Polydispersity obtained by GPC (THF linear PS calibration).

The activation ratio of complex I strongly depends on the copolymer type (**Figure 2**). The data for each copolymer represent the average results obtained from 6 independent experiments. Some copolymers, such as $A_9B_{106}A_9$, $A_{13}B_{110}A_{13}$, and $A_{14}B_{110}A_{14}$ (**1**, **7**, and **8**) induced a roughly similar or greater activation of complex I than the phospholipids (**9**), while others induced a significantly smaller activation of the enzyme (as for example $A_{21}B_{69}A_{21}$, **4**).

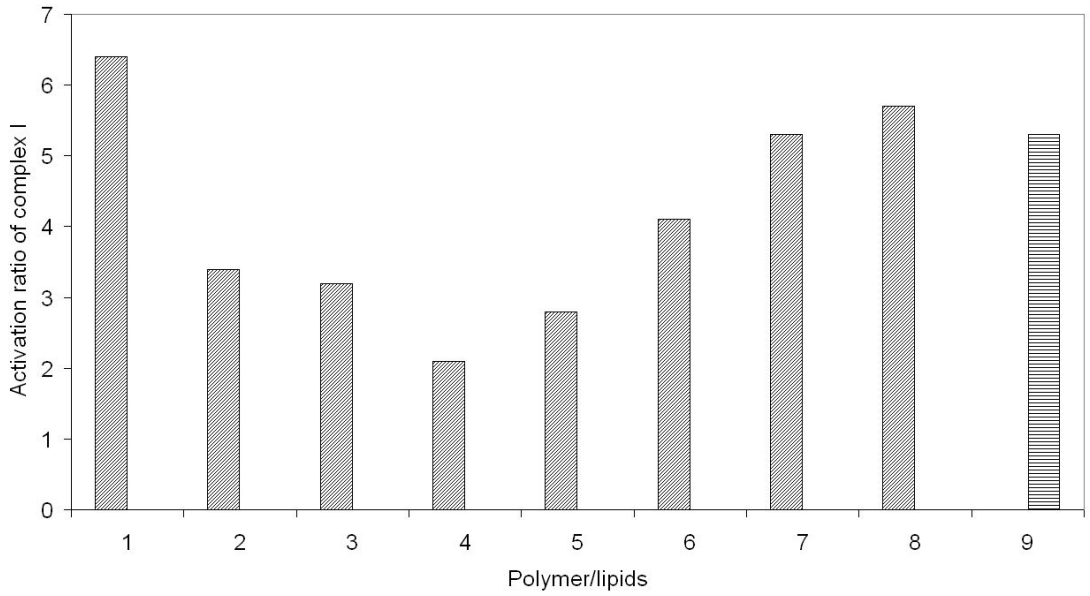

Figure 2. Activation ratio of complex I NADH: decyl-ubiquinone oxidoreductase activity for various copolymers $PMOXA_x$-$PDMS_y$-$PMOXA_x$ (1 – 8, see Table 1), and phospholipids. The ratio of additive/complex I is of 0.1 (w/w).

The distinct effects of the different copolymer types on the activation ratio of NADH:decyl-ubiquinone oxidoreductase activity supports the hypothesis that the molecular composition of the polymer (hydrophobic and hydrophilic block lengths) directly influences the active conformation of the complex. In order to decouple the possibly different effects of the hydrophilic and hydrophobic domains, we used two sets of copolymers: one set had an almost constant **A** block (13 to 15 monomer units) and a variable **B** block (23 to 110 monomer units), and the other set an almost constant **B** block (106 to 110 monomer units), and a variable **A** block (9 to 15 monomer units). The effect on the activation ratio of NADH:decyl-ubiquinone oxidoreductase activity of complex I as a function of these two sets of copolymers indicates a different influence of the hydrophobic and hydrophilic blocks, respectively (**Figure 3 a, b**).

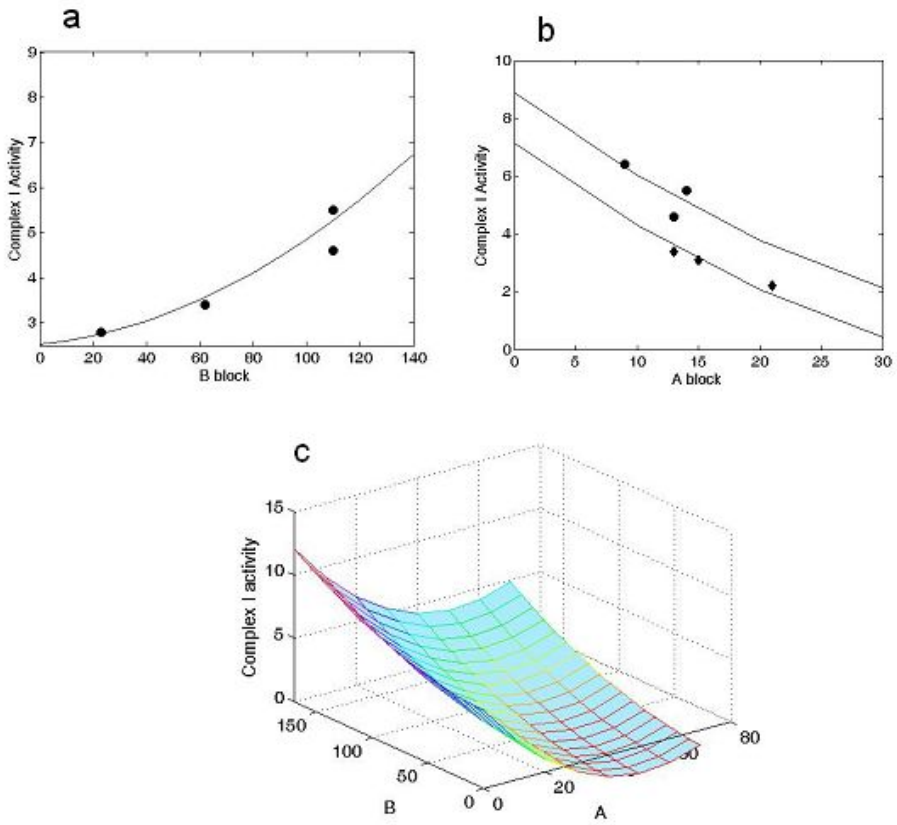

Figure 3. Activation ratio of complex I NADH:decyl-ubiquinone oxidoreductase activity as function of: a) number of monomer units in the hydrophobic B block, N_B (A block almost constant); b) number of monomer units in the hydrophilic A block, N_A (B block almost constant). c) Model for the activation ratio of complex I NADH:decyl-ubiquinone oxidoreductase activity as function of the number of monomers in both hydrophobic and hydrophilic blocks. The curves in a) and b) represent slices through the activation ratio surface with N_A constant, and N_B constant, respectively. Activation ratio of complex I NADH: decyl-ubiquinone oxidoreductase activity was calculated for a polymer/complex I ratio of 0.1 (w/w) and of 0.005 (w/w).

Within the limits of our experiments, increasing the length of the hydrophobic block while keeping the length of the hydrophilic block virtually constant leads to a stronger activation of complex I (**Figure 3 a**). On the other hand, we observed an inverse effect of the length of the hydrophilic block A on the activity of complex I, while keeping an almost constant length of the hydrophobic block (**Figure 3 b**). This effect is not as significant as the one of the hydrophobic domain, but it modulates the latter.

We modeled the combined effect of the hydrophobic and hydrophilic domains using a least squares approach based on a double parameter polynomial regression. The surface which describes the activation ratio of complex I NADH:decyl-ubiquinone

oxidoreductase activity as a function of the **A** and **B** block lengths indicates a domain of polymer properties that activates complex I and another domain (the minimum of this surface) which inactivates it (**Figure 3 c**). A slice through this surface, with either N_A or N_B constant (**Figure 3 a** and **3 b**), shows in more detail how each polymer affects complex I activity. It can be seen that the maximum activation of complex I is obtained when the copolymers have the biggest hydrophobic (**B**) block, while keeping the hydrophilic (**A**) block sufficiently small. We emphasize that this effect should be considered in the range of hydrophobic blocks we used, and under the conditions leading to complex I activation by reconstitution in copolymers. An upper limit for the dimension of the hydrophobic domain surely exists, above which the membrane imposes such a high distortion on the complex I that it may denature.

In order to exclude the possibility that the activity measured in the presence of polymers was not the physiological activity of complex I, we determined the inhibition of the NADH:decyl-ubiquinone oxidoreductase activity by piericidin A, a specific inhibitor of the ubiquinone binding-site (36). The amount of inhibitor needed to block 50% of the enzymatic activity, IC_{50} was determined for complex I reconstituted in phospholipids and polymer **7**, respectively. An IC_{50} value of 3 µM was obtained for complex I reconstituted either in phospholipids or in polymer 7. More than 90 % of the activity was inhibited in the presence of 10 µM piericidin A.

Construction of an electron-transfer nanodevice using complex I. The robustness of the electron transfer chain of complex I is a critical prerequisite for the design of an electron-transfer nanodevice when the enzyme is reconstituted in the membrane of vesicles formed by self-assembly of the PMOXA-PDMS-PMOXA copolymer.

The typical "L-shape" structure of the protein and its orientation – with the nucleotide binding site in contact with the aqueous phase and the other arm embedded in the hydrophobic membrane (37) – must be maintained in order to enable the transfer of electrons in a specific direction. This introduced an added complexity to vesicle formation during the preparation of our nanodevice. Usually, due to the statistical character of insertion during the self-assembly process of vesicle formation, proteins are inserted in both orientations relative to the membrane (14) In order to obtain the desired orientation of complex I within the polymer membrane we modified the method of membrane protein reconstitution in liposomes, introduced by Rigaud et al (33, 38), which has already been used to reconstitute complex I in liposomes (3).

We specially adopted and modified the concept of reconstitution of membrane proteins in pre-formed liposomes, known to induce a high percent of asymmetric orientation upon insertion, to the use of amphiphilic copolymers. In our modification, a mixture of complex I and surfactant was added to preformed surfactant-doped amphiphilic block copolymer vesicles. This generated a hybrid system of protein-polymer vesicles; named proteovesicles (see Supplementary information). After surfactant removal the solution of proteovesicles was analyzed by TEM in order to determine whether the vesicles were affected by complex I incorporation (**Figure 4**). The TEM image indicates that the surfactant procedure used to incorporate complex I in polymer membrane did not affect the morphology of the vesicles (for comparison, a TEM image of empty vesicles is included in the Supplementary Information, Figure S2).

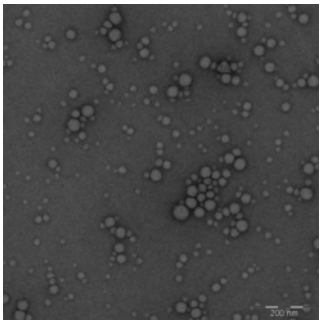

Figure 4. Transmission Electron Micrograph of complex I incorporated in $PMOXA_{13}PDMS_{110}PMOXA_{13}$ vesicles (room temperature; scale bar = 200 nm).

The presence of all complex I subunits in the preparation of the vesicles was confirmed by gel electrophoresis (**Supplementary Information S**), and the presence of the Fe/S cofactors by EPR spectroscopy (**Figure 5a**). SDS-PAGE revealed that complex I had been inserted in the polymer vesicle membrane. All subunits of complex I were present in both lanes, indicating that the protein was not cleaved during its insertion in the membrane of polymer vesicles (**Supplementary Information Figure S3** : lane II)

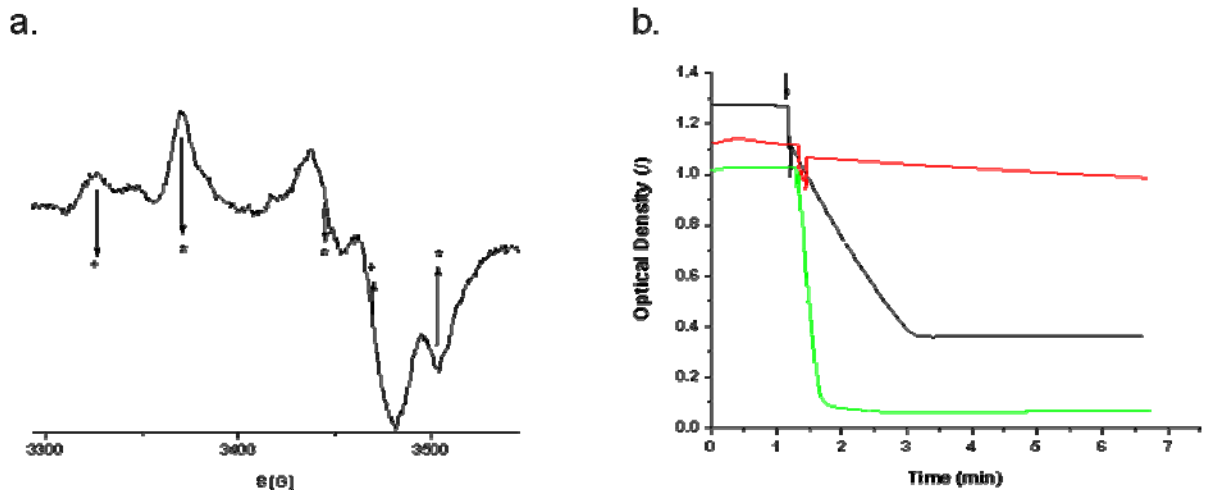

Figure 5. Completeness and functionality of of complex I after reconstitution in polymer membrane of the vesicles. a) EPR spectrum of NADH reduced complex I incorporated in the vesicles membrane, at 40K. ***** indicate the values of the gyromagnetic tensor for the binuclear Fe-S cluster N1a. **+** indicate the values of the gyromagnetic tensor for the binuclear Fe-S cluster N1b. b).NADH/ ferricyanide oxidoreductase activity measured at 410 nm and 25 °C. The reaction was started by an addition of NADH (represented by the arrow) to: complex I in solution (curve A), complex I incorporated in polymer vesicles (curve B), protein-free vesicles solution (curve C).

In addition, we investigated whether the proteovesicles contained the binuclear Fe/S clusters by using EPR spectroscopy. The EPR spectrum of NADH reduced complex I in the vesicle membrane (**Figure 5a**) at 40K is similar to that of free complex I (34) g-factor values of 1.94 and 2.03 were attributed to cluster N1b, and the values 1.92, 1.95 and 2.00 to the cluster N1a (39).

The amount of protein incorporated in the membrane of proteovesicles was estimated by a BCA protein assay. Approximately 40 - 60% of complex I in the mixture was incorporated into proteovesicles, (data not shown). These values are in good agreement with those obtained when complex I was reconstituted in liposomes (40).

To demonstrate the preferential orientation of the protein in proteovesicles membrane we measured the NADH/ferricyanide oxidoreductase activity. Ferricyanide binds to the NADH binding site, and neither involves quinone reduction nor proton translocation, representing a direct way to test the orientation of complex I once inserted into the polymer membrane (41). The NADH/ferricyanide oxidoreductase

activity was determined for purified complex I, proteovesicles, and protein-free polymer vesicles (**Figure 5b**). The activity of complex I (curve A) is preserved after its incorporation in the polymer membrane (curve B); the lower activity of proteovesicles is due to the reduced fraction of the incorporated protein and to a partially "wrong" complex I orientation once inserted into the polymer membrane.

Electron transfer mediated by complex I incorporated in polymer membranes. We wanted to determine whether and how far complex I mediates electron transfer from the vesicles' environment to their interior (**Scheme 1**).

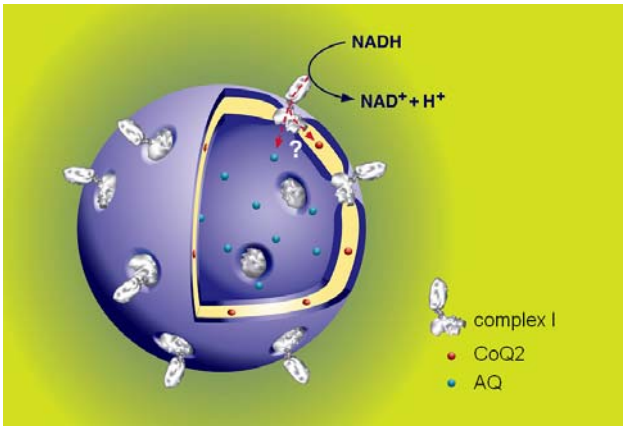

Scheme 1. Electron transfer nanodevice based on complex I reconstituted in the membrane of proteovesicles.

We used ubiquinone 2, CoQ_2 , known to be involved in the natural mechanism of energy conversion as electron acceptor (36, 42). Due to its hydrophobic character, CoQ_2 was incorporated simultaneously with complex I into the polymer membrane, using the method described above. After addition of NADH, the reduction of CoQ_2 mediated by the protein was followed with EPR spectroscopy. This was compared with the EPR spectrum of protein-free vesicles containing CoQ_2.

Prior tests on electrochemical reduction of free CoQ_2 were used to identify the semiquinone radical anion of CoQ_2, formed by direct electron transfer (43). The EPR spectrum generated by direct reduction of free CoQ_2 (**Figure 6–A a**) was simulated with hyperfine coupling constants compatible with those reported for the CoQ_2 radical anion, CoQ_2^- (**Figure 6-A b**) (44). Addition of 1 % TRITON™ X-100 (Triton) led to line broadening in the EPR spectrum according to increased viscosity, but had no influence on the hyperfine splitting representing CoQ_2^- (44, 45).

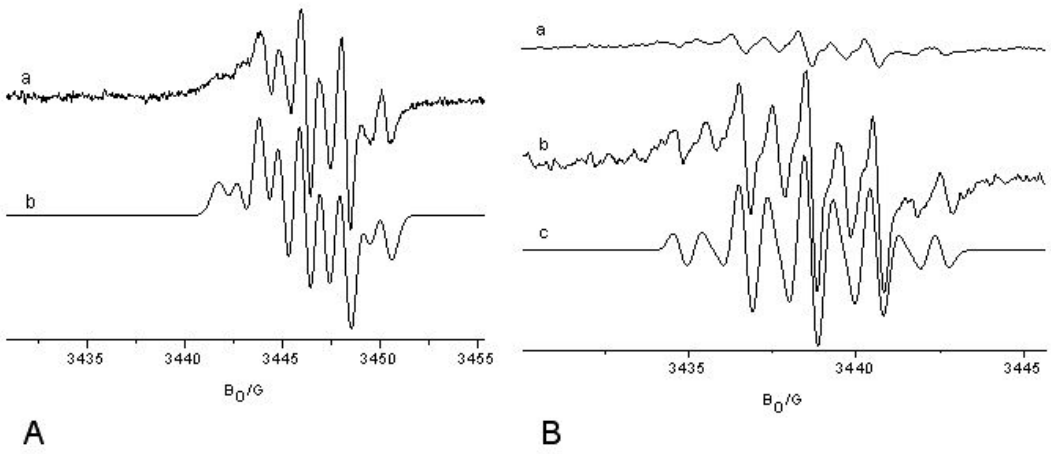

Figure 6. A. EPR spectrum of electrochemically reduced CoQ_2 at 283 K (a) together with its simulation (b). B. EPR spectrum of NADH-reduced species of CoQ_2 at 283 K, when CoQ_2 is incorporated in polymer vesicles (a), when CoQ_2 is incorporated in proteovesicles (b), together with its simulation (c). The solutions were prepared in 50 mM Tris/HCl, 50 mM NaCl, pH=7.0

When CoQ_2 is incorporated in the membrane of the polymer vesicles, a very weak EPR spectrum, similar to that of the anionic CoQ_2^- species, appears (**Figure 6-B a** compared with **Figure 6 – A a**). Its integrated area corresponds to approx. 6% of the radical anions which can be generated by electrolysis of an amount of CoQ_2 equivalent to that used for the incorporation in polymer vesicles.

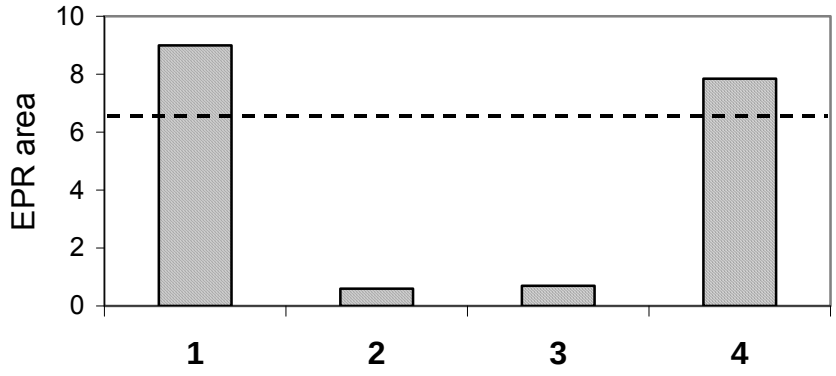

Figure 7. Double integral of the EPR spectrum of CoQ_2^- generated by: parent CoQ_2 (1), CoQ_2 incorporated in polymer vesicles (2), CoQ_2 and AQ incorporated in polymer vesicles (3), CoQ_2 incorporated in proteovesicles (4). The solutions in 50 mM Tris/HCl, 50 mM NaCl, were measured at 283 K. Dotted line indicates the double integral of the EPR spectrum of CoQ_2^- generated by CoQ_2 incorporated in polymer vesicles, after addition of 1% Triton.

This points to only a very low amount of CoQ_2 being present on or at the surface of the vesicles and therefore being accessible for direct electron transfer (**Figure 7 -2** compared with **-1**). After the addition of 1% Triton, the intensity of CoQ_2^- EPR signal increased significantly (dotted line in **Figure 7**). Due to their amphiphilic character, surfactants are known to partially solubilize the membrane at low concentration, while at higher concentration they disorganize it completely. Dynamic light scattering data confirmed that a considerable fraction of vesicles remained intact after the addition of detergent, explaining the residual fraction of CoQ_2 still not reduced. Addition of 1% Triton led to the partial destabilization of the polymer membrane, thus enhancing the reduction of CoQ_2, but does not lead to a complete release of the residual CoQ_2 (45).

The addition of NADH to the proteovesicle solution generated an EPR spectrum of CoQ_2^- with a significantly higher intensity (**Figure 6-B b**). Its double integral indicates that considerably more of the CoQ_2 incorporated in the proteovesicles is reduced (**Figure 7-4**), which proves that complex I mediates the electron transfer when reconstituted in the polymer membrane. The presence of CoQ2 that is not reduced can be explained by its location in the polymer membrane relative to the specific quinone-binding sites of complex I.

To determine whether the electron-transfer mediated by complex I reconstituted in polymer membranes is regio-selective, we used a second electron acceptor, anthraquinone-2,6-disulfonic acid (AQ). This is preferentially soluble in the aqueous phase, and therefore located in the inner cavity of proteovesicles. The addition of NADH to a free AQ solution in the presence of complex I (Supplementary Information, **Figure S4**) generated an EPR spectrum similar to that of the electrochemically reduced AQ (46), and did not change after addition of 1 % Triton. Thus, complex I mediates electron transfer to AQ, most likely involving the non-physiological quinone-site (36). As the EPR spectrum of reduced ubiquinone 2 is only partially overlapping to the one of reduced AQ (Supplementary Information, **Figure S5** and **S6**), this enables to distinguish to which of them is the electron transfer taking place, when they are both present in the nanodevice. However, no EPR signal was obtained when AQ was encapsulated in polymer vesicles, and only a very weak EPR spectrum of CoQ_2^- species appeared when both electron acceptors were incorporated (**Figure 7 -3**). The addition of NADH to proteovesicles containing both electron acceptors generated the EPR spectrum of CoQ_2^- similar in intensity to the one generated when only CoQ_2 was incorporated in proteovesicles (**Figure 1- 4**).

Discussion

The reactivation of complex I by phospholipids is most likely due to the need of specific lipids that provide an appropriate environment for the active conformation of the complex (3, 25, 26, 47). Although we did not establish the detailed molecular aspects of electron transfer and proton-translocation of complex I in copolymer membranes, our work shows that amphiphilic triblock copolymers are able to mimic biological membranes and that they support enzymatic activity of membrane proteins by providing an adequate medium for their physiological activity. By using a library of amphiphilic triblock copolymer $PMOXA_n$-$PDMS_m$-$PMOXA_n$ we found that for specific hydrophilic-hydrophobic domains, the polymer membrane promotes complex I activity in a similar way as natural phospholipids. The increase of the length of the hydrophobic block while keeping the length of the hydrophilic domains constant leads to a stronger activation of complex I. At the same time, the longer the hydrophilic block, the thicker is the membrane. These data can be explained by a higher mechanical stress imposed on the protein by the thickness of the membrane, and the conformational flexibility of the copolymer. Together the effects might favor an active conformation of complex I (**Figure 8**).

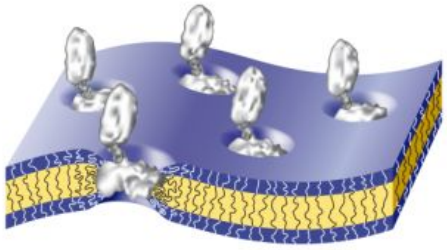

Figure 8. Graphical representation of complex I incorporated in copolymer membrane.

An upper limit for the hydrophobic domain surely exists, above which the membrane imposes such a high distortion on complex I that the protein complex disassembles. However, we did not reach this barrier within our experiments.

The inverse effect was obtained by increasing the length of the hydrophilic block while keeping the length of the hydrophobic block. However, this effect is not as significant as the one of the hydrophobic block. Changes in the length of the hydrophilic block only modulate the effects obtained by changes in the length of the hydrophobic block. The role of these two molecular parameters of the copolymer system gives some insight on the intermolecular forces acting between the copolymer membrane and the protein (**Figure 8**). The membrane domain of complex I is essential for the proton-translocation activity, tightly coupled to the electron

transfer (48). It was shown that conformational changes are exerted on this domain during turnover, in agreement with our model, indicating that the hydrophobic block has the major effect on the modulation of complex I activation. Contrarily, the hydrophilic block might interfere with proton access if its length goes beyond a certain threshold. In addition, the specific inhibition of the NADH:decyl-ubiquinone oxidoreductase activity by piericidin A demonstrates that the amphiphilic block copolymer PMOXA-PDMS-PMOXA does not affect the physiological quinone-binding site of complex I.

The activation of complex I by amphiphilic triblock copolymers can be controlled by varying the molecular properties of these block copolymer systems, that is, by varying the lengths of the specific hydrophilic-hydrophobic domains. This is remarkable in the context of using complex I for technological applications as the lipidic membrane environment previously considered as required for activation can now be replaced by amphiphilic block copolymers.

The ability of the copolymer to activate complex I as well as to provide a suitable hydrophobic environment for incorporation of electron acceptors represents the basis for the design of an electron transfer device at the nanometer scale, based on the incorporation of complex I in copolymer vesicles, as shown in **Scheme 1**. By adapting the method of membrane protein reconstitution in liposomes to our polymer vesicles, we incorporated the asymmetric protein without cleavage and in a suitable orientation to mediate electron transfer from the outside to the polymer membrane of proteovesicles. During incorporation the enzyme complex did not disassemble nor was the electron transfer chain affected. In addition, NADH/ferricyanide oxidoreductase activity proved that complex I was inserted with a high probability in the desired orientation, with the peripheral arm pointing outwards from the vesicles, thus favoring electron transfer from the environment of the vesicles, into their membranes.

The efficiency of the incorporation of complex I into the copolymer membrane of proteovesicles of 40 – 60% is in the same order as values obtained for reconstitution in liposomes (40). This is remarkable in the context of the higher stability of polymer membranes which requires a higher activation energy for the insertion of a membrane protein. Thus the driving force for the incorporation of membrane proteins in hydrophobic membranes must be very high. The distribution of incorporation efficiencies is due to the statistical character of the self-assembly process of proteovesicles formation. In biological membranes complex I guides a sub-millisecond electron transfer from NADH via the long chain of its redox cofactors to the substrate quinine (49). It contains at least two quinone binding sites, but only one

is considered as the physiological site due to its coupling with proton translocation (36). We studied the electron transfer mediated by complex I reconstituted in polymer membrane to various electron acceptors, without characterizing the molecular details of the reaction. By using two electron acceptors with different locations with respect to the copolymer membrane we established that electron transfer from the outside to the membrane of the proteovesicles takes place.

Conclusion

The synthetic membrane can be considered as a mimic of biological membranes, while offering specific advantages, such as high mechanical stability and inert chemical behavior, giving rise to an enhanced stability to the nanodevice. This hybrid system allows site-specific reactions, and is suitable for a variety of applications such as a trigger system in signalling, or a nanoreactor for specific follow-up reactions inside the membrane.

The hybrid protein-polymer nanodevice illustrates how complex I could be used to reduce suitable molecules in the membrane. In order to transfer electrons to the aqueous cavity of the vesicles and reduce molecules there, a second enzyme with a substrate reduction site on the opposite site of the membrane is needed, similar to what is seen in nature, where complex I acts in tandem with complex III. Using only complex I, the hybrid system provides two compartments: the membrane, where electrons can be transferred from the environment, and an aqueous compartment where other reactions can be followed simultaneously, without interference.

Material and Methods

Solutions of lipids (E.coli lipid polar extract) were obtained from Aventi Polar Lipids, Inc. The detergent dodecyl-maltoside was obtained from Anatrace, Inc. and added to lipids solutions (0.1%), and to polymer solutions (3.5%). Decyl-ubiquinone (ubiquinone 2), NADH, TRITON™ X-100 (Triton), potassium ferricyanide and anthraquinone-2,6-disulfonic acid (AQ) were purchased from Sigma-Aldrich. Other chemicals were obtained as described in the following sections.

Expression and purification of complex I

NADH: ubiquinone reductase (complex I) was isolated from Escherichia Coli, following an established protocol (3). The protein was stored in 50 mM MES/NaOH pH 6.0, 50 mM NaCl, 0.15% dodecyl-maltoside.

Synthesis of ABA triblock copolymer

A library of poly-(2-methyloxazoline)-block-polydimethylsiloxane-block-poly(2-methyloxazoline) copolymers was synthesized following the approach described by Nardin et al (13). The polydimethylsiloxane middle block was synthesized by acid catalyzed polycondensation of dimethoxydimethylsilane in the presence of water and end-capper, resulting in butylhydroxy terminated bi-functional PDMS. Upon purification and drying the hydroxyl groups were reacted with trifluoromethanesulfonic anhydride in cold hexane for three hours. The solvent was then removed under high vacuum and a portion of fresh hexane was added. The reaction mixture was filtered through a G4 filter at -10°C under argon. Upon removal of solvent the colorless triflate bi-functional macroinitiator was obtained. Addition of 2-methyl-2-oxazoline to the macroinitiator solution in dry ethyl acetate resulted in symmetric ring-opening cationic polymerization of poly-(2-methyloxazoline) blocks. The reaction was terminated by addition of potassium hydroxide in methanol. The reaction product was purified by ultrafiltration in a 1:5 ethanol/water mixture. In the case of $A_{21}B_{69}A_{21,}$ $A_{13}B_{62}A_{13,}$ $A_{15}B_{62}A_{15}$ and $A_{13}B_{23}A_{13}$ block copolymers the starting siloxane polymers were purchased from Wacker Chemie AG, purified, and reacted in a similar manner.

Preparation of ABA vesicles and proteovesicles by incorporation of complex I

The self-assembly of poly(2-methyloxazoline)-block-poly(dimethylsiloxane)-block-poly(2-methyloxazoline), PMOXA-PDMS-PMOXA amphiphilic triblock copolymers in aqueous solution has been described in a previous publication (13).

To prevent the presence of any traces of organic solvents, block copolymer vesicles were prepared by directly dissolving 50 mg of the copolymer in 4.950 g of buffer (50 mM Tris/HCl, 50 mM NaCl, pH 7.0) rather than using the common solvent displacement technique to induce self-assembly. Under over-night vigorous stirring, the amphiphilic block copolymers spontaneously self-assemble into vesicular structures. Their sizes and size distributions are large yet improved by sonication and sequential extrusion cycles through Millipore filters (0.45 μm and 0.22 μm pore size). Similar to the incorporation of proteins into surfactant-doped liposomes described by Rigaud *et al* (33) the addition of 0.5 % Triton to the dispersion of copolymer vesicles enables the incorporation of complex I into the synthetic membrane. The polymer vesicles were left to incubate with the surfactant for 1 hour prior to sonication (two cycles of 5 s). The protein solubilized in dodecylmaltoside (80 µL, 1 $mg.mL^{-1}$) was added to the surfactant-doped amphiphilic block copolymer vesicles and maintained under stirring for 3-6 hrs. Afterwards the surfactant was removed using Bio-Beads® SM-2(Bio-Rad Laboratories). The total amount of Bio-Beads (1g Bio-Beads for 200 mg Triton) was sequentially added in three steps spaced by 1 hour. The sample was then stirred for 6-8 h at 4 °C. The supernatant containing proteovesicles was then centrifuged (Heraeus, 5000 rpm during 20 min.) to remove the Bio-Beads. Non-incorporated protein was removed by gel permeation chromatography (Sepharose™ 4B, Amersham Biosciences).

Transmission electron microscopy

These measurements were conducted on vesicle and proteovesicles samples by using a Philips 400 microscope (Philips). The samples were prepared by dilution up to 1,000 times and then stained with 2% uranyl acetate on plasma-treated copper grids.

Integrity of complex I after its incorporation in polymer membrane

Gel electrophoresis. A solution of native complex I, a solution of proteovesicles containing 1 % (v/v) complex I, and a solution of pure polymer vesicles were analyzed with a 12% SDS-PAGE. The proteovesicle solution was concentrated by centrifugation and re-dissolved in SDS-PAGE buffer for analysis. Complex I subunits were detected by silver staining of the polyacrylamide gel (Silver Staining kit, Amersham Biosciences).

Electron Paramagnetic Resonance, EPR. The Fe-S clusters in NADH-reduced proteovesicles were detected with an X-band Bruker ESP300E spectrometer, at 40K.

The sample temperature was controlled with an Oxford Instruments helium flow cryostat and the magnetic field was calibrated using a strong pitch standard. The microwave power was 2mW, the modulation amplitude 6G. Multiple acquisitions were done to improve the signal-to-noise ratio. The solutions of vesicles/proteovesicles were mixed with NADH (5 mM final concentration) and measured immediately.

Complex I activity assays

NADH/ferricyanide oxidoreductase activity assay. Activities were determined with purified complex I and complex I in proteovesicles, and compared to the activity of polymer vesicles without complex I. The enzymatic activity of complex I was measured at 25 °C by following the reduction of ferricyanide by NADH at 410 nm. The assay was performed with 0.3 mL of vesicles (1mg/ml) (or proteovesicles) solution respectively, 0.185 mL of 50 mM Tris/HCl, 50 mM NaCl pH 7.0 buffer and 5 μL of 0.1 M potassium ferricyanide. After chromatographic removal of non-incorporated complex I the enzymatic activity was recorded by the addition of 10 μL of a 10 mM NADH solution. The NADH stock solution was freshly prepared for each set of experiments. Similar measurements were repeated with the surfactant-solubilized complex I: 5 μL of a 10 $mg.mL^{-1}$ solution was mixed with 0.485 mL of 50 mM Tris/HCl, 50 mM NaCl pH 7.0 buffer containing 0.1 % Triton X-100.

NADH-decylubiquinone oxidoreductase activity assay. Complex I (70 μg) was added to a solution of lipids or copolymer with different ratios (w/w) from 0.01 to 1, and the solutions were incubated for different times (20 minutes to 3 hours). The volume was then adjusted to a total volume of 1mL, and 50μM of decyl-ubiquinone was added. After a final incubation of 5 minutes at room temperature, 50μM of NADH was added to the solution and the decrease of absorbance was measured at 340nm. The buffer used for all titration experiments was 50mM MES/NaOH, 50mM NaCl, pH=6.0 Lipid solutions were prepared in similar conditions as previously used by Friedrich (3) (incubation time of 20 minutes at 0°C).

Inhibition assay. The same mixture was prepared as for the NADH-decylubiquinone oxidoreductase activity assay. During the 5 minutes incubation at room temperature, 10μM Piericidin A, a complexI inhibitor, was added to the solution. Finally 50μM of NADH was added to the solution and the decrease of absorbance was measured at 340nm.

Coupled NADH:ubiquinone–2/AQ oxidoreductase activity assay. 10 μM ubiquinone 2 (CoQ_2) was added and incubated for 1hr with the vesicles or

proteovesicles dispersion. The solution was washed by gel filtration prior to the EPR measurements. Anthraquinone 2,6-disulfonic acid, disodium salt (AQ) was dissolved in 50 mM Tris/HCl, 50 mM NaCl, pH 7.0 buffer, to a 10mM concentration. This solution was used to prepare the vesicles and proteovesicles according to the previous protocol. Non-encapsulated AQ were removed by ion exchange chromatography (Amberlyst A 26, Sigma-Aldrich).

Reductions of free ubiquinone 2, and AQ were carried out electrochemically, the experimental set-up employing a helical gold cathode as a working electrode and a platinum wire as a counter electrode. The electrolytic cell was placed inside the resonance cavity to allow *in situ* detection, and EPR measurements were performed at 283K, on a Bruker ESP300 spectrometer at X-band and with a microwave power of 1mW. The solutions of vesicles/proteovesicles incorporating the electron acceptors were mixed with 10 μL of a 10 mM NADH solution and measured immediately after preparation, with a Bruker ESP300 spectrometer at X-band and with a microwave power of 1mW, and modulation amplitude of 1G. EPR simulations were done with the public domain program WinSim.

ACKNOWLEDGEMENTS. We thank Stefan Stolpe, from Freiburg University, who purified complex I. We thank David Hughes (University of Basel) for reading and editing the manuscript. The authors are grateful for the Swiss National Science Foundation's financial support (Projects ZZZ).

REFERENCES:

1. Gust, D., Moore, T. A., & Moore, A. L. (1998) Mimicking bacterial photosynthesis.*Pure and Applied Chemistry* **70,** 2189-2200.
2. Moore, T. A., Moore, A. L., & Gust, D. (2002) The design and synthesis of artificial photosynthetic antennas, reaction centres and membranes.*Philosophical transactions of the royal society B, biological sciences* **357,** 1481-1498.
3. Stolpe, S. & Friedrich, T. (2004) The Escherichia coli NADH: ubiquinone oxidoreductase (complex I) is a primary proton pump but may be capable of secondary sodium antiport.*Journal Of Biological Chemistry* **279,** 18377-18383.
4. He, Q., Duan, L., Qi, W., Wang, K., Cui, Y., Yan, X., & Li, J. (2008) Microcapsules containing a biomolecular motor for ATP biosynthesis.*Advanced Materials* **20,** 2933-2937.

5. Parmar, M. M., Edwards, K., & Madden, T. D. (1999) Incorporation of bacterial membrane proteins into liposomes: factors influencing protein reconstitution.*Biochimica Et Biophysica Acta-Biomembranes* **1421,** 77-90.
6. Silvander, M., Bergstrand, N., & Edwards, K. (2003) Linkage identity is a major factor in determining the effect of PEG-ylated surfactants on permeability of phosphatidylcholine liposomes.*Chemistry and physics of lipids* **126,** 77-83.
7. Antonietti, M. & Forster, S. (2003) Vesicles and liposomes: A self-assembly principle beyond lipids.*Advanced Materials* **15,** 1323-1333.
8. Shimizu, T., Masuda, M., & Minamikawa, H. (2005) Supramolecular nanotube architectures based on amphiphilic molecules.*Chemical reviews* **105,** 1401-1443.
9. Choi, H. J., Lee, H., & Montemagno, C. D. (2005) Toward hybrid proteo-polymeric vesicles generating a photoinduced proton gradient for biofuel cells.*Nanotechnology* **16,** 1589-1597.
10. Graff, A., Sauer, M., Van Gelder, P., & Meier, W. (2002) Virus-assisted loading of polymer nanocontainer.*Proceedings Of The National Academy Of Sciences Of The United States Of America* **99,** 5064-5068.
11. Meier, W., Nardin, C., & Winterhalter, M. (2000) Reconstitution of channel protein in (polymerized) ABA triblock copolymer membranes.*Angewandte Chemie* **112,** 4747.
12. Kumar, M., Grzelakowski, M., Zilles, J., Clark, M., & Meier, W. (2007) Highly permeable polymeric membranes based on the incorporation of the functional water channel protein Aquaporin Z.*PNAS* **104,** 20719-20724.
13. Nardin, C., Thoeni, S., Widmer, J., Winterhalter, M., & Meier, W. (2000) Nanoreactors based on (polymerized) ABA-triblock copolymer vesicles.*Chemical Communications***,** 1433-1434.
14. Stoenescu, R., Graff, A., & Meier, W. (2004) Asymmetric ABC-triblock copolymer membranes induce a directed insertion of membrane proteins.*Macromolecular Bioscience* **4,** 930-935.
15. Axthelm, F., Casse, O., Koppenol, W. H., Nauser, T., Meier, W., & Palivan, C. G. (2008) Antioxydant nanoreactor based on superoxide dismutase encapsulated in superoxide-permeable vesicles.*The journal of physical chemistry B* **112,** 8211-8217.
16. Nallani, M., Benito, S., Onaca, O., Graff, A., Lindemann, M., Winterhalter, M., Meier, W., & Schwaneberg, U. (2006) A nanocompartment system (synthosome) designed for biotechnological applications.*Journal Of Biotechnology* **123,** 50-59.
17. Galaev, I. Y. & Mattiasson, B. (1999) 'Smart' polymers and what they could do in biotechnology and medicine.*Trends In Biotechnology* **17,** 335-340.
18. Kita-Tokarczyk, K., Grumelard, J., Haefele, T., & Meier, W. (2005) Block copolymer vesicles - using concepts from polymer chemistry to mimic biomembranes.*Polymer* **46,** 3540-3563.
19. Palivan, C. G., Vebert, C., Axthelm, F., & Meier, W. (2007) in *Nanotechnology in biology and medicine*, ed. Press, C., p. 467.
20. Baranova, E. A., Holt, P., & Sazanov, L. A. (2007) Projection Structure of the Membrane Domain of Escherichia coli Respiratory Complex I at 8 Å Resolution.*Journal of Molecular Biology* **366,** 140-154.
21. Brandt, U. (2006) Energy Converting NADH:Quinone Oxidoreductase (Complex I).*Annual Review of Biochemistry* **75,** 69-92.
22. Friedrich, T. (1998) The NADH : ubiquinone oxidoreductase (complex I) from Escherichia coli.*Biochimica Et Biophysica Acta-Bioenergetics* **1364,** 134-146.
23. Friedrich, T. & Bottcher, B. (2004) The gross structure of the respiratory complex I: A Lego-System (vol 1608, pg 1, 2004).*Biochimica Et Biophysica Acta-Bioenergetics* **1657,** 71-71.
24. Walker, J. E. (1992) *Reviews of biophysics* **25,** 253-324.

25. Sazanov, L. A., Carroll, J., Holt, P., Toime, L., & Fearnley, I. M. (2003) A role for native lipids in the stabilization and two-dimensional crystallization of the Escherichia coli NADH-ubiquinone oxidoreductase (complex I).*Journal of Biological Chemistry* **278,** 19483-19491.
26. Sharpley, M. S., Shannon, R. J., Draghi, F., & Hirst, J. (2006) Interactions between phospholipids and NADH : ubiquinone oxidoreductase (complex I) from bovine mitochondria.*Biochemistry* **45,** 241-248.
27. Sinegina, L., Wikstrm, M., Verkhovsky, M. I., & Verkhovskaya, M. L. (2005) Activation of Isolated NADH:Ubiquinone Reductase I (Complex I) from Escherichia coli by Detergent and Phospholipids. Recovery of Ubiquinone Reductase Activity and Changes in EPR Signals of Iron−Sulfur Clusters†.*Biochemistry* **44,** 8500-8506.
28. Lee, A. G. (2004) How lipids affect the activities of integral membrane proteins.*Biochimica et Biophysica acta* **1666,** 62-87.
29. Lee, A. G. (2005) How lipids and proteins interact in a membrane: a molecular approach.*Molecular BioSystems* **1,** 203.
30. Opekarova, M. & Tanner, W. (2003) Specific lipid requirements of membrane proteins-a putative bottleneck in heterologous expression.*Biochimica et Biophysica acta* **1610,** 11-22.
31. Palsdottir, H. & Hunte, C. (2004) Lipids in membrane protein structures.*Biochimica Et Biophysica Acta-Biomembranes* **1666,** 2-18.
32. Lange, C., Nett, J. H., Trumpower, B. L., & Hunte, C. (2001) Specific roles of protein-phospholipid interactions in the yeast cytochrome bc(1) complex structure.*Embo Journal* **20,** 6591-6600.
33. Rigaud, J. L., Pitard, B., & Levy, D. (1995) Reconstitution Of Membrane-Proteins Into Liposomes - Application To Energy-Transducing Membrane-Proteins.*Biochimica Et Biophysica Acta-Bioenergetics* **1231,** 223-246.
34. Leif, H., Sled, V. D., Ohnishi, T., Weiss, H., & Friedrich, T. (1995) Isolation And Characterization Of The Proton-Translocating Nadh-Ubiquinone Oxidoreductase From Escherichia-Coli.*European Journal Of Biochemistry* **230,** 538-548.
35. Pata, V. & Dan, N. (2003) The effect of chain length on protein solubilization in polymer-based vesicles (polymersomes).*Biophysical Journal* **85,** 2111-2118.
36. Esposti, M. D. (1998) Inhibitors of NADH-ubiquinone reductase: an overview.*Biochimica Et Biophysica Acta-Bioenergetics* **1364,** 222-235.
37. Friedrich, T., Brors, B., Hellwig, P., Kintscher, L., Rasmussen, T., Scheide, D., Schulte, U., Mantele, W., & Weiss, H. (2000) Characterization of two novel redox groups in the respiratory NADH : ubiquinone oxidoreductase (complex I).*Biochimica Et Biophysica Acta-Bioenergetics* **1459,** 305-309.
38. Rigaud, J. L., Levy, D., Mosser, G., & Lambert, O. (1998) Detergent removal by non-polar polystyrene beads - Applications to membrane protein reconstitution and two-dimensional crystallization.*European Biophysics Journal With Biophysics Letters* **27,** 305-319.
39. Uhlmann, M. & Friedrich, T. (2005) EPR signals assigned to Fe/S cluster N1c of the Escherichia coli NADH : ubiquinone oxidoreductase (Complex I) derive from cluster N1a.*Biochemistry* **44,** 1653-1658.
40. Brand, M. D. (2005) The efficiency and plasticity of mitochondrial energy transduction.*Biochemical Society Transactions* **33,** 897-904.
41. Lenaz, G. (1998) Quinone specificity of Complex I.*Biochimica Et Biophysica Acta-Bioenergetics* **1364,** 207-221.
42. Ohnishi, T. (1998) Iron-sulfur clusters semiquinones in Complex I.*Biochimica Et Biophysica Acta-Bioenergetics* **1364,** 186-206.
43. Joela, H., Kasa, S., Lehtovuori, P., & Bech, M. (1997) EPR, ENDOR and TRIPLE resonance and MO studies on ubiquinones (Q-n): Comparison of

radical anions and cations of coenzymes Q-10 and Q-6 with the model compounds Q-2 and Q-0.*Acta Chemica Scandinavica* **51,** 233-241.
44. Lehtovuori, P. & Joela, H. (2000) ENDOR spectroscopic and molecular orbital study of the dynamical properties of the side chain in radical anions of ubiquinones Q-1, Q-2, Q-6, and Q-10.*Journal Of Magnetic Resonance* **145,** 319-325.
45. Fato, R., Estornell, E., DiBernardo, S., Pallotti, F., Castelli, G. P., & Lenaz, G. (1996) Steady-state kinetics of the reduction of coenzyme Q analogs by complex I (NADH:Ubiquinone oxidoreductase) in bovine heart mitochondria and submitochondrial particles.*Biochemistry* **35,** 2705-2716.
46. Turro, N. J. & Khudyakov, I. V. (1995) Time-Resolved Electron-Spin-Resonance And Laser Flash Spectroscopy Investigation Of The Photoreduction Of Anthraquinone-2,6-Disulfonic Acid, Disodium Salt By Sodium-Sulfite In Aerosol Ot Reverse Micelles.*Journal Of Physical Chemistry* **99,** 7654-7662.
47. Sinegina, L., Wikstrom, M., Verkhovsky, M. I., & Verkhovskaya, M. L. (2005) Activation of isolated NADH : ubiquinone reductase I (complex I) from Escherichia coli by detergent and phospholipids. Recovery of ubiquinone reductase activity and changes in EPR signals of iron-sulfur clusters.*Biochemistry* **44,** 8500-8506.
48. Hirst, J. (2005) Energy transduction by respiratory complex I – an evaluation of current knowledge.*Biochemical Society Transactions* **33,** 525-529.
49. Hinchliffe, P. & Sazanov, L. A. (2005) Organization of iron-sulfur clusters in respiratory complexI.*Science* **309,** 771-774.

Supplementary Information:

1. Optimisation of the experimental conditions for complex I activation in polymer media

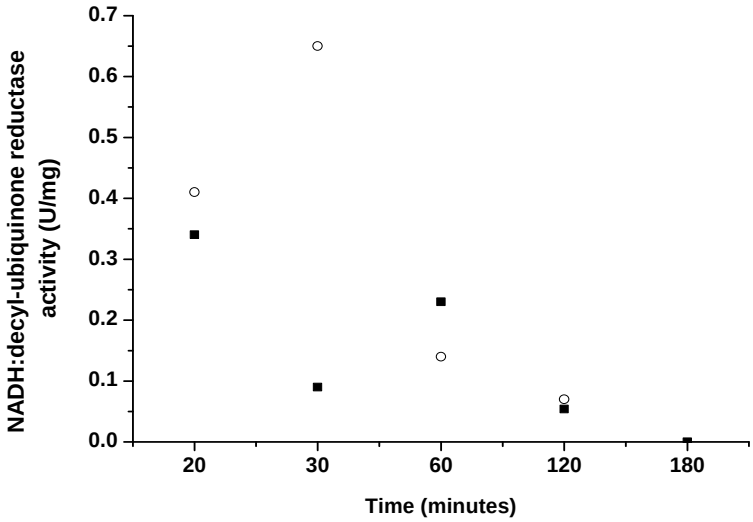

Figure S1: Dependence of the NADH:decyl-ubiquinone oxidoreductase activity of complex I (E. coli) on the protein incubation time and temperature in polymer media: at room temperature (black squares) and 0º C (empty circles). The polymer / complex I ratio is 0.1 (w/w). $PMOXA_{13}$-$PDMS_{110}$-$PMOXA_{13}$.

2. Transmission Electron Micrograph of empty polymer vesicles

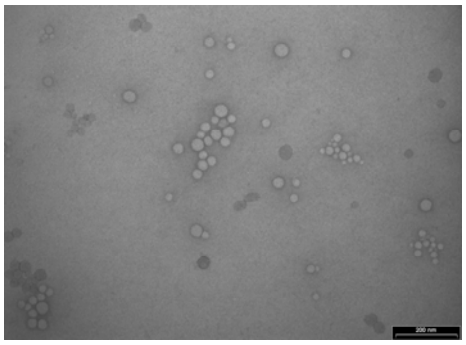

Figure S2. Transmission Electron Micrograph of $PMOXA_{13}PDMS_{110}PMOXA_{13}$ vesicles (room temperature; scale bar = 200 nm).

3. Integrity of Complex I in polymer membrane

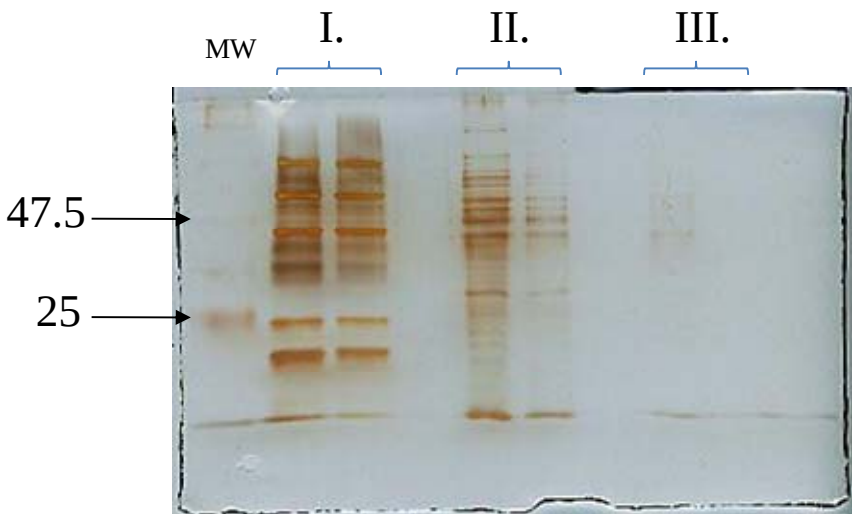

Figure S3 : Silver stained SDS-PAGE of: purified E. coli complex I, I, E. coli complex I incorporated in the membrane of PMOXA13-PDMS110-PMOXA13 vesicles, II, and pure PMOXA13-PDMS110-PMOXA13 vesicle membrane, III. MW: Molecular weight markers

4. NADH reduction of anthraquinone, AQ

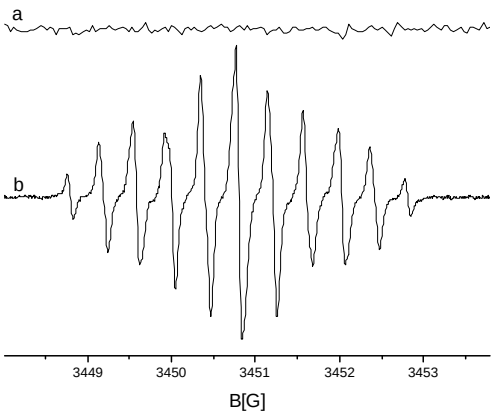

Figure S4. NADH reduction of anthraquinone, AQ: in a solution containing 1% triton a), in the presence of complex I, in a solution containing 1% triton b). The solutions were prepared in 50 mM Tris/HCl, 50 mM NaCl, pH=7.

5. Reduction of ubiquinone 2, and anthraquinone, AQ

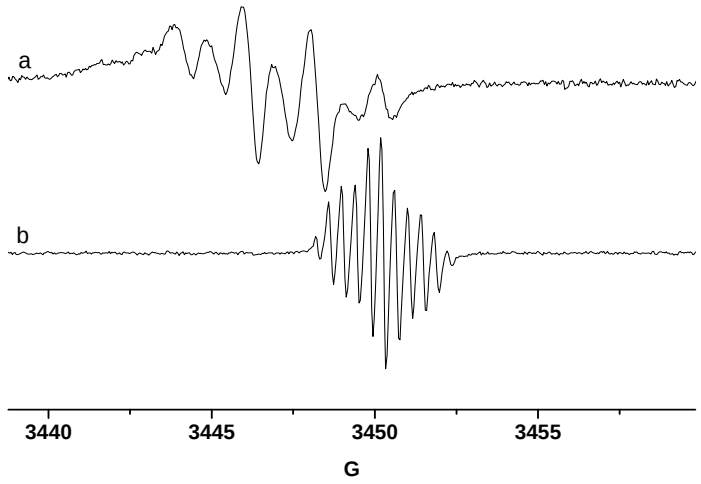

Figure S5. Electrolysis of ubiquinone 2 (a), and anthraquinone, AQ (b). The solutions were prepared in 50 mM Tris/HCl, 50 mM NaCl, pH=7.

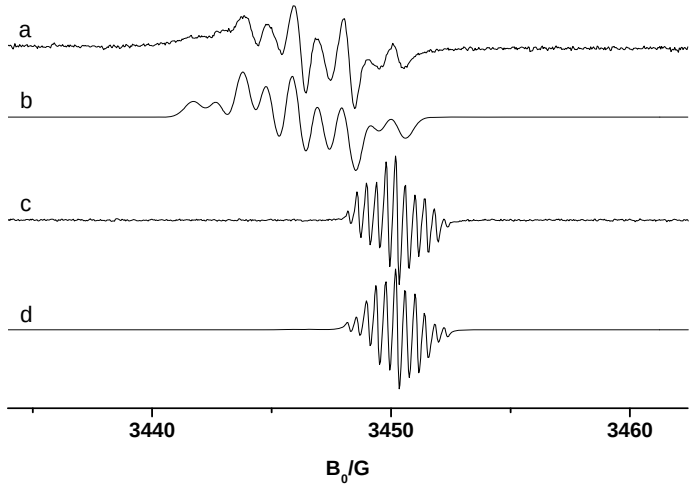

Figure S6. EPR spectrum of: reduced ubiquinone 2 (a), together with its simulation (b), and reduced anthraquinone (c), together with its simulation (d). The solutions were prepared in 50 mM Tris/HCl, 50 mM NaCl, pH=7.

2.4.5 Receptor-Targeted Polymer Vesicle-Tased Drug Delivery Formulation of Pravastatin

Inhibition of Macrophage Phagocytotic Activity by a Receptor-targeted Polymer Vesicle-based Drug Delivery Formulation of Pravastatin

Pavel Broz, MD, Nadav Ben-Haim, PhD,* Mariusz Grzelakowski, MSc,† Stephan Marsch, MD, PhD,* Wolfgang Meier, PhD,† and Patrick Hunziker, MD**

Abstract: Ruptures of macrophage-rich atherosclerotic plaques in the coronary arteries are the main reason for heart attack. Targeted therapeutic interventions with an inhibitory effect on the macrophages promise to be beneficial, but currently available drugs such as statins achieve event reductions of only 30%. Dose-limiting adverse effects in remote organs prohibit achieving higher drug levels known to have strong inhibitory effects on macrophages. Receptor-specific targeting using statin-loaded nanometer-sized triblock copolymer vesicles with targeting moieties might allow high-dose treatment for improved efficacy, while minimizing toxicity in other cells. Vesicle uptake by target cells but not other cell types and slow intracellular content release was observed. A major improvement in biologic efficacy was observed for polymer vesicles compared to free drug, whereas no increased cytotoxicity was observed in muscle cells. Such high-dose, targeted therapy of statins through cell-specific polymer vesicles allows novel treatment paradigms not only for atherosclerosis, but appears promising for a wide range of drugs and diseases.

Key Words: polymer vesicles, statins, macrophages, scavenger receptors, oxidized low-density lipoprotein

(*J Cardiovasc Pharmacol*™ 2008;51:246–252)

In recent years, ample evidence has accumulated supporting the hypothesis that local and systemic inflammatory processes play a key role in the pathogenesis of atherosclerotic diseases.[1–3] Activated macrophages initiate, maintain, and aggravate the various steps that finally lead to plaque rupture and vessel occlusion, the most common pathophysiological equivalent of myocardial infarction and stroke.[4,5] The amount of macrophages in a plaque correlates directly with the risk of plaque rupture, making the macrophage and inflammatory plaques important therapeutic targets in cardiovascular medicine.[3,6]

Anti-inflammatory drugs such as corticosteroids, calcineurin inhibitors, or cyclooxygenase inhibitors are not suitable for a selective inhibition of active plaque macrophages due to their low cell line selectivity and serious side effects. An ideal drug candidate would accumulate in highly active plaque macrophages, thereby sparing inactive macrophages, monocytes and other nontargeted cell types.

Lipid-lowering drugs of the 3-hydroxy-3-methylglutaryl coenzyme A (HMG-CoA) reductase inhibitor class have partial anti-inflammatory and immunomodulatory properties[7,8] and lead to a ~30% reduction of acute cardiac events.[9,10] In macrophages, statins exhibit several effects[11–13] that in combination lead to a reduced uptake of oxidized low-density lipoprotein (LDL), reduced secretion of leucotactic and tissue-degrading molecules,[14] and in consequence a reduced number of plaque ruptures and acute coronary syndromes.[15] These immunomodulatory effects are concentration dependent, whereby high concentrations of statins exhibit the most significant inhibition of macrophage activity and proliferation.[16] Furthermore, high-dose statins can directly downregulate the expression of scavenger receptor class A in macrophages by increasing the intracellular levels of transforming growth factor (TGF)-β1.[17] Statin concentrations used in this kind of receptor inhibition experiments (10 μmol/L), however, can never be achieved in humans without having life-threatening adverse side effects such as rhabdomyolysis (mean peak plasma concentration for 40 mg oral pravastatin per day is 7.17 nmol/L).[18] By targeting the drugs specifically to macrophages populating the atherosclerotic plaques, the high-dose toxicity of statins might be circumvented and the immunomodulatory effects might be fully exploited.[19]

Nanometer-sized vesicles self-assembled from biocompatible, protein-repellent and immune system evading amphiphilic block copolymers promise to be useful for selective delivery,[20] triggered activity,[21] and controlled release of high doses of therapeutic agents.[22] The copolymers form vesicles in aqueous solution and enclose a defined part of the dissolved drug molecules. Recently, it has been shown that the number of encapsulated molecules can simply be calculated from the original bulk concentration and the volume of the vesicles.[23] By functionalizing the vesicle surface with chemical targeting moieties, the nanostructures can be directed to specific cellular targets. In a previous study, the same targeted polymer vesicles made from (poly(2-methyloxazoline)-b-poly(dimethylsiloxane)-b-poly(2-methyloxazoline) triblock copolymers were filled with fluorescent markers to study the targeting properties, uptake kinetics, and toxicity in cell cultures of scavenger

Received for publication July 17, 2007; accepted November 13, 2007.
From the *Medical Intensive Care Unit; and †Department of Chemistry, University of Basel, Basel, Switzerland.
Supported by the Swiss National Science Foundation and the National Centre of Competence in Research Nanoscale Science.
The authors report no conflicts of interest.
Reprints: Dr. Pavel Broz, MD, Medical Intensive Care Unit, Petersgraben 4, 4031 Basel, Switzerland (e-mail: broz.pa@gmail.com).

receptor A1-expressing transgenic cell lines, human THP-1 macrophages, human smooth muscle cells and human endothelial cells. The vesicles were target specific to scavenger receptor expressing cells and macrophages, whereas no uptake to the other investigated cell lines or THP-1 macrophage precursor cells was observed. The targeted polymer vesicles did not exhibit significant toxic effects on both cells taking up and not taking up the vesicles.[20]

Here, we present the use of the receptor targeted polymer vesicles for encapsulation of the hydrophilic drug pravastatin. Pravastatin has a proven inhibitory effect on macrophage endocytotic activity and metabolism in cell cultures and in vivo.[15] The vesicles were functionalized with an oligonucleotide sequence (polyG) with a proven affinity to macrophage scavenger receptor A1 (SRA-1) and tested in cell cultures of human macrophages for efficacy, substance release properties, and toxicity compared to nonencapsulated pravastatin and empty polymer vesicles. Cell-line specificity and myocyte toxicity were tested in cell cultures of rat skeletal muscle cells. The myocytes are known to be sensitive to statins and are a valid model for statin toxicity prediction.[24]

METHODS

Pravastatin Vesicle Preparation

The polymer used in this work consists of a poly (dimethylsiloxane) (PDMS) middle block and two poly(2-methyloxazoline) PMOXA side chains (JW05, M_n 7090 g/mol)[25] with biotin-functionalized end groups as described previously.[20] To prepare the vesicles, the polymer (10% biotinylated, 90% unbiotinylated polymer) was dissolved in ethanol to give a 15% (wt/vol) solution; 250 μL of this ethanol solution was added dropwise into 5 mL of phosphate-buffered saline (PBS) containing 1.12 mmol/L pravastatin (Sigma-Aldrich, Buchs, Switzerland). After 4 h of continuous stirring, the solution was repetitively filtrated through filters of defined pore size (Millex-GV, 0.45 μm and 0.22 μm; Millipore) to produce a homogenous population of vesicles. Nonencapsulated pravastatin was removed chromatographically (Sepharose 4B, Sigma-Aldrich, in a 37-cm column with 1 cm inner diameter, Bio-Rad, Reinach, CH). To obtain ligand-bearing vesicles, 4 μmol/L streptavidin (Sigma-Aldrich) followed by 4 μmol/L biotinylated polyguanylic acid (polyG; Microsynth, Balgach, CH; 23 G, 3′ modified with biotin) were added (2 h each with continuous stirring). To produce fluorescence-labeled polymer vesicles, Alexa-610 streptavidin (Invitrogen, Basel, Switzerland) was used instead of unlabeled streptavidin. Vesicles were characterized as described earlier with light scattering and cryogenic transmission electron microscopy.[21]

Cell Culturing

THP-1 cells (ECACC, Salisbury, UK) were cultured as recommended by the manufacturer. Differentiation into functional adherent macrophages was initiated 72 hours prior to experiment with 100 nmol/L phorbol 12-myristate 13-acetate (PMA; Sigma-Aldrich) in 24-well multiwell plates (Becton-Dickinson, Basel, Switzerland) with glass cover slips (12-mm diameter), resulting in a mean cell density of approximately 1.25e5 cells/cm^2. L6 mouse skeletal muscle cells (ECACC) were grown in enriched Dulbecco's Modified Eagle Medium (DMEM) as recommended by the manufacturer and seeded in a mean cell density of approximately 5e4 cells/cm^2 24 hours prior to experiment. Experiments were performed at 37°C and 5% CO_2.

Cellular Uptake of Vesicles

Alexa-610 labeled polymer vesicles were administered to cell cultures of macrophages and skeletal muscle cells as described previously[20] for 2 hours in a final concentration of 4 nmol/L vesicles. Cell nuclei were stained with 18 μmol/L Hoechst 34580 (Invitrogen; stock solution with dimethyl sulfoxide) for 30 min.

Endocytotic Activity Assay

Polymer vesicles were added to the prepared macrophage cultures for 24 hours with final pravastatin concentrations in the medium from 0.02 μmol/L to 1.08 μmol/L. Alexa-488-labeled acetyled LDL (Invitrogen) or labeled polyG (same as above coupled to streptavidin-phycoerythrin from Sigma-Aldrich in a 1:1 proportion) were added for 1 h in final concentrations of 20 μmol/L and 1 μg/mL, respectively to test the endocytotic activity. After washing with PBS, the cells were fixed in 4% paraformaldehyde for 20 min at room temperature. Fixed cells were mounted with an antibleaching glycerol-based mounting medium (Sigma-Aldrich) on glass slides.

Calcein Release Assay

Calcein (Sigma-Aldrich) was encapsulated into functionalized vesicles as described above in a high self-quenching concentration of 50 mmol/L and checked for absence of fluorescence signal in fluorescence microscopy. Polymer vesicles were given to cultures of macrophages for different time points in a working concentration of 4 nmol/L. An intact carrier does not generate a significant signal in fluorescence microscopy due to the self-quenching properties of encapsulated calcein, whereas the generation of a signal indicates the disintegration of the carrier. Ratio of cells with significant green fluorescence (higher than background fluorescence) in the sample compared to total number of cells seen by phase contrast microscopy was taken as parameter for the integrity of the polymer vesicles (no fluorescence indicates intact vesicles).

Cytotoxicity Assay

Cytotoxicity in macrophages was studied with an acetoxymethyl (AM) ester derivate of calcein (1 mmol/L in DMSO; Invitrogen). Macrophages were incubated with polymer vesicles containing pravastatin or PBS and compared to controls. After 24 hours of incubation, the cells were washed with PBS and exposed to 1 μmol/L calcein AM for 60 min. The lipophilic, nonfluorescent calcein AM is hydrolyzed inside living cells by nonspecific esterases and stains selectively living cells. To assess the known toxic effects of pravastatin on skeletal muscle cells, we additionally performed a colorimetric LDH release assay (Sigma-Aldrich) in 96-well multiwell plates to confirm the results from the Calcein AM release assay.[26] Dead cells release intracellular LDH into the serum-free medium, where it is detected with a standard

method based on the NADH-mediated conversion of a tetrazolium dye. The dye was detected with an automated microplate absorption reader (MPP 4001, Mikrotek, Overath, Germany) at a wavelength of 490 nm. Ratio of living cells in the sample compared to the cell number in an untreated control was taken as cell survival parameter.

Data Acquisition and Statistics

Cells were examined using fluorescence microscopy (Olympus IX 50, Camera ColorView II FW, Software analySIS) and confocal laser scanning microscopy (Zeiss ConfoCor 2, HAL 100, HBO 100, Software LSM 510 Zeiss) by selecting multiple random fields of view in an unbiased way. Image acquisition settings were unchanged over the whole experiment. Digital images were treated according to *Nature*'s guide for digital images (Nature Publishing Group, UK). The resulting series of images were analyzed by standard data analysis software (ImageJ, National Institutes of Health, Bethesda, MD) with automated particle counting to determine the number of cells per field of view whenever necessary. Standard statistics were used, including calculation of means and standard deviations (SD), linear regression, least square fitting to the sigmoid function for determination of ED50, application of analysis of variance (ANOVA), and Student's *t* test for group comparisons.

RESULTS

Polymer Vesicle Characterization

Polymer vesicles with encapsulated pravastatin (Fig. 1) show a mean outer diameter of 97 nm (standard deviation 10 nm) in cryogenic transmission electron microscopy, whereof the inner diameter is 72 nm (SD 14 nm). The resulting mean width of the polymer membrane itself is 13 nm. Based on the inner diameter of 72 nm, the calculated inner volume of an idealized vesicle is approximately 1.8e-19 liter. Based on a mean vesicle concentration per ml watery solution of 5e12 vesicles per milliliter,[25] the total inner volume of all vesicles in 1 mL solution is 8.01 μL. Since the pravastatin encapsulated into the polymer vesicles has the same concentration as the initial bulk solution (1.12 mmol/L), it is possible to calculate the mean pravastatin concentration of the solution after chromatographic removal of all non-encapsulated pravastatin. The calculated pravastatin concentration in the resulting vesicle solution is 8.97 μmol/L.

Targeting of Polymer Vesicles

Polymer vesicles functionalized with polyG ligands show a strong uptake into active macrophages, but were not taken up in significant numbers into skeletal muscle cells due to their target selectivity to class A scavenger receptors (Fig. 2A and B). After 2 hours, the fluorescence-labeled vesicles can

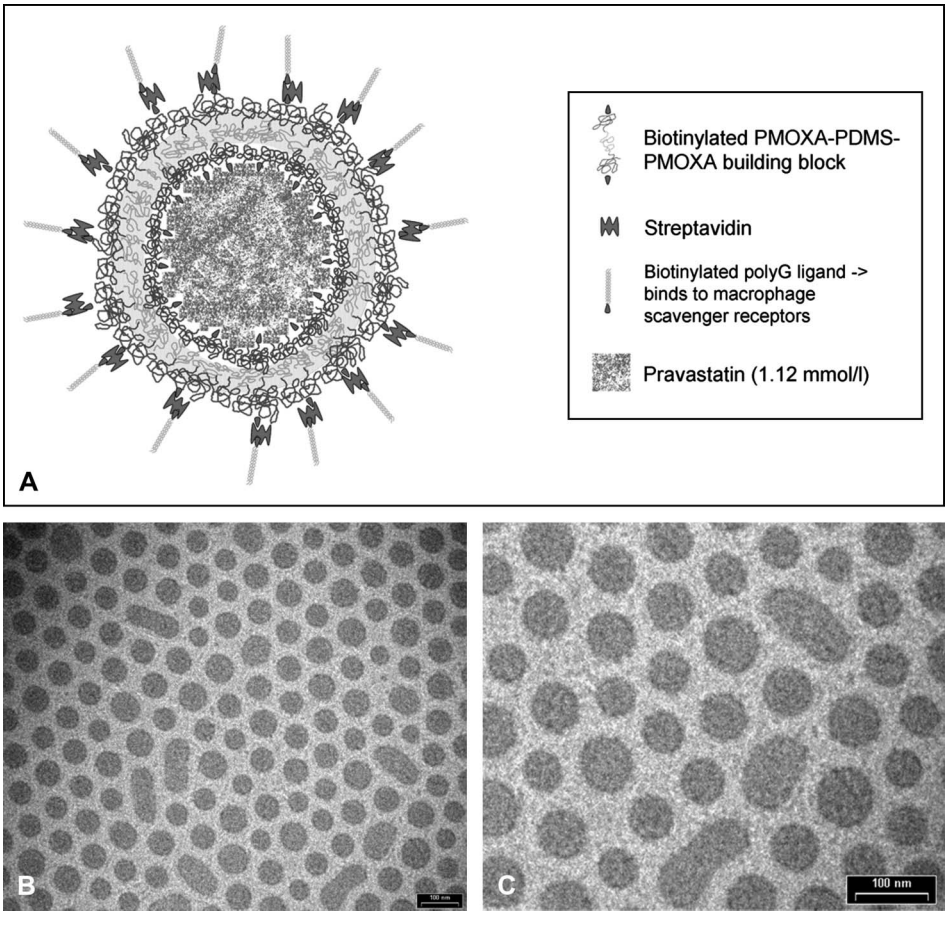

FIGURE 1. Vesicle characterization. A, Schematic drawing of a ligand-functionalized amphiphilic triblock copolymer vesicle with encapsulated pravastatin. B, Vesicles were visualized with cryogenic transmission electron microscopy. The images show a highly homogenous population of vesicles with a mean diameter slightly below 100 nm and an aqueous core. C, Detail of (B).

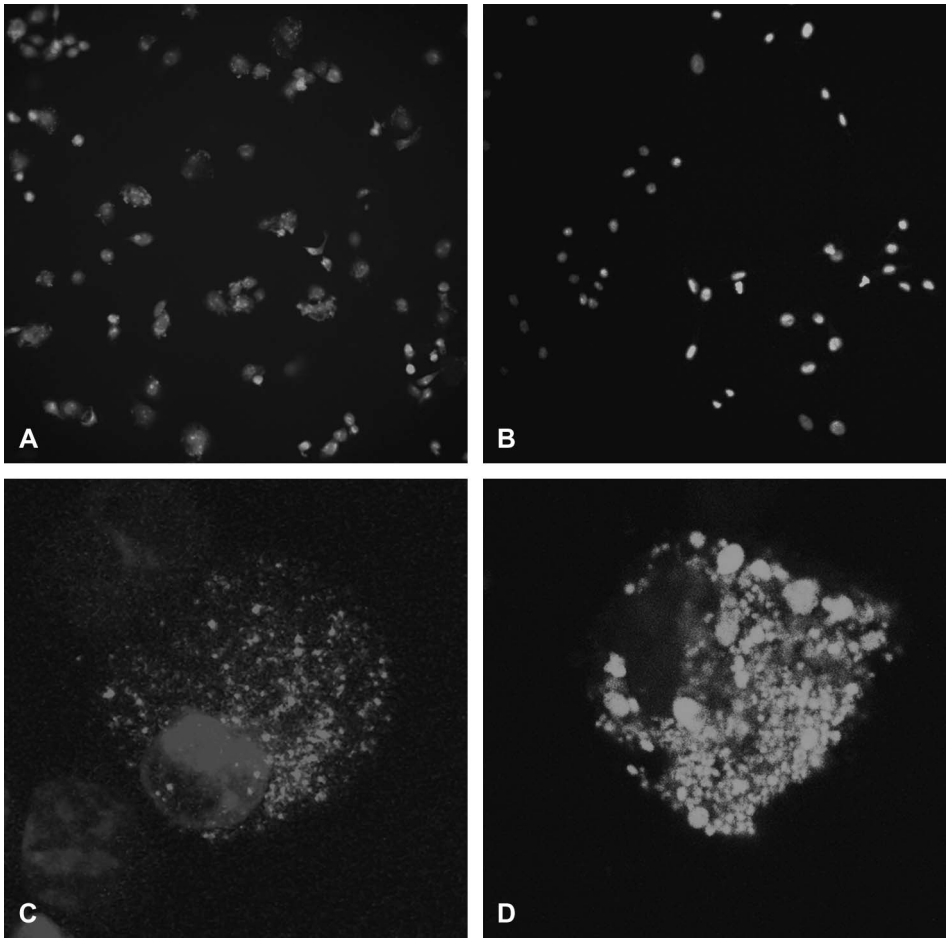

FIGURE 2. Cellular uptake of vesicles and substance release. A, Uptake of 4 nmol/L labeled ligand-functionalized polymer vesicles (red) into THP-1 macrophages (nucleus is stained blue) was visualized by fluorescence microscopy. B, L6 skeletal muscle cells were exposed to 4 nmol/L labeled polymer vesicles. The muscle cells do not take up any fluorescence-labeled polymer vesicles. C, Detailed analysis of a single macrophage with confocal microscopy demonstrates the intracellular localization of a large amount of polymer vesicles. D, Green fluorescent calcein is released from polymer vesicles upon time-dependent biodegradation of the polymer membranes in THP-1 macrophages. The image shows the aspect after 24 h of incubation.

be found in intracellular compartments of macrophages, most probably endolysosomes (Fig. 2C).

Inhibition of Endocytotic Activity

Fluorescence-labeled acetylated LDL (ac-LDL) was used to determine the effect of vesicle-encapsulated pravastatin on the endocytotic activity of macrophages. When treated with pravastatin-containing polymer vesicles for 24 hours, the macrophages showed a decreased endocytotic activity compared to cells treated with empty vesicles and untreated cells (Fig. 3). The effect on the activity was dependent on the concentration of pravastatin and the ED50 (dosage that produces a significant reduction of endocytotic uptake in half of the cell population) was 0.25 μmol/L final pravastatin concentration in the cell culture medium (Fig. 4A). The same experiments were performed with the fluorescence-labeled oligonucleotide polyG as an activity marker. Here, the effect was comparable to ac-LDL and the ED50 was 0.15 μmol/L final pravastatin concentration in the cell culture medium (Fig. 4B). These results confirm the equivalence of polyG as a marker for macrophage endocytotic activity. The ED50 for ligand uptake inhibition with nonencapsulated pravastatin was 11 μmol/L (final concentration of pravastatin in the cell culture medium). Empty targeted polymer vesicles that did not contain any drugs did not influence the endocytotic competence of macrophages significantly (Fig. 4C), indicating that the observed effect of vesicle-encapsulated pravastatin is only caused by the drug itself and not by the polymeric carrier.

Substance Release Assay

To investigate the substance release properties of the polymer vesicles inside the macrophages, the calcein release assay was used (see Methods for details). Experiments with different time points showed that the polymer vesicles remained intact for as long as 6 to 12 hours inside the macrophages (Fig. 4D). Between 12 hours and 36 hours, there was a gradual increase of fluorescent signal, indicating a continuous release and deposition of the dye inside the cell (Fig. 2D). The results indicate further that the polymer vesicles are biodegradable and show sustained release properties, features that render the results gained in experiments with pravastatin-containing vesicles even more valuable.

Toxicity Assay

To explore possible toxic effects, we exposed standardized cell cultures of macrophages to high concentrations of both pravastatin-containing polymer vesicles and empty vesicles for 24 hours. After 24 hours, 63% (SD 19.6%) of

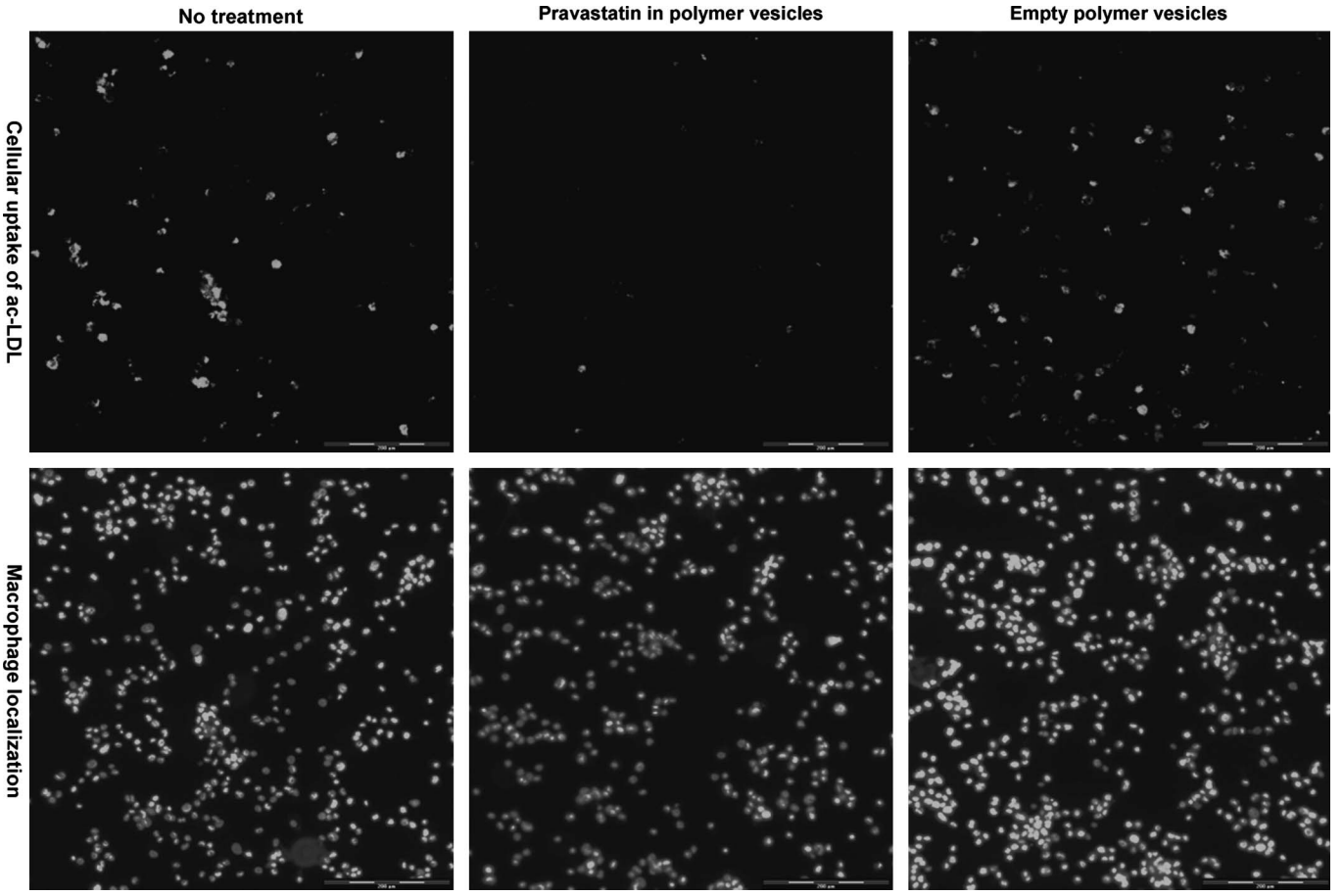

FIGURE 3. Inhibition of acLDL uptake into macrophages by pravastatin vesicles. Acetylated low density lipoproteins (ac-LDL) labeled with a green fluorescent dye were given to populations of THP-1 macrophages for 1 hour. The lower row shows the localization of the cells determined by nuclear staining. The upper row shows the presence of ac-LDL in untreated cells (left) and populations pretreated (for 24 h) with either 4 nmol/L pravastatin-containing polymer vesicles (middle) or 4 nmol/L empty polymer vesicles (right). In the untreated population, only about 20% of the cells take up significant amounts of ac-LDL, indicating an inhomogeneous endocytotic activity. Cells treated with pravastatin-containing vesicles show a clear decrease of ac-LDL uptake, whereas cells treated with the empty vesicles show only a minimal decrease of ac-LDL uptake. The images prove the inhibition of ac-LDL uptake into macrophages by pravastatin-containing polymer vesicles.

the untreated macrophages were vital, whereas cells treated with 10% ethanol showed a survival rate of 2.9% (SD 0.75%; $P < 0.01$, always versus untreated control). Treatment with a high concentration of 10 nmol/L polymer vesicles resulted in a survival rate of 54% (SD 15.2%; $P = 0.40$) for pravastatin-loaded vesicles and 57.9% (SD 16.7%; $P = 0.68$) for empty vesicles, respectively.

Cell cultures of rat skeletal muscle cells were incubated with free pravastatin or pravastatin-containing polymer vesicles to compare their effect on cell survival. Treatment with high concentrations of free pravastatin leads to significant acute toxic effects on the muscle cells in two different assays (Fig. 5). Viability decreased at concentrations of 2 to 3 times ED50, and at a concentration of 10-fold ED50 (corresponding to 110 μmol/L pravastatin in medium), only 12.5% (SD 6.4%; $P < 0.01$) of the cells remained viable after 24 hours. Ligand-functionalized polymer vesicles on the other hand lead to no significant increase in cell death up to 15-fold ED50.

DISCUSSION

We showed that receptor-targeted polymer vesicles can be used for safe encapsulation and highly efficient delivery of pravastatin and controlled intracellular release of encapsulated hydrophilic substances. With this novel delivery tool, it is possible to inhibit the endocytotic activity of macrophages defined by the uptake of known scavenger receptor ligands. With free pravastatin, the same effect can only be achieved with much higher doses that would lead to life-threatening side effects in humans. Polymer vesicles with or without encapsulated pravastatin exhibit no toxic effects in cell cultures in high concentrations and are known to be stable and target-specific drugs delivery tools. Due to their protein-repellent polymeric surface layer and specific ligand functionalization, the vesicles are only taken up by the desired target cell, but not by other cell types that might cause side effects in organisms.

After uptake into macrophages, the polymer vesicles are gradually degraded in intracellular compartments and release their encapsulated load in a time-dependent way. Released

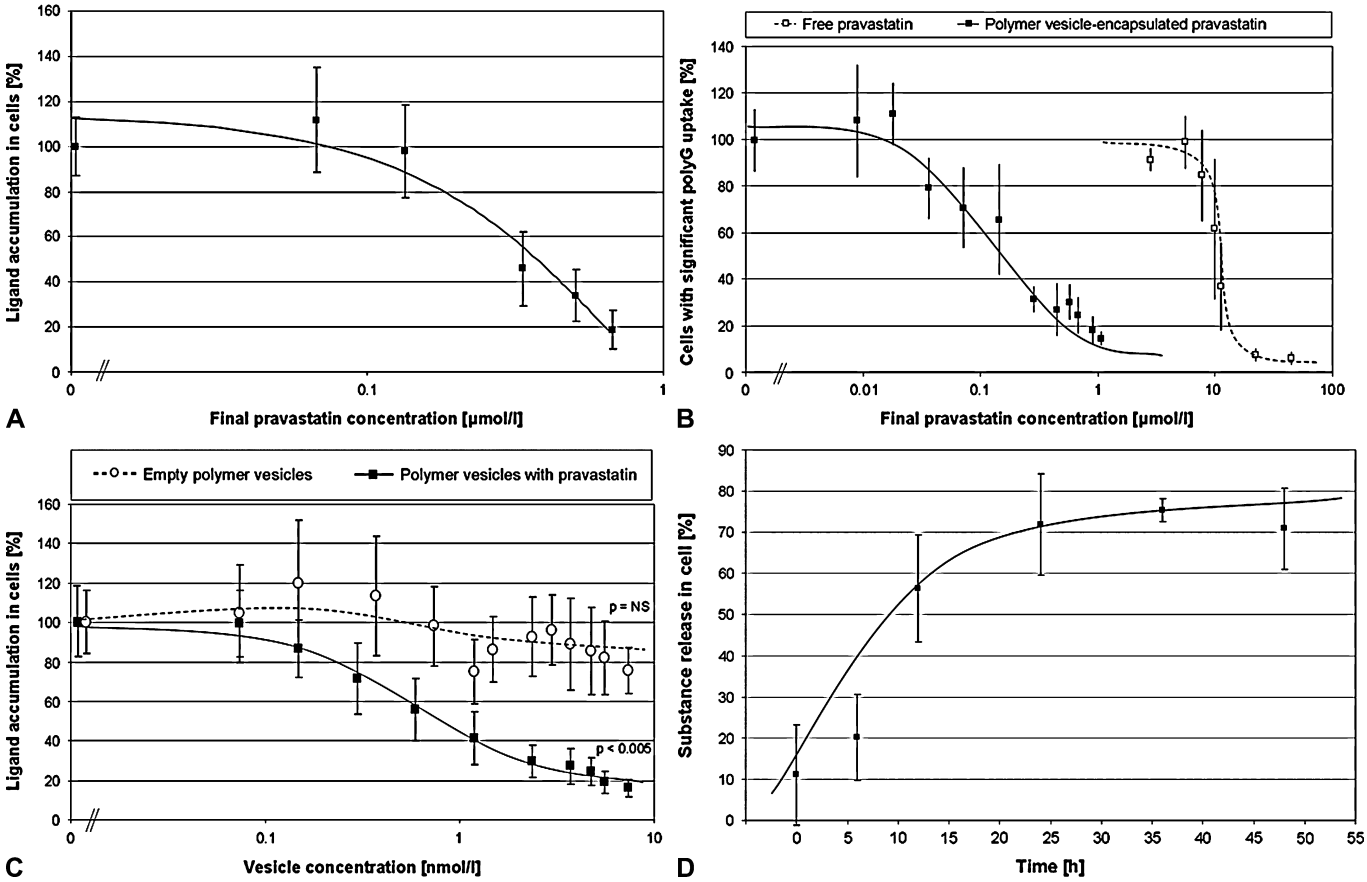

FIGURE 4. Inhibition of endocytotic activity and substance release. A, Quantification of the endocytosis inhibitory effect of pravastatin-containing polymer vesicles was performed with different drug concentrations. Macrophages with a significant (stronger than background) uptake of labeled ac-LDL were taken as quantification parameter. The necessary drug concentration to inhibit the endocytotic uptake of ac-LDL by 50% (ED50) is 0.25 μmol/L. B, The same experiment as in a) was repeated with the labeled oligonucleotide polyG instead of ac-LDL as an activity marker. For free pravastatin, ED50 is 11 μmol/L, whereas for the polymer vesicles containing pravastatin the ED50 is only 0.15 μmol/L. C, The effect on polyG uptake of pravastatin-containing polymer vesicles was compared to empty polymer vesicles. Pravastatin-containing polymer vesicles show again a strong inhibition of endocytotic activity, whereas empty vesicles exhibit no significant inhibitory effect on macrophage endocytosis. The results indicate that the inhibition of endocytotic activity is mainly due to the drug molecule and not due a blockade of scavenger receptors with the polymer vesicles. D, Release of self-quenching calcein from polymer vesicles inside the macrophages indicates the integrity of the vesicles. No fluorescence inside the cells indicates intact vesicles; strong green fluorescence indicates the disintegration of the vesicles and the controlled release of the hydrophilic content. After 6 hours of incubation, only few cells show fluorescence, whereas after 24 hours, almost 80% of the cells show significant fluorescence. The polymer vesicles are stable inside the cells for at least 6–12 hours and are degraded after 1 day. The encapsulated content is released in a controlled way. In graphs A–C, the number of untreated living cells was normalized to 1.0; the error bars represent the standard deviation over a series of experiments; curves represent the mathematical approximation to the data; in A–C, the x-axis is logarithmic.

drug molecules such as pravastatin reach instantly the cytosol and can exhibit strong effects on cell metabolism and immunological activity.

Until now, statins have scarcely been administered in controlled release or drug delivery formulations[27–29] due to their overall low toxicity when used in lipid-lowering concentrations. However, the application of higher doses seems to be profitable for the treatment of inflamed vulnerable plaques and is only limited by the adverse side effects. Encapsulation of extremely high doses of statins into target-specific polymeric vesicles promises to be useful for a selective inhibition of highly active macrophages in vulnerable plaques.

However, the current study has several important limitations that have to be investigated in future experiments. At the moment, the targeted polymer vesicles were only tested in cell cultures and there are no published results about the behavior of this type of polymer vesicles in animals. Crucial points for future experiments are in vivo targeting and biodistribution, biodegradability, efficacy, and short-term and long-term toxicity. Furthermore, in the current experimental setup, we only studied the effects of vesicle targeted pravastatin on the endocytotic activity of macrophages. In future, it will be interesting to see the effect of this treatment on cytokine production, cell motility, and survival and other important

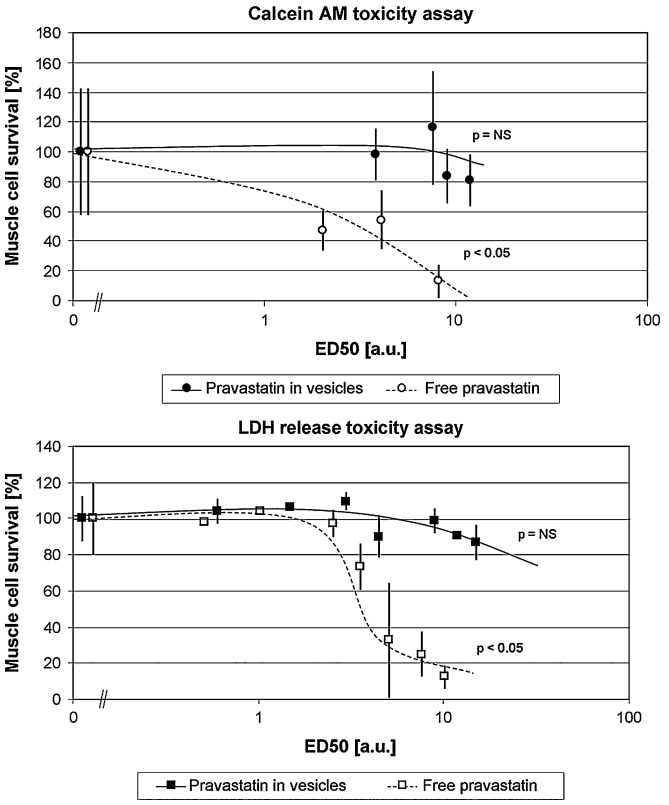

FIGURE 5. Cytotoxicity evaluation. Rat skeletal muscle cells were incubated with high concentrations of pravastatin-containing polymer vesicles or free pravastatin to determine toxic effects of the drug with two different assays (see Methods section for details). The free pravastatin shows strong acute toxic effects in concentrations necessary to inhibit macrophage endocytic activity with an estimated LD50 (dosage that induces cell death in half of the myocyte population) of 4 to 5 times ED50. The polymer vesicles containing encapsulated pravastatin on the other hand show no significant toxic effects in this assay even at concentrations up to 15 times ED50. (The number of untreated living cells was normalized to 1.0; curves represent the mathematical approximation to the data).

functions of macrophages that play crucial roles in the progression of vulnerable plaque inflammation and rupture.

Nevertheless, the current results build a strong basis of evidence that extremely high doses of statins that are targeted directly to macrophages might have hitherto unknown beneficial effects in vivo. The target specificity might help to increase the drug concentrations at sites such as the vulnerable plaques while sparing healthy tissues sensitive to the drug such as the skeletal muscle cells.

In future, this novel polymer vesicle based pravastatin formulation might be used in patients with a high load of vulnerable plaques in coronary or cranial arteries and may help to lower the inflammatory burden and prevent potentially deadly plaque ruptures.

REFERENCES

1. Libby P. Inflammation in atherosclerosis. *Nature*. 2002;420:868–874.
2. Casscells W, Naghavi M, Willerson JT. Vulnerable atherosclerotic plaque: A multifocal disease. *Circulation*. 2003;107:2072–2075.
3. Hansson GK. Inflammation, atherosclerosis, and coronary artery disease. *N Engl J Med*. 2005;352:1685–1695.
4. Fuster V, Badimon L, Badimon JJ, et al. The pathogenesis of coronary artery disease and the acute coronary syndromes (1). *N Engl J Med*. 1992; 326:242–250.
5. Fuster V, Badimon L, Badimon JJ, et al. The pathogenesis of coronary artery disease and the acute coronary syndromes (2). *N Engl J Med*. 1992; 326:310-318.
6. Fuster V, Lewis A. Conner Memorial Lecture. Mechanisms leading to myocardial infarction: insights from studies of vascular biology. *Circulation*. 1994;90:2126–2146.
7. Kwak B, Mulhaupt F, Myit S, et al. Statins as a newly recognized type of immunomodulator. *Nat Med*. 2000;6:1399–1402.
8. Ni W. Antiinflammatory and antiarteriosclerotic actions of HMG-CoA reductase inhibitors in a rat model of chronic inhibition of nitric oxide synthesis. *Circ Res*. 2001;89:415–421.
9. Ray KK, Cannon CP. Early time to benefit with intensive statin treatment: could it be the pleiotropic effects? *Am J Cardiol*. 2005;96:54–60.
10. Lewis SJ. Effect of pravastatin on cardiovascular events in older patients with myocardial infarction and cholesterol levels in the average range: Results of the cholesterol and recurrent events (CARE) trial. *Ann Intern Med*. 1998;129:681–689.
11. Sakai M. HMG-CoA reductase inhibitors suppress macrophage growth induced by oxidized low density lipoprotein. *Atherosclerosis*. 1997;133: 51–59.
12. Takemoto M, Liao JK. Pleiotropic effects of 3-hydroxy-3-methylglutaryl coenzyme a reductase inhibitors. *Arterioscler Thromb Vasc Biol*. 2001;21: 1712–1719.
13. Mach F. Statins as immunomodulatory agents. *Circulation*. 2004;109: II15–II17.
14. Bellosta S. HMG-CoA reductase inhibitors reduce MMP-9 secretion by macrophages. *Arterioscler Thromb Vasc Biol*. 1998;18:1671–1678.
15. Cannon CP, Steinberg BA, Murphy SA, et al. Meta-analysis of cardiovascular outcomes trials comparing intensive versus moderate statin therapy. *J Am Coll Cardiol*. 2006;48:438–445.
16. Cannon CP. Intensive versus moderate lipid lowering with statins after acute coronary syndromes. *N Engl J Med*. 2004;350:1495–1504.
17. Baccante G. Pravastatin up-regulates transforming growth factor-[beta]1 in THP-1 human macrophages: effect on scavenger receptor class A expression. *Biochem Biophys Res Commun*. 2004;314:704–710.
18. Jacobson TA. Comparative pharmacokinetic interaction profiles of pravastatin, simvastatin, and atorvastatin when coadministered with cytochrome P450 inhibitors. *Am J Cardiol*. 2004;94:1140–1146.
19. Jacobson TA. The safety of aggressive statin therapy: how much can low-density lipoprotein cholesterol be lowered? *Mayo Clin Proc*. 2006;81: 1225–1231.
20. Broz P. Cell targeting by a generic receptor-targeted polymer nanocontainer platform. *J Control Release*. 2005;102:475–488.
21. Broz P. Toward intelligent nanosize bioreactors: A pH-switchable, channel-equipped, functional polymer nanocontainer. *Nano Lett*. 2006;6:2349–2353.
22. Discher DE, Eisenberg A. Polymer vesicles. *Science*. 2002;297:967–973.
23. Rigler P, Meier W. Encapsulation of fluorescent molecules by functionalized polymeric nanocontainers: investigation by confocal fluorescence imaging and fluorescence correlation spectroscopy. *J Am Chem Soc*. 2006;128:367–373.
24. Kaufmann P. Toxicity of statins on rat skeletal muscle mitochondria. *Cell Mol Life Sci*. 2006;63:2415–2425.
25. Nardin C, Hirt T, Leukel J, et al. Polymerized ABA triblock copolymer vesicles. *Langmuir*. 2000;16:1035–1041.
26. Vellonen KS, Honkakoski P, Urtti A. Substrates and inhibitors of efflux proteins interfere with the MTT assay in cells and may lead to underestimation of drug toxicity. *Eur J Pharm Sci*. 2004;23:181–188.
27. Winkler K. Effect of fluvastatin slow-release on low density lipoprotein (LDL) subfractions in patients with type 2 diabetes mellitus: Baseline LDL profile determines specific mode of action. *J Clin Endocrinol Metab*. 2002;87:5485–5490.
28. Lukacsko P, Walters EJ, Cullen EI, et al. Efficacy of once-daily extended release lovastatin as compared to immediate-release lovastatin in patients with hypercholesterolemia. *Curr Med Res Opin*. 2004;20:13–18.
29. Bays HE. Comparison of once-daily, niacin extended-release/lovastatin with standard doses of atorvastatin and simvastatin [the advicor versus other cholesterol-modulating agents trial evaluation (ADVOCATE)]. *Am J Cardiol*. 2003;91:667–672.

2.4.6 Functionalized Nanocompartments (Synthosomes) with a Reduction-Triggered Release System

DOI: 10.1002/anie.200801076

Protein Modifications

Functionalized Nanocompartments (Synthosomes) with a Reduction-Triggered Release System**

*Ozana Onaca, Pransenjit Sarkar, Danilo Roccatano, Thomas Friedrich, Bernard Hauer, Mariusz Grzelakowski, Arcan Güven, Marco Fioroni, and Ulrich Schwaneberg**

Biologically derived compartments are constrained in design by their biological functions to ensure life at ambient temperature. Polymer vesicles can be designed to match application demands, such as mechanical stability, organic solvent, substrate and product tolerance, and permeation resistance, that are out of reach for biologically derived vesicles.[1] Synthosomes use, in contrast to polymersomes, a transmembrane channel for controlling the in and out compound fluxes. The block copolymers in synthosomes prevent compound penetration through the polymer shell, whereas polymersomes depend on the diffusion of substrate and product molecules through the polymer shell.

The main advantage of synthosomes over polymersomes is that, through protein engineering, it is possible to design functionalized protein channels. A protein channel that can function as an on/off switch offers opportunities for the design of functional nanocompartments with potential applications in synthetic biology (pathway engineering), medicine (drug release), and industrial biotechnology (chiral nanoreactors, multistep syntheses, bioconversions in nonaqueous environments, and selective product recovery).

The channel proteins FhuA,[2] OmpF,[3–5] and Tsx[6] have been incorporated, in functional active form, into block-copolymer membranes. FhuA, ferric hydroxamate uptake protein component, is a large monomeric transmembrane protein of 714 amino acids folded into 22 antiparallel β strands and made up of two domains. Crystal structures of FhuA have been resolved,[7,8] and a large passive diffusion channel (FhuA Δ1–160) was designed by removing a capping globular domain (deletion of amino acids 5–160).[9,10] FhuA and Tsx were crystallized as monomers and OmpF as a trimer. FhuA and its engineered variants have a significantly wider channel than OmpF (OmpF ≈ 27–38 Å, FhuA ≈ 39–46 Å)[11] and this allows even the translocation of single-stranded DNA.[12]

The aim and novelty of our work is the introduction of a triggering system, by means of a reduction-triggered "release switch" based on an engineered FhuA channel variant. To the best of our knowledge, in none of the reported triggered systems, was a channel protein employed as a switch.

In fact, for polymersomes, a pH trigger,[13] a temperature-assisted pH trigger,[14] and a combined pH/salt trigger[15,16] have been developed. Furthermore, hydrogen peroxide generation was used for polymer-vesicle degradation by glucose oxidase catalyzing glucose oxidation,[17] and a pH-triggered release system for a polypeptide vesicle has been reported.[18] For synthosomes, the activation of an encapsulated phosphatase after a change in the pH value has been reported.[19]

To build up a reduction-triggered release system in synthosomes, the amino-group-labeling agents 3-(2-pyridyldithio)propionic acid *N*-hydroxysuccinimide ester (pyridyl label) and (2-[biotinamido]ethylamido)-3,3′-dithiodipropionic acid *N*-hydroxysuccinimide ester (biotinyl label) were selected, due to size considerations and the presence of a cleavable disulfide bond within the labeling reagents. Reagents for the specific labeling of amino, hydroxy, carboxyl, and sulfhydryl groups have been well studied and are routinely used for protein modifications.[20–22]

The synthosome calcein release system proposed herein is a triggered release system in which the entrapped compound (calcein) is liberated through an engineered transmembrane channel (FhuA Δ1–160) upon addition of a reducing agent. Interestingly, label size played an important role in calcein release. A detection protocol for calcein release from liposomes through wild-type FhuA and FhuA Δ1–160 has been reported.[2] The liposomes were loaded with calcein at a self-quenching concentration (50 mM) and calcein release was achieved by addition of wild-type FhuA and FhuA Δ1–160. The fluorescence generation upon calcein release was used to record the release kinetics.

In order to build a reduction-triggered release system, the amino groups of lysine residues in FhuA Δ1–160 were modified with either a pyridyl or a biotinyl label (see above). Figure 1 illustrates the reactions for FhuA Δ1–160 with eight lysine residues (L167, L226, L344, L364, L455, L537, L556, and L586) chemically modified with pyridyl (left) or biotinyl labels (right).

Upon disulfide-bond reduction with DTT, a 3-thiopropionic amide group remains on the lysine residues of the FhuA Δ1–160 with both labels (Figure 1, upper part). Details

[*] Dr. O. Onaca, P. Sarkar, Dr. D. Roccatano, A. Güven, Dr. M. Fioroni, Prof. Dr. U. Schwaneberg
School of Engineering and Science, Jacobs University Bremen
Campus Ring 8, 28759 Bremen (Germany)
Fax: (+49) 421-200-3543
E-mail: u.schwaneberg@jacobs-university.de
Dr. T. Friedrich, Prof. Dr. B. Hauer
BASF AG, Fine Chemicals and Biocatalysis Research
GVF/D-A030, 67056 Ludwigshafen (Germany)
M. Grzelakowski
Department of Chemistry, University of Basel
Klingelbergstrasse 80, 4056 Basel (Switzerland)

[**] We thank BASF AG and the State of Bremen (SfBW award FV 161) for financial support. We are grateful to Prof. Dr. Werner Nau and his co-workers for assisting in the short-time fluorescence and dichroic measurements.

Supporting information for this article is available on the WWW under http://dx.doi.org/10.1002/anie.200801076.

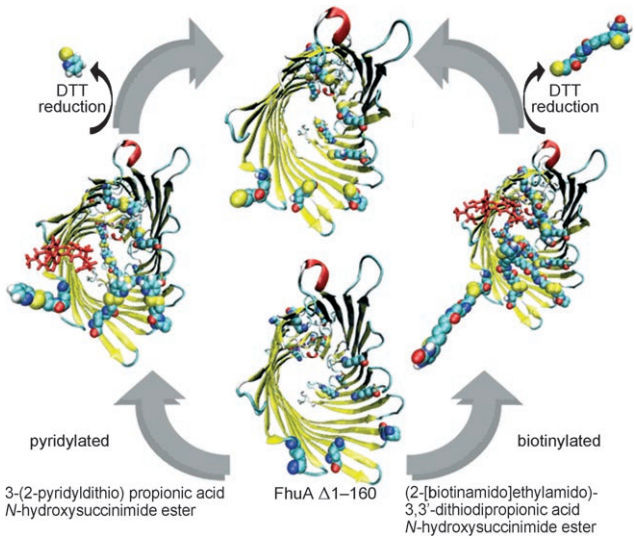

Figure 1. Reduction-triggered release system based on transmembrane channel FhuA Δ1–160. FhuA Δ1–160 is chemically modified with pyridyl or biotinyl labels at lysine residues in the barrel interior and at the rim. The translocation of the calcein molecule (red) through the pyridylated or biotinylated FhuA Δ1–160 is sterically hindered. Upon reduction with 1,4-dithio-D,L-threitol (DTT), the disulfide bond in the linker of the pyridyl or biotinyl label is broken and this results in calcein release. The FhuA Δ1–160 model was prepared from the crystal structure (Protein Data Bank entry: 1BY3) and all lysine residues have been labeled in the model. Further details can be found in the Supporting Information.

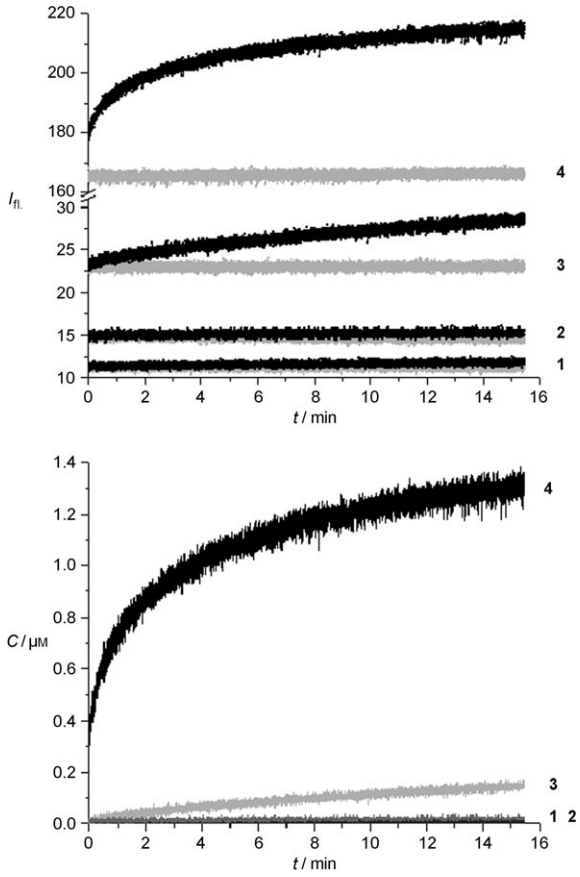

Figure 2. Upper panel: For the recording of the calcein-release kinetics, quadruple sets of data were measured and averaged in all four experiments. For each experiment, a data set with and without DTT addition was recorded for nanocompartments loaded with 50 mM calcein. Each experiment is specified by a number (1–4): 1) Nanocompartments without FhuA Δ1–160 before (——) and after (——) DTT addition; 2) synthosomes harboring FhuA Δ1–160 before (——) and after (——) DTT addition; 3) biotinylated FhuA Δ1–160 synthosomes before (——) and after (——) DTT addition; 4) pyridylated FhuA Δ1–160 synthosomes before (——) and after (——) DTT addition. Lower panel: calcein release in micromolar concentrations upon DTT reduction as calculated from the results in the upper panel: 1) Nanocompartments without (——) and 2) with (——) FhuA Δ1–160, 3) biotinyl-labeled FhuA Δ1–160 (——), and 4) pyridyl-labeled FhuA Δ1–160 (——).

of the chemistry of the pyridyl and biotinyl labeling of FhuA Δ1–160, the protein stability, vesicle dimensions, and FhuA Δ1–160 model generation can be found in the Supporting Information. The top view of the FhuA Δ1–160 channel in Figure 1 provides an impression of how the pyridyl and biotinyl labels restrict translocation after the lysine modification, especially the sterically more demanding biotinyl label. Figure 1 clearly shows how the transmembrane channel might open up after DTT-induced release of the pyridyl and biotinyl labels. However, the FhuA Δ1–160 models do not take into account the possible channel dynamics that have been recorded by conductance measurements.[10]

Figure 2 shows the calcein-release kinetics (upper panel) and the absolute calcein concentrations (lower panel) in the synthosomes before and after addition of the reduction trigger (DTT). There is no detectable calcein release before and after DTT addition in absence of the FhuA Δ1-160 (Figure 2, data set 1). In the case of the unlabeled FhuA Δ1–160, one would expect that the calcein would translocate through FhuA Δ1–160 as previously shown,[2] and it is therefore lost during synthosome purification (Figure 2, data set 2). For the biotinyl-labeled FhuA Δ1–160, a linear release kinetic is observed after DTT reduction. A greater than 30-fold faster and exponential initial calcein release is observed upon reduction of the less bulky pyridyl label, which leads to the same 3-thiopropionic amide labeled FhuA Δ1–160 (Figure 1). The strong size dependence of the initial release kinetics indicates that the biotinyl labels stay bound to the FhuA Δ1–160 channel upon DTT reduction. Interestingly, after approximately six minutes, the release kinetics reached a nearly constant increase for both labels, and this increase remained constant for 2 h (data not shown). The release kinetics trend is characteristic of passive diffusion processes and can be modeled by the monoexponential defined in Equation (1),[23] in which C is the calcein concentration versus time (t) and $P1$, $P2$, and $P3$ are fitting constants (Figure 2; Table 1).

$$C = -P1\exp\left(-\frac{t}{P2}\right)+P3 \qquad (1)$$

Constant $P1$ depends on the calcein concentration gradient inside and outside of the nanocompartments in the bulk suspension (Table 1). The significantly higher values for the pyridyl-labeled FhuA Δ1–160 channel (28.53 μ for pyridyl versus 7.24 μ for biotinyl) can be attributed to FhuA Δ1–160

Table 1: *P*1, *P*2, and *P*3 constants from Equation (1), calculated by fitting the recorded release kinetics data (Figure 2).

Nanocompartment system	*P*1 [μM][a]	*P*2 [min][a]	*P*3[a]
nanocompartments without FhuA Δ1–160	–	–	11.58
synthosomes with FhuA Δ1–160	–	–	14.53
synthosomes with FhuA Δ1–160 and biotinyl label	7.24	13.88	23.76
synthosomes with FhuA Δ1–160 and pyridyl label	28.53	3.99	165.72

[a] Further details given in the text.

limited diffusion because the employed samples were analyzed after purification with a Zeta-Sizer and, in quantity, were normalized by elution areas. The *P*2 value represents the time constant of the calcein-release process and describes the efflux from the nanocompartment sample through the FhuA Δ1–160 channel protein (Table 1); it is dependent on the number of FhuA Δ1–160 molecules per nanocompartment, the channel properties (size, charge, dynamics, chemical labeling), and the DTT concentrations. Upon unblocking, pyridyl-labeled FhuA Δ1–160 shows a time constant (3.99 min) that is four times shorter than that of biotinyl-labeled FhuA Δ1–160 (13.88 min). Apart from the labeled amino groups, all other factors were identical and, therefore, differences are directly connected to the nature of the labeling reagents. The *P*3 constant describes the background fluorescence of the nanocompartment systems (Table 1). The significantly higher background values for the pyridyl-labeled FhuA Δ1–160 channel (Figure 2) can be attributed to a slow release of calcein during storage. The pyridyl-labeled FhuA Δ1–160 suspension shows a calcein fluorescence buildup after storage overnight, which is in contrast to the biotinyl-labeled FhuA Δ1–160 suspension. A 4 h incubation period after DTT addition results in a further increase in the absolute fluorescence difference of less than 15% for both pyridyl- and biotinyl-labeled FhuA Δ1–160 synthosomes.

At the moment, it is unknown which lysine residue(s) is (are) decisive for blocking the calcein translocation in pyridyl- and biotinyl-labeled FhuA Δ1–160. The biotinylation degree found per single FhuA Δ1–160 molecule is 3.6 (see the Supporting Information). Over the 29 lysines contained in FhuA Δ1–160, 19 are on the protein surface which might be covered by detergent; and probably not avoidable to biotinylation. Another six are located in the channel interior and only four are on the channel rim. It is reasonable that the biotinylation occurs on the latter group because they are more accessible to the reagent. Future investigations by lysine-site-specific mutagenesis and modeling studies will shed light onto this problem.

In summary, a synthosome reduction-triggered release system with an engineered and chemically labeled FhuA Δ1–160 channel has been developed and validated by calcein release. Two labeling reagents of different sizes have been used. The release kinetics of calcein were strongly modulated by the size of the lysine-labeling reagents. In general, such on/off switches would be of high value for controlling and modulating cellular biosynthetic pathways and might become attractive for applications in the pharmaceutical and/or chemical industries. In ongoing studies, we aim to generate a reversible switch by chemically "remodifying" the free sulfhydryl groups that are formed upon reduction in the FhuA Δ1–160 transmembrane channel protein.

Received: March 5, 2008
Published online: August 4, 2008

Keywords: controlled release · polymers · proteins · synthosomes · transmembrane channels

[1] O. Onaca, M. Nallani, S. Ihle, A. Schenk, U. Schwaneberg, *Biotechnol. J.* **2006**, *1*, 795.
[2] M. Nallani, S. Benito, O. Onaca, A. Graff, M. Lindemann, M. Winterhalter, W. Meier, U. Schwaneberg, *J. Biotechnol.* **2006**, *123*, 50.
[3] W. Meier, C. Nardin, M. Winterhalter, *Angew. Chem.* **2000**, *112*, 4747; *Angew. Chem. Int. Ed.* **2000**, *39*, 4599.
[4] C. Nardin, J. Widmer, M. Winterhalter, W. Meier, *Eur. Phys. J. E* **2001**, *4*, 403.
[5] A. Ranquin, W. Versees, W. Meier, J. Steyaert, P. Van Gelder, *Nano Lett.* **2005**, *5*, 2220.
[6] J. Ye, B. van den Berg, *EMBO J.* **2004**, *23*, 3187.
[7] A. D. Ferguson, V. Braun, H. P. Fiedler, J. W. Coulton, K. Diederichs, W. Welte, *Protein Sci.* **2000**, *9*, 956.
[8] A. D. Ferguson, E. Hofmann, J. W. Coulton, K. Diederichs, W. Welte, *Science* **1998**, *282*, 2215.
[9] M. Braun, H. Killmann, V. Braun, *Mol. Microbiol.* **1999**, *33*, 1037.
[10] M. Braun, H. Killmann, E. Maier, R. Benz, V. Braun, *Eur. J. Biochem.* **2002**, *269*, 4948.
[11] R. Koebnik, K. P. Locher, P. Van Gelder, *Mol. Microbiol.* **2000**, *37*, 239.
[12] M. Nallani, O. Onaca, N. Gera, K. Hildenbrand, W. Hoheisel, U. Schwaneberg, *Biotechnol. J.* **2006**, *1*, 828.
[13] F. Checot, J. Rodriguez-Hernandez, Y. Gnanou, S. Lecommandoux, *Biomol. Eng.* **2007**, *24*, 81.
[14] F. Ahmed, R. I. Pakunlu, G. Srinivas, A. Brannan, F. Bates, M. L. Klein, T. Minko, D. E. Discher, *Mol. Pharm.* **2006**, *3*, 340.
[15] M. Sauer, W. Meier, *Chem. Commun.* **2001**, *36*, 55.
[16] U. Borchert, U. Lipprandt, M. Bilang, A. Kimpfler, A. Rank, R. Peschka-Suss, R. Schubert, P. Lindner, S. Forster, *Langmuir* **2006**, *22*, 5843.
[17] A. Napoli, M. J. Boerakker, N. Tirelli, R. J. M. Nolte, N. A. J. M. Sommerdijk, J. A. Hubbell, *Langmuir* **2004**, *20*, 3487.
[18] E. G. Bellomo, M. D. Wyrsta, L. Pakstis, D. J. Pochan, T. J. Deming, *Nat. Mater.* **2004**, *3*, 244.
[19] P. Broz, S. Driamov, J. Ziegler, N. Ben-Haim, S. Marsch, W. Meier, P. Hunziker, *Nano Lett.* **2006**, *6*, 2349.
[20] J. Carlsson, H. Drevin, R. Axen, *Biochem. J.* **1978**, *173*, 723.
[21] B. G. Davis, *Curr. Opin. Biotechnol.* **2003**, *14*, 379.
[22] H. J. Schramm, T. Dulffer, *Adv. Exp. Med. Biol.* **1977**, *86A*, 197.
[23] P. Macheras, A. Iliadis, *Modeling in Biopharmaceutics, Pharmacokinetcs and Pharmacodynamics: Homogeneous and Heterogeneous Approaches*, *Vol. 30*, Springer, New York, **2006**.

2.4.7 Monolayer Interactions between Lipids and Amphiphilic Block Copolymers

Monolayer Interactions between Lipids and Amphiphilic Block Copolymers

Katarzyna Kita-Tokarczyk[a,*], Fabian Itel[b], Mariusz Grzelakowski[a], Stefan Egli[a], Peggy Rossbach[c], Wolfgang Meier[a,*]

[a] University of Basel, Department of Chemistry, Klingelbergstrasse 80, 4056 Basel, Switzerland
[b] University of Basel, Swiss Nanoscience Institute, Klingelbergstrasse 82, 4056 Basel, Switzerland
[c] Swiss Federal Laboratories for Materials Testing and Research (Empa), Nanoscale Materials Science, Überlandstrasse 129, 8600 Dübendorf, Switzerland

* corresponding authors: k.kita@unibas.ch; phone: +41 61 2673832; fax: +41 61 2673855; wolfgang.meier@unibas.ch; phone: +41 61 2673802; fax: +41 61 2673855

Abstract

Interactions in binary mixed monolayers from lipids: 1,2-dipalmitoyl-*sn*-glycero-3-phosphocholine (DPPC) and 1,2-dioleoyl-*sn*-glycero-3-phosphocholine (DOPC), and amphiphilic poly-(2-methyloxazoline)-*block*-poly-(dimethylsiloxane)-*block*-poly-(2-methyloxazoline) block copolymers were studied using the Langmuir balance technique and Brewster angle microscopy. It is shown that monolayers from the saturated lipid (DPPC) are more sensitive to the presence of polymers in the film, resulting in phase separation and the formation of pure lipid domains at high surface pressure. The morphology and composition of such phase separated lipid-polymer films were studied by fluorescence microscopy and ToF-SIMS. In contrast, in DOPC-containing monolayers, the polymers tend to phase-separate at low surface pressures only and homogeneous films are obtained upon further compression, due to higher lipid fluidity. The analysis of excess energy of mixing shows, that while the separation effect in densely packed DPPC-containing films is strongly dependent on the polymer size (with the larger polymer having a much stronger influence), in the case of monolayers with DOPC much smaller effects are observed. The results are discussed in terms of the monolayer composition, lipid fluidity and polymer size.

1. Introduction

Self-assembly properties of amphiphilic block copolymers make them an emerging platform for applications in biosciences. In particular, similarly to small amphiphiles, they aggregate in solution, the process being controlled, among others, by the polymer chemistry and block size [1]. So far, sub-micrometer sized structures like micelles and vesicles were studied in the context of drug delivery [2-5]. Micelles and vesicular membranes are preferentially used to host hydrophobic drugs, while the aqueous cavities of the vesicles encapsulate water-soluble drugs. Literature data show, that drug-loaded self-assemblies (vesicles) are able to enter cells and release their cargo [6], which subsequently leads to effects such as tumor size decrease [7]. All those phenomena involve the vesicle integration with cells: at some stage of that process the vesicular membrane will come into close contact with a cellular membrane (either outside or inside the cell) and interactions between the two membranes can

be expected. This process may be critical for the drug delivery process and depending on the synergy / antagonism between the cell membrane components and the polymeric amphiphile may lead to stabilization or disruption of the cell membrane. Therefore, it is important to study the membrane interactions in such mixed lipid-polymer systems, in order to optimize the delivery vehicles and avoid unwanted effects on the cell membranes.

The goal of our work was to investigate interactions between lipids and amphiphilic block copolymers by a monolayer technique. This method allows for simultaneous monitoring of the morphology of spread films (by Brewster angle microscopy) and energetic effects associated to the mixing / demixing phenomena in two-dimensional binary systems. This is, to our best knowledge, the first report presenting the behavior of mixed assemblies consisting of natural (lipid) and artificial (polymer) components. Earlier work in this field essentially focused on lipid-lipid interactions [8] and influence of soluble surfactants [9, 10] and insoluble amphiphiles [11] on lipid monolayers.

Concerning adsorption of polymers to lipid Langmuir monolayers, those systems are different from the one studied here. In particular, partitioning of a surfactant between a monolayer and solution (subphase) depends on the surface pressure, and at high lipid packing density the equilibrium will be well shifted towards solution due to steric hindrance. This way, the amount of polymer in the film cannot exceed a certain limiting value, dependent on the initial polymer concentration and surface pressure. In this manuscript, we use amphiphilic polymers, which build stable Langmuir monolayers on their own – therefore, the lipid to polymer ratio can be changed freely. Moreover, to our best knowledge, this is the first report presenting quantitative data on phase separation in spread lipid-polymer films.

Certain literature evidence exists concerning the behavior of amphiphilic block copolymers at the air-water interface. In particular, monolayer characterizations were presented of poly(ethyl acrylate)-*block*-poly(styrene) [12], poly(ethylene oxide)-*block*-poly(styrene) (and their pH-controlled interpolymer complexes with poly(acrylic acid) in the subphase) [13], poly(ethyl ethylene)-*block*-poly(ethylene oxide) [14], poly(ethylene oxide)-*block*-poly(butylenes oxide) [15] and polystyrene-*block*-poly(ethylene oxide) [16]. Molecular orientation of hydrophobic polyleucine helices of polyleucine-*block*-poly(ethylene oxide) at the air-water interface was analyzed by FT-IR and circular dichroism on Langmuir-Blodgett films [17]. Eisenberg et al. investigated interfacial micelle formation from block polyelectrolytes [18].Finally, the monolayer behavior of poly-(2-methyloxazoline)-*block*-poly-(dimethylsiloxane)-*block*-poly-(2-methyloxazoline), PMOXA-PDMS-PMOXA, block copolymers was described in the context of monolayer interactions with alamethicin, an amphiphilic peptide [19].

PMOXA-PDMS-PMOXA polymers spread at the air-water interface from organic solvents to produce fluid, yet exceptionally stable monolayers. The detailed analysis of monolayer phases shows a possibility of conformational transitions in the PDMS block, which are mostly responsible for film fluidity. Depending on the polymer size, these rearrangements are reflected in an extensive plateau region in surface pressure-area isotherms. It was also shown [19], that such polymers are able to rearrange to adapt to the presence of more rigid species in the film (like peptide helices), without large energetic expenses.

In this work, we analyzed monolayer interactions between two PMOXA-PDMS-PMOXA polymers (with distinctly different molar masses) and two lipids, 1,2-dipalmitoyl-*sn*-glycero-3-phosphocholine (DPPC) and 1,2-dioleoyl-*sn*-glycero-3-phosphocholine (DOPC). The lipids were

chosen based on differences in their monolayer packing, i.e. DPPC, being saturated, tends to form liquid crystalline monolayers, while DOPC, containing double bonds, forms condensed liquid films. We compare the monolayer morphology at different surface pressures depending on the lipid-polymer ratio in the film and discuss the energetic effects related to monolayer mixing / phase separation and their dependence on the lipid structure (fluidity) and the polymer size.

2. Materials and Methods

Block copolymers were synthesized and purified as described previously [20]. We used two symmetric poly-(2-methyloxazoline)-*block*-poly-(dimethylsiloxane)-*block*-poly-(2-methyloxazoline) copolymers: $PMOXA_{15}$-$PDMS_{110}$-$PMOXA_{15}$, further referred to as $A_{15}B_{110}A_{15}$ (mass 10700 g/mol, polydispersity index 1.62), and $PMOXA_{65}$-$PDMS_{165}$-$PMOXA_{65}$, further referred to as $A_{65}B_{165}A_{65}$ (mass 23200 g/mol, polydispersity index 1.63). For visualization of polymer phases in $A_{15}B_{110}A_{15}$-containing monolayers, we used up to 5 mole % of an analogous polymer, $A_{10}B_{85}A_{10}$ (mass 7200 g/mol), covalently labeled with sulforhodamine B (SRB) [21]. 1,2-Dipalmitoyl-*sn*-glycero-3-phosphocholine (DPPC, M = 734.05 g/mol), 1,2-dioleoyl-*sn*-glycero-3-phosphocholine (DOPC, M = 786.15 g/mol) and fluorescent 1-palmitoyl-2-[12-[(7-nitro-2-1,3-benzoxadiazol-4-yl)amino]dodecanoyl]-*sn*-glycero-3-phosphocholine (NBD-PC, M = 856.05 g/mol) were purchased from Avanti Polar Lipids, Inc. as chloroform solutions.

Polymer and lipid solutions were prepared using HPLC-grade chloroform (Sigma Aldrich). Langmuir troughs were cleaned with HPLC-grade chloroform, ethanol purum ≥ 99.8% (Sigma Aldrich) and bi-distilled water, and the barriers were washed with ethanol and bi-distilled water. Langmuir monolayers were spread on bi-distilled water subphase. Silicon surfaces were cleaned in hot 'piranha' solution (concentrated hydrogen peroxide / sulphuric acid, 1:1 v/v) for 10 minutes, rinsed with bi-distilled water and dried with nitrogen. Glass microscopy slides were washed with ethanol, bi-distilled water and dried under a nitrogen stream.

Monolayers were investigated with a KSV Inc. (Finland) Langmuir Teflon ™ trough, area 420 cm^2, equipped with two symmetric, hydrophilic Delrin ™ barriers, and a Wilhelmy plate (ashless filter paper, perimeter 20 mm) surface pressure sensor, accuracy of 0.1 mN/m. The trough was housed in a plastic cabinet to prevent dust contaminations, in an air-conditioned lab (20^0C). Before spreading a film, the cleanliness of the subphase was carefully checked by recording surface pressure of clean water and monitoring the surface by Brewster angle microscopy. Monolayers were spread drop-wise on the water surface as chloroform solutions (typically 0.5-1.0 mg/mL). The solvent was allowed to evaporate for 10 min, and the monolayers were compressed at the rate of 10 mm/min. After each measurement, the surface was cleaned and checked for impurities.

Monolayer transfers on solid substrates (silicon and glass) were performed by the Langmuir-Blodgett (LB) technique, using a KSV Inc. (Finland) mini-LB trough (area 242 cm^2), equipped with an identical surface pressure sensor as the large Langmuir trough. Prior to film spreading, the substrate was dipped down and the water surface was checked for impurities again (and cleaned if necessary). After compressing a film to a desired pressure, a monolayer was transferred upon dipper upstroke at 0.5 mm/min.

An EP^3 system (imaging ellipsometer and Brewster angle microscope, BAM) from Nanofilm, Göttingen, Germany, was used for monolayer visualization at the air-water interface and silicon wafers, as well as for film thickness determination. The EP^3 system, equipped with a Nd-YAG laser (532 nm), Nikon 20x objective, and monochrome CCD camera attached to real-time frame grabber was used, mounted over the Langmuir trough (or solid sample stage). Ellipsometry measurements on silicon were performed at the angle of incidence range from 40 to 70^0 in steps of 5^0 in four-zone mode, and fitted with an n_k_fix algorithm using database parameters for silicon and silicon oxide, and silicon oxide thickness of 2.2 nm, as determined independently. Best fits were obtained using the refractive index of the material equal to 1.2.

Fluorescence microscopy of monolayers transferred to glass surfaces was performed using a Leica DM-RP microscope. Fluorescence from SRB-labeled polymer was monitored at 586 nm, while from NBD-labeled DPPC at 534 nm.

ToF-SIMS measurements (Time of Flight - Secondary Ion Mass Spectrometry) were done using a ToFSIMS5 spectrometer from ION-TOF, Münster, Germany. We used Bi_3^{++} ions, energy of 25 kV, as primary ions for both spectra and imaging acquisition. All spectra (references and $A_{15}B_{110}A_{15}$-DPPC mixed film) were acquired with high mass resolution and characteristic peaks were identified for the DPPC and the polymer using negatively charged secondary ions. The imaging of the $A_{15}B_{110}A_{15}$-DPPC mixed monolayer was done in the so-called burst alignment mode, which gives very good lateral resolution (between 0.5 and 1 μm) at unit mass resolution in a reasonable acquisition time.

3. Results and Discussion

3.1 Monolayers from pure amphiphiles

Langmuir monolayers from lipids and triblock copolymers were measured first as reference systems. Since those compounds were extensively investigated earlier and literature data are available (DPPC [22, 23]; DOPC [24, 25], analogous block copolymers [19]), we present their surface pressure-area isotherms as supporting information (Figure S1), and shortly discuss the details most relevant for further experiments.

The main difference between DOPC and DPPC is the structure of alkyl chains, namely, DPPC contains two saturated hydrocarbon chains, while DOPC has one double bond in each chain. This structural difference influences the organization properties of the two lipids at the air-water interface (Figure S1 A). At room temperature, DPPC forms a liquid crystalline phase at surface pressure above 10 mN/m, manifested by an almost vertical slope of the isotherm, corresponding to mean molecular area of ca. 0.5 nm^2/molecule. On the other hand, the unsaturated DOPC chains lead to a less condensed Langmuir film, the isotherm of which is characterized by a smaller slope and the smallest molecular area to which the film can be compressed is considerably lower (ca. 0.7 nm^2/molecule at the collapse pressure) than in the case of DPPC (~0.45 nm^2/molecule). Thus, the monolayer can be described as more fluid, and no long-range crystalline packing of molecules can be observed.

Concerning the triblock copolymers (Figure S1 B), monolayer behavior of very similar polymers was discussed previously [19], and no major differences were observed here apart from changes in lift-off areas consistent with different molar masses of the investigated block copolymers.

For this work, we performed additional control experiments on $A_{15}B_{110}A_{15}$ and $A_{65}B_{165}A_{65}$ monolayers to investigate the influence of certain experimental conditions on the film behavior. In summary, our data show that the surface pressure-area isotherms are insensitive to the amount of material spread at the air-water interface, meaning that the material efficiently spreads to form monolayers, and also that the polymer does not dissolve in the subphase. Additionally, isotherms from block copolymers do not show any temperature dependence in the range from 10 to 35^0C, which confirms our previous conclusion [19] that the broad plateau region is not related to a first order phase transition, and can be attributed to conformational rearrangements of the polymer molecules. The isotherms are fully reversible upon multiple compression-expansion cycles - we could not observe any hysteresis, which means that the polymer does not dissolve in water, and also that the film elastically responds to area changes. We also monitored polymer film stability at constant area and at different surface pressures (from 5 to 45 mN/m), at 20^0C. Even at the highest surface pressure (45 mN/m), the films were excellently stable and maintained the pressure for longer than 30 minutes. This result is significant for our further LB film preparation, where the film stability is essential for successful transfers. The calculations of compressibility modulus for different phases of the polymer monolayers were also performed [19], from which we conclude that the polymer molecules are in a liquid state throughout the compression (C_s^{-1} ~ 40 - 50 mN/m), and no solid (crystalline) packing is observed.

3.2 Mixed systems $A_{15}B_{110}A_{15}$-DPPC and $A_{65}B_{165}A_{65}$-DPPC

In this section, we discuss the behavior of mixed monolayers containing a triblock copolymer ($A_{15}B_{110}A_{15}$ or $A_{65}B_{165}A_{65}$) and DPPC, at the whole range of the components' molar ratios. The monolayers were characterized by surface pressure-area isotherms and imaged with Brewster angle microscopy. Isotherm data were used to calculate excess free energy of mixing between the two components at low (7.5 mN/m) and high (25 mN/m) surface pressure.

Langmuir monolayers and Brewster angle microscopy

Figure 1 presents surface pressure-area isotherms from DPPC mixtures with $A_{15}B_{110}A_{15}$ (A) and $A_{65}B_{165}A_{65}$ (B), respectively, at different molar ratios. Obviously, the lift-off area of the films decreases stepwise with the addition of lipid. The $A_{15}B_{110}A_{15}$-containing system (Figure 1 A) displays equal decrease steps with the addition of lipid (i.e. when the molar ratio of DPPC increases), from polymer molar ratio of 1.0 to 0.2. For the mixtures with $A_{15}B_{110}A_{15}$ ratio of 0.2 and 0.1, a large gap is observed, which corresponds to the change of miscibility properties, as will be visualized later with BAM and showed by excess free energy calculations. A similar gap is also present for $A_{65}B_{165}A_{65}$-containing mixtures (Figure 1 B), this time for the $A_{65}B_{165}A_{65}$ molar ratio between 0.3 and 0.4. This shift, compared to the $A_{15}B_{110}A_{15}$, is explained by the size difference between the two polymers. If the large step in the lift-off area corresponds to a change of monolayer organization, it should be more pronounced at a yet smaller lipid ratio when a larger polymer is present in the system, as is indeed observed.

For all lipid-polymer mixtures, the characteristic plateau visible in DPPC isotherms (at 6-7 mN/m) disappears, indicating good polymer-lipid miscibility in the low surface pressure region. Such

behavior was observed before for mixtures of: polymers [26], aliphatic alcohols and polymers [27], and lipids and calixarenes [28]. On the other hand, the plateau present in isotherms from pure polymers (at 10 to 17 mN/m), and corresponding to the conformational rearrangement of the polymer chains, is still present in all isotherms from polymer-lipid mixtures. Due to a decreasing amount of polymer molecules with the addition of lipid, the span of the plateau decreases. Since this isotherm feature is not associated with a polymer first-order phase transition, its surface pressure should not be affected by the addition of a second component. Obviously, the lipid molecules may affect the packing and chain rearrangements of the macromolecules, however, given the large difference in size between the lipid and the polymer (one order of magnitude difference in molar mass between DPPC and $A_{15}B_{110}A_{15}$), it would rather be expected that the packing and organization of lipid will be more affected by the presence of the polymer, than the other way around. This is shown by BAM micrographs, both at low and high surface pressure.

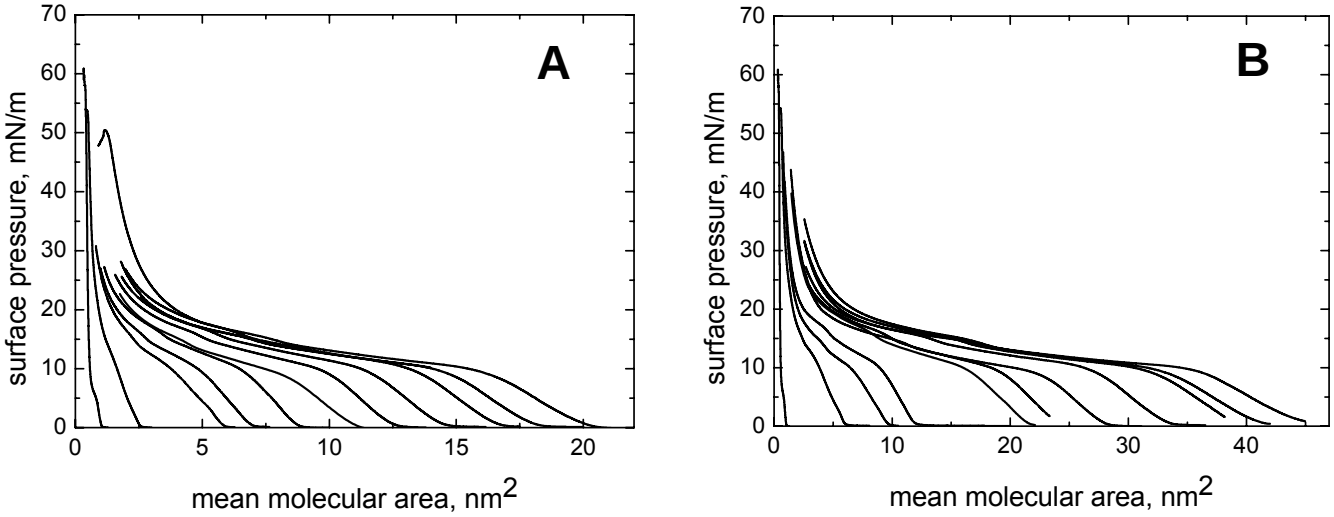

Figure 1 Isotherms from, respectively, A: $A_{15}B_{110}A_{15}$ (largest area), DPPC (smallest area), and $A_{15}B_{110}A_{15}$–DPPC mixtures at different molar ratios (in steps of 0.1); and B: $A_{65}B_{165}A_{65}$ (largest area), DPPC (smallest area), and $A_{65}B_{165}A_{65}$–DPPC mixtures at different molar ratios (in steps of 0.1), at 20^0C on aqueous subphase. The lines in the graphs from left to right correspond to (molar ratios DPPC): DPPC 1.0; DPPC 0.9; DPPC 0.8; etc., DPPC 0.0

The isotherm behavior at high (20 – 30 mN/m) surface pressures for all DPPC-polymer mixtures corresponds to well-packed polymer-lipid monolayers. All isotherms display slopes in the range between the respective values for the polymer and DPPC monolayers, the former being smaller due to the fact that the polymers form a condensed liquid phase, while DPPC forms a liquid crystalline phase. On the other hand, depending on the mixture composition, BAM imaging reveals very interesting morphological features in this surface pressure region.

Figure 2 presents BAM micrographs of DPPC-$A_{15}B_{110}A_{15}$ monolayers at low (A) and high (B-D) surface pressure, respectively. It needs to be stressed that the features visible here are only characteristic for particular compositions of the lipid-polymer mixtures, as described below. For any other mixture composition, as well as for the pure components, homogeneous monolayers are observed, the only features being small bright aggregates which are always present in polymer films (presumably surface micelles, as reported previously [18, 29]). We need to mention here, however, that BAM resolution with the 20x objective is 1 μm, and therefore any features at the nanoscale will not be visible with this technique, yet cannot be ruled out completely. We will return to this point when discussing free excess energy of mixing.

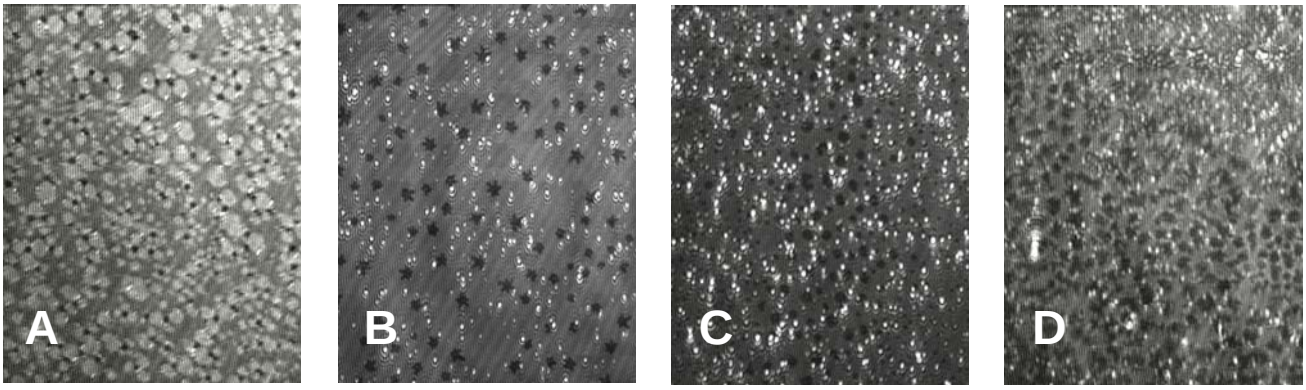

Figure 2 Brewster angle microscopy images of monolayers from $A_{15}B_{110}A_{15}$-DPPC: A - 0.1-0.9 at 10 mN/m; B - 0.3-0.7 at 25 mN/m; C - 0.2-0.8 at 25 mN/m; D - 0.1-0.9 at 25 mN/m. Image width: 220 μm.

Concerning the low surface pressure region (Figure 2 A), we can observe four different grayscale levels, corresponding to four different film thicknesses: black (the smallest film thickness), dark gray, light gray (the largest film thickness), and very bright dots. Given the size difference between the film components, we interpret the black regions as aqueous subphase (not covered by a monolayer), dark gray regions as a lipid film, perhaps containing some polymer and the light gray domains as the polymer phase, which may also contain some lipid. This interpretation is plausible when one considers fluid-in-fluid, partially miscible binary monolayers [30], and literature examples of three-phase coexistence at similar surface pressures [31]. Alternatively, the domain formation could result from polymer film viscosity; however this interpretation is not supported by excellent reversibility of the polymer monolayers, even at high compression-expansion rates.

As mentioned before, the bright white structures are characteristic to the polymer monolayers and appear also in the films from pure polymers. Upon compression, the black regions disappear with the pressure increase and turn into a mixture of dark and light gray, until the film becomes homogeneous along the plateau region. This phase separation at low surface pressure is consistent with the miscibility gap visible in the surface pressure-area isotherm at the same lipid-polymer composition. The important fact is that at this surface pressure, both components are in a liquid state. Therefore, the features observed by BAM also display liquid-like character, which is manifested by

round shapes of the domains resulting from the fact that both components try to minimize their contact area. This will no longer be the case when the lipid's crystallinity comes into play.

At higher surface pressures (25 mN/m and above), mixed monolayers phase-separate at the polymer molar ratio of 0.3 and below. This means, it is necessary to have an amount of lipid in the film large enough so that the crystalline packing (and the corresponding alkyl chain interactions) prevails over the hydrophobic interactions present in large polymer chains. The resulting structures are presented in Figure 2 B-D. We can essentially see a dark-gray film, in which bright dots and black star-like structures (10 to 20 μm) appear. In contrary to Figure 2 A, the black structures do not correspond to the pure aqueous subphase anymore: due to the fact, that the polymer film becomes thicker upon compression, there is a larger amount of the reflected light entering the camera, which at some point becomes saturated. Therefore, it is necessary to decrease the camera gain in order to obtain the images, and as a result, the film regions of lower thickness will now appear very dark. From the light reflectivity, and thus the monolayer thickness, we interpret the star-like structures as DPPC domains, the gray region as the polymer film (which may also contain the lipid), and the bright dots again correspond to interfacial polymer aggregates. Further on we show detailed surface analysis to support this interpretation, and here we will discuss the formation of DPPC star-shaped domains.

As mentioned before, DPPC domains appear at 25 mN/m at the polymer ratio 0.3 and lower. Contrary to the low pressure separation presented in Figure 2 A, we do not observe round features anymore, due to the fact that at such high surface pressure, the lipid, if it is able to form a monolayer phase on its own, will preferentially pack in a liquid-crystalline fashion within that phase. The size of the domains, contrary to their surface density, is not influenced by the polymer content in the mixture (in the 0.3-0.1 polymer molar ratio range), which suggests that the stars are not an intermediate phase, but rather stable lipid domains. Their size and shape do not change with film compression up to the collapse pressure, which is indicative of the most condensed packing state the lipid molecules can adopt, i.e. the liquid crystalline state. Their appearance in the film is also very sudden: they virtually show in the image from one second to another, even at very slow compression rates (3 mm/min), and grow instantly to their final dimensions. The domain size is influenced by temperature: at 35^0C they grow to 30-40 μm. As the polymer monolayers are temperature-insensitive in this range, this suggest a fluidizing temperature effect on the lipid domains (T_c for DPPC is 41^0C) and subsequent expansion of the liquid crystalline lipid domains. As shown later, the dimensions of DPPC domains can be regulated to some extent by the polymer size, and it is obvious that the amphiphilic block copolymer has a stabilizing effect on both size and shape of the lipid stars. The polymer, as soft material, may also lead to edge 'softening' of those structures, yet this effect could be also due to the fact that DPPC is in a liquid crystalline, and not truly crystalline state, for which sharp edges would rather be favored. Additionally, we expect this effect to result from low interfacial tension between the two phases, especially if the polymer phase also contains a certain amount of DPPC, as shown later by Tof-SIMS experiments.

Due to the fact that $A_{65}B_{165}A_{65}$ is twice as big as $A_{15}B_{110}A_{15}$, phase separation in mixed monolayers containing this polymer is even more pronounced. Again, at low surface pressure (10 mN/m), we observe the formation of circular polymer domains (Figure 3 A-C), which appear already at the polymer molar ratio of 0.3, which is consistent with the surface pressure-area isotherm shift for this system, as seen in Figure 1 B. With the increase of the polymer content, the separation effect leads to

smaller domains and their increased surface density. Throughout the plateau region, the domains merge to a homogeneous film, and similarly to mixtures containing $A_{15}B_{110}A_{15}$, star-like lipid structures appear above 25 mN/m (Figure 3 D-H). With this bigger polymer, the star formation is present at yet lower lipid content in the mixture, starting from lipid molar ratio of 0.5 (0.7 for $A_{15}B_{110}A_{15}$). This effect is explained by the larger size mismatch between the two components.

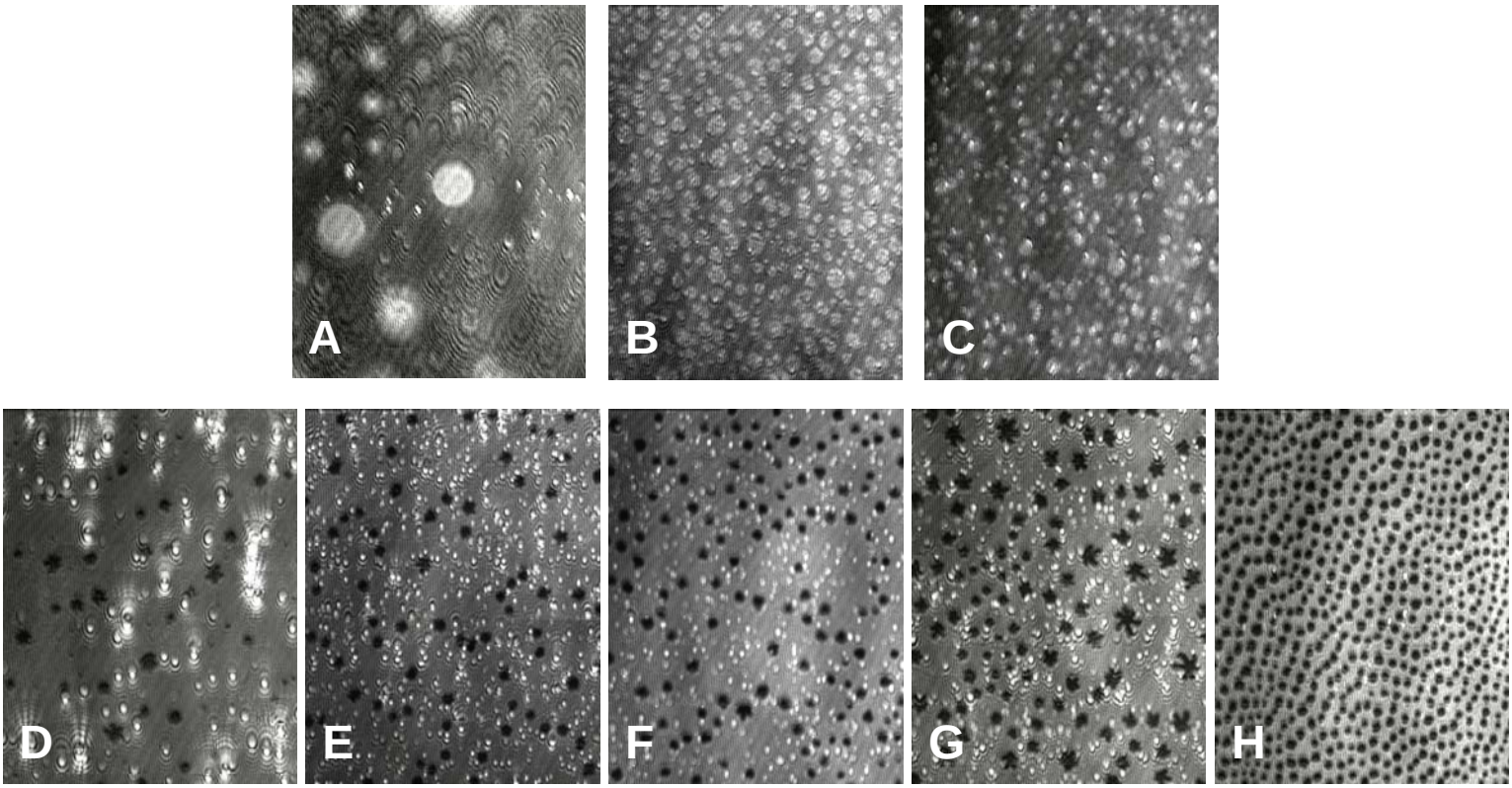

Figure 3 Brewster angle microscopy images of monolayers from $A_{65}B_{165}A_{65}$-DPPC at 10 mN/m (A – C): A - 0.3-0.7, B - 0.2-0.8, C - 0.1-0.9 and at 25 mNm (D – H): D - 0.5-0.5, E - 0.4-0.6, F – 0.3-0.7, G – 0.2-0.8, and H – 0.1-0.9. Image width: 220 μm

Brewster angle microscopy reveals essentially the same DPPC structures as described for $A_{15}B_{110}A_{15}$. The only difference is a slightly larger size of the stars, up to ca. 25 μm, and the behavior of the mixture containing the molar ratio of the polymer of 0.1 (Figure 3 H). In this case, the lipid domains adopt more circular shapes and distribute homogeneously in the polymer matrix to form a network-like morphology. Worth mentioning is the size monodispersity of the domains, presumably due to a better thermodynamic stabilization, as compared to star-like structures. The increase of the interfacial (contact) area can be explained by the better phase separation, i.e. more lipid molecules being expelled from the polymer phase, leading to a two-dimensional emulsion analogue. There also seems to be a certain order concerning the organization of lipid domains: in particular, they tend to form necklace-like chains where the distances between the chains are always larger than between the domains within one chain. This particular lipid-polymer system will be investigated in more detail after we have measured the surface pressure effect on component distribution in the film – we hope to conclude on thermodynamic equilibrium (in the sense of time-dependent domain composition

changes). In the next section, we will analyze the excess free energies of mixing in lipid-polymer films, in order to explain the thermodynamic effects leading to the observed morphologies.

Interaction analysis

Excess free energy of mixing in binary monolayers, $\Delta G^{exc} = \int_0^{\pi} A^{exc} d\pi$, where A^{exc} is excess molecular area resulting from system non-idealities, and π is surface pressure, is indicative of interactions and stability of the mixed film [32]. For a given surface pressure, the excess molecular area is calculated as $A^{exc} = A_{12} - (X_1A_1 + X_2A_2)$, where A_{12} is the mean molecular area in a mixed film, X_1 and X_2 are molar ratios of components 1 and 2 in the mixed monolayer, and A_1 and A_2 are mean molecular areas of the pure components 1 and 2 at this surface pressure. Similarly to three-dimensional binary mixtures, $\Delta G^{exc} = 0$ means ideal miscibility, $\Delta G^{exc} > 0$ indicates repulsion, while $\Delta G^{exc} < 0$ indicates attractive interactions between the mixture components. In the case of Langmuir monolayers, repulsion means expansion of the film, while attractive interactions lead to 'contraction' (or 'condensation') of the monolayer, and negative ΔG^{exc} means thermodynamic stabilization of the system. On the other hand, phase separation may also lead to negative A^{exc}, especially when one or both components have very good packing properties, like in the case of DPPC.

Figure S2 presents the excess free energies of mixing for DPPC-containing mixed monolayers with $A_{15}B_{110}A_{15}$ (Fig. S2 A) and $A_{65}B_{165}A_{65}$ (Fig. S2 B), at two different surface pressures, i.e. 7.5 mN/m, and 25 mN/m, plotted versus monolayer composition. We will be mostly interested in discussing the thermodynamic effects for those monolayer compositions, which display distinct features by BAM imaging. For clearer visualization, schematic phase diagrams for DPPC-polymer mixtures are shown in Figure 4 (for phase description of pure components, see [19, 22, 23]).

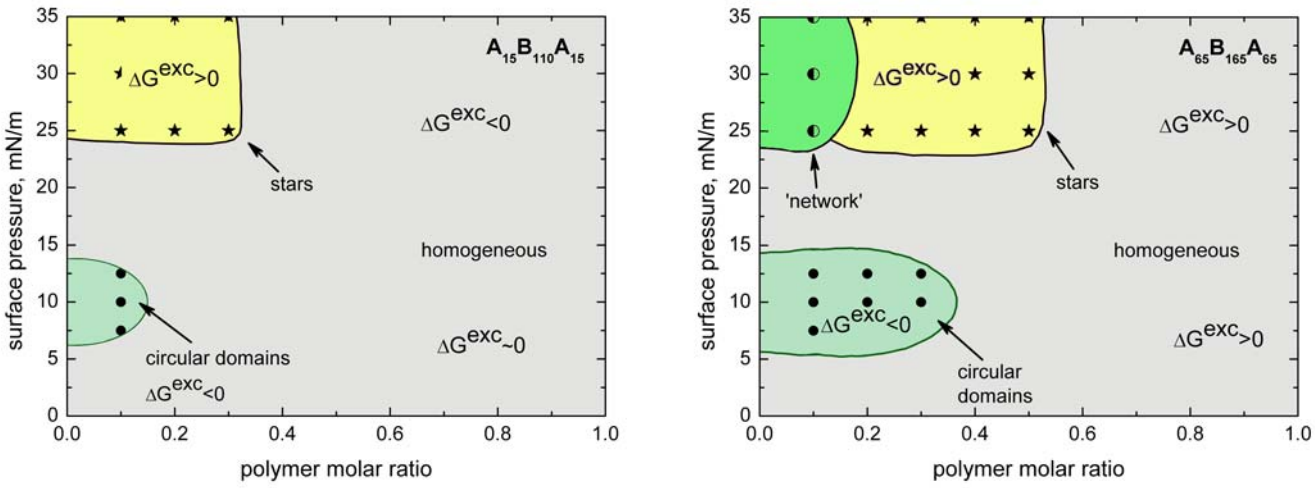

Figure 4 Schematic phase diagrams (surface pressure versus mixture composition) for the polymer-DPPC mixtures

Concerning the $A_{15}B_{110}A_{15}$-DPPC monolayers, we observe the formation of polymer domains at low pressures for the polymer molar ratio of 0.1 only. This feature is reflected by negative ΔG^{exc} for this composition. The minimum ΔG^{exc} value is not exceptionally large, however, it is distinctly lower than the values for all other compositions at this pressure, which fall in the semi-ideal (ΔG^{exc} close to zero) miscibility regime. Curiously, the high pressure (25 mN/m) effect, visualized as star-like domain formation, is not significantly pronounced in the ΔG^{exc} values. Given the phase separation, one could expect large positive values for the polymer molar ratio 0.3 and lower; instead only the maximum of 235 J/mol is observed for the $A_{15}B_{110}A_{15}$ molar ratio of 0.2. This result is consistent with our discussion on the thermodynamic stabilization of the lipid star domains by the block copolymer, as the energetic effect connected to the phase separation is very small. Additionally, the miscibility between the two components at high surface pressure and at the polymer ratio above 0.3 increases as compared to low surface pressure and is reflected by negative ΔG^{exc}, indicative of attractive interactions between the lipid and polymer.

The energetic contributions to miscibility between DPPC and the large polymer, $A_{65}B_{165}A_{65}$, (Figure S2 B) are substantially larger, up to 2.5 kJ/mol, resulting from the fact that the chemical and size incompatibility between the mixture components is more pronounced than with $A_{15}B_{110}A_{15}$. Most importantly, at low surface pressure (7.5 mN/m), we observe a large ΔG^{exc} minimum (-1.5 kJ/mol) exactly where BAM reveals the formation of polymer circular domains, i.e. at the molar ratio of $A_{65}B_{165}A_{65}$ of 0.3 (Figure 4). At higher polymer content, the mixing seems unfavorable, and can be interpreted as a nanoscale phenomenon, where either the lipid would have preferred to form a film on its own, but is at the same time disturbed by large macromolecules, or the lipid molecules hinder free conformational changes of $A_{65}B_{165}A_{65}$, and therefore we observe the film expansion, and thus positive values for the excess free energy.

At the high surface pressure, 25 mN/m, the situation is different: we never observe negative ΔG^{exc}. This suggests unfavorable mixing in the whole composition range, and especially for the polymer molar ratio of 0.4 – 0.5, where the star domains of DPPC first appear. It seems that the stabilization of those structures is more efficient with the smaller polymer, $A_{15}B_{110}A_{15}$, which can be explained by the smaller size of $A_{15}B_{110}A_{15}$ and thus smaller size mismatch. On the other hand, the bigger $A_{65}B_{165}A_{65}$ could be expected to have more conformational possibilities to adapt to the lipid phase and stabilize it further, yet it seems that the area constraints in the high surface pressure region hinder any conformational rearrangements, and thus the polymer frustration is demonstrated as positive ΔG^{exc}.

Langmuir-Blodgett film analysis: composition of phase-separated monolayers

So far we discussed the polymer-lipid phase separation based on the BAM observation of star-like structures, assuming that those film domains, characterized with smaller film thickness than their surrounding, should be formed by DPPC, which at high surface pressure organizes in a liquid-crystalline fashion. Since the star structures appear very dark in BAM in contrast to the surrounding film, it could be argued that micrometer-sized holes are produced in the film upon compression. As unlikely as it sounds (we would not know why the holes should have star-like shapes, and why the very elastic polymer would not instantly expand to occupy the empty areas in the film), we found it

important to perform the analysis of the films in order to definitely determine the component distribution in the film. We analyzed Langmuir-Blodgett monolayers from polymer-DPPC mixtures at the molar ratios where star structures were visible, transferred from the air-water interface at 25 mN/m.

Firstly, we performed ellipsometry studies of monolayers transferred on silicon (Figure 5 A). Imaging ellipsometry of a $A_{65}B_{165}A_{65}$-DPPC monolayer shows that the structures visible by BAM do not become destroyed during the transfer, and that the film morphology is retained. Film thickness was measured at various regions, corresponding to different light reflectivity (and thus different thicknesses). For DPPC-containing mixtures (with both polymers), the gray film has the thickness of 5.0-6.5 nm, consistent with the polymer size assuming a 'cigar' phase, as described earlier [19]. The dark, star-like structures always have the thickness of ca. 1.5-2.2 nm, which is consistent with the thickness of a lipid monolayer. This result also shows that the dark regions do contain some material. The problem here, however, is that the silicon surface is always covered by a silicon oxide layer. We have obviously included the silicon oxide layer in the fitting procedure; yet it can be argued that the silicon oxide thickness is not homogeneous throughout the whole surface, and produces artifacts during ellipsometry data fitting.

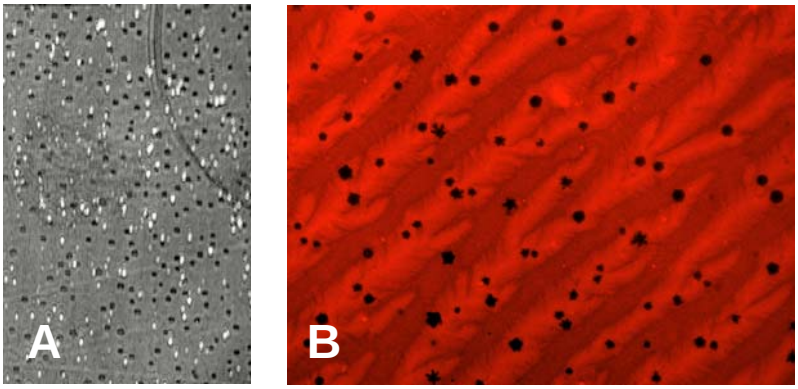

Figure 5 (A) Ellipsometry image of a Langmuir-Blodgett monolayer from $A_{65}B_{165}A_{65}$-DPPC, molar ratio 0.2-0.8, transferred to silicon surface at 25 mN/m. Image width: 220 µm. (B) Fluorescence microscopy image of a Langmuir-Blodgett monolayer from $A_{15}B_{110}A_{15}$ (labelled with sulforhodamine)-DPPC, molar ratio polymer-lipid 0.3-0.7. The monolayer was transferred to a microscopy glass slide at 25 mN/m. Image width: 250 µm

In order to show where the polymer and lipid are present in the LB films, we used fluorescently labeled polymer and lipid as markers, and performed fluorescence microscopy after film transfer on microscopy glass slides. The fluorescence image of a labeled polymer-containing mixed film is presented in Figure 5 B. We can see here that transfer on glass surfaces also retains the film morphology, and that the labeled polymer distributes exclusively outside the star-like domains, which must therefore be either holes in the film or purely lipid domains. The bright ridges visible across the picture may be due to the polymer experiencing shear stress during the LB transfer or a dewetting effect, as the sample was imaged in the dry state a few hours after the transfer.

We performed an analogous experiment using a fluorescently labeled lipid, NBD-PC (Figure S3), which lead to somewhat confusing results. Namely, we observe the NBD fluorescence from

exactly the same regions where the SRB-labeled polymer emits, i.e. outside the stars. The explanation of that effect could be that indeed, holes are produced in the film while some molecules are squeezed out into the subphase, and the remaining lipid material is mixed with the polymer phase. On the other hand, the stability of such holes could not be explained, and especially not as a long-term effect, and not in the presence of materials as elastic as our block copolymers. Literature data on lipid monolayers studied with fluorescence microscopy [33, 34], however, describe the dye exclusion from organized lipid phases, which therefore always appears black in fluorescence micrographs. Knowing that DPPC tends to build a liquid crystalline phase at room temperature, we can expect that NBD-PC, which contains a bulky dye attached to one of the alkyl chains, would have different packing properties due to its smaller symmetry. It is therefore possible, that NBD-PC preferentially accumulates in the more liquid polymer phase, and we visualize the DPPC domains as black.

In order to solve this problem, we analyzed the mixed LB films by ToF-SIMS. In control experiments, we first recorded mass spectra from a clean silicon wafer, an $A_{15}B_{110}A_{15}$ film, and a lipid film. We identified the following peaks, which will further help to differentiate between lipid and polymer regions in the mixed film: for $A_{15}B_{110}A_{15}$, the characteristic peaks are CN^- (m/z = 26.00), and CNO^- (m/z = 42.00), while for DPPC we observe a PO_2^- peak at m/z = 62.97, a PO_3^- peak at m/z = 78.92, and a peak corresponding to alkyl chains, $C_{16}H_{31}O_2^-$, at m/z = 255.25. To determine the spatial distribution of the two components in the film, we performed ToF-SIMS imaging, results are presented in Figure 6. In Fig. 6 A, the yellow color intensity corresponds to the CN^- peak characteristic to $A_{15}B_{110}A_{15}$, while in Fig. 6 B-D, the yellow color corresponds to, respectively, PO_2^- (Fig. 6 B); PO_3^- (Fig. 6 C), and $C_{16}H_{31}O_2^-$ (Fig. 6 D).

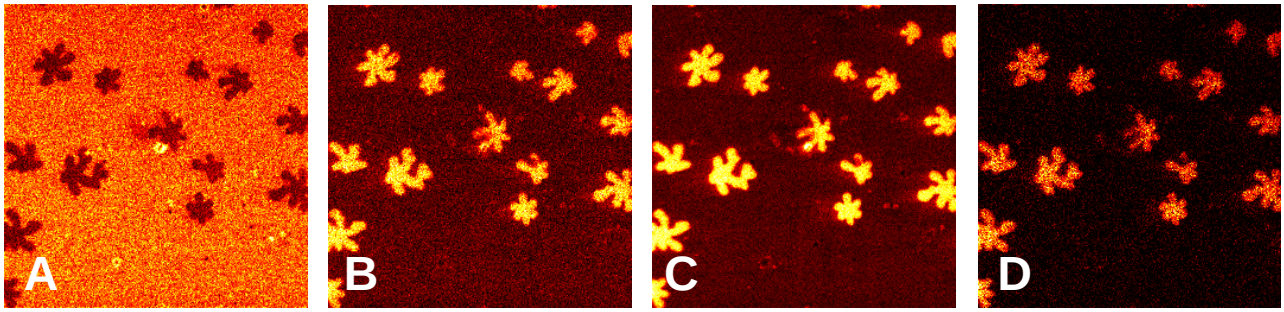

Figure 6 ToF-SIMS images (100 x 100 μm) of Langmuir-Blodgett monolayers from $A_{15}B_{110}A_{15}$-DPPC, molar ratio 0.3-0.7 on silicon surface. The intensity of yellow color corresponds to, respectively: A – CN^-, B - PO_2^-, C - PO_3^-, and D - $C_{16}H_{31}O_2^-$.

The analysis of surface coverage shows that in star-like structures there is 4.5 % of the overall CN^- intensity, 31.2 % of PO_2^- intensity, 37.3 % of PO_3^- intensity, and 41.5 % of $C_{16}H_{31}O_2^-$ intensity (mean values from three measurements at different sample regions). This result indicates that while there might still be a very small amount of $A_{15}B_{110}A_{15}$ present in the star-like structures (especially visible on the edges, as the lateral resolution is 0.5-1.0 μm), they are composed predominantly of DPPC, around 40 % of which is expelled from the monolayer and phase-separates, while the remaining lipid (60 %) forms a mixed film with $A_{15}B_{110}A_{15}$. Therefore, at surface pressure of 25 mN/m, the limiting DPPC amount in the monolayer is 70 mole %, and 28 mole % would be found in star structures.

In summary, we have shown that the phase separation in polymer-DPPC mixed monolayers at high surface pressure leads to the exclusion of some lipid from the film and the formation of characteristic star-like structures. This phenomenon is related to the chemical structure of the lipid and the resulting ability to form liquid crystalline phase at the air-water interface.

3.3 Mixed systems $A_{15}B_{110}A_{15}$-DOPC and $A_{65}B_{165}A_{65}$-DOPC

As presented before, miscibility of DPPC with soft, liquid-like polymer monolayers can be discussed as long as the amount of lipid in the film is small enough not to build lipid domains. At large lipid content, phase separation occurs, as the interactions present in the liquid crystalline packing state of the lipid are strong enough to lead to the formation of exclusively lipid-containing domains. We were also interested in the properties of polymer-lipid assemblies when a more fluid lipid were used, like DOPC. The properties of DOPC monolayers are discussed shortly in section 3.1, and here we will analyze mixed monolayers of DOPC with the same polymers as used with DPPC mixtures, i.e. $A_{15}B_{110}A_{15}$ and $A_{65}B_{165}A_{65}$.

Langmuir monolayers and Brewster angle microscopy

Surface pressure-area isotherms of DOPC-containing monolayers are presented in Supporting Information, Figure S4. In general, the pattern of the isotherms is the same as seen for DPPC-containing lipid-polymer mixtures (Figure 1). The difference is that we do not observe the isotherm shift corresponding to a change in miscibility at low surface pressure. In the case of DOPC-containing monolayers, the distances in mean molecular area for the mixtures differing (by equal steps) in the molar ratio of the components, are equal. From this observation, we would not expect any polymer-lipid phase separation at low surface pressure, however when we analyze Brewster angle microscopy images, we can observe the formation of two phases below 10 mN/m.

BAM micrographs for DOPC-containing monolayers at low surface pressure are presented in Figure 7. Compared to DPPC-containing mixtures described in the previous sections, the main difference is that the lipid induces the formation of circular (thicker, therefore containing mostly the polymer) domains for both polymers, and that the domains appear at exactly the same lipid-polymer ratio (0.3-0.7) with both investigated polymers. With the increasing lipid content, the effect is stronger as demonstrated by the increasing size of the polymer domains. When the monolayers are compressed to higher surface pressure, the domains merge (throughout the plateau region), which means that the lipid becomes accommodated and ‘buried’ in the polymer phase, and this is possible due to the liquid properties of DOPC. Finally, at surface pressures where DPPC phase-separates to star-like domains, i.e. at 25 mN/m, smooth films are observed and no structural details can be visualized by BAM.

Obviously, we cannot expect exactly the same mixing behavior of the polymers with DOPC as with DPPC, since these two lipids have markedly different organization properties at the air-water interface. Interestingly, in the expanded fluid phase, DOPC seems to have identical influence on the polymers independent from the polymer size. This effect can be explained by the interplay of two phenomena: firstly, even at low surface pressure, DOPC has a more liquid character (and thus poorer

organization properties) than DPPC. The calculation of the compressibility modulus for the polymer monolayers indicate [19], that the organization of polymer chains is already quite high at this surface pressure, and therefore strong hydrophobic attraction will be the prevailing force leading to the separation of polymer domains from the lipid (or possibly lipid-polymer) film. The second effect results from the fact that the two polymers of markedly different dimensions will have different possibilities of chain rearrangements, with $A_{65}B_{165}A_{65}$ being more flexible, and thus they will differently adopt to the presence of a second (lipid) component in the film. It seems that the $A_{65}B_{165}A_{65}$ is somewhat less sensitive to the presence of a fluid lipid than $A_{15}B_{110}A_{15}$, which means that it is easier for the large chains to find their energetically most favorable state, and therefore we observe the separation only starting from the polymer molar ratio of 0.3, i.e. at the same composition as with $A_{15}B_{110}A_{15}$. In both cases, the decrease of polymer ratio leads to increased extent of phase separation, as manifested by the growth of the domains. This effect may seem counter-intuitive, yet considering the molar ratios in the mixed film, the polymers, as considerably larger components, will occupy more space at the air-water interface than lipid molecules, even if the polymer content is considerably small. It should be also remembered, that at polymer molar ratios of 0.3, there may be a certain number of polymer molecules in the thinner phase, while with the increasing lipid content more polymer will be phase-separated, and therefore we observe larger domains.

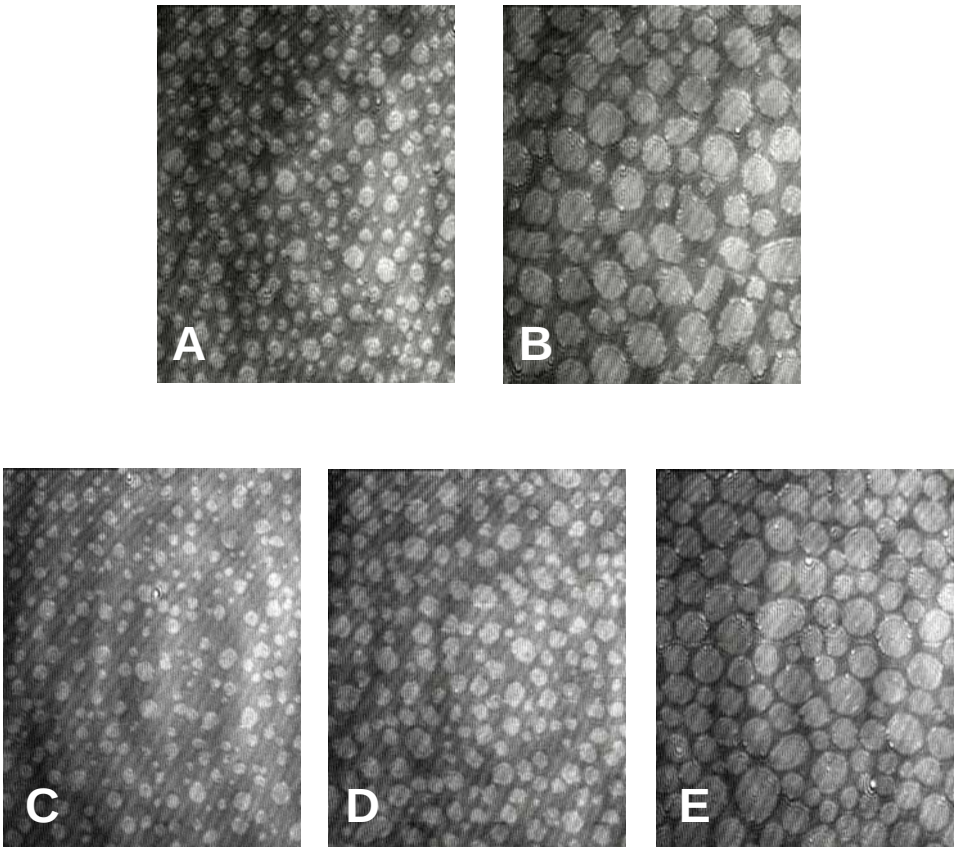

Figure 7 Brewster angle microscopy images of monolayers (at 8 mN/m) from $A_{15}B_{110}A_{15}$-DOPC (A, B): A - 0.3-0.7, B - 0.2-0.8; and $A_{65}B_{165}A_{65}$-DOPC (C – E): C - 0.3-0.7, D - 0.2-0.8, E - 0.1-0.9. Image width: 220 μm

Interaction analysis

Mixing of the two components at low surface pressure and at the polymer molar ratio of 0.3 and lower is characterized by the domain formation, and therefore film contraction, leading to a small energy gain, as demonstrated by excess free energy calculations, Figure 8. While for $A_{15}B_{110}A_{15}$, the ΔG^{exc} is always small and negative (Fig. 8 A), for $A_{65}B_{165}A_{65}$ negative values are only obtained for polymer molar ratios below 0.3 (Fig. 8 B). Especially with the large polymer, this result clearly demonstrates the difference in energetic contributions to the film organization resulting from different packing preferences of the lipid.

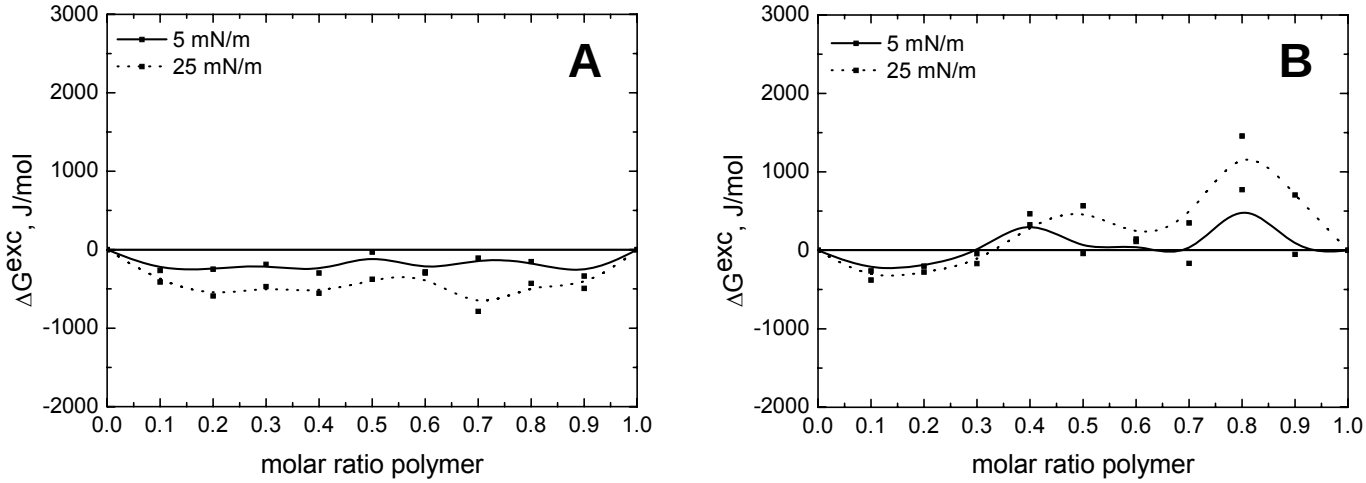

Figure 8 Excess free energy of mixing for A: $A_{15}B_{110}A_{15}$-DOPC and B: $A_{65}B_{165}A_{65}$-DOPC monolayers versus mixture composition, at 5 mN/m (solid lines) and 25 mN/m (dotted lines)

Concerning the ΔG^{exc} values at high surface pressure (25 mN/m), we can instantly observe more favorable mixing of the liquid lipid with a smaller polymer, as could be actually expected considering that both components are in the condensed liquid region at this pressure, and both have certain possibilities for conformational changes in the film. With the larger polymer this effect is only seen at small molar ratios of the polymer, while at the compositions above 0.4 (polymer molar ratio), a positive energetic contribution is observed (Fig. 8 B). This result should be interpreted in the context of BAM images presented above: film contraction, and thus area decrease and negative ΔG^{exc} are seen exactly in the same region where the circular domains appear, and at the higher polymer content the amount of lipid is apparently too small to induce a phase separation on micrometer-scale, yet molecularly the components are not compatible and therefore their repulsion leads to positive excess energy of mixing. With $A_{15}B_{110}A_{15}$, the small negative ΔG^{exc} contribution (Fig. 8 A) must be related to the fact that with the smaller polymer the lipid molecules can be more comfortably accommodated and the system is finally relatively stable.

4. Conclusions

Artificial block copolymers attract increasing attention in biomedical applications such as drug delivery [35], tissue engineering [36, 37] and diagnostics [38]. Despite extensive research activities in this area, certain basic aspects have not been investigated so far, in particular interfacial effects such as membrane interactions. It is obvious, however, that interactions of cellular membrane components with polymers in the body may have important implications on the performance of polymer-based materials. Depending on the size and chemical structure of the polymer, different effects can be expected (and thus optimized), as shown in this report.

In summary, by studying Langmuir monolayers as membrane models, we have demonstrated that the behavior of cell membrane lipids is influenced by the presence of a polymer, in particular when the lipid, such as DPPC, has a tendency to form condensed phases in the membrane. What is more, relatively small amount of the polymer inserted in the membrane may be enough to force DPPC molecules to phase separate and form domains at high surface pressure. We have analyzed such phase separation phenomena in the context of domain shape, composition, and energetic contributions resulting from the polymer-lipid mixing / demixing process.

In general, when we consider the cell membrane components of liquid crystalline character, smaller polymers, like our $A_{15}B_{110}A_{15}$, have a moderate energetic effect, and in a narrower lipid-to-polymer composition range. The success of applications such as vesicular drug delivery will strongly depend on this composition: when the polymer membrane comes into contact with a cellular membrane, a number of polymer molecules per cell membrane area can be directly correlated to our experiments and the energetic and morphological effect predicted. On the other hand, the fluid cell membrane component, DOPC, does not display strong energetic effect at high surface pressures, which means that the more fluid the cell membrane, the more resistant it should remain to the presence of macromolecular entities.

In this work, we focused on energetic contributions resulting from mixing amphiphilic triblock copolymers with individual lipids. At this stage, our results cannot be directly translated to cell membranes as a whole, due to cell membrane compositional complexity: in particular, we have not considered charged lipids, abundantly present in cell membranes, cholesterol, and any membrane proteins. On the other hand, we believe that studying individual membrane components provides basic information leading to straightforward comparison of thermodynamic data and should serve as the basis for the future research in this fascinating field.

Acknowledgements

We are grateful to Swiss National Science Foundation and NCCR-Nanoscale Science and NEST projects 029084 and 043431 for financial support.

References

(1) K. Kita-Tokarczyk; J. Grumelard; T. Haefele; W. Meier; Polymer **46**, (2005), 3540

(2) C.J.F. Rijcken; O. Soga; W.E. Hennink; C.F. van Nostrum; J. Controlled Release **120**, (2007), 131

(3) D.H. Levine; P.P. Ghoroghchian; J. Freudenberg; G. Zhang; M.J. Therien; M.I. Greene; D.A. Hammer; R. Murali; Methods **46**, (2008), 25
(4) K. Mondon; R. Gurny; M. Moller; Chimia **62**, (2008), 832
(5) V. San Miguel; A.J. Limer; D.M. Haddleton; F. Catalina; C. Peinado; Eur. Polym. J. **44**, (2008), 3853
(6) P. Broz; N. Ben-Haim; M. Grzelakowski; S. Marsch; W. Meier; P. Hunziker; J. Cardiovasc. Pharmacol. **51**, (2008), 246
(7) F. Ahmed; R.I. Pakunlu; A. Brannan; F. Bates; T. Minko; D.E. Discher; J. Controlled Release **116**, (2006), 150
(8) H.-D. Doerfler; C. Koth; W. Rettig; J. Colloid Interface Sci. **180**, (1996), 478
(9) R. Ionov; A. El-Abed; M. Goldmann; P. Peretti; Biochim. Biophys. Acta, Biomembr. **1667**, (2004), 200
(10) D.S. Johnston; E. Coppard; G.V. Parera; D. Chapman; Biochemistry **23**, (1984), 6912
(11) K. Hoda; H. Kawasaki; N. Yoshino; C.-H. Chang; Y. Morikawa; G. Sugihara; O. Shibata; Colloids Surf., B **53**, (2006), 37
(12) M. Niwa; N. Katsurada; N. Higashi; Macromolecules **21**, (1988), 1878
(13) M. Niwa; T. Hayashi; N. Higashi; Langmuir **6**, (1990), 263
(14) A. Wesemann; H. Ahrens; R. Steitz; S. Foerster; C.A. Helm; Langmuir **19**, (2003), 709
(15) C.S. Hodges; F. Neville; O. Konovalov; R.B. Hammond; D. Gidalevitz; I.W. Hamley; Langmuir **22**, (2006), 8821
(16) S. Rivillon; M.G. Munoz; F. Monroy; F. Ortega; R.G. Rubio; Macromolecules **36**, (2003), 4068
(17) T. Doi; T. Kinoshita; Y. Tsujita; H. Yoshimizu; Sen'i Gakkaishi **56**, (2000), 221
(18) J. Zhu; A. Eisenberg; R.B. Lennox; J. Am. Chem. Soc. **113**, (1991), 5583
(19) T. Haefele; K. Kita-Tokarczyk; W. Meier; Langmuir **22**, (2006), 1164
(20) M. Kumar; M. Grzelakowski; J. Zilles; M. Clark; W. Meier; Proc. Natl. Acad. Sci. U. S. A. **104**, (2007), 20719
(21) S. Egli; P. Rigler; W. Meier, (manuscript in preparation)
(22) A. Aroti; E. Leontidis; E. Maltseva; G. Brezesinski; J. Phys. Chem. B **108**, (2004), 15238
(23) G. Ma; H.C. Allen; Langmuir **22**, (2006), 5341
(24) S. Perez; J. Minones, Jr.; M. Espina; M.A. Alsina; I. Haro; C. Mestres; J. Phys. Chem. B **109**, (2005), 19970
(25) P. Dynarowicz-Latka; K. Hac-Wydro; Colloids Surf., B **37**, (2004), 21
(26) Y.-L. Lee; W.-P. Hsu; S.-H. Liou; Colloids Surf., A **272**, (2006), 37
(27) V.S. Kulkarni; S.S. Katti; Colloids Surf. **9**, (1984), 101
(28) B. Korchowiec; A. Ben Salem; Y. Corvis; J.-B. Regnouf de Vains; J. Korchowiec; E. Rogalska; J. Phys. Chem. B **111**, (2007), 13231
(29) M. Meszaros; A. Eisenberg; R.B. Lennox; Faraday Discuss. **98**, (1995), 283
(30) C.L. Hirshfeld; M. Seul; J. Phys. (Paris) **51**, (1990), 1537
(31) P. Heinig; S. Wurlitzer; P. Steffen; F. Kremer; T.M. Fischer; Langmuir **16**, (2000), 10254
(32) P. Dynarowicz-Latka; K. Kita; Adv. Colloid Interface Sci. **79**, (1999), 1
(33) H. Loesche; H. Moehwald; Colloids Surf. **10**, (1984), 217
(34) C.K. Park; F.J. Schmitt; L. Evert; D.K. Schwartz; J.N. Israelachvili; C.M. Knobler; Langmuir **15**, (1999), 202
(35) D.E. Discher; V. Ortiz; G. Srinivas; M.L. Klein; Y. Kim; D. Christian; S. Cai; P. Photos; F. Ahmed; Prog. Polym. Sci. **32**, (2007), 838
(36) D. Beattie; K.H. Wong; C. Williams; L.A. Poole-Warren; T.P. Davis; C. Barner-Kowollik; M.H. Stenzel; Biomacromolecules **7**, (2006), 1072
(37) T. Smart; H. Lomas; M. Massignani; M.V. Flores-Merino; L.R. Perez; G. Battaglia; Nano Today **3**, (2008), 38
(38) V.S. Trubetskoy; Adv. Drug Delivery Rev. **37**, (1999), 81

Monolayer Interactions between Lipids and Amphiphilic Block Copolymers

K. Kita-Tokarczyk, F. Itel, M. Grzelakowski, S. Egli, P. Rossbach and W. Meier

Supporting Information

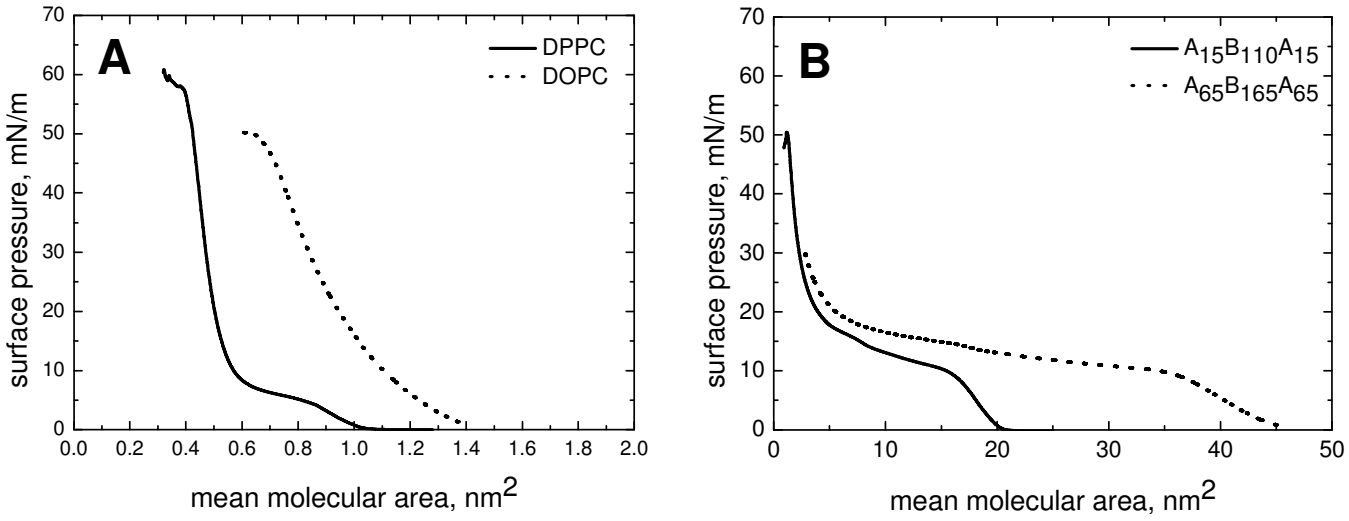

Figure S1 Isotherms from lipids (A: DPPC (solid line) and DOPC (dotted line)), and polymers (B: $A_{15}B_{110}A_{15}$ (solid line) and $A_{65}B_{165}A_{65}$ (dotted line)); at 20^0C on aqueous subphase

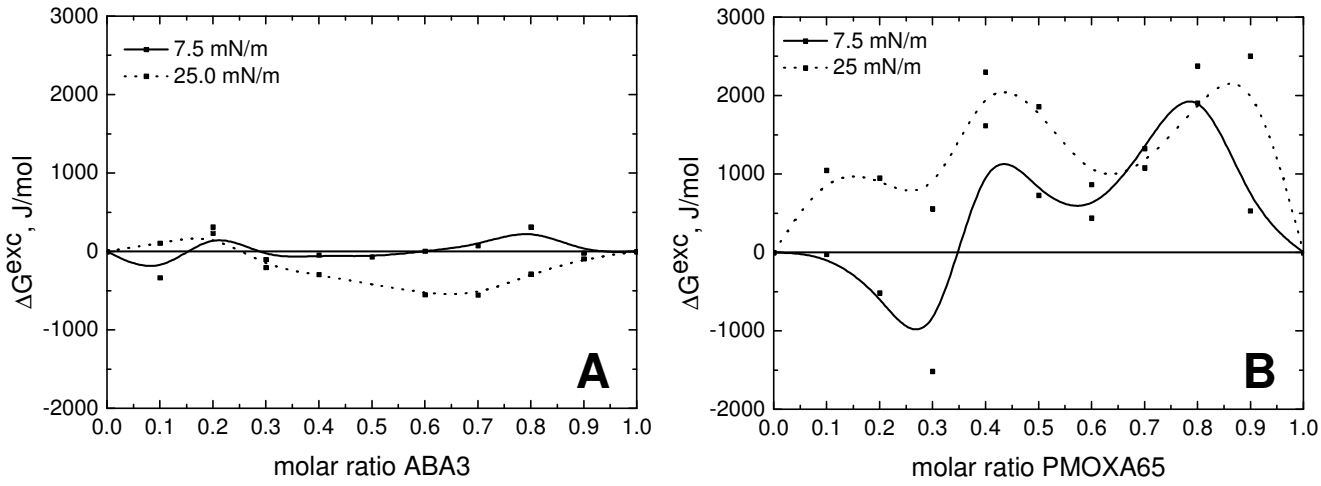

Figure S2 Excess free energy of mixing for A: $A_{15}B_{110}A_{15}$-DPPC and B: $A_{65}B_{165}A_{65}$-DPPC monolayers versus mixture composition, at 7.5 mN/m (solid lines) and 20 mN/m (dotted lines)

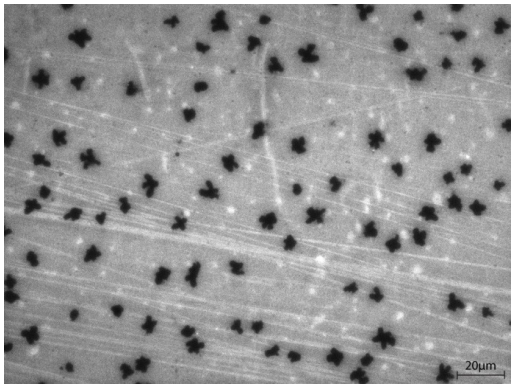

Figure S3 Fluorescence microscopy image of a Langmuir-Blodgett monolayer from $A_{15}B_{110}A_{15}$ – NBD-PC, molar ratio polymer-lipid 0.3-0.7. The monolayer was transferred to a microscopy glass slide at 25 mN/m. Image width: 250 µm.

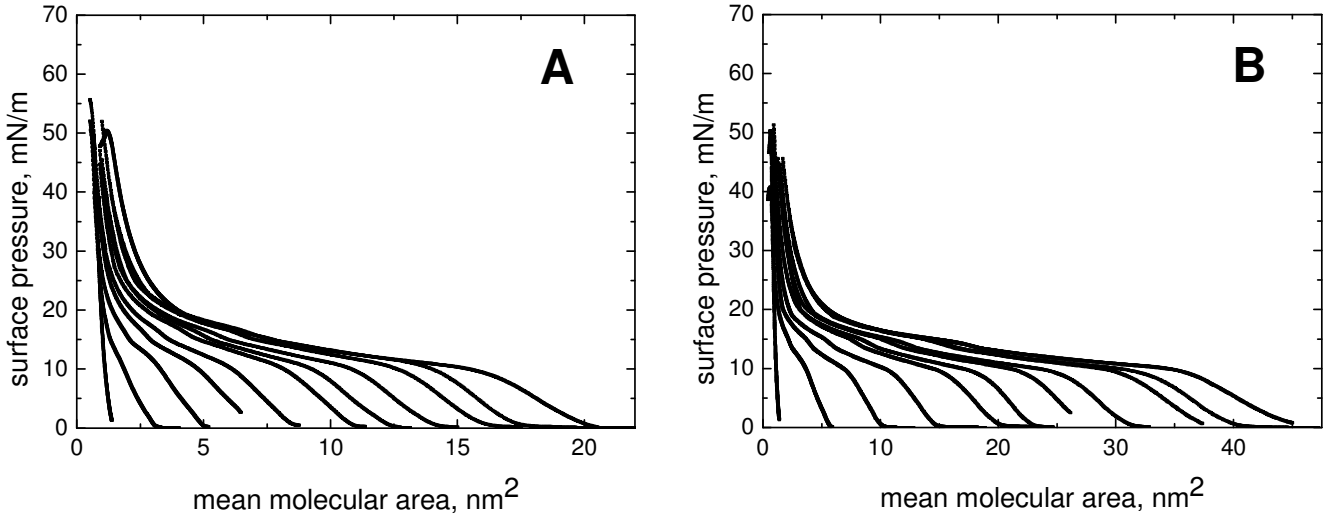

Figure S4 Isotherms from respectively: A: $A_{15}B_{110}A_{15}$ (largest area), DOPC (smallest area), and $A_{15}B_{110}A_{15}$–DOPC mixtures at different molar ratios (in steps of 0.1), and B: $A_{65}B_{165}A_{65}$ (largest area), DOPC (smallest area), and $A_{65}B_{165}A_{65}$–DOPC mixtures at different molar ratios (in steps of 0.1), at 20^0C on aqueous subphase. The lines in the graphs from left to right correspond to (molar ratios DOPC): DOPC 1.0; DOPC 0.9; DOPC 0.8; ...; DOPC 0.0

3. Conclusions

Biomimetic, membrane-forming PMOXA-PDMS-PMOXA block copolymers library was successfully synthesized and characterized with appropriate spectroscopic and chromatographic techniques. Previously published synthetic route for synthesizing PMOXA-PDMS-PMOXA copolymer was modified in order to get full control over the molecular weight of each of the blocks of the resulting block copolymer, reduce the level of contaminants and molecular weight polydispersity. To introduce additional functionality, expanding the utility of the synthesized block copolymers, the end-groups were modified with biotin (enabling specific binding) and methacrylate (enabling crosslinking). End functionalization was confirmed by FCS and FTIR experiments. The self-assembly properties of the synthesized ABA block copolymers into vesicular structures in dilute aqueous solutions were studied and cross-confirmed by light scattering, fluorescence correlation spectroscopy, electron microscopy, atomic force microscopy, encapsulation studies and indirectly by stopped-flow spectroscopy. It was also found that the choice of the appropriate technique to trigger the self-assembly process influences the ratio of resulting morphologies (micelles vs. vesicles). Film hydration method was preferentially used to generate aggregates resulting in up to 99.8 % of monodisperse vesicles in the case of dilute solutions of $A_{12}B_{55}A_{12}$.

Membrane forming capabilities of the synthesized block copolymers were employed together with functionality of natural membrane proteins and enzymes in the design of novel functional polymer-protein hybrid materials and as a stable biomimetic platform for conducting basic research over the proteins themselves.

We have shown successful incorporation of the bacterial water-channel protein Aquaporin-Z into an ABA triblock copolymer resulting in biomimetic membranes of high water permeability and selectivity for small solutes. The magnitude of increase in permeability and the excellent solute rejection capabilities demonstrate the potential benefit of such membranes for water treatment.

We have used the ABA block copolymer membrane as a platform for investigating the properties of Aquaporine-Z. Aquaporin Z (AqpZ) was reported to be not gated in a narrow pH range in previous studies, and the physiological relevance of this protein is unknown. The use of a synthetic biomimetic polymer of low permeability allowed sensitive examination of AqpZ permeability over a wide pH range. AqpZ incorporated in this polymer was gated between pH values of 4 and 6 and this gating was reversible. Whole experiments with E. Coli AqpZ mutants confirmed this observation. Furthermore, AqpZ mutants exhibit reduced survival under acid stress. pH gating of AqpZ may be important for cell survival at low pH values.

We have demonstrated that the immobilized biotinylated ABA block copolymer vesicles permeabilized with bacterial outer membrane protein F can serve as a novel tool to generate chemically/biologically active surfaces. This enables precise control over reaction environment and location and may be relevant for studies involving sensitive enzymes, single molecule spectroscopy, sensors and drug delivery.

We have also demonstrated that synthetic membranes of amphiphilic triblock copolymer vesicles can be actively reconstituted with NADH:ubiquinone oxidoreductase (complex I), to form hybrid systems at the nanoscale that allow site-specific reactions driven by location and redox-potential differences. Nanoscale devices involved in energy conversion require the transfer of electrons from one compartment to another in order to properly function. These electron transfer nanodevices are suitable for a variety of applications such as signaling devices or nanoreactors for follow-up redox reactions inside the synthetic membrane.

The drug delivery application potential of vesicles prepared from ABA triblock copolymers was demonstrated in receptor-specific targeting using statin-loaded triblock copolymer vesicles with targeting moieties promising advancement in high-dose treatment for improved efficacy, while minimizing toxicity in other cells. Vesicle uptake by target cells but not other cell types and slow intracellular content release was observed. A major improvement in biologic efficacy was observed for polymer vesicles compared to free drug, whereas no increased cytotoxicity was observed in muscle cells. Such targeted therapy through cell-specific polymer vesicles allows novel treatment for a wide range of drugs and diseases. In addition, we have reported a potential drug delivery triggered release system based on engineered FhuA channel variant incorporated into ABA block copolymer vesicles. This engineered membrane protein releases the cargo of the vesicle in response to reductive stimuli (dithiothreitol) upon disulfide bond reduction.

Due to drug delivery potential application of PMOXA-PDMS-PMOXA block copolymer vesicles, where interactions between polymeric and natural cell membranes are crucial and furthermore, due to the fact that membrane proteins extracts contain certain amount of lipids, the interactions between two types of lipids and synthesized ABA block copolymers were investigated using Langmuir monolayers as membrane models. We have demonstrated that the behavior of cell membrane lipids is influenced by the presence of a polymer, in particular when the lipid, has a tendency to form condensed phases in the membrane. We analyzed phase separation of lipids/block copolymers in the context of domain shape, composition, and energetic contributions resulting from the polymer-lipid mixing / demixing process.

In summary we synthesized and characterized PMOXA-PDMS-PMOXA amphiphilic block copolymer library, studied their self-assembly properties and further applied the biomimetic polymer in development of novel polymer-protein hybrid materials promising new advancements in areas of water treatment, microfluidics, sensors and drug delivery.

4. Outlook

The Aquaporin-Z protein-polymer membranes developed here have salt rejection properties and excellent control over the permeability of polymers, ideal for desalination. Incorporation of AQPs (or suitable molecular mimics) into compatible synthetic polymers (such as the block copolymer system investigated in this study) is an innovative approach for making membranes for medical, industrial, and municipal desalting applications. For this new type of membranes to become useful for industrial water treatment and desalination, they have to be formed in flat sheets of large surface area, rather than vesicular aggregates. This can be achieved either by immobilization of aggregates or templating of membrane growth on supported porous membranes. Additionally, it is planned to fluorescently label the N-terminus of AQP-Z in order to quantify the reconstitution efficiency ofmembranes from block copolymers of different block lengths ratios.

The methodology developed for novel immobilized nanoreactors enabling investigation of water soluble enzymes may serve as an investigation tool for studies over a wide range of different reactions or bioconversions and can be applied as a novel method for construction of chemically/biologically active surfaces for analytics, sensors and even controlled reactions. The studied immobilization methodology can be easily extended by the use of covalent attachment onto different types of substrates, by modifications of the functional end-groups of the block copolymer with control over the density of reactive species. In addition, post modification of the block-copolymer may lead to introduction of further functionality at the surface of the nanoreactors and accompanied by insertion of active compounds in the hydrophobic part of the membrane - enabling studies of cascade reactions. The morphology of the reactive surface is dependent on the structure of the PDMS mask used and may be chosen for specific application.

5. Materials and methods

In this chapter information on materials and methods not included in the original publications are discussed.

5.1 PMOXA-PDMS-PMOXA triblock copolymer synthesis and modifications

The ABA block copolymer synthetic route is discussed on the example of $A_{12}B_{55}A_{12}$ block copolymer.

5.1.1 α,ω-Bis(4-hydroxybutyl) polydimethylsiloxane synthesis.

250 ml round-bottom flask, equipped with reflux condenser and magnetic stirrer, was charged with 100 g (0.8317 mol) of dimethoxydimethylsilane, 5.1482 g (0.01848 mol) of 1-3-Bis(hydroxybutyl)tetramethyldisiloxane and 14.97 g (0.8317 mol) of bi-distilled water. 2 ml of concentrated HCl was injected and the reaction mixture was heated at 60°C for 1 h. Methanol was than distilled of and 66 ml were collected. The stirring was changed to mechanical and upon addition of 66 ml of 6 M HCl, the reaction mixture was stirred at 1920 RPM, 60°C for 4 h. The crude product was separated from the aqueous layer. Diethyl ether was added and the solution was extracted with saturated solution of sodium bicarbonate twice and with bi-distilled water, until washings were neutral. Upon removal of solvent, the product was vacuum stripped at 80°C for 1 h. The purified product was added dropwise to vigorously stirred equal weight mixture of methanol and bi-distilled water. Product was than extracted with diethyl ether and the precipitation procedure was repeated twice. To the last precipitation mixture small amount of diethyl ether (20 ml) was added to enable removal of small molecular weight oligomers not removed by first vacuum stripping procedure. The product was further high-vacuum stripped, at 80°C in the rotary ball tube distiller (Buechi) for 8 h. The reaction yield including purification steps was found to be 60% of the polymer of Mn = 4070g/mol.

5.1.2 Symmetric attachment of poly-2-methyl-2-oxazoline

250 ml three neck round-bottom flask was charged with 33.82 g (8.3096×10^{-3} mol) of α,ω-bis(4-hydroxybutyl) polydimethylsiloxane and kept under high vacuum for 24 h. Upon multiple freeze drying cycles a Soxhlet extractor filled with dried molecular sieves (3A) and reflux condenser is mounted under argon flow onto the three neck flask containing dried PDMS. Dry hexane (150 ml) was added under argon flow to the PDMS. The solvent was recirculated for 48h under argon in order to remove the last traces of water. Upon removal of Soxhlet extractor the hexane solution of PDMS was cooled down to -10˚C and 1.8078 g (1.7865×10^{-2} mol, 7.5 % excess in respect to hydroxyl groups of PDMS) of dry triethylamine was added. Than 4.9261 g (1.745×10^{-2} mol, 5% excess in respect to hydroxyl groups of PDMS, in 19 ml of hexane) of trifluoromethanesulfonic anhydride was added

dropwise to the stirred and cooled reaction mixture. After 3 h, the solvent was removed under high vacuum and a fresh portion of dry hexane was added. The reaction mixture was filtered under argon via home-made G4 ceramic filtration unit equipped with the cooling envelope. Solvent was then removed under high vacuum resulting in colorless triflate activated PDMS. Dry ethyl acetate (100 ml) was added, followed by addition of 27.1422 g (0.3193 mol, 20% excess in respect to hydroxyl groups of PDMS, 16 units of PMOXA targeted) of 2-methyl-2-oxazoline. Ring opening polymerization was terminated by addition of 33.23 ml (9.3096 x 10^{-3} mol) of 0.5M KOH in methanol. Upon removal of solvents the resulting ABA block copolymer was purified in small parts (c.a. 5 g) by subsequent ultrafiltration in 1:5 (w/w) ethanol-water mixture, until washings did not show any dissolved solids. The purified product was further dissolved in 1:5 water ethanol mixture and most of the ethanol was removed by rotary evaporation. The remaining solution was freeze-dried to obtain fine powder. Traces of unreacted PDMS were removed by subsequent precipitation in hexane.

5.1.3 End-group methacrylation

$A_{15}B_{110}A_{15}$ - methacrylation

In a three neck round-bottom flask, equipped with reflux condenser, 2 g (1.8691 x 10^{-4} mol) of the hydroxy-terminated $A_{15}B_{110}A_{15}$ triblock copolymer was dissolved at room temperature, under argon in 20 mL of dry ethyl acetate. To this solution 60 mg (4.0044 x 10^{-4} mol, 3.5% excess) of 2-isocyanatoethylmethacrylate (IEM) and about 40 mg of dibutyltin dilaureate were added. The solution was stirred for 48 h in the absence of light at 40°C. Solvent was evaporated under high vacuum and the raw product was purified by ultrafiltration in a 1:5 (w/w) water-ethanol mixture to remove low molecular weight impurities.

$A_{12}B_{55}A_{12}$ – methacrylation

In a three neck round-bottom flask, equipped with reflux condenser 4 g (6.5466 x 10^{-4} mol) of the hydroxy-terminated $A_{12}B_{55}A_{12}$ triblock copolymer was dissolved at room temperature, under argon in 40 mL of dry ethyl acetate. To this solution 210 mg (1.3552 x 10^{-3} mol, 3.5% excess) of 2-isocyanatoethylmethacrylate (IEM) and about 40 mg of dibutyltin dilaureate were added. The solution was stirred for 48 h in the absence of light at 40°C. Solvent was evaporated under high vacuum and the raw product was purified by ultrafiltration in a 1:5 (w/w) water-ethanol mixture to remove low molecular weight impurities.

5.1.4 End-group biotinylation

$A_{14}B_{110}A_{14}$ – biotinylation

In a three neck round-bottom flask, equipped with reflux condenser 1 g (9.4056×10^{-5} mol) of the hydroxy-terminated $A_{65}B_{165}A_{65}$ triblock copolymer was dissolved at room temperature, under argon in 20 mL of dry chloroform. To this solution 213 mg (8.7184×10^{-4} mol, 4 fold excess) of D-biotin, 300 mg of N,N'-dicyclohexylcarbodiimide and catalytic amout of 4-dimethylaminopyridine were added. The solution was stirred for 48 h at 40°C. Solvent was evaporated under high vacuum and the raw product was purified by ultrafiltration in a 1:5 (w/w) water-ethanol mixture to remove low molecular weight impurities.

$A_{65}B_{165}A_{65}$ – biotinylation

In a three neck round-bottom flask, equipped with reflux condenser 2 g (8.5984×10^{-5} mol) of the hydroxy-terminated $A_{65}B_{165}A_{65}$ triblock copolymer were dissolved at room temperature, under argon in 20 mL of dry chloroform . To this solution 167.9 mg (6.8788×10^{-4} mol, 4 fold excess) of D-biotin and 141.8 mg of N,N'-dicyclohexylcarbodiimide and catalytic amout of 4-dimethylaminopyridine was added. The solution was stirred for 48 h at 40°C. Solvent was evaporated under high vacuum and the raw product was purified by ultrafiltration in a 1:5 (w/w) water-ethanol mixture to remove low molecular weight impurities.

5.2 Polymer characterization

5.2.1 NMR

NMR spectra were acquired on a Varian Unity 400 NMR spectrometer, operated at 400 MHz with a sweep width of 8278.146 Hz and 22° pulse width of 2.96 μs. $CDCl_3$ was used as solvent.

5.2.2 GPC

GPC measurements were performed with a PLgel Mixed-C (5 μm particle size) column (300x7.5 mm) and THF as eluent in an Agilent modular system (Agilent 1100 Series Module GPC). Two

detectors were used, a UV fixed wavelength (λ=254 nm) and a refractive index (RI). Polystyrene standards of narrow molecular weights (Polystyrene Easical vials, Agilent technologies) were used for calibration. Injection volumes were 50 μL and polymer concentrations 1 mg/ml. Samples were filtered through 0.2 μm milipore filters. Flow rates were 1ml/min and measurements were performed in thermostized columns at 23°C. Chromatograms, molecular weight distributions, and molecular weight averages were analyzed with the software ChemStation for GPC.

5.2.3 Fourier Transform Infrared (FTIR) spectroscopy.

A 30-50 mg sample of polymer was dissolved in 5 ml $CHCl_3$ and transferred to a glass slide. In the case of $A_{15}B_{110}A_{15}$ it was left overnight to dry and form a thick film. For $A_{12}B_{55}A_{12}$ the glass slide was put in a vacuum evaporator to dry off the $CHCl_3$. Attenuated total reflectance Fourier transform infrared (ATR-FTIR) spectrometry was used to assess changes in characteristic functional groups of the methacrylated triblock co-polymer during UV crosslinking. Analyses were performed with a NEXUS 670 FTIR spectrometer (Thermo Nicolet Corporation, Madison, WI) equipped with a smart golden gate accessory, DTGS-KBr detector, KBr beam-splitter and diamond crystal. An IR source at 45° incident angle was employed. Samples of polymer were put in direct contact with the diamond crystal and 32-64 scans were conducted in the range of 600 to 4000 cm-1 for each sample. The information from these scans was averaged by the instrument to provide IR spectra which were then analyzed.

5.3 Native polymers self assembly: physico-chemical characterization

5.3.1 Vesicles preparation methods

Vesicles preparation methods involve solvent free-techniques and techniques where an amphiphilic block copolymer is initially solubilized in organic solvent. Some applications, like encapsulation of sensitive materials or membrane protein insertion, require solvent-free preparations. Depending on the system, each method can yield varying self-assembled superstructures (micelles, vesicles, tubes). Homogenization and decrease of the size distribution of vesicle in dispersion can be achieved through vortexing, freeze–thaw cycles, extrusion and sonication, or a combination of these methods. These steps usually also lead to the decrease of the mean vesicle diameter as well as lamellarity of vesicles.[10]

5.3.1.1 Solvent displacement

In the solvent displacement method, the amphiphile is first dissolved in an appropriate organic solvent and then added dropwise to an aqueous solution under vigorous stirring. This leads to the dispersion of vesicles of a rather broad size distribution. It is a very fast and convenient method to produce vesicles, with the drawback of having low amount of organic solvent remaining in the vesicles and the surrounding liquid. Solvent residues may interfere in biological applications and may cause fluidization of membranes leading to decreased vesicle stabilities.[10] Utilizing the solvent displacement technique for generating aggregates in dilute aqueous solutions of PMOXA-PDMS-PMOXA resulted in the formation of two populations of aggregates with broad size distribution seen in DLS measurement. The estimated size PDI of the aggregates was 0.4 (Figure 27).

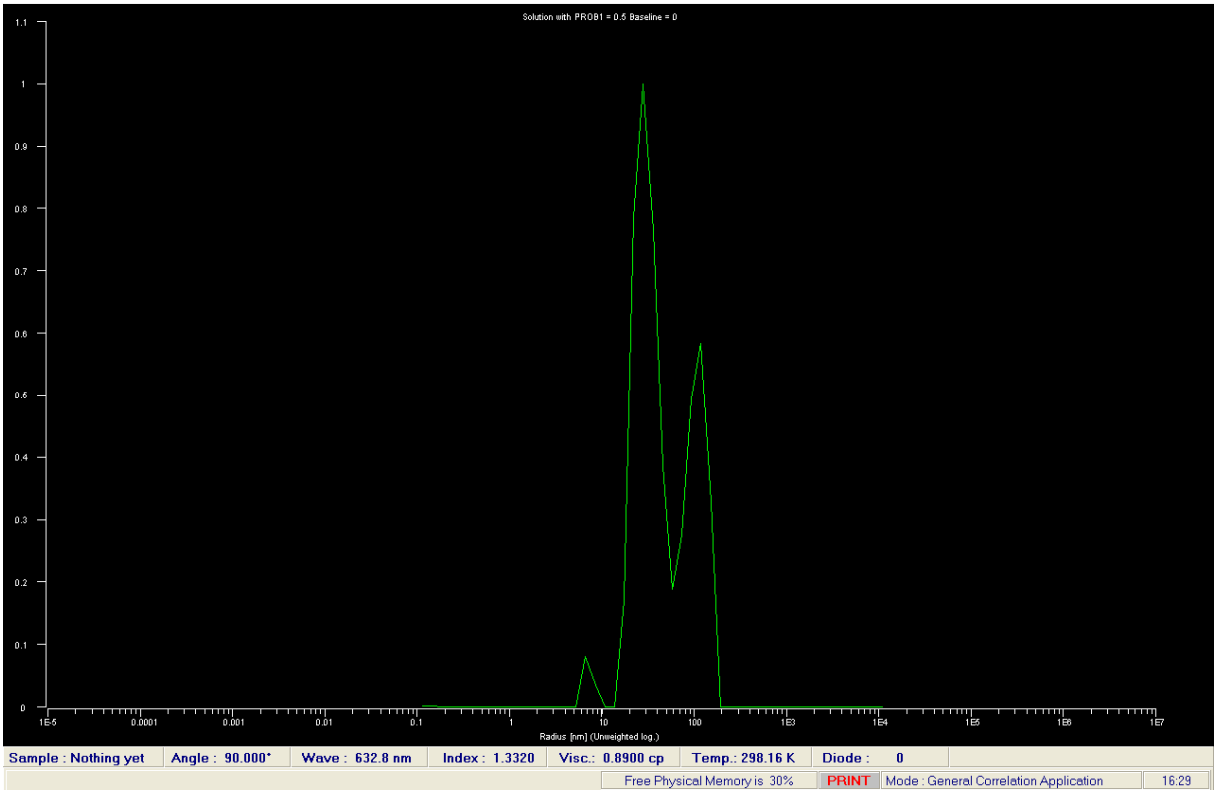

Figure 27. DLS data obtained at 90° for mixed aggregates (vesicles and micelles) prepared with the solvent displacement method (10 mg/ml of $A_{12}B_{55}A_{12}$ in PBS buffer, pH 7.4).

5.3.1.2 Detergent removal

In the detergent removal method the amphiphilic block copolymer is solubilized in a detergent solution. Upon removal of detergent the superstructures are formed.[10] Detergent removal can be achieved with the aid of different techniques: dialysis[49], adsorption on hydrophobic porous beads[49] or chromatography[50]. Each of the approaches offers different ways of controlling the removal rate. The

rate at which the detergent is removed influences the sizes and morphologies of the resulting aggregates: slow detergent removal generally leads to formation of large aggregates. Figures 28 and 29 show different sizes and morphologies of the aggregates resulting from different detergent removal rates.

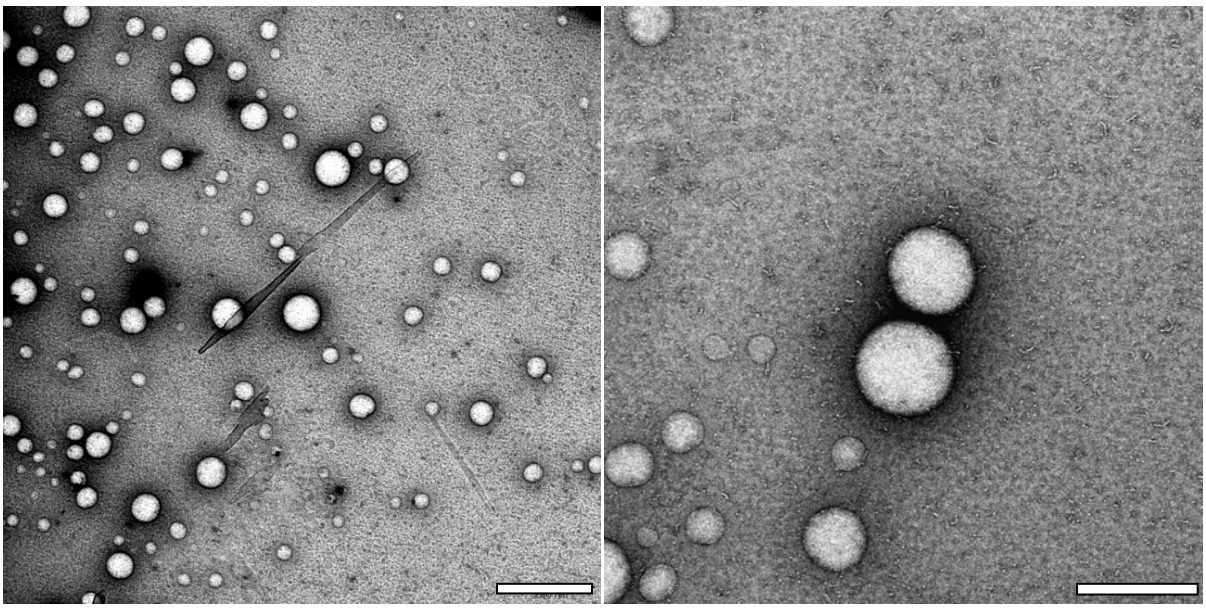

Figure 28. TEM micrographs of giant vesicles, stained with 2% uranyl acetate, upon slow detergent removal (2 weeks, 4˚C). Scale bar 5000 nm (left) and 2000 nm (right).

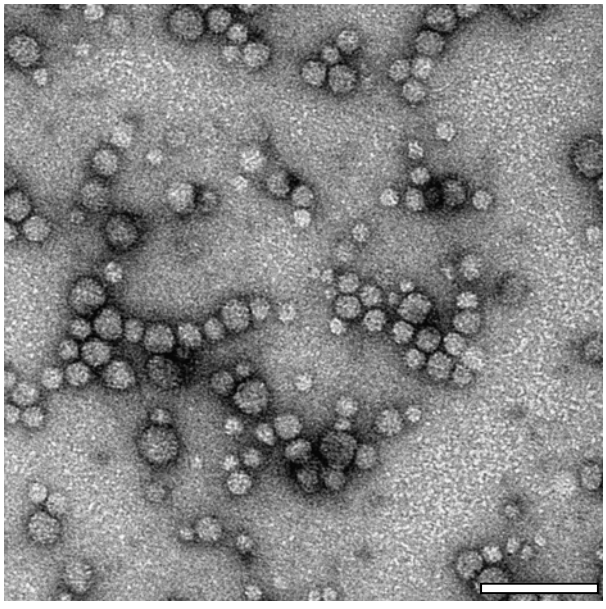

Figure 29. TEM micrographs of micelles/vesicles, stained with 2% uranyl acetate, resulting from fast detergent removal (3 days, ambient temperature). Scale bar 100nm.

5.3.1.3 Film hydration

In the film hydration method, the amphiphilic block copolymer is first dissolved in organic solvent. Slow, controlled removal of the solvent leads to the formation of a thin polymer film on solid support. After further drying, the thin film is exposed to the aqueous solution resulting in swelling of the polymer film. Water molecules permeate through the defects of the film allowing its hydration.[10] The lamellar structures present in the polymer film and dilute vesicles were well characterized in literature, but the intermediate phases are not well understood.[14] Film hydration was the preferential technique, to generate vesicular aggregates of well defined sizes. For instance, $A_{12}B_{55}A_{12}$ vesicles prepared with this method are characterized by low size polydispersity (PDI < 0.15) of uniform vesicles, as shown in Figure 30. Additionally, this technique was utilized in experiments involving bio-molecules (enzymes, membrane proteins), incompatible with the solvent displacement approach.

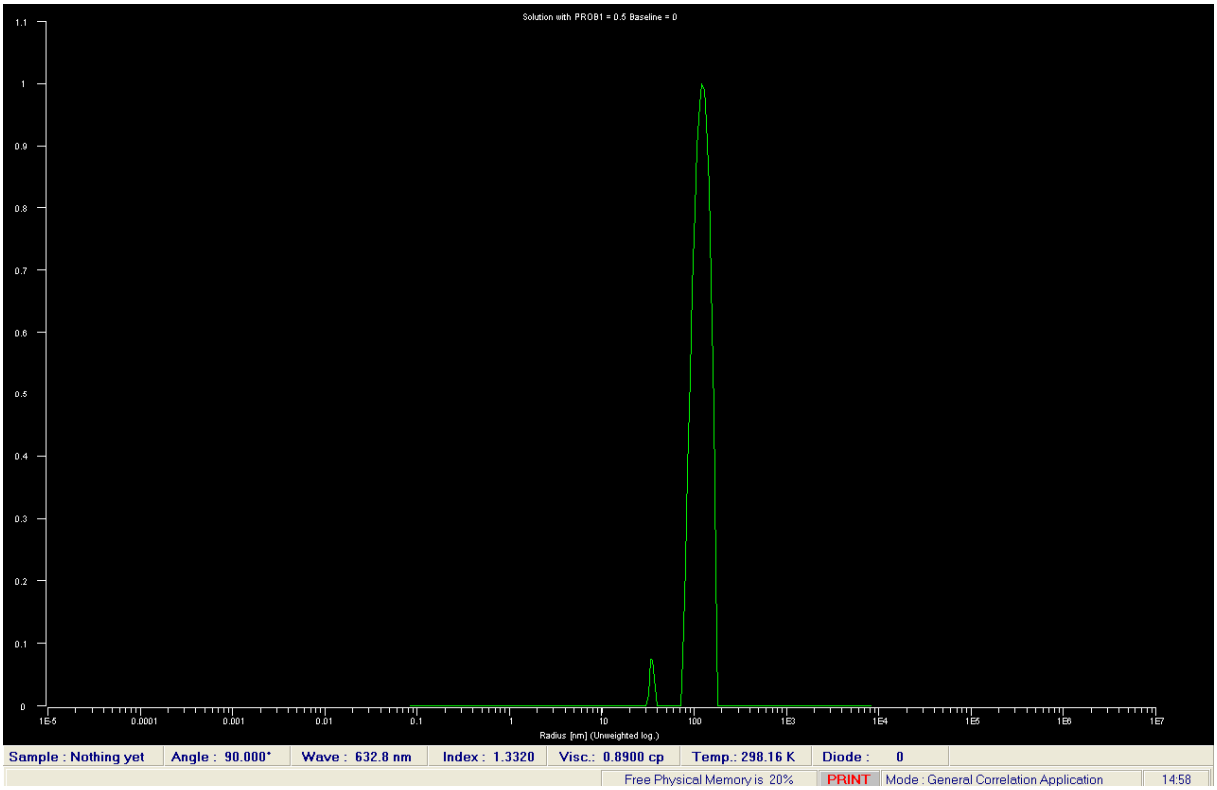

Figure 30. DLS data obtained at 90° for uniform vesicles prepared with film hydration method (6 mg/ml of $A_{12}B_{55}A_{12}$ in PBS buffer, pH 7.4).

5.3.2 Self-assembly characterization toolbox

Self-assembly properties of PMOXA-PDMS-PMOXA block copolymers were investigated, with the set of analytical methods commonly used in physicochemical characterization of colloidal superstructures. Techniques employed for investigation of the size and morphology of aggregates included: transmission electron microscopy (TEM), cryogenic- transmission electron microscopy (cryo-TEM), dynamic and static light scattering (DLS, SLS), fluorescence correlation spectroscopy (FCS) and atomic force microscopy (AFM). laser scanning microscopy (LSM) was used for visualization of particles and processes involving fluorescent products formation. The interfacial behavior of block copolymers membranes was studied using the Langmuir balance (LB) and Brewster angle microscopy (BAM).

5.3.2.1 FCS

Fluorescence correlation spectroscopy (FCS) measurements were accomplished on a ZEISS LSM 510 META/Confocor2 microscope equipped with different laser lines.

5.3.2.2 Chemicals

- Acetone-D_6, Fluka, puriss.,
- Acid phosphatase, Sigma-Aldrich, lyophilized powder, 3-10 units/mg solid
- 1,3-Bis(hydroxybutyl)tetramethyldisiloxane, 95% ABCR GmbH,
- Biotin-D, Sigma-Aldrich,
- Chloroform, Sigma-Aldrich, 98.8%,
- Dicyclohexylcarbodiimide (DCC), Fluka, puriss.,
- Dibutyltin dilaurate, Sigma-Aldrich, 95%
- 4-dimethylaminopyridine (DMAP), Aldirch, 99%,
- Diethyl ether, technical Schweizerhall, distilled,
- Dimethoxydimethylsilane, Sigma-Aldrich, 95%,
- ELF 97®, Invitrogen,
- Ethanol, 96% EP, Schweizerhall,
- Ethyl acetate, Sigma-Aldrich, anhydrous, 99.8%.,
- Hexane, Fluka, puriss.,
- Hydrochloric acid, Sigma-Aldrich, ACS reagent, 37%,
- 2-isocyanatoethylmethacrylate, Sigma-Aldrich, 98%,
- Sodium bicarbonate, Sigma-Aldrich, puriss.,
- Sodium hydroxide, Sigma-Aldrich, reagent ACS,
- Triethylamine, Sigma-Aldrich, puriss.,
- Triflic anhydride, Sigma-Aldrich, purum.,

6. References

1. Fred, W. and J. Billmeyer, *Textbook of polymer science*. 1984: A Wiley-Interscience Publication John Wiley & Sons.
2. Jones, R.A.L., *Biomimetic nanotechnology with synthetic macromolecules.* J. Polym. Sci., Part B: Polym. Phys., 2005. **43**(23): p. 3367-3368.
3. Conroy, R.S. and C. Danilowicz, *Unravelling DNA.* Contemp. Phys., 2004. **45**(4): p. 277-302.
4. Barron, A.E. and R.N. Zuckermann, *Bioinspired polymeric materials: in-between proteins and plastics.* Curr Opin Chem Biol, 1999. **3**(6): p. 681-7.
5. Bates, F.S. and G.H. Fredrickson, *Block copolymers-designer soft materials.* Phys. Today, 1999. **52**(2): p. 32-38.
6. J. M., et al., *Biomimicry: Innovation Inspired by Nature*. 1997: Harper Collins Publishers.
7. A. D., J., et al., *GLOSSARY OF BASIC TERMS IN POLYMER SCIENCE (IUPAC Recommendations 1996).* 1996.
8. Xiao, *Synthesis and self-assembly of amphiphilic dendronized conjugated polymers* Polymer chemistry 2007. **46**(2): p. 574.
9. Lodge, P.C.H.i.P., *Polymer Chemistry*. 2007: CRC Press.
10. Kita-Tokarczyk, K., et al., *Block copolymer vesicles-using concepts from polymer chemistry to mimic biomembranes.* Polymer, 2005. **46**(11): p. 3540-3563.
11. Caruso, F., *Colloids and colloid Assembly*. 2004: Wiley-VCH GmbH & Co. KGaA.
12. Ottewill, R.H., et al., *Micellar Structure in Solutions of an Ultralong Chain Zwitterionic Surfactant.* Langmuir, 1994. **10**(10): p. 3493-9.
13. Bangham, A.D., *Liposomes: The Babraham connection.* Chem. Phys. Lipids, 1993. **64**(1-3): p. 275-85.
14. Battaglia, G. and A.J. Ryan, *The evolution of vesicles from bulk lamellar gels.* Nat. Mater., 2005. **4**(11): p. 869-876.
15. Shen, H.Z., L.; Eisenberg, A., J. Am. Chem. Soc., 1999(121): p. 2728-2740.
16. Determan, M.D., et al., *Supramolecular Self-Assembly of Multiblock Copolymers in Aqueous Solution.* Langmuir, 2006. **22**(4): p. 1469-1473.
17. Zhang, L.E., A., J. Polym. Sci., Part B: Polym. Phys., 1999(37): p. 1469-1484.
18. B. Alberts, et al., *Molecular Biology of The Cell*. 2002: Garland Science Taylor & Francis Group.

19. Allison, A.G. and G. Gregoriadis, *Liposomes as immunological adjuvants.* Nature, 1974. **252**(5480): p. 252.

20. Gregoriadis, G., *Engineering liposomes for drug delivery: progress and problems.* Trends Biotechnol., 1995. **13**(12): p. 527-37.

21. Christian, D.A., et al., *Polymersome carriers: From self-assembly to siRNA and protein therapeutics.* Eur. J. Pharm. Biopharm., 2009. **71**(3): p. 463-474.

22. Yilgor, I., et al., *Novel triblock siloxane copolymers: synthesis, characterization, and their use as surface modifying additives.* J. Polym. Sci., Part A: Polym. Chem., 1989. **27**(11): p. 3673-90.

23. Cesana, S., et al., *Polymer-bound thiol groups on poly(2-oxazoline)s.* Macromol. Rapid Commun., 2007. **28**(5): p. 608-615.

24. Goddard, P., et al., *Soluble polymeric carriers for drug delivery. Part 2. Preparation and in vivo behavior of N-acylethylenimine copolymers.* J. Controlled Release, 1989. **10**(1): p. 5-16.

25. Nardin, C., et al., *Polymerized ABA Triblock Copolymer Vesicles.* Langmuir, 2000. **16**(3): p. 1035-1041.

26. Borgnia, M.J., et al., *Functional reconstitution and characterization of AqpZ, the E. coli water channel protein.* J Mol Biol, 1999. **291**(5): p. 1169-79.

27. Boukobza, E., A. Sonnenfeld, and G. Haran, *Immobilization in surface-tethered lipid vesicles as a new tool for single biomolecule spectroscopy.* J. Phys. Chem. B, 2001. **105**(48): p. 12165-12170.

28. Przybylo, M., et al., *Lipid diffusion in giant unilamellar vesicles is more than 2 times faster than in supported phospholipid bilayers under identical conditions.* Langmuir, 2006. **22**(22): p. 9096-9099.

29. Wollert, T., et al., *Membrane scission by the ESCRT-III complex.* Nature (London, U. K.), 2009. **458**(7235): p. 172-177.

30. Pata, V. and N. Dan, *The effect of chain length on protein solubilization in polymer-based vesicles (polymersomes).* Biophys. J., 2003. **85**(4): p. 2111-2118.

31. Meier, W., C. Nardin, and M. Winterhalter, *Reconstitution of channel proteins in (polymerized) ABA triblock copolymer membranes.* Angew. Chem., Int. Ed., 2000. **39**(24): p. 4599-4602.

32. Nardin, C. and W. Meier, *Hybrid materials from amphiphilic block copolymers and membrane proteins.* Rev. Mol. Biotechnol., 2002. **90**(1): p. 17-26.

33. Mecke, A., C. Dittrich, and W. Meier, *Biomimetic membranes designed from amphiphilic block copolymers.* Soft Matter, 2006. **2**(9): p. 751-759.

34. King, L.S., D. Kozono, and P. Agre, *From structure to disease: the evolving tale of aquaporin biology.* Nat Rev Mol Cell Biol, 2004. **5**(9): p. 687-98.

35. Kozono, D., et al., *Aquaporin water channels: atomic structure and molecular dynamics meet clinical medicine.* J. Clin. Invest., 2002. **109**(11): p. 1395-1399.

36. Koebnik, R., K.P. Locher, and P. Van Gelder, *Structure and function of bacterial outer membrane proteins: barrels in a nutshell.* Mol. Microbiol., 2000. **37**(2): p. 239-253.

37. Sazanov, L.A. and P. Hinchliffe, *Structure of the hydrophilic domain of respiratory complex I from Thermus thermophilus.* Science, 2006. **311**(5766): p. 1430-6.

38. Zickermann, V., et al., *Challenges in elucidating structure and mechanism of proton pumping NADH:ubiquinone oxidoreductase (complex I).* J. Bioenerg. Biomembr., 2008. **40**(5): p. 475-483.

39. Ahmed, F., et al., *Biodegradable polymersomes loaded with both paclitaxel and doxorubicin permeate and shrink tumors, inducing apoptosis in proportion to accumulated drug.* J. Controlled Release, 2006. **116**(2): p. 150-158.

40. Lai, Y.-C., R. Ozark, and E.T. Quinn, *Synthesis and characterization of alpha ,w-bis(4-hydroxybutyl) polydimethylsiloxanes.* J. Polym. Sci., Part A: Polym. Chem., 1995. **33**(11): p. 1773-82.

41. Terreau, O., C. Bartels, and A. Eisenberg, *Effect of Poly(acrylic acid) Block Length Distribution on Polystyrene-b-poly(acrylic acid) Block Copolymer Aggregates in Solution. 2. A Partial Phase Diagram.* Langmuir, 2004. **20**(3): p. 637-645.

42. Lynd, N.A. and M.A. Hillmyer, *Influence of polydispersity on the self-assembly of diblock copolymers.* Macromolecules, 2005. **38**(21): p. 8803-8810.

43. Young, R.J. and P.A. Lovell, *Introduction to Polymers.* XRC Press, 1991.

44. W. Steglich, G.H., Angewandte Chemie, International Edition in English, 1969. **8**(981).

45. Meier, W., *Reversible Cell Aggregation Induced by Specific Ligand-Receptor Coupling.* Langmuir, 2000. **16**(3): p. 1457-1459.

46. Rigler, P. and W. Meier, *Encapsulation of fluorescent molecules by functionalized polymeric nanocontainers: investigation by confocal fluorescence imaging and fluorescence correlation spectroscopy.* J. Am. Chem. Soc., 2006. **128**(1): p. 367-373.

47. Herrington, R. and K. Hock, *Flexible Polyurethanes Foams.* The Dow Chemical Company, 1977.

48. Lovell, R.J.Y.P.A., *Introduction to polymers*. 1991: CRC Press

49. Rigaud, J.L., et al., *Detergent removal by non-polar polystyrene beads. Applications to membrane protein reconstitution and two-dimensional crystallization.* Eur. Biophys. J., 1998. **27**(4): p. 305-319.

50. Levy, D., et al., *Two-Dimensional Crystallization on Lipid Layer: A Successful Approach for Membrane Proteins.* J. Struct. Biol., 1999. **127**(1): p. 44-52.

Appendix

Table of Contents

1. Two-dimensional (2D) crystallization of membrane proteins in ABA block copolymer matrix-preliminary work

The difficulty in crystallizing channel proteins in three dimensions limits the use of X-ray crystallography in solving their structures. In contrast, the amphiphilic character of integral membrane proteins promotes their integration into artificial lipid bilayers. Protein–protein interactions may lead to ordering of the proteins within the lipid bilayer into two-dimensional crystals that are amenable to structural studies by electron crystallography and atomic force microscopy. While insertion of membrane proteins in lipid membranes is readily achieved[1], the mechanisms for crystal formation during or after membrane reconstitution are not well understood. The nature of the detergent and lipid, as well as pH and counter-ions are known to influence the crystal type and quality [1](ref). Protein–protein interactions may also promote crystal stacking and aggregation of the sheet-like crystals, posing problems in data collection [1].

Electron crystallography is a structure determination technique that produced excellent results for prokaryotic and eukaryotic membrane proteins (ref). It has the attractive feature of studying the protein within an environment (the lipid bilayer) close to its natural surroundings. In the case where a channel of interest is present only in small amounts, is greatly dispersed in the membrane, and cannot be easily manipulated into crystalline arrays, 2D crystallization of purified channel proteins offers an alternative. Three major processes are involved in 2D crystallization of membrane channels: reconstitution of the bilayer with the protein; arrangement or rearrangement of the protein into a lattice order, the actual crystallization event; and crystal folding and clustering. These processes may occur sequentially or concurrently, depending on many poorly understood parameters.[1]

To produce high-quality 2D crystals, the protein of interest must usually be purified from other proteins and contaminants. This involves solubilization of the original membrane with detergent and commonly requires several subsequent separation steps. Finally, the pure protein is obtained in a detergent solution, often with residual lipids. The nature of the detergent in both protein purification and subsequent crystallization trials is a critical determinant of success. Most frequently, detergents with a high critical micelle concentration (CMC), such as octyl-b-glucoside (OG) or n-dodecyl-β-d-maltoside (DDM) have been used, because of the ease with which they can be removed by dialysis [1]. The bilayer reconstitution with membrane proteins is achieved by decreasing the detergent concentration in the presence of lipids.[1]

There is clear relationship between detergent concentration and the sizes of the formed structures. The ‘‘three-stage’’ Lichtenberg’s model (ref) involves: stage I characterized by a detergent concentration that is low enough not to disrupt the lipid bilayer, stage II where the lipid bilayer and mixed micellar structures coexist, and stage III covers the high detergent concentration where only small micellar structures occur. These specific regions are the ‘‘saturation’’ and ‘‘solubilization’’ points that define completion of the solubilization of large structures upon addition of detergent. The micelle-bilayer transition region (Stage II) was found key to reconstitution and - by implication, to 2D crystallization. In the next steps detergent concentration is decreased, lipid and protein interact due to the exposure of their hydrophobic surfaces. With an excess of lipid over protein, the protein is mainly incorporated into lipid bilayers, similarly to its native state. In an excess of protein over lipid, the protein mostly forms amorphous aggregates, where it is most probably denatured. Another important parameter is therefore the lipid:protein ratio (LPR), which should be low enough to promote crystal contacts between protein molecules, but not so low that the protein is lost to aggregation. Reconstitution is closely linked to the properties of the detergents used during both purification and the reconstitution itself (the detergents used for purification can be exchanged for a different detergent used for reconstitution). The manner in which the detergent concentration is decreased is an important factor. .[1, 2]

Utilization of established protocols allowed studies of various membrane proteins in the form of two-dimensional crystals (2DX). The scope of our research focused on 2D crystallization of: OmpF channels, Maltoporine, Aquaporin-Z and F_oF_1 ATPase. Two-dimensional crystals of these proteins were obtained earlier via protein solubilization in detergent/lipid mixtures followed by detergent removal – results are shown here for comparison: OmpF figure1[1], Maltoporine Figure 2 ,[1] Aquaporin-Z Figure 3, [3] and F_0F1 ATPase Figure 5 and 6[4] and Figure 7.

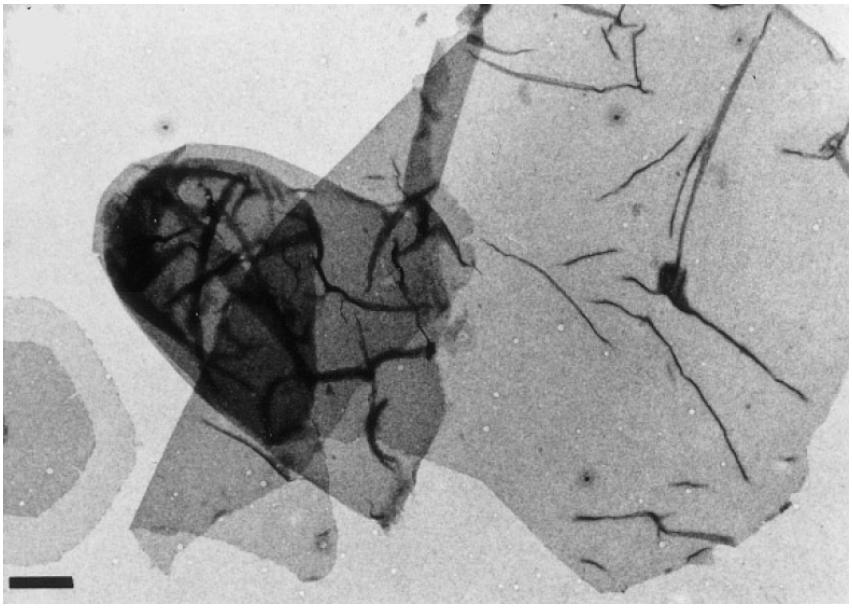

Figure 1. Large folded vesicle-type DMPC (1,2-dimyristoyl- sn -glycero-3-phosphocholine) membranes reconstituted with OmpF at LPR = 1.0 (scale bar: 1μm).[1]

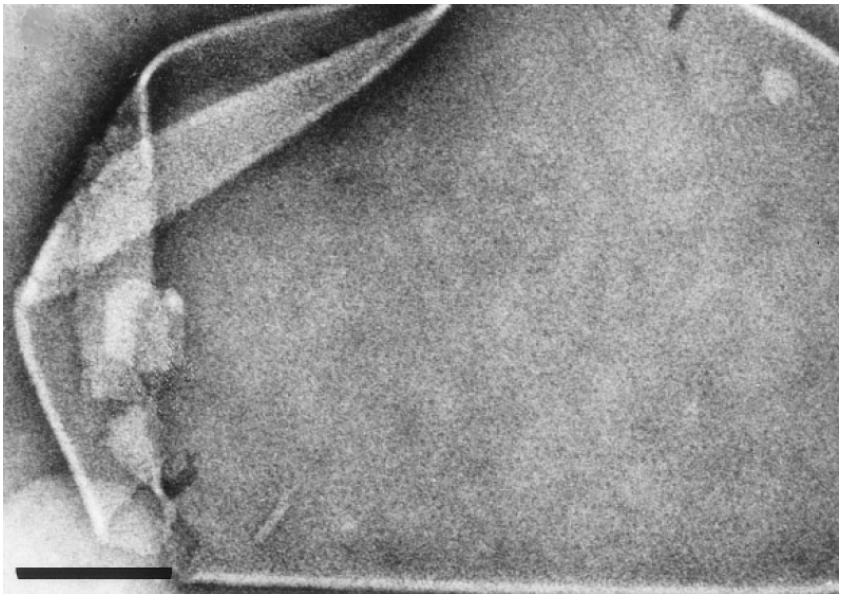

Figure 2. Membrane from *E. coli* lipids reconstituted with Maltoporin at LPR 0.1 (vesicles with double bilayers in flat areas) (scale bar: 200 nm).[1]

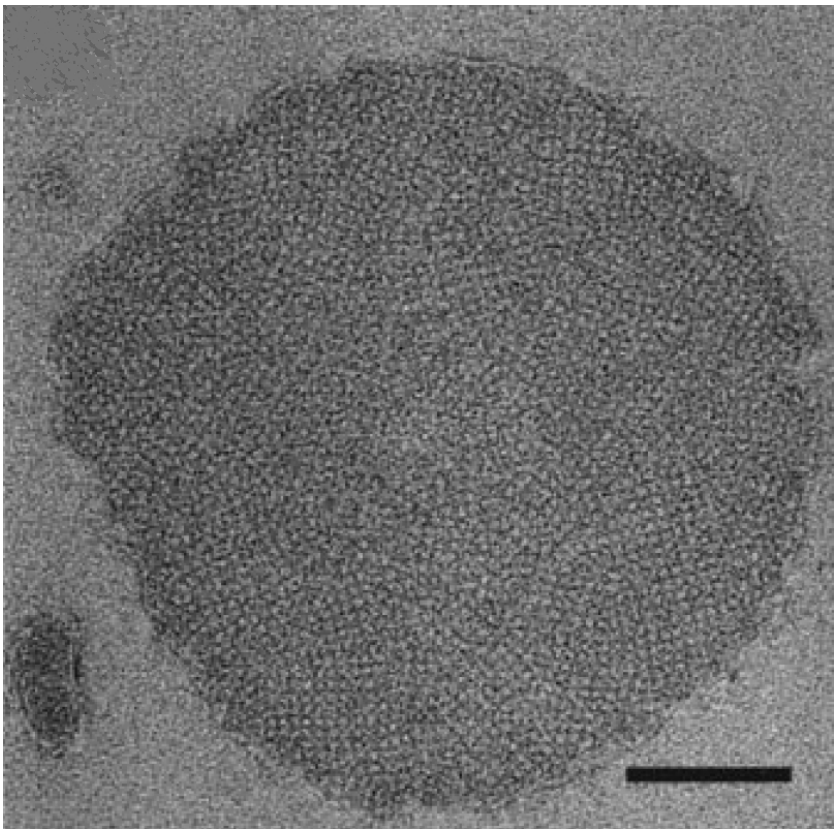

Figure 3. Electron micrograph of negatively stained lipid bilayer reconstituted with AqpZ tetramers. Flattened vesicles with densely packed square-shaped particles corresponding to AqpZ tetramers self-assembled into mosaic tetragonal lattices at the lipid-to-protein ratio of 2. Scale bar represents 100 nm.[3]

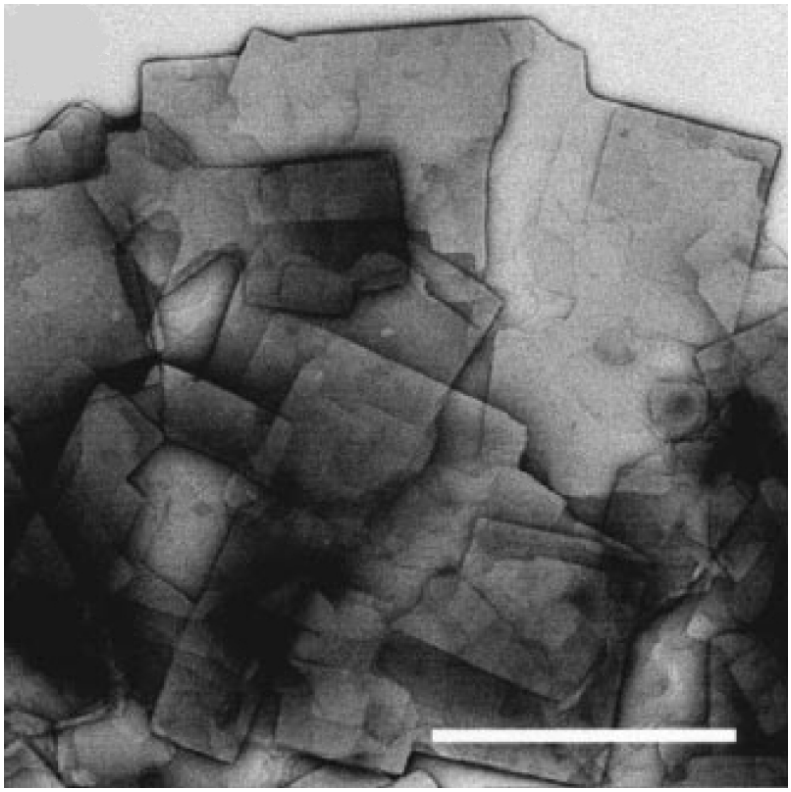

Figure 4. Electron micrograph of negatively stained lipid bilayers reconstituted with AqpZ tetramers. Large piled-up AqpZ 2D crystal sheets. Scale bar represents 1 μm.[3]

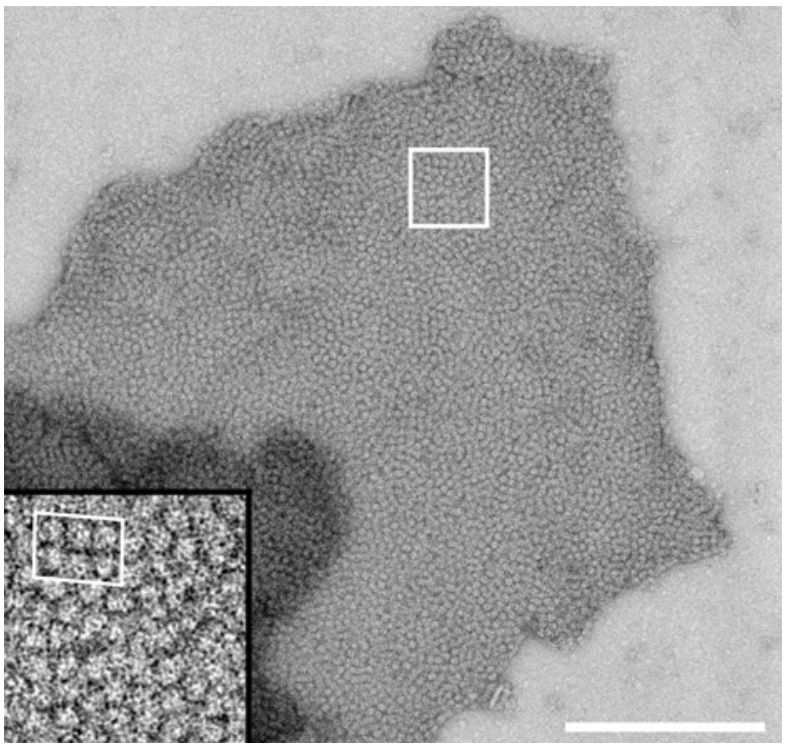

Fig. 5. Electron micrograph of negatively stained bovine F_oF_1-ATP synthase proteoliposomes. Proteoliposomes from egg yolk phosphatidylcholine PC at the LPR of 1 and protein pre-

incubated with 0.16 mM DCCD, 0.6 mM ADP, 1 mM AMP-PNP at pH 8. Detergent (DDM) was removed by addition of Bio-Beads. Large paracrystalline arrays were visible after 4–5 days incubation (inset, lower left). Scale bar 250 nm.[4]

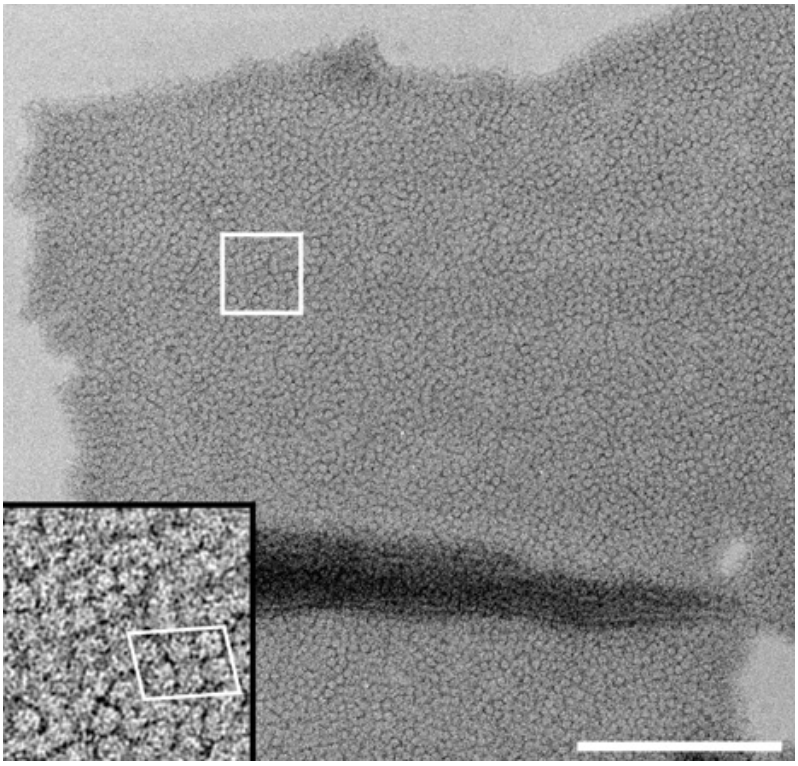

Figure 6. Electron micrograph of negatively stained membrane from a lipid mixture of egg yolk PC:DOPC (3:1), reconstituted with F_1F_0-ATPase, at the LPR of 0.5 (w/w) and pH 7.3 (no DCCD added). Detergent (DDM) was removed by addition of Bio-Beads. Large paracrystalline arrays (>1 μm) were visible after 4–5 days incubation (inset, lower left). Scale bar 250 nm.[4]

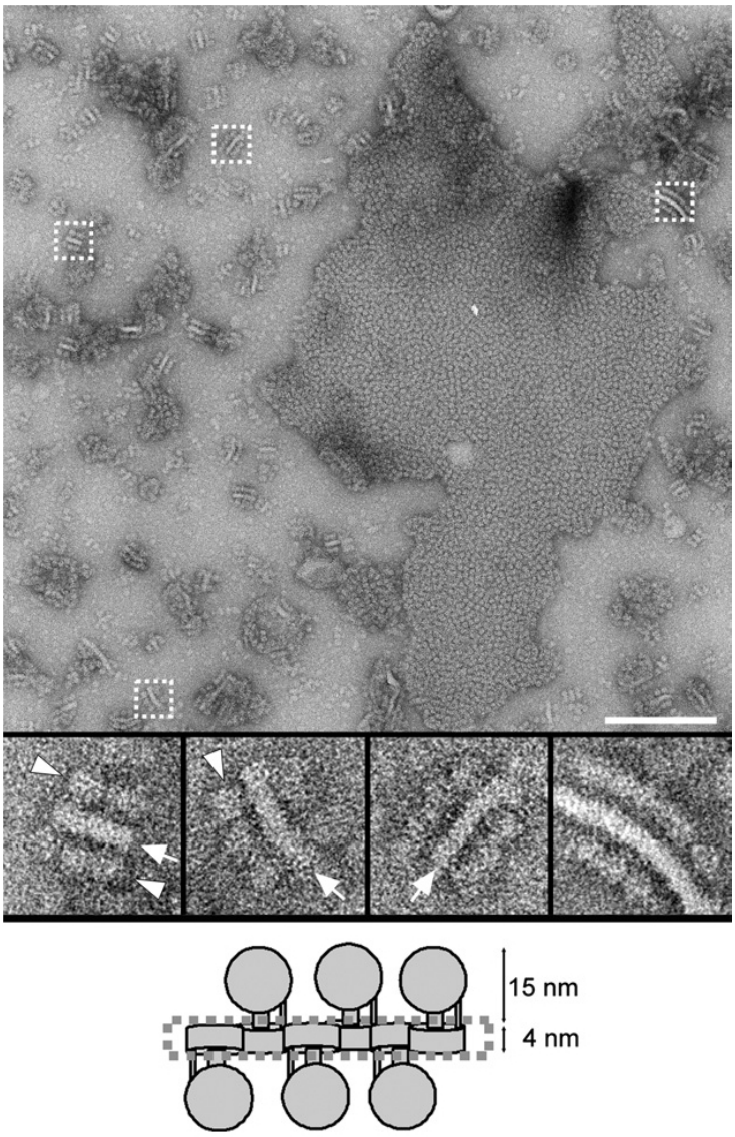

Fig. 7. Electron micrograph of stained lipid (?) membrane reconstituted with bovine F_1F_0-ATP synthase at low LPR. Electron micrograph: egg yolk PC membrane reconstituted with ATP synthase at the LPR of 0.4 (w/w). Detergent (DDM) was removed by addition of Bio Beads. Gallery: The areas in the electron micrograph marked by broken squares were magnified. Strings of F_1F_0-ATPase complexes in an up-down orientation are discerned. F_1 and F_0 domains are indicated by arrowheads and arrows, respectively. Bottom: Proposed model for the orientation of the ATP synthase in the imaged strings. Scale bar: 200 nm. Frame sizes of insets: 65 nm.[4]

Analysis of two-dimensional protein crystals in lipid bilayers provides structural information on the membrane proteins. The lipid bilayer, reconstituted with the protein, resembles the protein's natural environment - cell membrane. In our studies, we screened the possibility of two-dimensional crystallization of membrane proteins in ABA block copolymer matrix. Successful 2D crystallization of membrane proteins in block copolymer membraned

proves not only membrane reconstitution, but may also result in possibilities of protein structure determination in such a synthetic environment. In the case of the Aquaporin-Z, additional information is obtained for the design of densely packed, flat polymer-protein arrays for application in water treatment. Protocols used for 2D crystallization of the series of membrane proteins in ABA block copolymers followed the methodology developed for lipid-based systems, taking into account the molecular weight differences between the stabilizing matrixes (lipid / block copolymer). The two methods applied involved: the detergent removal method and template method utilizing Ni-NTA functionalized diblock polymer as a template at the water/air interface.

1.1 $A_{12}B_{55}A_{12}$ block copolymer-assisted 2D crystallization of membrane proteins – detergent removal method

Detergent removal from lipid-protein-detergent micellar solutions is the most successful strategy for proteoliposome reconstitution with integral membrane proteins or into two-dimensional crystall.[2] The protocol commonly used for lipid-based 2D crystallization of membrane proteins, utilizing detergent removal with the use of hydrophobic Biobeads SM-2,[2] was adapted to block copolymer-assisted crystallization studies of: Aquaporin-Z, Outer membrane protein F and F_0F_1 ATPase. Figure 8 shows the outline of the detergent removal method used.

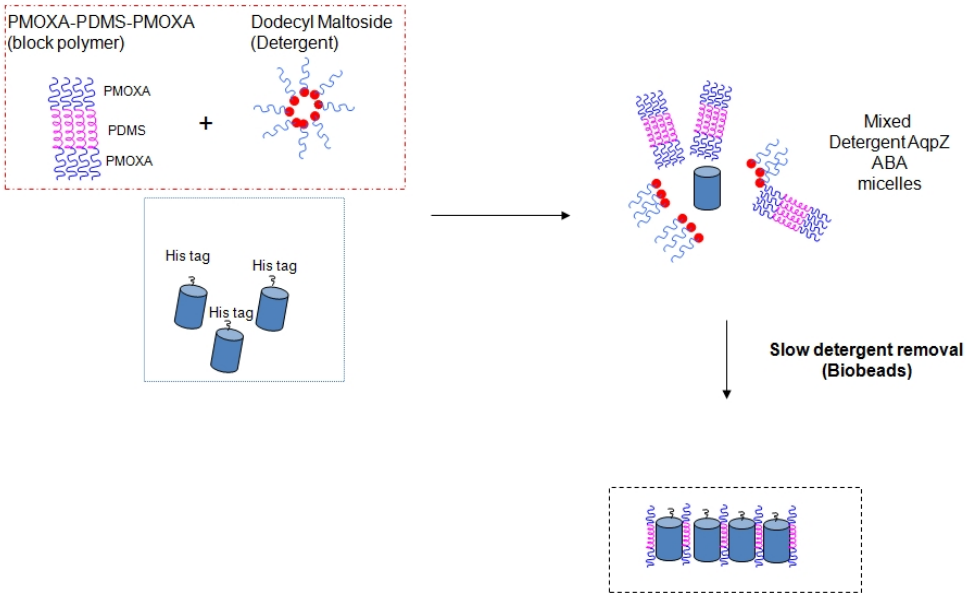

Figure 8. Outline of detergent removal experiments.

The general protocol used for all the investigated membrane proteins involved solubilization of the block copolymer, together with the protein in 10% DDM (w/v) solution in appropriate buffer. Upon overnight incubation at 4°C, the detergent was removed by subsequent addition of appropriate amount of hydrophobic beads[2] (Biobeads, Bioraid SM-2).

Conditions for 2D crystallization were screened by varying polymer to protein ratio (PoPR) and detergent removal rate. For Aquaporin-Z, the most suitable conditions resulting in large protein-rich sheets were found at PoPR=0.2, with slow detergent removal by subsequent addition of biobeads, for 14 days, at 4°C. Figure 9 shows a large Aquaporin-Z rich sheet of $A_{12}B_{55}A_{12}$ membrane. Figure 10 shows the presence of the same type of structures at PoPR=1 incubated at the same conditions but the structures populate the TEM grids in a much smaller number. Figure 11 shows results of experiments performed at ambient temperature were the detergent removal was complete within 3 days, resulting in formation of small crystalline domains for PoPR of 0.2 and 0.1.

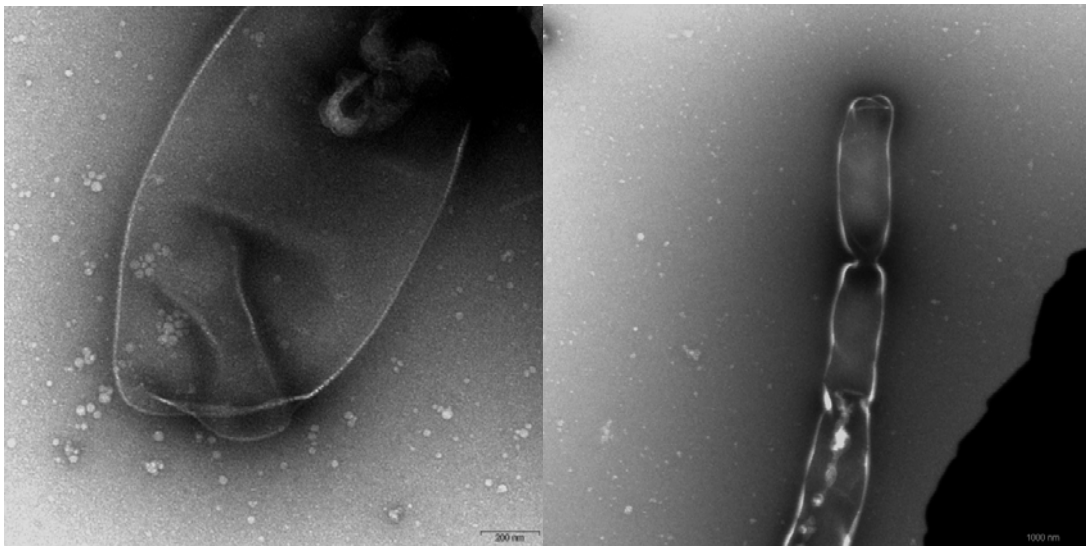

Figure 9. Electron micrographs of stained Aquaporin-Z - copolymer arrays obtained at 0.2 PoPR upon slow detergent removal (2 weeks, 4°C).

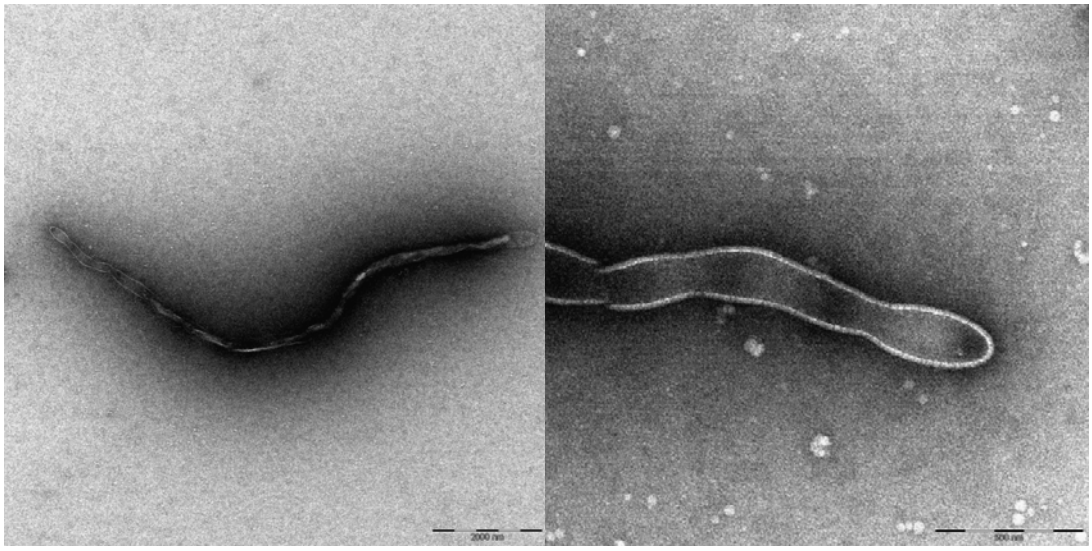

Figure 10. Electron micrographs of stained Aquaporin-Z - copolymer arrays obtained at 1 PoPR upon slow detergent removal (2 weeks, 4°C).

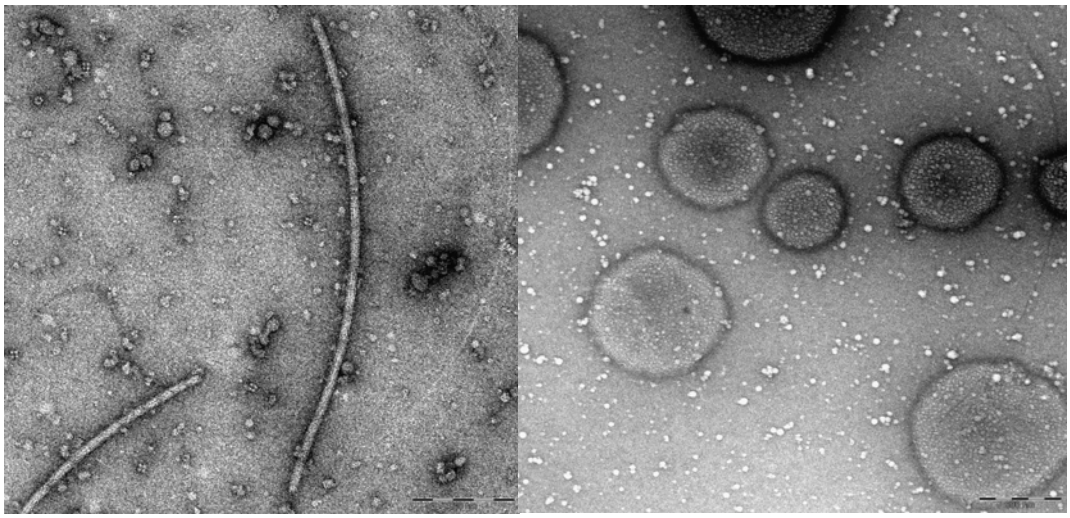

Figure 11. Electron micrographs of: stained Aquaporin-Z - copolymer array obtained at PoPR 0.2, upon fast detergent removal (left). Small crystalline structures formed and free protein tetramers are visible. Scale bar: 200 nm; Large copolymer vesicles reconstituted with Aquaporin-Z tetramers obtained at PoPR 0.1 (right), upon fast detergent removal. Scale bar: 200 nm.

The same conditions were further applied for 2D crystallization of OmpF and F_oF_1 ATPase. In the case of OmpF, both PoPR=0.2 and PoPR=2 showed formation of crystal

structures, upon fast removal of detergent. Figure 12 shows the crystalline structures obtained for OmpF channel at PoPR=2.

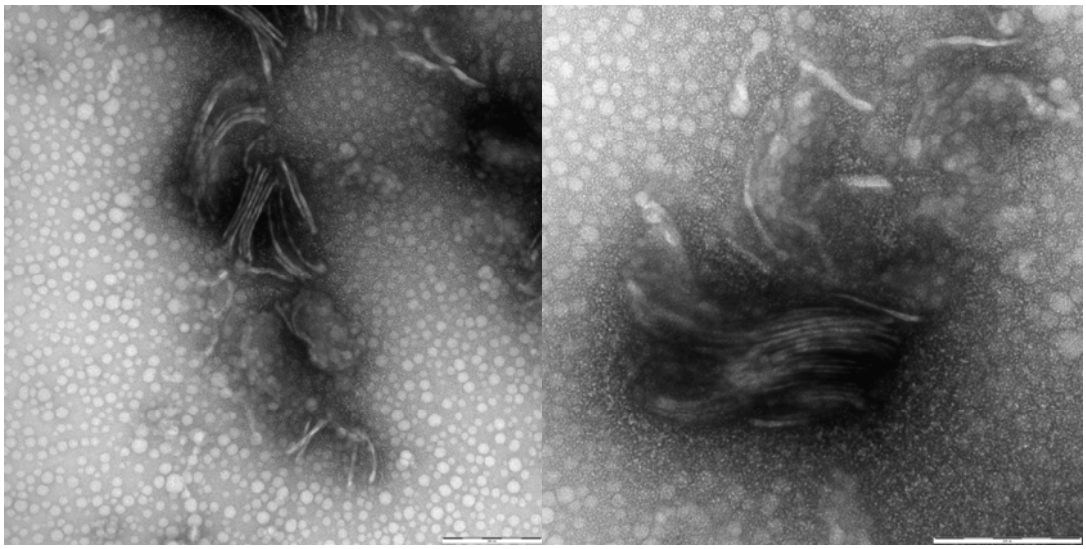

Figure 12. Electron micrographs of OmpF - copolymer crystals obtained at PoPR=2, with fast detergent removal. Scale bars: 200 nm.

F_oF_1 ATPase is the most fragile and the most complicated of the membrane proteins used in our 2D crystallization studies. In the case of this protein, detergent removal resulted in the formation of ordered structures. Figure 13 shows electron micrographs of the copolymer – ATPase ordered structures. Analysis of the obtained electron micrographs, based on the literature research, did not allow clear conclusions on membrane reconstitution or ATPase crystallization in ABA block copolymer system. It is difficult to assess whether the protein remained intact during detergent removal procedure, and to associate the ordered structures formed to either the protein or the copolymer.

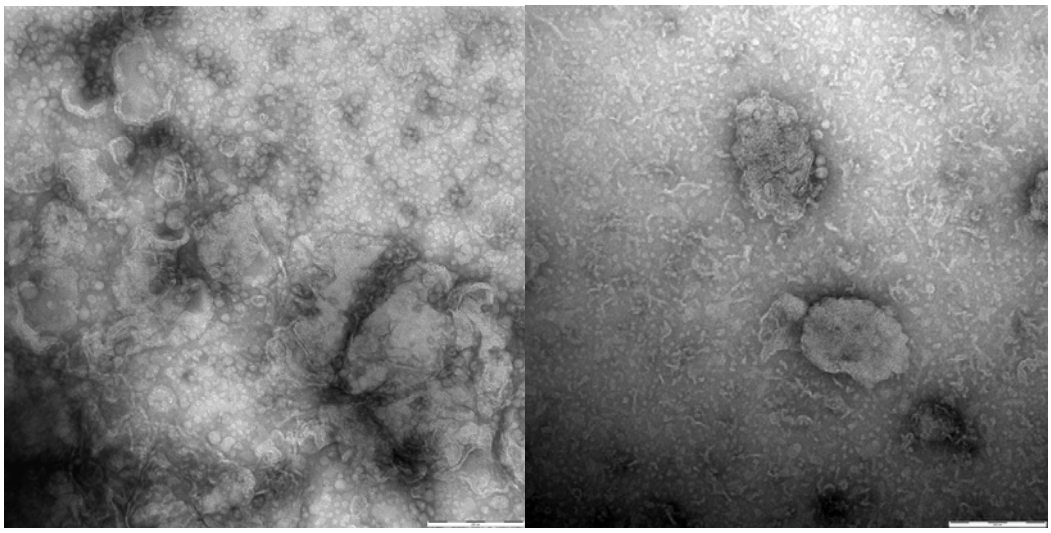

Figure 13. Electron micrographs of ATPase - copolymer aggregates, obtained at PoPR=2 (left), PoPR=0.2 (right), with slow detergent removal. Scale bars: 200 nm.

Detergent removal method, usually used for structure determination of membrane proteins in lipid-assisted 2D crystallization, was shown to be applicable for the membrane protein-block copolymer system. Densely packed protein arrays in block copolymer matrix were obtained in the case of almost all studied membrane proteins. In order to confirm crystallinity of the samples, further measurements of electron diffraction in transmission electron microscopy and/or cryogenic- transmission electron microscopy are required. Performing liquid state atomic force microscopy on the generated protein arrays would also allow structural protein studies. These measurements need to be performed.

1.2 $A_{12}B_{55}A_{12}$ block copolymer-assisted 2D crystallization of membrane proteins – template method

Membrane proteins bearing polyhistidine tag: AQP-Z and F_oF_1 ATPase were used in polymer monolayer templated crystallization. Figure 14 shows the outline of the experiments.

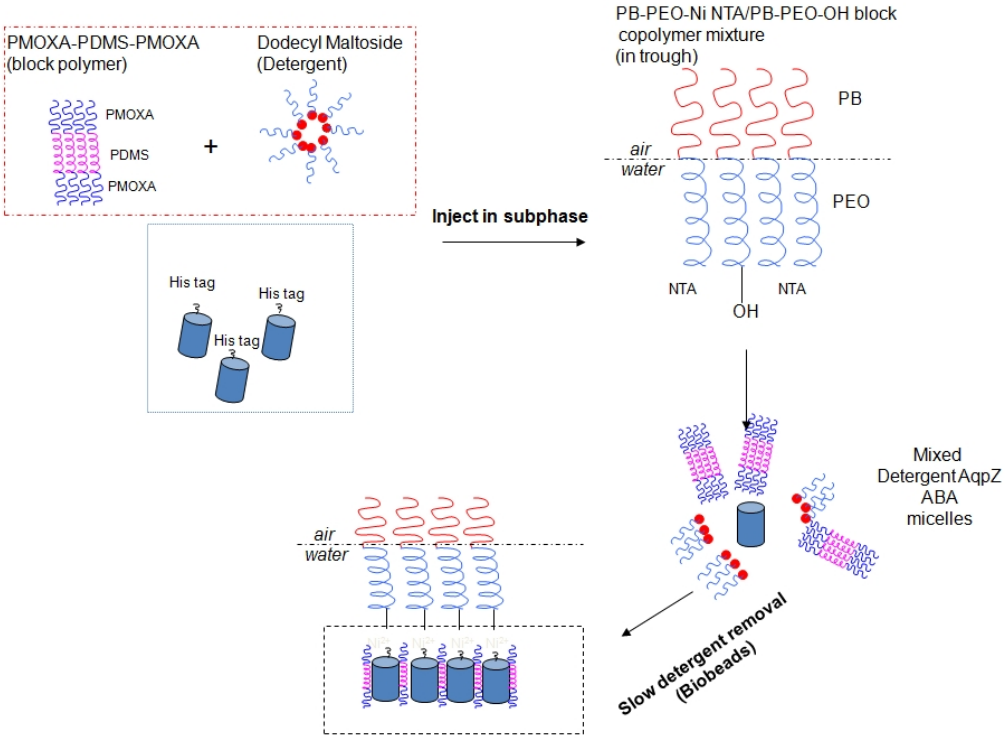

Figure 14. Outline of polymer monolayer template technique.

All experiments were performed in the Teflon troughs initially designed for lipid-templated 2D crystallization of membrane proteins.[5] The schematic design of the trough is shown in figure 15.

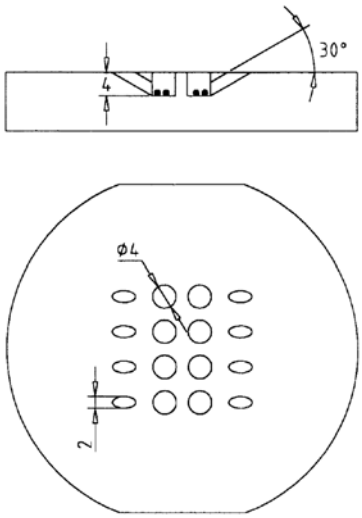

Figure 15. Teflon wells for lipid layer 2D crystallization experiments. Teflon plates consist of eight wells of about 60 µl. Each well is connected to a side hole which allows injections of either micellar protein solutions or Bio-Beads. Stainless steel beads of 1 mm diameter (black

circles) allow gentle stirring without perturbing the surface lipid layer. Side and top views of Teflon wells are drawn to scale.[5]

The concentration of the polybutadien-polyethylene oxide PB-PEO diblock copolymer forming the monolayer at the air-water interface was chosen on the basis of Langmuir monolayer experiments (not discussed in this thesis)[6]. The monolayer concentration of nickel complexes exposed to the water phase was regulated by mixing the nickel-NTA-functionalized diblock copolymer with native, hydroxyl-terminated one, at the ratio of 20/80 mol/mol. The ratio was adapted from procedures used in the lipid monolayer crystallization techniques.[5, 7] The membrane protein of interest was solubilized together with ABA polymer in 10% (w/v) DDM detergent solution. Concentrations and ratios targeted a protein concentration of 100 μg/L in the subphase. Resulting solutions were stirred overnight at 4°C. The trough wells were filled with the appropriate, filtered buffer. Monolayer of nickel-NTA-functionalized PB-PEO was formed at the water-air interface, by spreading of chloroform solution (0.6 μL). Upon evaporation of chloroform (ca. 1 h), the ternary mixture (ABA block copolymer and protein of interest) was added to the side port of the well. After stabilization of the mixture (ca. 1 h), appropriate amounts of Biobeads SM-2 were added every two hours. The resulting template-assembled protein arrays were transferred onto the plasma untreated, carbon-coated TEM grids. Grids were held by tweezers and dfilms were horizontally transferred from the air-water interface. After transfer, the resulting template-assisted assemblies were stained with 1% uranyl acetate, rinsed, dried and imaged with transmission electron microscopy. PoPR values and detergent removal rates were varied.

Conclusions drawn from the investigation of the detergent removal rate influence on the polymer template-assisted 2D crystallization of the membrane proteins using $A_{12}B_{55}A_{12}$ are that the fast detergent removal in ambient temperature is favored, and leads to formation of large areas of protein arrays. Figure 16 shows a large area of the TEM grid covered with a protein array.

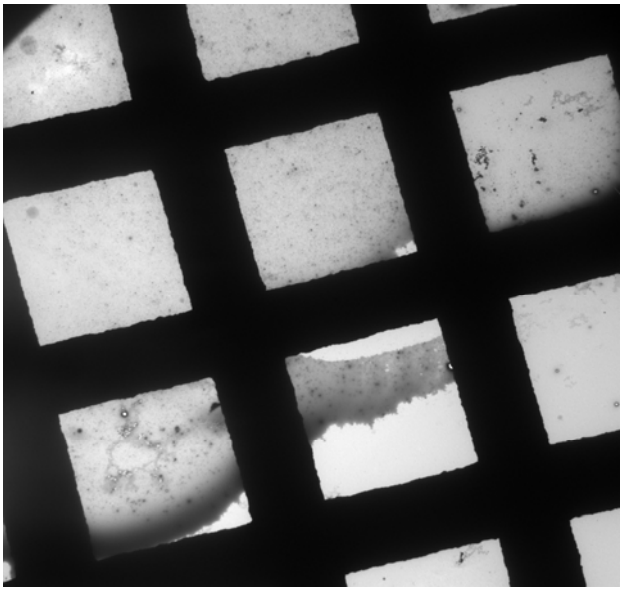

Figure 16. Electron micrograph of the stained PB-PEO template-assembled Aquaporin-Z array covering a large area of the grid.

The optimal PoPR values for polymer template-assisted crystallization of Aquaporin-Z were found in the range of 1-1.2 and resulted in protein-rich arrays. Figure 17 shows the comparison of the resulting template-assembled $A_{12}B_{55}A_{12}$ protein array, with the one utilizing lipid matrix as template.

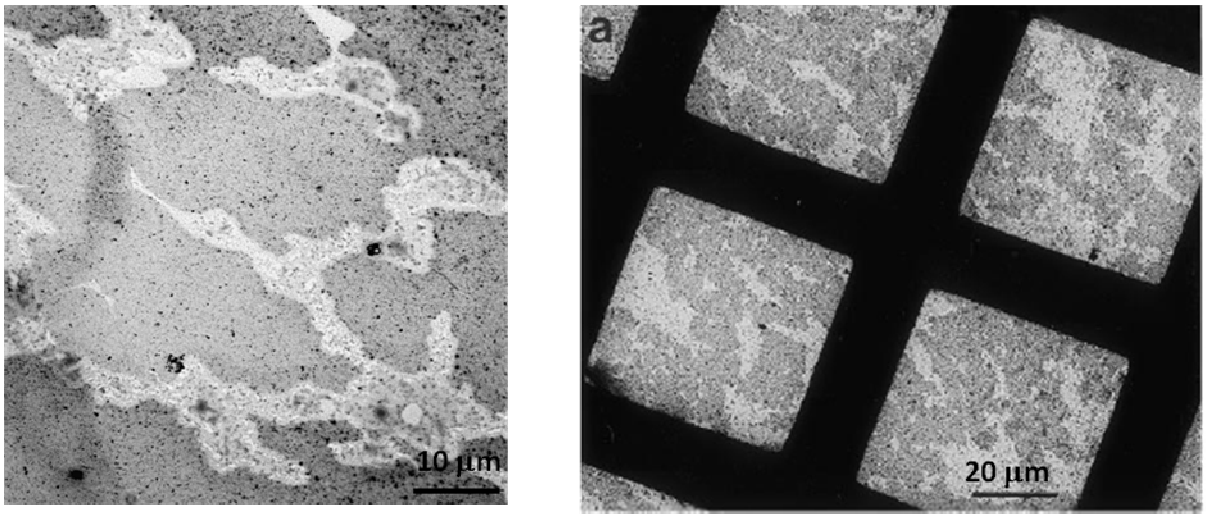

Figure 17. Comparison of the template-assembled $A_{12}B_{55}A_{12}$ - Aquaporin-Z array (left), with the one utilizing lipid matrix as template [5] (right) - TEM.

Figure 18 shows the set of template-assembled $A_{12}B_{55}A_{12}$ - Aquaporin-Z arrays with PoPR=1.

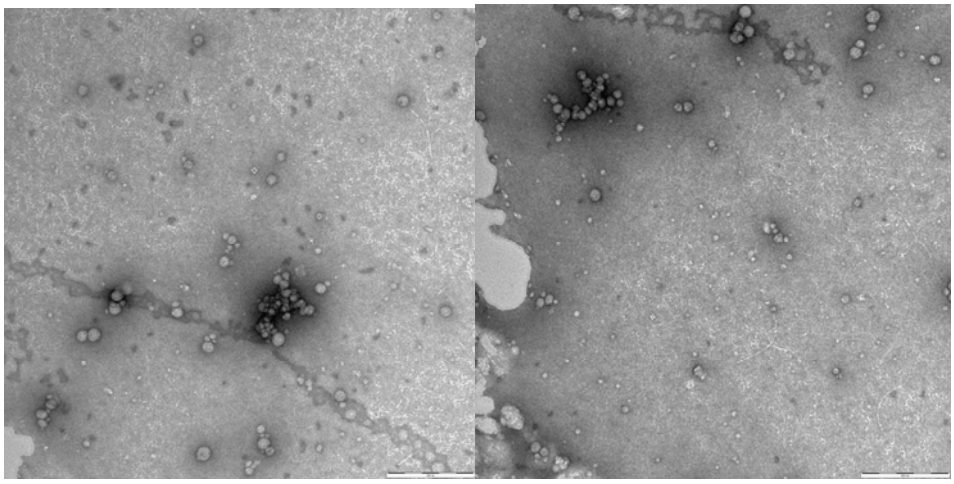

Figure 18. Template-assembled $A_{12}B_{55}A_{12}$ - Aquaporin-Z arrays with PoPR=1 (scale bars: 200 nm)

Figure 19 shows single and multi-stack $A_{12}B_{55}A_{12}$ - Aquaporine-Z arrays at PoPR=1.2. It is difficult to conclude whether the multi-stacking of the polymer-protein arrays occurs during the transfer to TEM grids, or is a property of the generated assemblies.

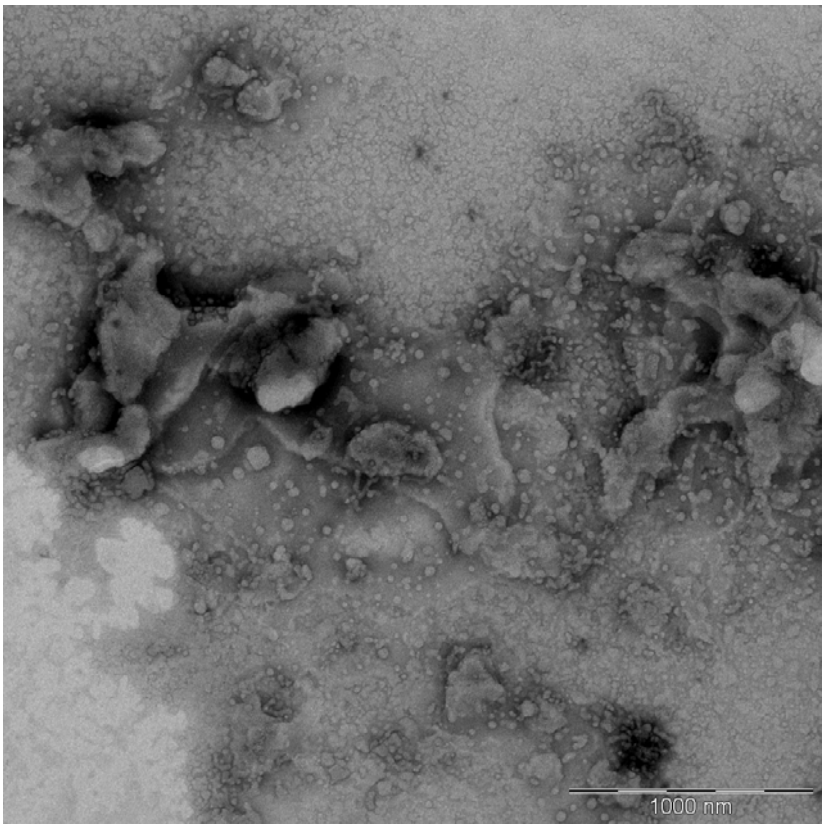

Figure 19. Template-assembled single and multi-stack $A_{12}B_{55}A_{12}$-Aquaporine-Z array with PoPR=1.2 - TEM (scale bar: 1000 nm).

Confirmation of crystallinity of those arrays and analysis of protein structure requires further analysis utilizing electron diffraction in transmission electron microscopy and/or cryogenic-transmission electron microscopy. Performing liquid state atomic force microscopy on the generated protein arrays would also allow additional structural protein studies. The choice of the hydrophobic substrate (highly ordered pyrolic graphite, for instance) for AFM experiments is preferable and would allow undisturbed transfer of the protein arrays to the substrate due to hydrophobicity match with the surface of the PB-PEO template at the water air interface. These measurements are not discussed in this thesis.

In case of FoF1 ATPase template monolayer crystallization attempt, the control experiments showed template reconstitution of the membrane proteins into the structures built by lipid molecules present in the stock solution of the protein. Due to the high lipid concentration in the stock solution of the protein, further experiments were put on hold until the source of the lipid free protein is established.

2. ABA polymer vesicle reconstitution with FoF1

Biomimetics has proved very useful in the design and fabrication of new functional, structured materials on the micro- and nanometer scale (reference). Biomimetic refers to human-made processes, devices, or systems that mimic or imitate certain aspects of biological systems; this has proven possible using biological inspiration from efficient natural designs. Biomimetics is not limited to just copying nature: scientists can directly utilize biological units themselves, taking advantage of the development of modern biology, in order to construct hybrid nanostructured materials. Thus, some of the manufacturing difficulties of biomimetics can be avoided. Active proteins, such as kinesin, myosin, and ATP synthase (or ATPase) are called ‘‘molecular motors’’ and play an essential role in the cell activity and regulate specific functions through their stimuli-responsive mechanical motions. The confluence of scientific developments in modern biology and nanoscience now offers the potential to design functional hybrid nanomaterials. A major challenge for the construction of functional hybrid nanomaterials is how to integrate natural molecular machines such as motor proteins into the engineered, active biomimetic systems.[8]

Molecular motors such as myosin, kinesin, dynein and ATPase abound in living cells. Myosin motors drive muscle contraction and kinesin or dynein motors transport vesicles from one end of the cell to the other. All of these linear motors are supplied by biological energy through hydrolysis of the universal ‘‘fuel’’ molecule, adenosine 50-triphosphate (ATP). The F_0F_1-ATP synthase (or F_0F_1 ATPase) is responsible for the catalytic synthesis of ATP molecules in biological organisms. They are widely present in the membranes of mitochondria, chloroplasts and prokaryotic cells, where they convert transmembrane electrochemical proton gradients into ATP. The F_0F_1-ATPase is a well-known rotary motor and probably the best-understood biological molecular motor. It comprises two separate domains: F_0, the hydrophobic membrane-bound portion that is responsible for proton translocation and F_1, which is responsible for ATP hydrolysis or synthesis. The extramembranous F_1 catalytic subcomplex is attached to the membrane-intrinsic F_0 subcomplex by a central stalk and a peripheral stalk. Synthesis of ATP in F_1 is driven by rotation of the central stalk, driven by protons passing through the membrane domain F_0. The enzyme can also catalyze the reverse reaction, with ATP hydrolysis in F_1 driving proton pumping in F_0. The rotor is formed by the central stalk and a ring of C subunits in F_0 which contain an essential carboxylic group. Rotation is generated by the binding and release of protons to the carboxylic group in the C-

ring as it enters the interface with the membrane subunit A of F_0. The peripheral stalk acts as a stator that prevents the a3b3-subcomplex in F_1 from following the rotation of the central stalk. Direct proof of the rotation of the central stalk within F_1-ATPase hydrolysis was obtained by monitoring a fluorescently labeled actin filament or a micrometer particle to the g subunit. This experiment provided important insights into the mechanism of this molecular motor. Another important work (ref) showed an ATP-powered motor with nanofabricated propellers linked to the genetically engineered protein F_1-ATPase. The rotational motion of F_1-ATPase was coupled with hydrolysis of ATP. The work showed that F_1-ATPase possesses energy transduction properties, that is, can convert chemical energy to mechanical energy. As a rotary molecular motor and ATP producer, the ATPase has attracted great interest and demonstrated numerous potential applications, from the generation of bioenergy to the design of novel nanodevices.[8]

In order to enable fusion of nanotechnology with biology and study the possibility of incorporation of active biological molecular motor protein into synthetic PMOXA-PDMS-PMOXA membranes, insertion of (*E. coli* derived) EF_0F_1 ATP synthase, into polymeric ABA block copolymer vesicles was performed. Reconstitution procedures involved detergent removal method and membrane destabilization method. Initial experiments involving detergent removal method are not discussed here. All conclusions drawn from those studies are summarized with results from membrane destabilization procedures.

Polymer vesicles were prepared from two polymer batches, $A_{12}B_{55}A_{12}$ and $A_{21}B_{54}A_{21}$; with two preparation methods (film hydration and solvent displacement method). In film hydration method, 50 mg of each polymer was solubilized in chloroform in a round bottom flask. Evaporation of the solvent on rotary evaporator led to formation of thin films. Films were hydrated by 10 ml of HEPES buffer by rotation on rotary evaporator for 3 h and left stirred over night. Turbid solutions were filtered 5 times via 0.45 μm membranes on the barrel extruder (pressure 10 bar) and 15 times via 0.22 μm membranes, resulting in homogeneous turbid solutions. In solvent displacement method, 100 mg of polymers were dissolved in 0.5 ml of absolute ethanol and added dropwise to 10 ml of stirred HEPES buffer. The solutions were stirred overnight and extruded as described above. Resulting solutions were slightly turbid, indicating the higher amount of micellar aggregates in solution in comparison to the ones obtained with film rehydration.

Electron microscopy micrographs of polymer vesicles were recorded with PhilipsCM100 microscope at 80 kV. Figure 20 shows micrographs of stained vesicles prepared with $A_{12}B_{55}A_{12}$ block copolymer in film hydration method and figure 21 - of stained vesicles prepared with $A_{21}B_{54}A_{21}$ commercial polymer (PolymerSource, Canada).

FoF1 reconstitution

Polymer vesicles were destabilized by incubation with sodium cholate for 3 h (0.5% w/v cholate final concentration). All further treatment was done on crushed ice. To destabilized vesicles, the stock solution of EF_0F_1 was added to reach the polymer to protein ratio of 50:1, and incubated with gentle shaking for 30 minutes. Resulting solutions were purified (detergent removal) on NAP5 columns equilibrated with cold HEPES buffer. Turbid fractions were collected and used immediately for activity assays.

Activity assays

The assay follows the procedure developed for liposome reconstitution with F_0F_1 (azolectin) involving 9-amino-6-chloro-2-methoxyacridine (ACMA) kinetic fluorescence quenching, upon addition of ATP, and fluorescence recovery upon addition of $(NH_4)_2SO_4$. In the assay, 100 µl of eluted sample was diluted with 900 µl of HEPES buffer and 0.2 µl of ACMA stock solution (30 µM final concentration). The fluorescence of samples with the dye was measured at the excitation of 410 nm and emission of 490 nm (slit width 3 nm). The quenching was performed by addition of 10 µl of 0.1 M ATP solution and the kinetic decrease of fluorescence intensity was recorded for proteopolymerosomes. The immediate fluorescence restoration was observed upon addition of 5 µl of saturated $(NH_4)_2SO_4$ solution. All of the proteopolymerosomes samples follow the same behavior (see Figure 20), with minor deviations of intensity, related to the preparation method. The proteopolymerosomes show kinetic quenching of the fluorescence intensity of the ACMA pH-sensitive dye, indicating proton pumping activity of the protein. Control measurements with polymer vesicles alone show no kinetic activity quenching (Figure 21).

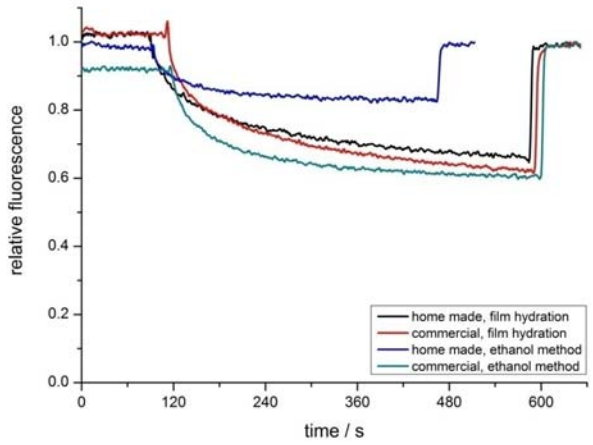

Fig 20. Fluorescence quenching in proteopolymersomes.

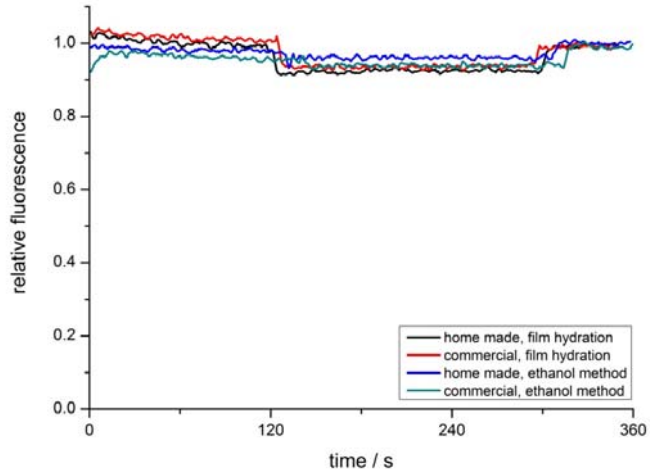

Fig 21. No kinetic fluorescence quenching for polymer control samples.

The initial conclusions of successful synthetic membrane reconstitution with the motor protein were doubtful, as the protein control sample of the stock solution investigated with the same assay showed higher activity, than in the case of proteopolymersomes (Figure 22). Activity observed in control stock protein solution shows that the protein is stored in proteoliposomal form. This result indicates that lipid molecules (0.8 % w/v) present in stock protein solution, when incubated with destabilized vesicles form either mixed aggregates with block copolymer molecules, or pure proteoliposomes upon detergent removal. The removal of the lipid molecules from the stock solution, on the other hand, may trigger protein denaturation.

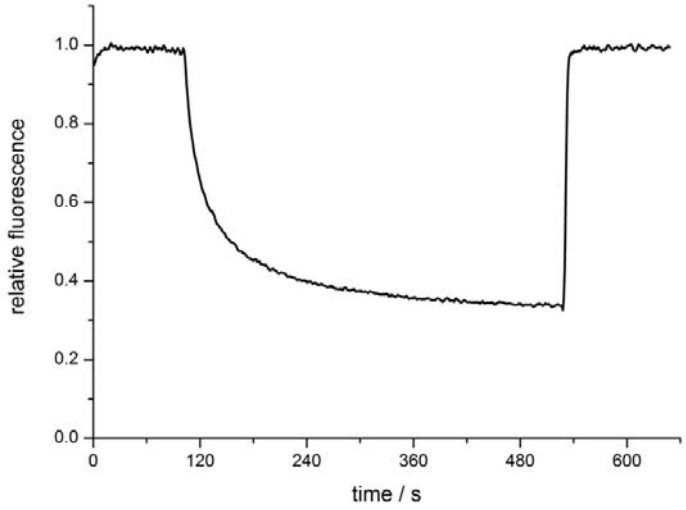

Fig 22. Fluorescence quenching in enzyme control sample.

The results of the experiments do not allow clear conclusions on whether the activity in sample solutions comes from proteopolymerosomes, mixed lipid-polymer aggregates or purely lipidic vesicles.

The encountered problem could be potentially overcome by fluorescent dye labeling of the protein, polymer and/or lipid, and performing FCS measurements. This could lead to relatively easy conclusions on incorporation of the lipid molecules in the polymeric membrane together with the inserted enzyme. Thus, the most promising way to approach and overcome the "lipid problem" is to prepare the enzyme stock solutions without lipid addition during the extraction step, and in parallel to perform protein extraction with ABA block copolymer as an alternative amphiphile, to have the opportunity of working with a more defined system.

Conclusions drawn from the activity assays were additionally confirmed by means of attempts of crystallization of F_0F_1 ATPase with monolayer technique. The stock solution of the protein showed reconstitution into lipid aggregates and the influence of the polymer cannot be assessed . See chapter 1 of appendix.

Materials and methods

Buffer composition

HEPES buffer

20 mM HEPES/KOH (pH 8.0), 100 mM KCl, 5 mM $MgCl_2$, 0.1 mM EDTA

Extraction buffer

50 mM Tris/HCl (pH 7.5), 100 mM KCl, 250 mM sucrose, 40 mM aminocaproic acid, 15 mM p-aminobenzamidine, 5 mM $MgCl_2$, 0.1 mM EDTA, 0.8 % (w/v) asolectin, 0.5 % sodium deoxycholate, 0.5 % (w/v) sodium cholate, 1.5 % (w/v) octylglucoside, 2.5 % (w/v) glycerol, 30 mM imidazole

3. TEM of the block copolymer library

Direct visualization of PMOXA-PDMA-PMOXA vesicles in TEM is difficult, due to the high vacuum in the microscope chamber (high vacuum). Therefore most of the samples were stained with uranyl acetate. Appropriate dilution and successful staining results in either staining of the vesicular wall, or visualization of the aggregates by exclusion of the stain, from the area where the aggregate was present. Exclusion of the staining agent makes the aggregates appear bright in the dark area of the stain.

Vesicles solutions were usually diluted 100-fold with appropriate aqueous solution (pure water or buffer). Typically 5 µL of the sample solution was deposited on a carbon-coated 300 mesh copper grid. After 1 minute incubation the remaining liquid was blotted, washed 2 times with pure water, and stained with 2% uranyl acetate by 10 seconds incubation followed by blotting. Samples were imaged with a Philips CM100 268D operated at 80 kV.

Figure 23 shows the only successful direct visualization of $A_{13}B_{110}A_{13}$ and Figure 24 of $A_{15}B_{110}A_{15}$ vesicles.

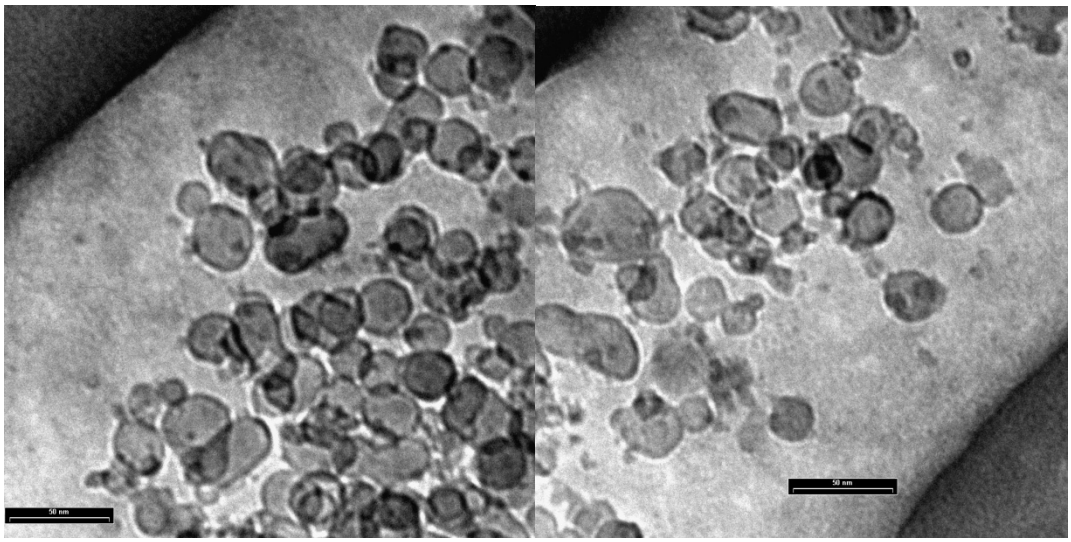

Figure 23. TEM micrographs of direct visualization of $A_{13}B_{110}A_{13}$ vesicles prepared with film hydration method.

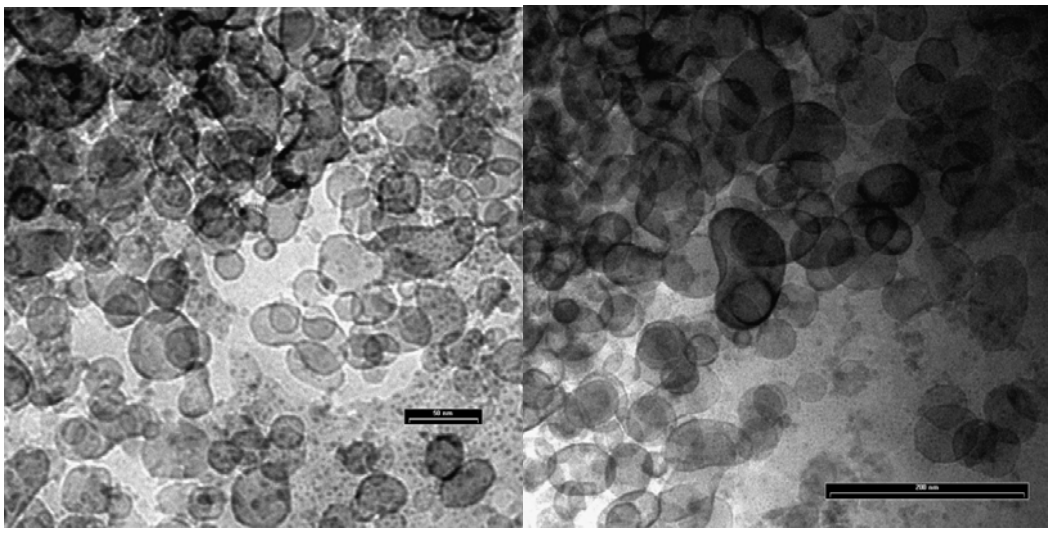

Figure 24. TEM micrographs of direct visualization of $A_{15}B_{110}A_{15}$ vesicles prepared with film hydration method.

As direct visualization of the vesicles was problematic due to destructive effect of vacuum on the vesicular structures, staining became a routine part of the visualization of aggregates in TEM. Figure 25 shows series of TEM micrographs of stained vesicles prepared with solvent replacement method for: $A_9B_{106}A_9$, $A_{65}B_{165}A_{65}$, $A_{13}B_{110}A_{13}$ and $A_{15}B_{110}A_{15}$.

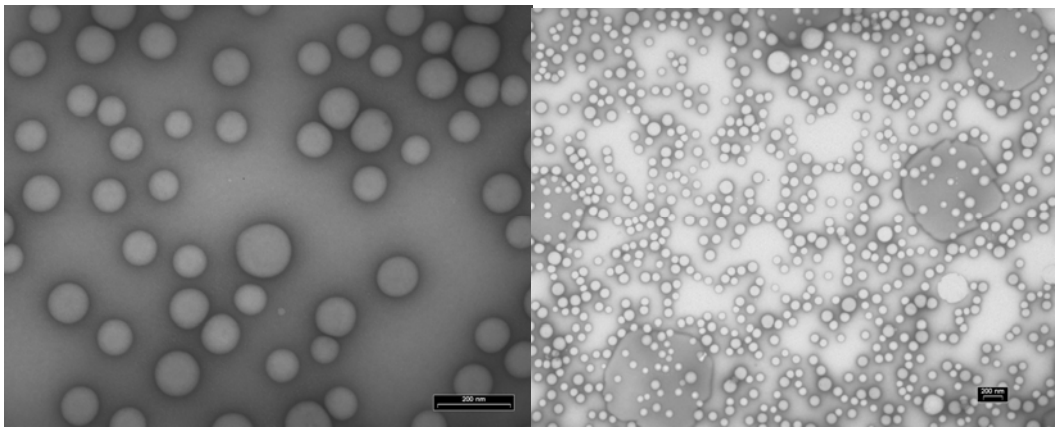

A). $A_9B_{106}A_9$

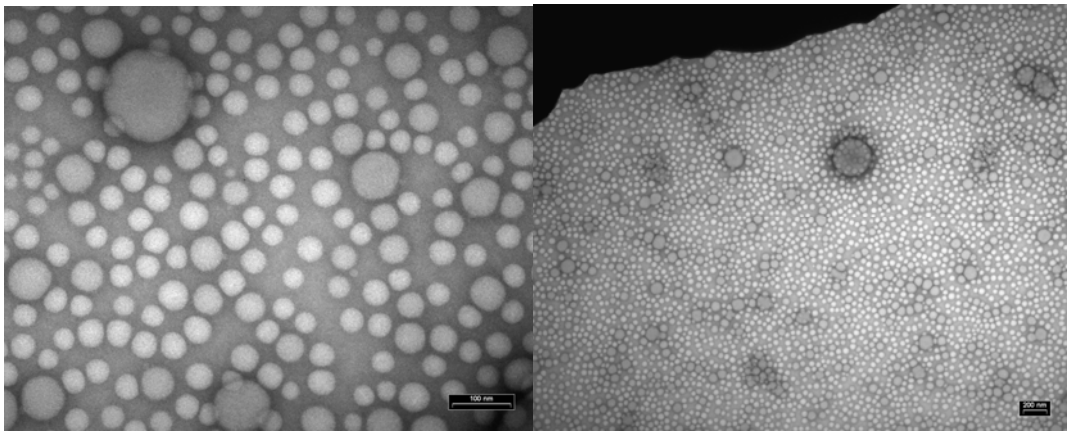

B). $A_{65}B_{165}A_{65}$

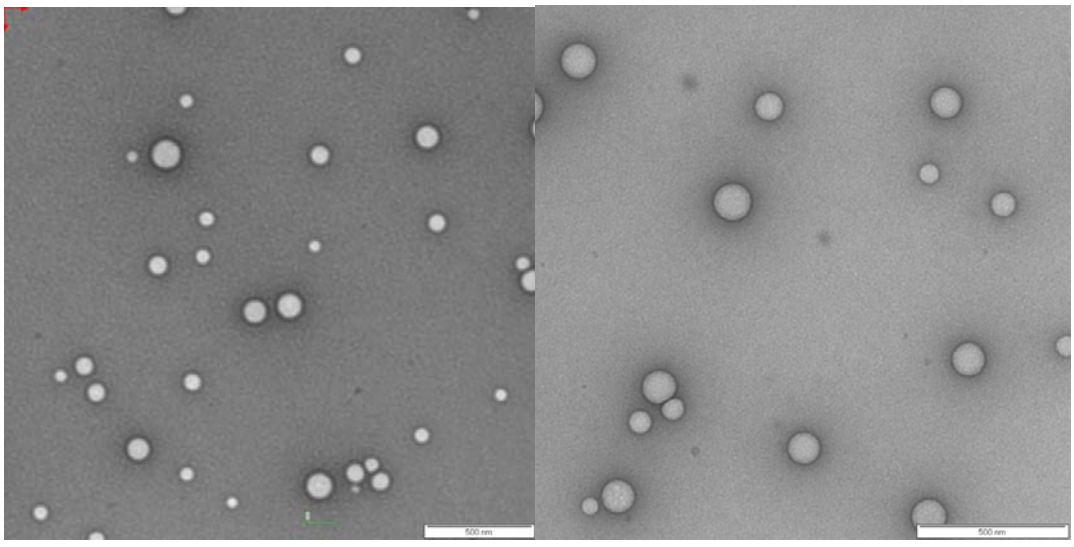

C). $A_{13}B_{110}A_{13}$

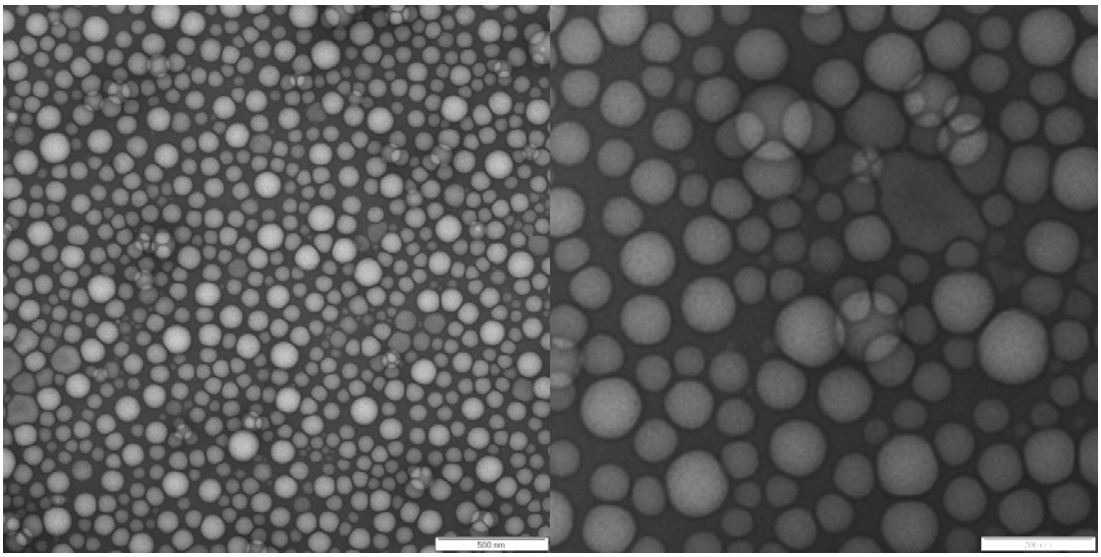

D). $A_{15}B_{110}A_{15}$

Figure 25. Series of TEM micrographs of stained vesicles prepared with solvent replacement method for: $A_9B_{106}A_9$ - (A), $A_{65}B_{165}A_{65}$ – (B), $A_{13}B_{110}A_{13}$ – (C) and $A_{15}B_{110}A_{15}$ – (D).

Vesicles prepared in film hydration method were imaged with TEM. Figure 26 shows TEM micrographs of stained vesicles of $A_{12}B_{55}A_{12}$ prepared in film hydration method. Figure 27 shows TEM micrographs of the commercial $A_{21}B_{54}A_{21}$ polymer prepared in film hydration method.

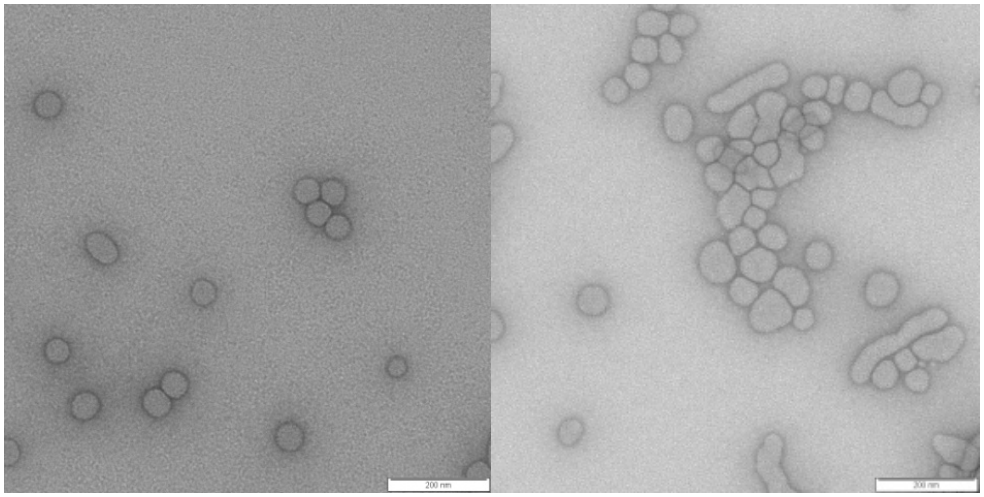

Fig 26 . TEM micrographs of $A_{12}B_{55}A_{12}$ block copolymer vesicles prepared with film hydration method.

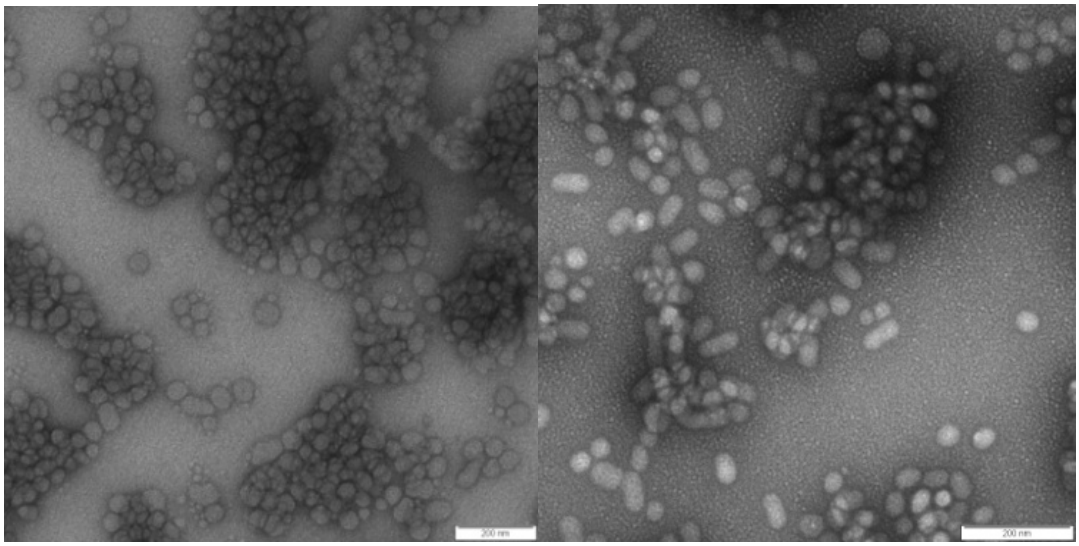

Fig 27 . TEM micrographs of $A_{21}B_{54}A_{21}$ block copolymer vesicles prepared with film hydration method.

The detergent removal method introduced and discussed in the chapter 2.2.1.2 of the main part of the thesis results in formation of aggregates of different sizes dependent on the detergent removal rate. Figure 29 shows small vesicles/micelles prepared by BioBeads SM-2 fast detergent removal (10% sodium cholate removed in 8 h).

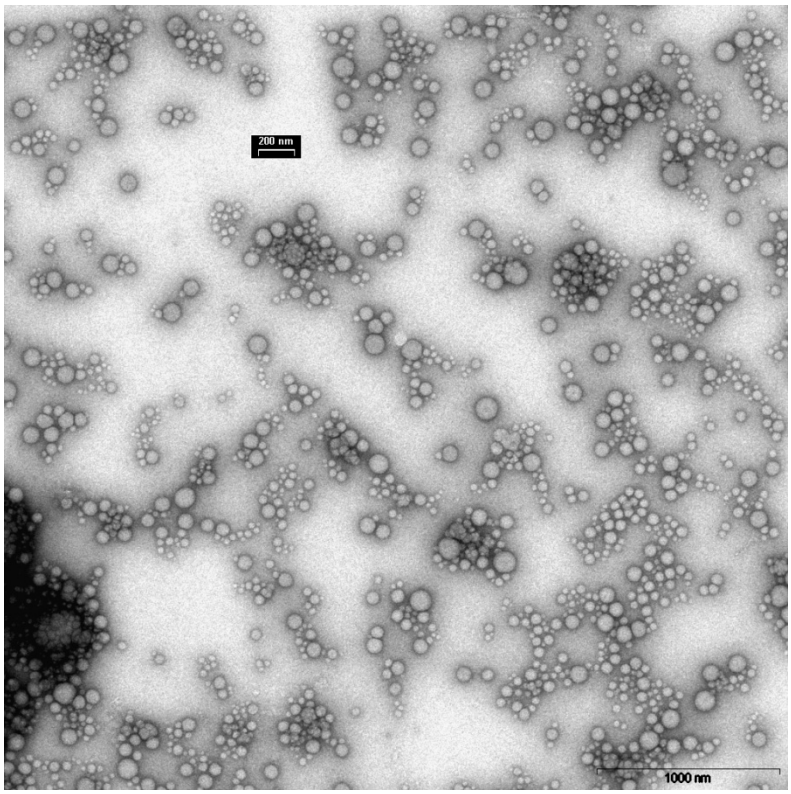

Figure 29. TEM micrograph of stained small vesicles/micelles prepared from $A_{65}B_{165}A_{65}$ by fast detergent removal.

TEM analysis of investigated vesicles solutions showed formation of vesicles (direct visualization) and formation of spherical aggregates (stained samples). In cases of TEM imaging of stained samples the morphology of the aggregates is not being resolved (micellar vs. vesicular structures). Nevertheless careful TEM analysis taking into account staining artifacts, combined with additional characterization techniques (DLS/SLS) provided significant information on self-assembly properties of investigated block copolymers.

REFERENCES

1. Hasler, L., et al., *2D crystallization of membrane proteins: rationales and examples.* J. Struct. Biol., 1998. **121**(2): p. 162-171.
2. Rigaud, J.L., et al., *Detergent removal by non-polar polystyrene beads. Applications to membrane protein reconstitution and two-dimensional crystallization.* Eur. Biophys. J., 1998. **27**(4): p. 305-319.
3. Ringler, P., et al., *Structure of the water channel AqpZ from Escherichia coli revealed by electron crystallography.* J. Mol. Biol., 1999. **291**(5): p. 1181-1190.
4. Arechaga, I. and D. Fotiadis, *Reconstitution of mitochondrial ATP synthase into lipid bilayers for structural analysis.* J. Struct. Biol., 2007. **160**(3): p. 287-294.
5. Levy, D., et al., *Two-Dimensional Crystallization on Lipid Layer: A Successful Approach for Membrane Proteins.* J. Struct. Biol., 1999. **127**(1): p. 44-52.
6. Nehring, R., et al., *Amphiphilic Diblock Copolymers for Molecular Recognition: Metal-Nitrilotriacetic Acid Functionalized Vesicles.* Langmuir, 2009. **25**(2): p. 1122-1130.
7. Mosser, G., *Two-dimensional crystallogenesis of transmembrane proteins.* Micron, 2001. **32**(5): p. 517-540.
8. He, Q., et al., *Microcapsules containing a biomolecular motor for ATP biosynthesis.* Adv. Mater. (Weinheim, Ger.), 2008. **20**(15): p. 2933-2937.

Mariusz Grzelakowski

m.grzelakowski@unibas.ch

Education

- **University of Basel, Basel, Switzerland**
  PhD candidate in Physical Chemistry, Department of Chemistry, May 2009
- **Nicholas Copernicus University, Toruń, Poland**
  Master of Science in Polymer Chemistry, Department of Chemistry, 2002
- **Nicholas Copernicus University, Toruń, Poland**
  Bachelor of Science in Polymer Chemistry, Department of Chemistry, 2000

Research Experience

Research Assistant (Advisor: Professor Wolfgang Meier)
University Basel, Basel, Switzerland
Dissertation: *Development, characterization and application of biomimetic block copolymer membranes*

- Synthesis, modification and characterization of bio-inspired, self assembling, amphiphilic block copolymers
- Studies involved novel combinations of synthetic polymer membranes with biological proteins for development of desalination membranes and surface immobilized nanoreactors
- Managed collaborations with multiple research groups across Europe and US
- Coordinated the work of new graduate and undergraduate students

Research Assistant (Advisor: Professor Wojciech Czerwinski)
Nicholas Copernicus University, Toruń, Poland
Thesis: *Conductive polymers based on polythiophenes*

- Conducted research on the synthesis and modification of polythiophene based conductive copolymers
- Investigated doping effects for potential application in sensors

Undergraduate Research Assistant (Advisor: Professor Wojciech Czerwinski)
Nicholas Copernicus University, Toruń, Poland
Thesis: *Recycling of polyamide 66*

- Investigated industry recycling procedures for nylon 66 used in carpets and suggested improvements

Professional Experience

LEAD DISCOVERY CENTER, Novartis Pharma AG Basel 2003 - 2004
Chemist.

- Classification and registration of pharmaceutical compounds, intermediates and natural products according to their chemical and structural properties
- Evaluation of suitability of compounds for high throughput screening
- Operation of the newly built automated solution production robot

DEVELOPMENT DIVISION, Zachem S.A. Bydgoszcz, Poland 2002 - 2003
Technology Specialist.

- Planning development areas for company involved in producing polymer intermediates
- Assistance with technology and production organization and recognition of product markets, technology availability, license, know-how
- Supervision of realization of strategic company development plans

Activities

- Teaching Assistant Physical Chemistry Lab Courses
- Mentoring new graduate students
- Conference organization

Skills and Competence

- Diverse laboratory techniques in polymer synthesis, separation, and analysis: Nuclear Magnetic Resonance, Gel Permeation Chromatography, UV-Vis spectrometry, Fluorimetry, Membrane and Vapor Osmometry
- Diverse characterization techniques Transmission Electron Microscopy, cryogenic-Transmission Electron Microscopy, Atomic Force Microscopy, Fluorescence Correlation Spectroscopy, Laser Scanning Microscopy, Quartz Cristal Microbalance, Dynamic and Static Light Scattering, Stopped-flow spectroscopy, Chromatography
- Computer, software and database usage – including specialist chemistry software and database products
- Languages: English – fluent, German – basic, Polish – native

Professional Affiliations and Collaborations

- Swiss Chemical Society
- NanoMot
- PolyAmphi
- University of Illinois – M. Kumar, Dr. M. Clark, Dr. J. Zilles
- University of Osnabrueck – Dr. W. Junge
- ETH Zurich – Dr. R. Kissner
- Technical University of Eindhoven - Dr. N.A.J.M. Sommerdijk
- Biozentrum Basel – Dr. A. Engel
- University of Bayreuth – Dr. A. Mueller

Publications and Patents

1. M. Kumar, **M. Grzelakowski,** J. Zilles, M. Clark, W. Meier. Highly permeable polymeric membranes based on the incorporation of the functional water channel protein Aquaporin Z. *Proceedings of the National Academy of Sciences of the United States of America* (2007), 104(52), 20719-24.

2. **M. Grzelakowski**, O. Onaca, P. Rigler, M. Kumar, W. Meier. Immobilized Protein-Polymer nanoreactors. *In submission process to the Nano Letters (ACS publications) and to the European Patent Office.*

3. M. Kumar, **M. Grzelakowski**, M. Clark, W. Meier, J. Zilles. pH gating of Aquaporin Z reconstituted into triblock copolymer membranes and in whole cells *In submission process to Science/AAAS.*

4. C. Fraysse-Ailhas, A. Graff , C. G. Palivan, **M. Grzelakowski**, T. Friedrich, C. Vebert, G. Gescheidt, W. Meier Amphiphilic copolymer membranes promote NADH: Ubiquinone Oxidoreductase activity: An Electron-Transfer Nanodevice. *In submission process to the Proceedings of the National Academy of Sciences of the United States of America.*

5. P. Broz, N. Ben-Haim, **M. Grzelakowski,** S. Marsch, W. Meier, P. Hunziker. Inhibition of Macrophage Phagocytotic Activity by a Receptor-targeted Polymer Vesicle-based Drug Delivery Formulation of Pravastatin. *Journal of Cardiovascular Pharmacology* (2008), 51(3), 246-252.

6. O. Onaca, P. Sarkar, D. Roccatano, T. Friedrich, B. Hauer, **M. Grzelakowski**, A.Guven, M. Fioroni, and U. Schwaneberg. Functionalized Nanocompartments (Synthosomes) with a Reduction-Triggered Release System *Angewandte Chemie* (2008), 47(37), 7029-7031.

7. K. Kita-Tokarczyk, F. Itel, **M. Grzelakowski**, S. Egli, P. Rossbach, W. Meier Monolayer Interactions between Lipids and Amphiphilic Block Copolymers. In submission process to the Journal of the American Chemical Society (ACS Publications).

8. M. Kumar, W. Meier, J. Zilles, M. Clark, **M. Grzelakowski,** R. Nehring. Highly permeable polymer membranes, US Provisional Patent number 60992660, filed Dec 5th, 2007, Assignee: University of Illinois.

9. V. Malinova, L. Kind, **M. Grzelakowski** Polymer-based Nanostructures: Medical Applications. Chapter: Strategies for triggered release from polymer based nanostructures. Submitted to Royal Society of Chemistry Publishing

Abstracts and Presentations

1. **Block copolymer vesicles for biological membrane mimetics**; Nanosciencetech Summer School *Nanobio: The live cell from nano to micro*: *Mind the gap* CNRS, Corsica, France, 2006
2. **Block copolymer based vesicles as carriers and biological membrane mimetics;** BIOSURF VII, Zurich, Switzerland, 2007
3. **Block copolymer based vesicles carriers**; Swiss Chemical Society Fall meeting, Lausanne, Switzerland, 2007
4. **Novel membranes for water treatment**, PolyAmphi Summer School *Polyelectrolytes in solutions and at interfaces: synthesis, theory, applications,* Biezenmortel, Netherlands, 2007
5. **Block copolymer vesicles** SONS Polymers, Amph. and Nanost. Mat. Workshop, Bristol, UK, 2007
6. **Inhibition of macrophage phagocytotic activity by a receptor-targeted polymer vesicle-based drug delivery formulation of pravastatin;** Swiss Medical Forum, Lausanne, Switzerland, 2008
7. **Antioxidant nanoreactors: A way to fight superoxide radicals in oxidative stress,** Swiss Chemical Society Fall meeting, Zurich, Switzerland 2008
8. **Block copolymer nano-reactors;** Polymers in Life Sciences, 2008, Basel
9. **Amphiphilic Block Copolymers for Selective Protein Immobilization,** NANOMOT, Zurich, Switzerland, 2009
10. **pH gating of the bacterial water channel protein Aquaporin Z**, selected for presentation at the American Society of Microbiology Symposium, Philadephia, May 2009

References

Dr. Wolfgang Meier
Department of Chemistry
University of Basel
Phone +41 (0)61 267 38 02 (direct)
wolfgang.meier@unibas.ch
Klingelbergstrasse 80
CH-4056 Basel, Switzerland

Dr. Ulrich Schopfer
Director, Head Biochemical Screening
Novartis Institutes for BioMedical Research
Phone: +41 61 3244951 (direct)
ulrich.schopfer@novartis.com
WSJ-88.10.11 CH-4056 Basel/Switzerland